

Doctoral thesis

**DIRECT NUMERICAL SIMULATIONS
OF THE IGNITION CHARACTERISTICS
OF HYDROCARBON FUEL/AIR
MIXTURES UNDER HCCI/SCCI/RCCI
CONDITIONS**

Minh Bau Luong

Department of Mechanical Engineering
Ulsan National Institute of Science and Technology
(UNIST)

2017

**DIRECT NUMERICAL SIMULATIONS
OF THE IGNITION CHARACTERISTICS
OF HYDROCARBON FUEL/AIR
MIXTURES UNDER HCCI/SCCI/RCCI
CONDITIONS**

Minh Bau Luong

**Department of Mechanical Engineering
Ulsan National Institute of Science and Technology
(UNIST)**

Direct Numerical Simulations of the Ignition
Characteristics of Hydrocarbon Fuel/Air Mixtures
under HCCI/SCCI/RCCI Conditions

A dissertation
submitted to the Graduate School of UNIST
in partial fulfillment of the
requirements for the degree of
Doctor of Philosophy

Minh Bau Luong

05th June, 2017

Approved by

Advisor
Chun Sang Yoo

Abstract

This study investigates the ignition characteristics of various hydrocarbon fuel/air mixtures under homogeneous charge compression ignition (HCCI) conditions using direct numerical simulations (DNS). The ignition processes of various types of HCCI combustion including HCCI with thermal stratification (TS), stratified-charge compression ignition (SCCI), and reactivity-controlled compression ignition (RCCI), and direct dual fuel stratification (DDFS) are numerically studied. HCCI engines are designed to operate under low-temperature conditions by utilizing ultra-lean, highly-diluted, well-mixed fuel/air mixture like SI engines while relying on compression ignition by an elevated compression ratio like diesel engines. Accordingly, HCCI combustion can provide high diesel-like thermal efficiency while avoiding excessive NO_x and particulate emissions. Therefore, prototypes of the HCCI combustion engines have been developed as an alternative to conventional gasoline and diesel engines. However, several key issues still remains unresolved in the development of HCCI combustion engines: for instance, how to control the ignition timing and how to mitigate excessive heat release rate (HRR) under a wide range of load conditions. Therefore, several variants of HCCI combustion are developed to overcome these issues.

With the help of high-fidelity DNSs, fundamental understanding of the combustion modes, flame speeds, turbulence-chemistry interactions, key species and controlling reactions of the variants of HCCI combustion can be obtained. The main objectives of the study are (1) to provide more insights into the effect of thermal and compositional stratification levels under different temperature regimes, and fuel compositions on the ignition mechanism of HCCI combustion; (2) to investigate the relative effect of $T/\phi/\text{PRF}$ stratifications coupled with the turbulence effect on the ignition process and combustion mode of HCCI/SCCI/RCCI using several different fuels including primary reference fuels (PRFs), *n*-heptane, and biodiesel; (3) to identify the key species and critical reactions of the SCCI and RCCI combustion using chemical explosive mode analysis (CEMA); and finally (4) to elucidate the effect of the late-direct-injection timing on the DDFS combustion process by developing a pseudo-*iso*-octane model. The results of this study can aid in the development of the next-generation high-efficiency IC engines.

By systematically investigating the effects of T , ϕ and PRF inhomogeneities and their relative roles on the HCCI combustion process at the low-, intermediate-, and high-temperature chemistry regimes, the generalization of their effects on the HCCI combustion is made. It was found that the effect of thermal and compositional stratifications on HCCI combustion, in general, depends on the initial mean temperature, T_0 , of the fuel/air mixture. TS is most effective at the high-temperature chemistry (HTC) regime regardless of fuel types (i.e. both single- and two-stage ignition fuels). Similar to the single-stage ignition fuels, with T_0 lying within the HTC regime in which only the HTC governs the ignition, the mean HRR of the two-stage ignition fuels is more distributed over time, and its peak HRR is more reduced with increasing T' . On the contrary, for the two-stage ignition fuels with T_0 lying within the LTC and ITC regime, ϕ and PRF stratifications play dominant roles in enhancing deflagration mode, and thereby spreading out HRR and reducing the peak HRR. These results suggest that (1) TS is most suitable for single-stage ignition fuels for tailoring the rate and timing of the overall heat release of HCCI combustion (2) while SCCI and RCCI combustion concepts work better if they are operating within/near the negative temperature coefficient (NTC) regime because the ignition delays are more sensitive to ϕ and PRF than temperature in this regime. It is also found that high turbulence intensity with short-time scale is more likely to homogenize thermally and compositionally stratified mixtures such that the overall combustion becomes similar to the 0-D ignition with excessive HRR.

CEMA shows that at the first ignition delay, the low-temperature chemistry (LTC) represented by the isomerization of RO_2 chain branching reactions of KOOH , and H-atom abstraction of n -heptane is predominant for both RCCI and SCCI combustion. Temperature is identified to be the predominant factor, and HTC represented by $\text{H} + \text{O}_2 \rightarrow \text{O} + \text{OH}$ is responsible for the thermal ignition. At deflagrations, temperature, CO, and OH are the most important variables while the conversion reaction of CO to CO_2 , and high-temperature chain branching reaction of $\text{H} + \text{O}_2 \rightarrow \text{O} + \text{OH}$ are identified to be important.

Finally, a novel PC_8H_{18} model is developed, which has the capability to reproduce the timing, duration, and cooling effect of the late direct injection timing, t_{inj} . The PC_8H_{18} model was then adopted to explore the effect of DI timing on the DDFS combustion. It is found that regardless of t_{inj} , the DDFS combustion has much lower peak HRR and longer combustion duration than the RCCI combustion. This is primarily attributed to the sequential injection of $i\text{-C}_8\text{H}_{18}$. The combustion phasing of the DDFS combustion exhibits a non-monotonic behavior with increasing t_{inj} due to the different effect of fuel evaporation on the low-, intermediate-, and high-temperature chemistry of the PRF oxidation.

Contents

List of Figures	x
List of Tables	xvii
1 Introduction	1
1.1 Principles and fundamentals of HCCI combustion	2
1.2 HCCI with thermal stratification	6
1.3 Stratified charge compression ignition (SCCI)	7
1.4 Reactivity controlled compression ignition (RCCI)	9
1.5 Direct dual fuel stratification (DDFS)	11
1.6 Scope and objective	12
2 Formulation of compressible reacting flows and numerical methods	14
2.1 Governing equations for reacting flows in conservative form	15
2.2 Turbulent flow fields and scalar fields	17
2.3 The S3D DNS Code	18
3 Ignition of lean primary reference fuel/air mixtures with temperature inhomogeneities	19
3.1 Introduction	20
3.2 PRF reduced mechanism	21
3.3 Initial conditions	23
3.4 Effects of fuel composition and initial temperature RMS	28
3.4.1 Overall characteristics of PRF HCCI combustion	28
3.4.2 Chemical explosive mode analysis	30
3.4.3 Front speed and burning rate	32
3.5 Effect of turbulence	36
3.6 Conclusions	39
4 Ignition of a lean biodiesel/air mixture with temperature and composition inhomogeneities at high pressure and intermediate temperature	40
4.1 Introduction	41

4.2	Initial conditions	42
4.3	Effect of T' and ϕ'	45
4.3.1	Overall combustion characteristics	46
4.3.1.1	Baseline cases	49
4.3.1.2	Cases with uncorrelated $T - \phi$	50
4.3.1.3	Cases with negatively-correlated $T - \phi$	50
4.3.1.4	Instantaneous HRR fields	51
4.3.2	Chemical explosive mode analysis	52
4.3.3	Combustion mode	56
4.4	Effect of turbulence	58
4.5	Discussion	59
4.6	Conclusions	62
5	Ignition of a lean n-heptane/air mixture with temperature and composition inhomogeneities relevant to HCCI and SCCI combustion	64
5.1	Introduction	65
5.2	Initial conditions	66
5.3	Effects of T' and ϕ' at different T_0	70
5.3.1	0-D ignition characteristics	70
5.3.2	Effects of T' or ϕ' at different T_0 : BL cases	71
5.3.2.1	First-stage ignition: BL cases	71
5.3.2.2	Second-stage ignition: BL cases	73
5.3.3	Effects of negatively-correlated $T - \phi$ fields: NC cases	75
5.3.4	Effects of uncorrelated $T - \phi$ fields: UC cases	79
5.3.5	Combustion mode	81
5.4	Chemical aspects of the ignition	83
5.4.1	Characteristics of temporal species evolution	84
5.4.2	Chemical explosive mode analysis	89
5.5	Discussion	93
5.6	Conclusions	96
6	Ignition of a lean PRF/air mixture under RCCI/SCCI conditions: A comparative DNS study	98
6.1	Introduction	99
6.2	Initial conditions	100
6.3	Results and discussion	103
6.3.1	Effects of PRF', ϕ' , and T' at different regimes	103
6.3.2	Combustion mode analysis	105
6.3.3	Effect of turbulence	109

6.4	Conclusions	110
7	Ignition of a lean PRF/air mixture under RCCI/SCCI conditions: Chemical aspects	111
7.1	Introduction	112
7.2	Methodology	113
7.3	Results and discussion	115
7.3.1	Overall RCCI/SCCI combustion	115
7.3.2	CEMA: 0-D ignition	117
7.3.3	CEMA: 2-D DNS of RCCI/SCCI combustion	119
7.4	Conclusions	123
8	On the effect of injection timing on the ignition of lean PRF/air/EGR mixtures under direct dual fuel stratification conditions	125
8.1	Introduction	126
8.2	Model development	128
8.2.1	Compression heating model	128
8.2.2	Pseudo-iso-octane model	131
8.3	Initial conditions	132
8.4	Results and discussion	137
8.4.1	Overall combustion characteristics	137
8.4.2	Combustion mode analysis	141
8.4.3	Misfire	146
8.5	Conclusions	147
9	Conclusion and future work	150
9.1	Conclusion	151
9.2	Future research directions from DNS towards LES	153
	References	155

List of Figures

Figure 1-1	(a) Illustrative diagram of ϕ -temperature ranges for soot and NO_x formation in spark ignition, diesel, HCCI, and diesel LTC engines combustion concepts, and (b) conceptual schematics of the conventional diesel combustion [1].	3
Figure 1-2	Schematic of spark ignition (SI) gasoline, compression ignition (CI) diesel, and homogeneous charge compression ignition (HCCI) engine combustion concepts, adapted from [2].	4
Figure 1-3	Illustration of spontaneous autoignition, and a mixed mode of flame-front propagation (also referred to as deflagration) and spontaneous autoignition.	5
Figure 1-4	Comparison of advanced compression ignition combustion strategies in terms of fuel stratification, reproduced from Dempsey et al. [3].	6
Figure 1-5	Initial condition of different combustion concepts including HCCI with thermal stratification (TS), spark-assisted compression ignition (SACI), stratified-charge compression ignition (SCCI), and reactivity-controlled compression ignition (RCCI).	7
Figure 1-6	Illustration of stratified-charge compression ignition (SCCI) combustion concept. PFI, DI, and SOI denote port fuel injection, direct injection, and start of injection, respectively. m_1 and m_2 are the amount of fuel for PFI and DI, respectively. ATDC denotes after top dead center (TDC). ϕ and T denote equivalence ratio and temperature. The area of blue and red boxes represents the relative quantity of each injection.	8
Figure 1-7	Illustration of RCCI combustion concept. PFI and DI denote port fuel injection and direct injection, respectively. m_1 and m_2 are the amount of fuel for PFI and DI, respectively.	10
Figure 1-8	Illustration of SCCI, RCCI, and DDFS combustion concepts reproduced from [4]. PFI, CRI, and SOI denote port fuel injection, common-rail direct injection, and start of injection, respectively. The area of each box represents the relative quantity of each injection.	12

Figure 3-1	Comparison of the 171-species skeletal and the 116-species reduced mechanisms with the detailed mechanism for PRF/air mixtures at different pressures and $\phi = 0.3$	23
Figure 3-2	Comparison of the ignition delay of the 171-species skeletal and the 116-species reduced mechanisms with the detailed mechanism for PRF/air mixtures at different pressures and equivalence ratios.	24
Figure 3-3	Comparison of the extinction residence time of the 171-species skeletal and the 116-species reduced mechanisms with the detailed mechanism for PRF/air mixtures at different pressures and equivalence ratios	25
Figure 3-4	Comparison of the laminar flame speed versus the equivalence ratio between experiments (symbols) and calculations with the reduced mechanism (lines) for different PRF/air flames at various pressures.	26
Figure 3-5	Initial temperature and vorticity fields for Case 9.	27
Figure 3-6	Homogeneous ignition delays of different PRF/air mixtures at a constant volume with an initial pressure of 20 atm as a function of the initial temperature.	28
Figure 3-7	Temporal evolution of the mean pressure and the mean heat release rate for Cases 1–9. Thin lines represent the corresponding cases of 0-D homogeneous ignition.	29
Figure 3-8	Isocontours of the normalized heat release rate for Cases 1–3 (from left to right) at $t/\tau_{ig}^0 = 0.95, 0.82,$ and $0.56,$ respectively.	30
Figure 3-9	Isocontours of (a) the timescale of the chemical explosive mode, (b) $Da_c,$ (c) temperature, and (d) χ for Case 1 ($T' = 15$ K) at $t/\tau_{ig}^0 = 0.95.$ The solid line denotes the reaction front ($Da_c = 1$).	32
Figure 3-10	Isocontours of (a) the timescale of the chemical explosive mode, (b) $Da_c,$ (c) temperature, and (d) χ for Case 3 ($T' = 60$ K) at $t/\tau_{ig}^0 = 0.56.$ The solid line denotes the reaction front ($Da_c = 1$).	33
Figure 3-11	Temporal evolution of (a) S_d^* for one-dimensional reference cases and (b) the mean front speed, $\overline{S_d^*},$ for Cases 1-9.	34
Figure 3-12	Temporal evolution of the fraction of the heat release rate from the deflagration mode and the mean heat release rate for Cases 1–9.	35
Figure 3-13	Temporal evolution of the mean pressure and the mean heat release rate for Cases 1, 4, 7, 10–12 ($T' = 15$ K) and 3, 6, 9, 13–15 ($T' = 60$ K).	36
Figure 3-14	Temporal evolution of the mean front speed, $\overline{S_d^*},$ for Cases 1, 4, 7, 10–12 ($T' = 15$ K) and 3, 6, 9, 13–15 ($T' = 60$ K).	38
Figure 3-15	Temporal evolution of the fraction of the heat release rate from the deflagration mode and the mean heat release rate for Cases 1, 4, 7, 10–12 ($T' = 15$ K) and 3, 6, 9, 13–15 ($T' = 60$ K).	38

Figure 4-1	Ignition delay of biodiesel/air as function of the initial temperature for constant pressure auto-ignition equivalence ratio of 0.3 and different pressures, calculated with the detailed and reduced mechanisms, respectively.	42
Figure 4-2	Initial $T - \phi$ distribution for (a) Cases 2, 4, 12 and (b) Case 8, and (c) initial ϕ field for Case 12.	45
Figure 4-3	0-D ignition delays at a constant volume with an initial pressure of 40 atm as a function of (a) initial temperature for different ϕ and of (b) equivalence ratio for different T .	46
Figure 4-4	Temporal evolution of mean pressure and heat release rate for (a) Cases 1–4, (b) Cases 5–8, and (c) Cases 9–12, and the 95% range of τ_{ig}^0 for (d) Cases 1-4, (e) Cases 5–8, and (f) Cases 9–12. Thin lines represent the corresponding 0-D auto-ignition.	47
Figure 4-5	Temporal evolution of mean pressure rise rate for (a) Cases 1–4, (b) Cases 5–8, and (c) Cases 9–12. Thin lines represent the corresponding 0-D auto-ignition.	48
Figure 4-6	Isocontours of normalized heat release rate for Cases 1, 2, 8, and 12 (from left to right) at different times (from top to bottom).	52
Figure 4-7	Isocontours of (a) the time scale of chemical explosive mode, (b) Da_c , (c) temperature, and (d) χ for Case 8 (UC: $T' = 60$ K and $\phi' = 0.10$) at $t/\tau_{ig}^0 = 0.90$. The solid isoline denotes the reaction front.	54
Figure 4-8	Isocontours of (a) the time scale of chemical explosive mode, (b) Da_c , (c) temperature, and (d) χ for Case 12 (NC: $T' = 60$ K and $\phi' = 0.10$) at $t/\tau_{ig}^0 = 1.07$. The solid isoline denotes the reaction front.	55
Figure 4-9	Temporal evolution of the fraction of heat release rate from the deflagration mode and mean heat release rate for (a) Cases 1–4, (b) Cases 5–8, and (c) Cases 9–12.	57
Figure 4-10	Temporal evolution of mean pressure and heat release rate for long τ_t (Cases 4, 8, and 12; thin lines) and short τ_t (Cases 13–15; thick lines).	59
Figure 4-11	Temporal evolution of the fraction of heat release rate from the deflagration mode and mean heat release rate for Cases 13–15 with $\tau_t/\tau_{ig}^0 = 0.2$ and the corresponding cases (Cases 4, 8, and 12) with $\tau_t/\tau_{ig}^0 = 1.0$.	60
Figure 4-12	Schematics of 0-D ignition delay vs. initial temperature for (a) one-stage ignition fuels and (b) two-stage ignition fuels.	60
Figure 5-1	Initial $T - \phi$ distribution for (a) Cases 2, 7, 14 and (b) Case 21.	69
Figure 5-2	Initial field of (a) temperature and (b) equivalence ratio for Case 14.	69
Figure 5-3	0-D ignition delay of n -heptane/air mixtures as a function of initial temperature for different ϕ_0 at $p_0 = 40$ atm.	71

Figure 5-4	Temporal evolutions of the mean pressure and mean HRR for the BL cases with $T_0 = 805$ K (a & d), $T_0 = 933$ K (b & e), and $T_0 = 1025$ K (c & f) during the first-stage (left) and second-stage (right) ignition.	72
Figure 5-5	The 95% range of τ_{ig}^0 for the BL cases with (a) $T_0 = 805$ K, (b) $T_0 = 933$ K, and (c) $T_0 = 1025$ K.	74
Figure 5-6	Temporal evolutions of the mean HRR for the BL (left column) and NC & UC (right column) cases with $T_0 = 805$ K (a & d), $T_0 = 933$ K (b & e), and $T_0 = 1025$ K (c & f) during the second-stage ignition. The first-stage ignitions are shown in the small boxes.	76
Figure 5-7	The 95% range of τ_{ig}^0 for the NC (left) and UC (right) cases with $T_0 = 805$ K (a & d), $T_0 = 933$ K (b & e), and $T_0 = 1025$ K (c & f).	77
Figure 5-8	Isocontours of normalized HRR for Cases 15–18 (from left to right) at times of 15% (first row), 40% (second row), and 95% (last row) cumulative mean HRR and at the maximum HRR (third row).	79
Figure 5-9	The probability density function of (a) 0-D ignition delay and (b) its spatial gradient of initial mixtures for Cases 15–18.	80
Figure 5-10	Temporal evolution of the fraction of heat release rate from the deflagration mode and mean heat release rate for the BL (left) and NC/UC (right) cases.	82
Figure 5-11	Schematic of reaction pathways of <i>n</i> -heptane oxidation at different temperatures [5].	84
Figure 5-12	Temporal evolutions of the mean mass fractions of important species and mean HRR at $T_0 = 805$ K for (a) 0-D ignition, (b) Case 2, (c) Case 7, (d) Case 11, (e) Case 14, and (f) Case 21.	86
Figure 5-13	Temporal evolutions of the mean mass fractions of important species and mean HRR at $T_0 = 933$ K for (a) 0-D ignition, (b) Case 6, (c) Case 8, (d) Case 15, (e) Case 16, and (f) Case 22.	87
Figure 5-14	Temporal evolutions of the mean mass fractions of important species and mean HRR at $T_0 = 1025$ K for (a) 0-D ignition, (b) Case 9, (c) Case 19, and (d) Case 23.	88
Figure 5-15	Isocontours of (a) HRR, (b) temperature, (c) $Y_{C_7H_{16}}$, (d) $\text{sign}(\text{Re}(\lambda_e)) \times \log(1 + \text{Re}(\lambda_e))$, and EI of (e) temperature, (f) <i>n</i> -heptane, (g) H_2O_2 , (h) CO, and (i) OH for Case 16 ($T_0 = 933$ K, NC: $T' = 15$ K and $\phi' = 0.10$) at $t/\tau_{ig}^0 = 0.67$. The white solid line represents $Da_c = 1.0$	91
Figure 5-16	Isocontours of PIs of controlling reactions for Case 16 ($T_0 = 933$ K, NC: $T' = 15$ K and $\phi' = 0.10$) at $t/\tau_{ig}^0 = 0.67$. The white solid line represents $Da_c = 1.0$	92

Figure 5-17 Isocontours of (a) HRR, (b) temperature, (c) $Y_{C_7H_{16}}$, (d) $\text{sign}(\text{Re}(\lambda_e)) \times \log(1 + |\text{Re}(\lambda_e)|)$, and EI of (e) temperature, (f) *n*-heptane, (g) H_2O_2 , (h) CO, and (i) OH for Case 16 ($T_0 = 933$ K, NC: $T' = 15$ K and $\phi' = 0.10$) at $t/\tau_{ig}^0 = 0.83$. The white solid line represents $Da_c = 1.0$ 93

Figure 5-18 Isocontours of PIs of controlling reactions for Case 16 ($T_0 = 933$ K, NC: $T' = 15$ K and $\phi' = 0.10$) at $t/\tau_{ig}^0 = 0.83$. The white solid line represents $Da_c = 1.0$ 94

Figure 6-1 Initial PRF, ϕ , and T fields for Cases 6 (top row) and 8 (bottom row). 102

Figure 6-2 Initial T -PRF and $T - \phi$ relations for (a) Cases 6 (RCCI) and (b) 8 (SCCI). 102

Figure 6-3 Temporal evolution of the mean HRR for (a) Cases 1–4, (b) 5–8, and (c) 9–12. The first-stage ignitions are also shown in the small boxes. 104

Figure 6-4 0-D ignition delays of PRF/air mixtures at $p_0 = 40$ atm as a function of T_0 for different (a) PRF and (b) ϕ 105

Figure 6-5 Isocontours of normalized HRR for Cases 2, 4, 6, 8, 10, and 12 (from left to right) at times of 15% (first row), 40% (second row), and 95% (last row) cumulative mean HRR and at the maximum HRR (third row). 106

Figure 6-6 Probability density function of 0-D ignition delay (left column) and its spatial gradient (right column) of initial mixtures for Cases 1–12. 107

Figure 6-7 Temporal evolution of the fraction of the heat release rate from the deflagration mode and the mean HRR for Cases 5–8. 108

Figure 6-8 Temporal evolution of the mean HRR for Cases 6, 13, and 14 (RCCI), and Cases 8 and 15 (SCCI) with different u' . Temporal evolution of the first-stage ignitions are also shown in the small box. 109

Figure 7-1 Temporal evolution of (a) the mean HRR and temperature and (b) the mean mass fraction of *n*-heptane and *iso*-octane for RCCI, SCCI, and 0-D ignition. 116

Figure 7-2 Temporal evolution of (a) temperature, $\lambda_{\text{exp}} = \text{sign}(\text{Re}(\lambda_e)) \times \log(1 + |\text{Re}(\lambda_e)|)$, and HRR, (b) EI of important variables, and (c) PI of key elementary reactions for 0-D ignition of PRF30/air mixture. 118

Figure 7-3 Schematic of reaction pathways of *n*-heptane and *iso*-octane oxidation at different temperatures [5–7]. 119

Figure 7-4 Isocontours of (a) temperature, (b) HRR, (c) λ_{exp} , EI of (d) temperature and (e)–(h) critical species, and (i)–(l) PI of critical reactions at the first-ignition delay, $\tau_{ig,1}/\tau_{ig}^0 = 0.22$ 120

Figure 7-5	Conditional mean of HRR, λ_{exp} , and EI of critical species, and PI of critical reactions at the first-stage ignition for RCCI (left column) and SCCI (right column).	121
Figure 7-6	Conditional means of HRR, λ_{exp} and EI of critical species, and PI of critical reactions at 10% CHRR for RCCI (left column) and SCCI (right column).	122
Figure 7-7	Isocontours of (a) temperature, (b) HRR, (c) λ_{exp} , EI of (d) temperature and (e)–(f) critical species, and (g)–(h) PI of critical reactions at 10% CHRR, $t/\tau_{ig}^0 = 0.65$	123
Figure 8-1	Experimental and modeled motored-pressure history as a function of crank angle degrees ($^{\circ}\text{CA}$). Experimental motored-pressure trace is taken from experiment by Wissink and Reitz [4] operating at 1300 RPM and $p_{\text{in}} = 1.84$ atm.	130
Figure 8-2	Temporal evolutions of the mass fraction of $i\text{-C}_8\text{H}_{18}$, PC_8H_{18} , and $n\text{-C}_7\text{H}_{16}$, temperature, and heat release rate of the 0-D ignition for Case 3 with and without reaction. The initial pressure, temperature, and t_{inj} are 35 atm, 735 K, and -25°CA ATDC, respectively. The effective injection duration, t_{dur} , is approximately 0.8 ms.	132
Figure 8-3	Temporal evolutions of the pressure and the HRR of the 0-D ignition for Cases 1 and 2 with the initial pressure of 35 atm and temperature of 735 K. The dot line represents the modeled motored-pressure trace.	134
Figure 8-4	Initial ϕ and PRF fields for $n\text{-C}_7\text{H}_{16}$ stratification only before the injection of $i\text{-C}_8\text{H}_{18}$ (top) and both $n\text{-C}_7\text{H}_{16}$ and PC_8H_{18} stratifications after the injection of $i\text{-C}_8\text{H}_{18}$ (bottom).	135
Figure 8-5	Initial distributions of (a) the mass fractions of n -heptane and pseudo- iso -octane, $Y_{n\text{-C}_7\text{H}_{16}} - Y_{\text{PC}_8\text{H}_{18}}$, (b) $T - Y_{n\text{-C}_7\text{H}_{16}}$, and (c) $T - \phi$ and $T - \text{PRF}$, and (d) the distributions of $T - \phi$ and $T - \text{PRF}$ after the injection of $i\text{-C}_8\text{H}_{18}$ for Cases 3–8.	136
Figure 8-6	Isocontours of (a) initial PC_8H_{18} field, (b) its corresponding T_{drop} field ($T' = 19.2$ K) after the conversion of PC_8H_{18} to $i\text{-C}_8\text{H}_{18}$ for Cases 3–8, and (c) initial temperature field with $T' = 20$ K for all Cases 1–8.	137
Figure 8-7	Temporal evolutions of the mean pressure and the mean HRR for Cases 1–7 (top), and the mean HRR during the first-stage ignition (bottom). During the first-stage ignition, the temporal evolutions of the mean HRR for Cases 6 and 7 are identical to that of Case 1.	138
Figure 8-8	Scatter plots of temperature and the mass fraction of pseudo- iso -octane colored by the heat release rate for (a) Cases 5 at t_{inj} of 2.5 ms, (b) Case 7 at t_{inj} of 3.5 ms.	140

Figure 8-9	Temporal evolutions of the mean mass fraction of the fuels, temperature, and HRR (left), and important minor species (right) for Cases 5 (top) and 7 (bottom). In order to display in the same scale, the mean mass fractions of H_2O_2 , OH, and HO_2 species are increased by a factor of 8, 100, and 100, respectively.	141
Figure 8-10	Temporal evolutions of the mean temperature fluctuation RMS and the mean temperature gradient for Cases 1–7.	143
Figure 8-11	Isocontours of normalized HRR for Cases 1–3, 5, and 7 (from left to right) at times of 15% (first row), 40% (second row), 50% (third row) and 80% (last row) cumulative heat release rate (CHRR).	144
Figure 8-12	(a) Isocontours of normalized HRR, (b) scatter plot of temperature versus reaction and diffusion rates of CO colored by normalized HRR for Case 5 at 4.5 ms (40% cumulative HRR), and (A)–(D) spatial profiles of reaction and diffusion rates of CO along each cut line in (a).	145
Figure 8-13	Temporal evolutions of the fraction of HRR from the deflagration mode and the mean HRR for Cases 1–7.	146
Figure 8-14	Temporal evolutions of (a) the mean pressure, the mean temperature, the mean HRR, and the maximum temperature, and (b) the mean mass fractions of OH, CO, HO_2 , and H_2O_2 for Cases 8 and 9. In order to display in the same scale, the mean mass fractions of H_2O_2 and HO_2 species are increased by a factor of 8 and 100, respectively.	148
Figure 8-15	Isocontours of temperature (top) and HRR (bottom) for Cases 8 and 9 at 3.6 ms (3°CA ATDC).	149

List of Tables

Table 3-1	Physical parameters of the DNS cases.	27
Table 4-1	Physical and numerical parameters of the DNS cases. BL, UC, and NC represent baseline, uncorrelated $T - \phi$, and negatively-correlated $T - \phi$ distribution, respectively.	44
Table 5-1	Physical parameters of Cases 1–23. BL represents a baseline case with either T' only or ϕ' only. UC and NC represent uncorrelated $T - \phi$ and negatively-correlated $T - \phi$ distribution, respectively.	67
Table 5-2	Quantitative data of the DNS cases. \bar{q}_m is the maximum mean HRR; τ_{bd} is the burn duration which represents the period from 10% to 90% cumulative HRR; \bar{q}_{def} is the total fraction of HRR from the deflagration mode.	83
Table 6-1	Physical parameters of the DNS cases.	101
Table 8-1	Engine specifications [4] and key parameters of the DNS cases. RPM, °CA ATDC, and EGR denote revolutions per minute, degrees of crank-angle after the top dead center, and exhaust gas recirculation, respectively. . . .	130
Table 8-2	Mean mole, \bar{x} , of n -C ₇ H ₁₆ , PC ₈ H ₁₈ , and i -C ₈ H ₁₈ in RCCI and DDFS cases. Both n -C ₇ H ₁₆ and PC ₈ H ₁₈ fields are initialized by $x = \bar{x} + x'$, where \bar{x} of 0.324, and x' of 0.1 represent the mean value and variance, respectively.	133
Table 8-3	Physical parameters of the eight 2-D DNS cases. For all 2-D DNS cases, $l_e = l_{Te} = l_{n-C_7H_{16}e} = l_{P_8H_{18}e} = 1.2$ mm, $u' = 0.4$ m/s, and $\tau_t = 3.0$ m/s. Note that Case 1 is a baseline (BL) case in which PC ₈ H ₁₈ is not converted into i -C ₈ H ₁₈ . t_{inj} and τ_{ig}^0 denote the injection timing and the 0-D ignition delay time, respectively. τ_{ig} represents the time at which the maximum mean HRR occurs for both 0-D and 2-D simulations and the superscript 0 denotes 0-D simulation. Case 8 has no τ_{ig}^0 due to misfire. . . .	133

Nomenclature

Abbreviation

LTC	Low-temperature combustion
HCCI	Homogeneous-charge compression ignition (HCCI)
SCCI	Stratified-charge compression ignition
RCCI	Reactivity-controlled compression ignition
SACI	Spark-assisted compression ignition
DDFS	Direct duel fuel stratification
ICE	Internal combustion engine
CI	Compression ignition
SI	Spark ignition
PPC	Partially premixed combustion
GCI	Gasoline compression ignition
PFI	Port fuel injection
DI	Direct injection
CRI	Common rail injection
TDC	Top dead center
BTDC	Before the top dead center
ATDC	After the top dead center
IMEP	Indicated mean effective pressure
RPM	Revolutions per minute
DNS	Direct numerical simulation
S3D	The Sandia DNS code
MPI	Message passing interface
HPC	High-performance computing
0-D (2-D)	Zero-dimensional (two-dimensional)
PM	Particulate matters
EGR	Exhaust gas recirculation
GHG	Green house gases
PRF	Primary reference fuel, a blend of <i>n</i> -heptane and <i>iso</i> -octane
MD	Methyl decanoate
MD9D	Methyl 9-decanoate
DME	Dimethyl ether
E10	A blend of 10% ethanol and 90% gasoline
UC	Uncorrelated distribution
NC	Negatively-correlated
BL	Baseline
HRR	Heat release rate
CHRR	Cumulative heat release rate
PRR	Pressure release rate

NTC	Negative-temperature coefficient
ITC	Intermediate-temperature chemistry
HTC	High-temperature chemistry
LTHR	Low-temperature heat release
ITHR	Intermediate-temperature heat release
HTHR	High-temperature heat release
CEMA	Chemical explosive mode analysis
EI	Explosive index
PI	Participation index
LLNL	Lawrence Livermore National Laboratory
DRG	Directed relation graph
DRGX	DRG with expert knowledge
DRGASA	DRG-aided sensitivity analysis
PSR	Perfectly stirred reactors
LQSSA	Linearized quasi-steady state approximation
PDF	Probability density function
CMC	Conditional moment closure
RMS	Root mean square

Symbols

$^{\circ}\text{CA}$	Degrees of crank angle
t_{inj}	Injection timing
t_{dur}	Injection duration
τ_{ig}	Ignition delay time
t_{inj}	Injection timing
τ_{ig}	Ignition delay time
τ_{ig}^0	0-D ignition delay time
$\tau_{\text{ig},1}^0$	0-D first-stage ignition delay time
\bar{x}	Mean mole of fuels
x'	Mole fluctuation RMS
p_0	Initial mean pressure
T_0	Initial mean temperature
T'	Temperature fluctuation RMS
ϕ	Equivalence ratio
ϕ'	Equivalence ratio fluctuation RMS
PRF_0	Initial mean PRF number
PRF'	PRF fluctuation RMS
\bar{p}	Mean pressure
l_e	Most energetic turbulent length scale
l_{Te}	Temperature fluctuation length scale
$l_{\phi e}$	Equivalence ratio fluctuation length scale

u'	Turbulence velocity fluctuation
τ_t	Turbulence time scale
\dot{q}	Heat release rate
\dot{q}_m^0	0-D heat release rate
\bar{q}	Mean heat release rate
χ	Scalar dissipation rate
c	Progress variable
D	Thermal diffusivity
Da	Damköhler number
Da_c	CEM Damköhler number
λ_e	Real part of the eigenvalue
Y_k	Species mass fraction
$V_{j,k}$	Diffusion velocity of species k in the j -direction
$\dot{\omega}_k$	Net production rate of species k
ρ_u	Density of the unburnt mixture
S_L	Laminar flame speed
S_d^*	Density-weighted displacement speed
$\overline{S_d^*}$	Mean front speed

Chemical formula

$n\text{-C}_7\text{H}_{16}$	n -Heptane
$i\text{-C}_8\text{H}_{18}$	i so-Octane
PC_8H_{18}	Pseudo- i so-octane
NO_x	Nitric oxides
CO	Carbon monoxide
CO_2	Carbon dioxide
O_2	Oxygen
OH	Hydroxyl
H_2O_2	Hydrogen peroxide
HO_2	Hydroperoxyl
CH_2O	Formaldehyde
RH	Fuel molecule
R	Alkyl
RO_2	Alkylperoxy
QOOH	Hydroperoxyalkyl
O_2QOOH	hydroperoxyalkylperoxy
KOOH	Keto-hydroperoxide

Chapter 1

Introduction

1.1 Principles and fundamentals of HCCI combustion

Humankind has relied heavily on reciprocating internal combustion (IC) engines for transportation, commerce, and power generation. In 2012, there were 750 million passenger cars on the world's roads and 60 million cars manufactured worldwide, which is a 50% increase over ten years [8]. A study estimates an increase from 1.2 billion vehicles in 2014 to 2 billion vehicles by 2035 on world's roads [9]. The increase is partially because of growing demands in China and India's automobile market. For several upcoming decades, we will still rely heavily on IC engines. Since SI engines consume a massive amount of oil usage, they produce several billion tons of carbon dioxide CO_2 , and discharge toxic pollutants including nitric oxides NO_x , and particulate matters (PMs). CO_2 production from SI engines contributes partially to green house gases (GHG), which can induce global warming with unpredictable consequences while toxic pollutants have negative impacts on human health and environmental issues. Because of serious environmental and health implications, most governments have planned to impose more stringent emission regulations on IC engines to limit the emission of NO_x and soot as well as CO_2 .

Two thirds of the world energy supply relies on combustion of fossil and alternative fuels, and recent reports predict growing energy demand through combustion with an increasing share of renewables. Therefore, combustion will remain the major role in transportation and power generation. Because of growing worldwide demand for transport energy and limited resources of fossil fuels, energy prices keep increasing. Moreover, the emission regulations are also tightened due to the human health and environmental impacts caused by the engine-out emissions. The urgent fuel usage and pollutant emission problems have been driving the strong desires for more fuel-efficient clean combustion technology alternative to the conventional spark ignition (SI) and diesel compression ignition (CI) engines [1, 8, 10–12]. Even small improvement in IC combustion efficiency can have a significant influence on the economy and environmental and health implications worldwide. Although these emission issues have been improved substantially over the past decade, further reductions are needed to meet more stringent future emission regulations while improving fuel efficiency with reasonable cost.

Over several decades, CI engines have demonstrated to be the most fuel-efficient engines for transportation. It is primarily attributed to their high compression ratios and lack of throttling losses compared to SI engines. The conventional diesel CI engines, however, suffer from two major drawbacks of high nitric oxides NO_x and soot emissions as schematically shown in Fig. 1-1 [1, 13–15]. Figure 1-1 reveals the main factors that restrict the further reduction of emissions of the conventional diesel engines. The combustion of diesel engines inherently occurs in diffusion process of rich fuel/air mixtures due to the low volatility of diesel. The high-temperature diffusion flame of diesel engines leads to a significant amount of soot and NO_x formations [1, 13–15].

On the contrary, SI engines with the high volatility of gasoline produce significantly lower soot emission. However, SI engines are limited by high NO_x emission mainly due to high flame temperature of stoichiometric mixture. Moreover, SI engines have lower thermal efficiencies than diesel engines due to their lower compression ratios and throttling losses. Thanks to advanced injection systems with elevated pressures, exhaust gas recirculation (EGR) addition, and improved in-cylinder mixing process between fuel and air, substantial reductions in emissions have been achieved in the conventional IC engines. Despite these achievements, the conventional IC engines without expensive aftertreatment devices are unlikely to meet future stringent emission standards, and thus more research efforts are needed.

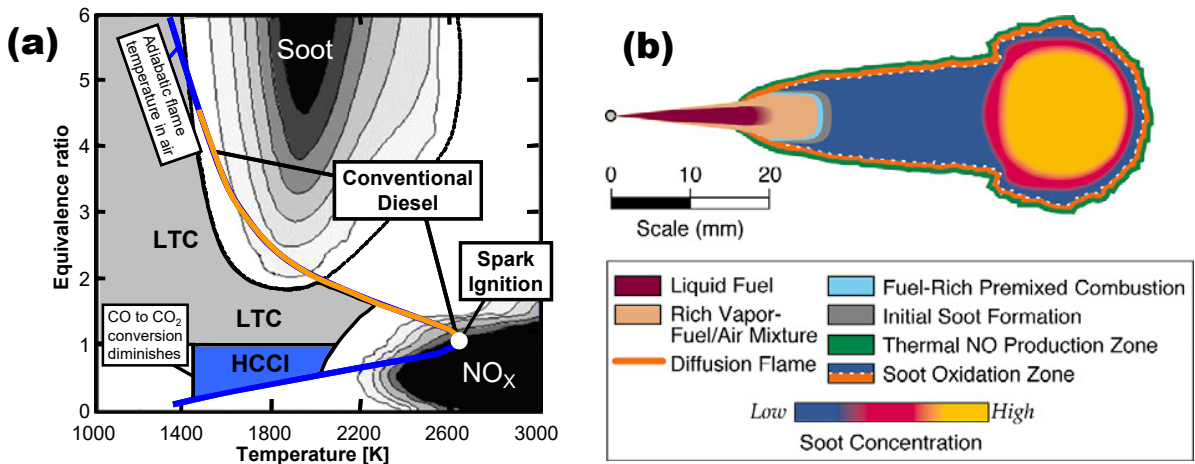


Figure 1-1: (a) Illustrative diagram of ϕ –temperature ranges for soot and NO_x formation in spark ignition, diesel, HCCI, and diesel LTC engines combustion concepts, and (b) conceptual schematics of the conventional diesel combustion [1].

Continuous efforts in the research and development have been made by the engine community over past decades for improving fuel efficiency and better understanding of in-cylinder combustion process. Thanks to successful collaboration between industrial and academic partners, many novel advanced combustion engine concepts have been proposed, which can offer tremendous reduction in fuel consumption and pollutant emissions. Among various advanced combustion concepts, low-temperature combustion (LTC) engines have been considered as an emerging engine technology as an alternative to the conventional DI gasoline and CI diesel engines. Homogeneous-charge compression ignition (HCCI) engine is a type of LTC engines [1, 10–12, 16–19].

The LTC and HCCI combustion engines are conceptually illustrated on a equivalence ratio versus temperature diagram in Fig. 1-1. As shown in Fig. 1-1 & 1-2, HCCI combustion engines are designed to operate under low-temperature conditions by utilizing ultra-lean, highly-diluted, well-mixed fuel/air charge like SI engines. Similar to diesel engines, the use of high compression ratios and removal of the throttling valve in the HCCI combustion engines enables high efficiency

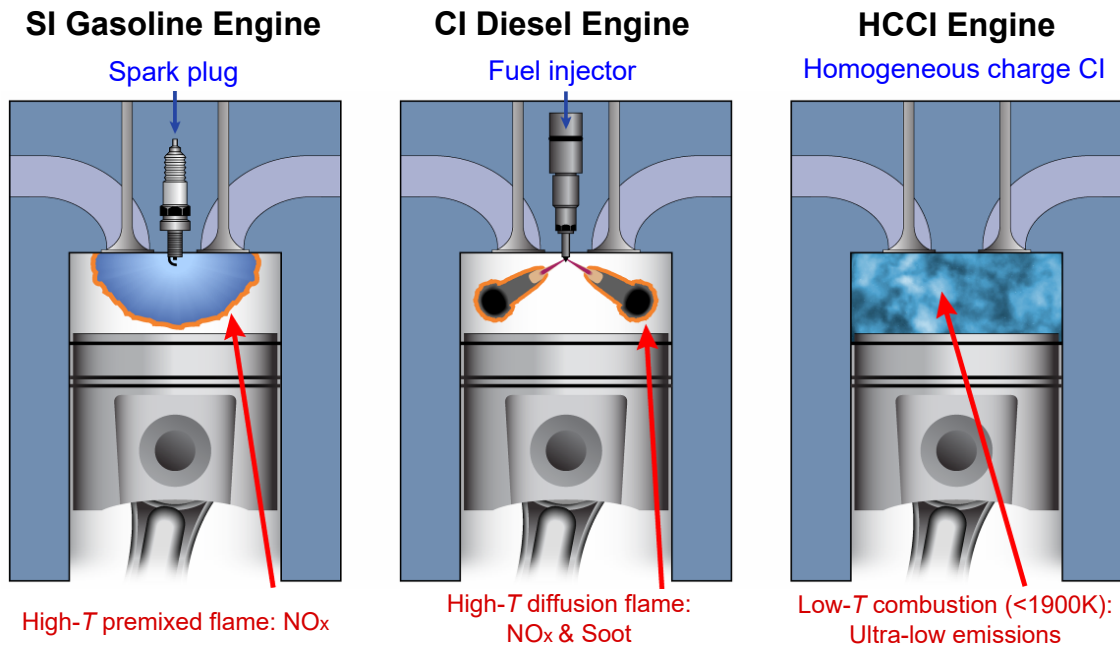


Figure 1-2: Schematic of spark ignition (SI) gasoline, compression ignition (CI) diesel, and homogeneous charge compression ignition (HCCI) engine combustion concepts, adapted from [2].

operation, thereby allowing lower CO_2 emissions per unit of work generated by the engine. The use of a highly-diluted and well-mixed fuel/air charge reduces the emissions of nitrogen oxides, soot, and particulate matters. Accordingly, HCCI combustion simultaneously offers low engine-out NO_x and soot emissions without high-price after-treatment systems while providing high-thermal efficiency. Therefore, prototypes of HCCI combustion engines have been developed as an alternative to conventional gasoline SI and diesel CI engines [1, 10–12, 16–19].

Despite their promising advantages, however, several key issues in the development of HCCI engines still remain unresolved: for instance, how to (1) mitigate the peak pressure rise rate (PRR) at high load and (2) how to accurately control combustion timing. HCCI combustion relies primarily on the condition of a premixed charge prior to the onset of combustion such that the fuel oxidation chemistry plays a predominant role in determining combustion characteristics. In addition, the overall combustion in an HCCI engine cylinder is generally believed to occur by spontaneous autoignition. Therefore, HRR and PRR in HCCI combustion engines are significantly higher than in SI and CI engines, where flame propagation speeds or mixing and vaporization rates limit the maximum HRR. Excessive HRR under high-load conditions can result in engine knock, reducing the engine integrity, and hence, must be avoided through careful engine design and operation.

Several variants of HCCI engines have been proposed to enhance the ignition timing control and to extend the engine operation range. The typical approach to overcome the excessive PRR under high-load operating conditions in the HCCI engine is to generate a sequential ignition event by using in-cylinder mixture inhomogeneities [17, 20]. The autoignition in the

HCCI engine is primarily determined by the in-cylinder conditions such as overall pressure, temperature, equivalence ratio, and their fluctuations [17, 20]. As such, the precise control of ignition timing and burning rate of HCCI combustion could be achieved by a well-designed mixture composition with a certain amount of exhaust gas recirculation (EGR) addition [17, 21]. Numerous experimental and numerical studies of HCCI combustion have shown that thermal and compositional stratifications of the in-cylinder charge can provide a smooth combustion process under high-load conditions by changing the combustion mode from spontaneous ignition into a mixed combustion mode of spontaneous ignition and deflagration as conceptually shown in Fig. 1-3. A mixed combustion mode of spontaneous ignition and deflagration help to prolong the combustion duration, which subsequently alleviates the fuel burning rate and lowers the peak HRR.

Among the derivatives of HCCI combustion concepts, HCCI with thermal stratification (TS), spark-assisted compression ignition (SACI), stratified-charge compression ignition (SCCI), and reactivity-controlled compression ignition (RCCI) engines have been paid considerable attention by the engine community [1, 3, 8, 10–12, 16–19, 22–25]. Figure 1-4 shows various advanced compression ignition combustion strategies in terms of fuel stratification. These HCCI-type engines can provide better combustion phasing controlling, mitigate PRR, and lower fuel consumption and pollutant emissions than the conventional HCCI engines. Henceforth, the terms of ‘HCCI-type’ and ‘HCCI-variant’ are interchangeably for general reference to any combustion concepts with thermal and/or compositional stratification.

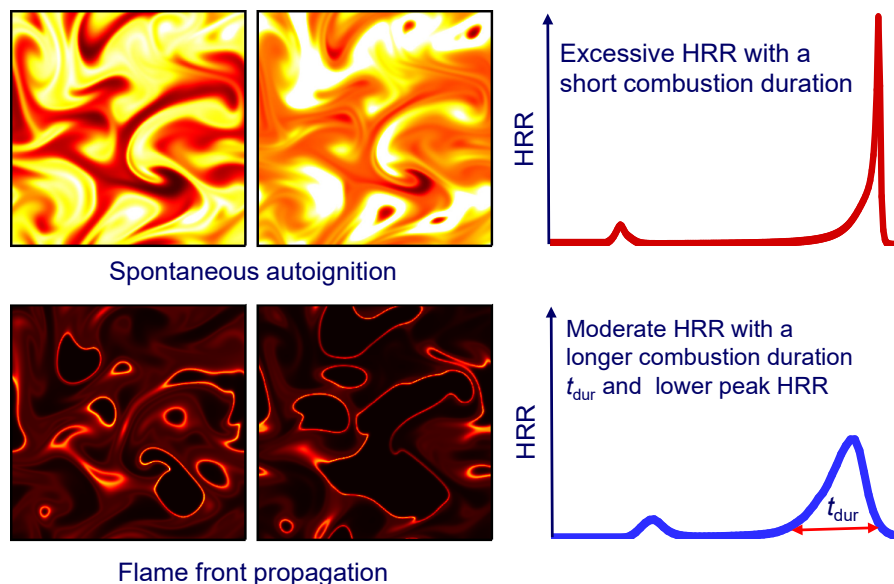


Figure 1-3: Illustration of spontaneous autoignition, and a mixed mode of flame-front propagation (also referred to as deflagration) and spontaneous autoignition.

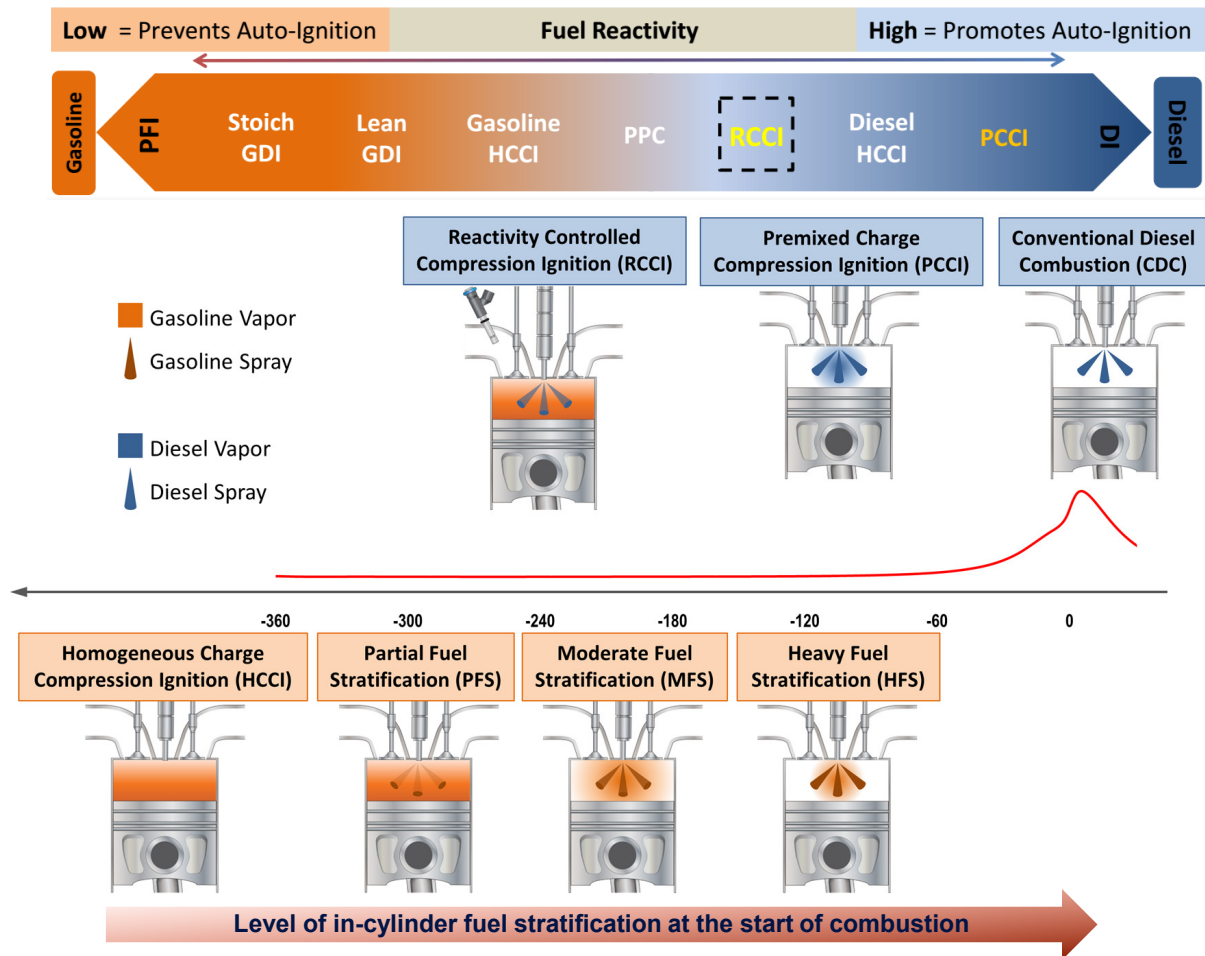


Figure 1-4: Comparison of advanced compression ignition combustion strategies in terms of fuel stratification, reproduced from Dempsey et al. [3].

1.2 HCCI with thermal stratification

Despite its name of ‘homogeneous charge’, some levels of thermal inhomogeneities always exist in a real HCCI engine cylinder due to wall heat transfer, convection, and imperfect mixing of fuel and air mixture [1, 17, 20]. The thermal inhomogeneities of the in-cylinder charge naturally develop for several reasons including (1) inhalation of charge with nonuniform temperature, (2) nonuniform heat transfer during the intake and compression stroke, (3) turbulent mixing for low-residual engines, and (4) incomplete mixing between the fresh charge and hot residuals for engines with high levels of retained residuals [17]. In fact, some degrees of thermal stratification (TS) are preferred at high-load conditions because they can help extend high-load operating limits of the HCCI engine as shown in Fig. 1-5. These temperature gradients cause different chemical reaction rates throughout the charge which in turn result in sequential autoignition events, lowering the maximum HRR and the ringing intensity.

Three main methods can be utilized to intentionally improve the thermal stratification:

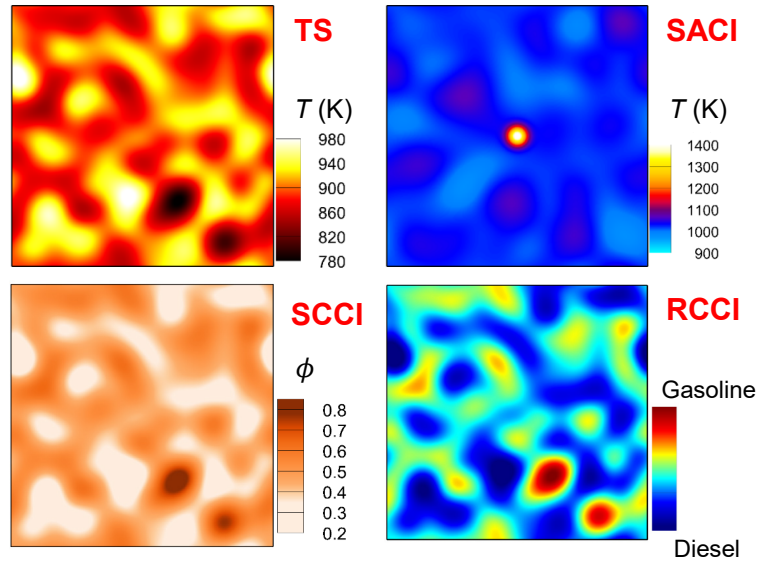


Figure 1-5: Initial condition of different combustion concepts including HCCI with thermal stratification (TS), spark-assisted compression ignition (SACI), stratified-charge compression ignition (SCCI), and reactivity-controlled compression ignition (RCCI).

(1) increasing the heat transfer to the walls by using lower engine coolant temperatures, (2) increasing the heat transfer to the walls through more in-cylinder turbulence such as with higher swirl, and (3) utilizing the cooling effect of fuel vaporization by using late DI of fuel [17]. The first two methods were demonstrated as being effective in lowering the peak HRR rates and ringing intensities, but with trade-offs of lower power output and increased fuel consumption due to the increased heat loss. The third strategy works better for the diesel-like fuels, which exhibit two-stage ignition such as diesel, *n*-heptane, DME, and PRF50.

Generally, the ignition process of thermally-stratified charge in HCCI engines occurs sequentially throughout the in-cylinder fuel/air mixture with the onset of combustion originated from the hottest regions. A higher temperature results in faster chemical reactions, and thus local mixtures with high temperature are more apt to ignite first. However, for fuels exhibiting a two-stage ignition under low-temperature and high-pressure conditions, their ignition process become quite complicated and inconclusive due to the complex interactions of the low-temperature chemistry and turbulence intensity. Moreover, the manipulation and exploitation of the thermal stratification of in-cylinder charge is not easy and remains a challenge. For this reason, stratified-charge compression ignition (SCCI) combustion has been investigated as an alternative solution for enlarging the operating range of HCCI combustion.

1.3 Stratified charge compression ignition (SCCI)

HCCI in its strictest sense has a completely 'homogeneous charge', meaning that there are no mixture composition stratifications. In reality, however, even port fuel injection (PFI) engines

1.3 Stratified charge compression ignition (SCCI)

may produce mixture stratifications if there is inadequate time and turbulence for fuel and air mixing. Similar to the advantage of thermal stratification for spreading out the HRR, fuel stratification is also utilized to extend the high-load limit of SCCI combustion engines. By using an injection scheme illustrated in Fig. 1-6, flexibly adjusting the late direct injection (DI) timing and/or the fraction of PFI/DI generates desired levels of mixture stratifications or appropriate equivalence ratio distributions. It should be noted that the cooling effects of fuel vaporization from late DI also produce some levels of thermal stratification, which typically have competing and adverse effects over fuel stratification.

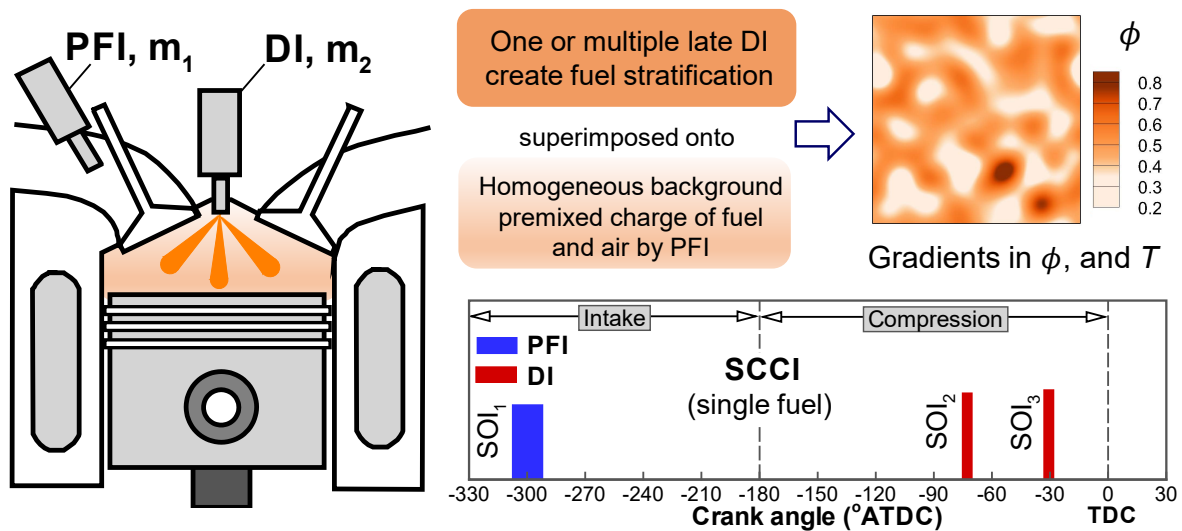


Figure 1-6: Illustration of stratified-charge compression ignition (SCCI) combustion concept. PFI, DI, and SOI denote port fuel injection, direct injection, and start of injection, respectively. m_1 and m_2 are the amount of fuel for PFI and DI, respectively. ATDC denotes after top dead center (TDC). ϕ and T denote equivalence ratio and temperature. The area of blue and red boxes represents the relative quantity of each injection.

In general, mixtures with high equivalence ratio tend to ignite earlier and the ignition fronts sequentially propagate towards mixtures with low equivalence ratio. The sequential ignition process leads to mitigating the excessive HRR, which in turn enables the high-load operation of SCCI engines. The effectiveness of partial fuel stratification in lowering the HRR and ringing intensity by a sequential autoignition process depends highly on the ϕ -sensitivity of the fuel. Fuels exhibiting high ϕ -sensitivity are typically diesel-like fuels, which are more conducive to the SCCI strategy. Fuels exhibiting two-stage ignition such as diesel, *n*-heptane, and biodiesel are more ϕ -sensitive than the single-stage ignition fuels such as gasoline-like fuels. For ϕ -sensitive fuels, the use of DI fraction and direct injection timing can be adopted as controlling parameters for adjusting the degrees of fuel stratification and for tailoring the HRR under particular operating conditions.

Fuel stratifications can be easily achieved in an engine with DI by using multiple injections or late injection strategies. Normally, port fuel injection (PFI) or early direct injection (DI)

are used to produce a relatively homogeneous fuel/air mixture while adjusting the PFI/DI mass fraction and DI timing to generate some levels of equivalence ratio stratification. More specifically, a majority of the fuel is injected into the intake manifold or directly injected into the cylinder very early to allow premixing, while a small amount of fuel (up to 20%) is directly injected late to create areas with locally higher equivalence ratio. As such, most of the fuel is well mixed while local regions of higher equivalence ratio exist.

The ϕ -sensitivity of fuel is an essential parameter to measure the impact of varying equivalence ratio on combustion duration and timing when all other factors are held constant. Generally, fuel with highly ϕ -sensitive characteristics exhibits larger changes in combustion duration and timing as the equivalence ratio is varied. In addition, for ϕ -sensitive fuel, under the same conditions, the regions of richer fuel/air mixtures will ignite earlier than the leaner ones. Previous studies has revealed that fuels exhibiting strong two-stage ignition behavior are more apt to be ϕ -sensitive. Fuels, which contain straight-chain molecules $-\text{CH}_2-\text{CH}_2-\text{CH}_2-$, tend to display stronger two-stage ignition, and thus more ϕ -sensitive. For example, *n*-heptane, PRF50, biodiesel, and other diesel-like fuels with a two-stage ignition is highly ϕ -sensitive showing significant advancement in ignition timing with increased equivalence ratio. For these fuels, mixture stratifications using DI can be intentionally created to allow a sequential autoignition which can be used to achieve improved high-load operations without experiencing an excessive HRR and excessive ringing.

On the contrary, gasoline-like fuels with a single-stage ignition such as *iso*-octane, gasoline, and natural gas are less ϕ -sensitive and thus do not display a significant preignition reactions with varying equivalence ratio. For example, *iso*-octane and gasoline exhibit very little low-temperature heat release under naturally-aspirated intake conditions. It is attributed to the fact that their branched-chain structure creates more primary bonds inhibiting the initial hydrogen abstraction reactions to occur, leading to decreased rate of isomerization, and in turn lowering the first-stage ignition.

In short, fuel stratifications can have similar effect as temperature stratifications for producing more sequential ignition processes but this strategy is generally effective only for fuels which exhibit strong ϕ -sensitivity.

1.4 Reactivity controlled compression ignition (RCCI)

In addition to thermal and equivalence ratio stratification, reactivity stratification is also a promising method to control the timing and rate of the main combustion process in HCCI engines, which is commonly referred to as reactivity controlled compression ignition (RCCI), or dual-fuel HCCI. The RCCI approach relies on the injection of two fuels with opposite ignition

characteristics. One fuel is highly reactive (e.g. diesel fuel) while the other is less reactive (e.g. gasoline). The injection scheme of RCCI engines is conceptually illustrated in Fig. 1-7. By varying the relative amounts of two fuels and the DI timing, combustion timing can be tailored more accurately and flexibly. Typically, gasoline is port-injected while diesel is pilot direct-injected into the cylinder. One or multiple pilot direct injections of diesel are delivered into the cylinder just prior to the desired combustion timing to initiate combustion, which then ignites the rest of the mixture. The fuel/air mixture autoignites sequentially in a downward reactivity-gradient order starting from the regions of high diesel concentration, accompanied by the regions with progressively lower diesel concentration. This sequential ignition process makes the combustion duration last longer, resulting in a lower peak HRR [22–24].

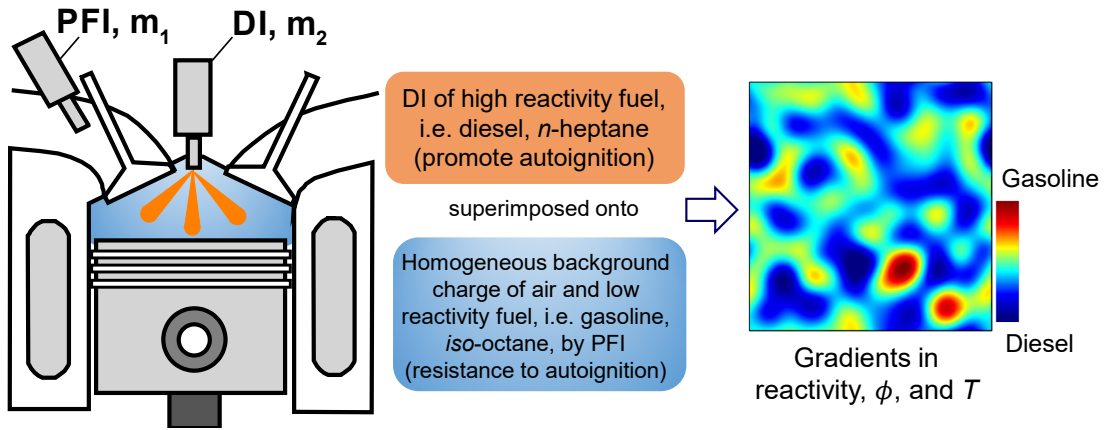


Figure 1-7: Illustration of RCCI combustion concept. PFI and DI denote port fuel injection and direct injection, respectively. m_1 and m_2 are the amount of fuel for PFI and DI, respectively.

The dual-fuel approach provides an effective method of rapid combustion-phasing control because the amount of directly injected diesel fuel can be adjusted from cycle to cycle. Moreover, RCCI can provide high efficiency in both heavy-duty and light-duty engines with very low NO_x and particulate emissions. However, this comes with trade-offs of requiring both DI-diesel and gasoline fueling systems and dealing with two fuels. A potential difficulty with RCCI is that the maximum loads are restricted by the low-reactivity fuel. Under full-load conditions, we cannot take full advantage of the RCCI combustion because it becomes more like an HCCI combustion. As the load increases, the overall reactivity of the charge decreases, leading to too advanced combustion phasing. To compensate for this, the supply of direct-injected high-reactivity fuel needs to be reduced, and ultimately it vanishes when the load becomes high enough. At this point, there is no means to effectively control the combustion phasing and process of the RCCI combustion. Additionally, since the port-injected low-reactivity fuel is usually well-premixed with oxidizer, and hence the overall combustion can virtually occur by volumetric auto-ignition, which is essentially similar to the HCCI combustion.

Another remedy for expanding the operation range to a higher load and avoiding excessive premixing of the charge of RCCI combustion is to replace gasoline with a much lower-reactivity fuel such as ethanol [26, 27] and natural gas [28], which have a high resistance-to-autoignition quality to counterbalance with increasing load. At high load, the high-reactivity fuel just serves as an ignition source to determine the onset of combustion while most of the heat release comes from low-reactivity fuel. As such, this method can offer a robust control of the combustion phasing with good combustion stability [29, 30].

1.5 Direct dual fuel stratification (DDFS)

A strategy of extending the high-load limit of the RCCI combustion is to stratify both fuels by directly injecting both gasoline and diesel into the engine cylinder. This concept is known as direct dual fuel stratification (DDFS) as conceptually illustrated in Fig. 1-8 [4, 30–33]. This method allows more flexible controllability of the in-cylinder reactivity distribution of two fuels.

Kavuri et al. elucidated the characteristics of the RCCI combustion using direct injection of both gasoline and diesel fuels at high load and compared its performance with gasoline compression ignition (GCI) combustion [33]. They found that both RCCI and GCI combustion have similar overall combustion characteristics with a near top dead center (TDC) injection; however, the RCCI combustion has better control of the combustion phasing than GCI combustion. Lim et al. studied numerically the RCCI combustion with dual direct injections of *iso*-octane and *n*-heptane under high-load conditions [30]. They showed that the RCCI combustion can achieve very-high gross thermal efficiency of 48.7% with 21 bar gross indicated mean effective pressure (IMEP) by an optimal injection strategy compared to 47–48% efficiency with up to 16 bar gross IMEP in a boosted HCCI engine using E10 fuel (a 10% ethanol and 90% gasoline blend) [34].

Wissink and Reitz demonstrated that DDFS is beneficial for distributing HRR and reducing peak PRR at high load condition [4, 31, 32]. The advantages of RCCI and partially premixed combustion (PCC) were effectively combined with DDFS by controlling the start of the heat release event with the diesel injection and the peak and duration of the heat release event with the near-top dead center (TDC) gasoline injection. The DDFS combustion combines the high thermal efficiency of the RCCI combustion with the high load capability of partially premixed combustion (PPC). Moreover, DDFS requires less exhaust gas recirculation (EGR) rate than RCCI, while the noise intensities and combustion instabilities are significantly lowered than those of PPC.

In the DDFS combustion, the start of heat release is controlled by the DI timing of diesel while the peak and duration of the heat release are governed by near-TDC pilot injection of

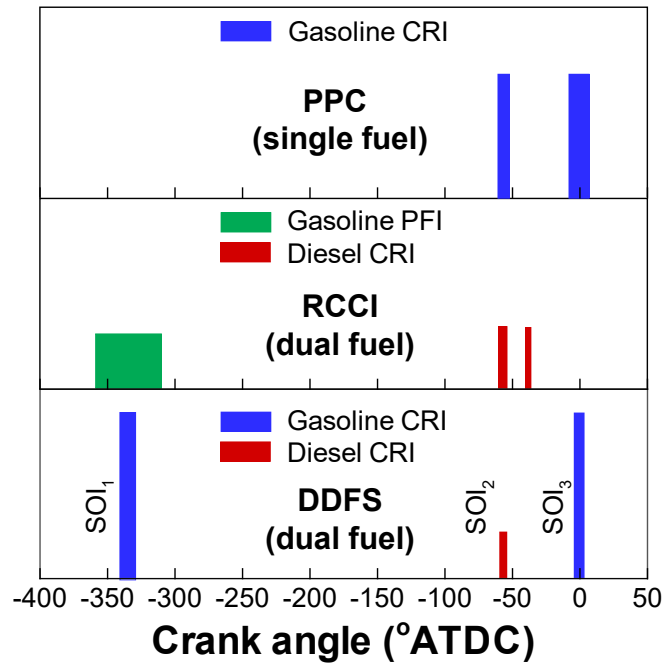


Figure 1-8: Illustration of SCCI, RCCI, and DDFS combustion concepts reproduced from [4]. PFI, CRI, and SOI denote port fuel injection, common-rail direct injection, and start of injection, respectively. The area of each box represents the relative quantity of each injection.

gasoline. Similar to the RCCI combustion, an early injection of gasoline is used in the DDFS combustion to have premixed background charge, then accompanied by direct injection of diesel to generate some degrees of inhomogeneities in both reactivity and equivalence ratio. These first two injections are designed to control the start of the main combustion occurring at about 10°CA before the TDC (bTDC). Inspired by the PPC, the DDFS combustion utilizes direct injection of remaining gasoline right bTDC to control the combustion rate. As such, DDFS combustion can achieve capability to independently control ignition timing and combustion duration by combining reactivity stratification with diffusion-limited gasoline injection [4, 31, 32]. However, the effect of the timing of the late gasoline injection on the combustion process of both fuel stratification is not well-understood.

1.6 Scope and objective

Recent advancement and progress in experimental studies have provide valuable insights into the overall characteristics of HCCI combustion process. However, engine experiments can provide only limited information such as the overall pressure and HRR, 2-D line-of-sight chemiluminescence or planar images of select species. The more in-depth insight into the physical-chemical interactions occurring in a combustion chamber is still elusive. Thanks to high-fidelity direct numerical simulations (DNSs), fundamental understanding of the in-cylinder combustion process including combustion modes, flame speed, turbulence-chemistry interactions, controlling

species and reactions of the HCCI-type engines can be achieved. A better understanding of the ignition characteristics of HCCI engines will assist the research and development of prototypes of HCCI engines in extending the high-load limit and improving fuel efficiency.

With the help of DNSs, the objective of the present study is (1) to provide better understandings of the effect of thermal and compositional stratification levels under different low-to-high temperature regimes and fuel compositions on the overall ignition characteristics of HCCI combustion; (2) to investigate the relative effect of temperature/equivalence ratio/reactivity stratification coupled with the turbulence intensity under HCCI/SCCI/RCCI on combustion modes using several different fuels including primary reference fuels (PRF)—a blend of *n*-heptane and *iso*-octane, *n*-heptane, and biodiesel; (3) to identify the key species and critical reactions under SCCI/RCCI by using chemical explosive mode analysis (CEMA); and (4) to elucidate the effect of the late-direct-injection timing on the combustion process of direct dual fuel stratification (DDFS) by developing a pseudo-*iso*-octane model with the capabilities of reproducing the timing and duration of the late direct injection.

The thesis is organized as follows. First, Chapter 2 is devoted to discussing the formulation of chemically reacting flows and numerical methods used in the present study. Next, the ignition characteristics of lean primary reference fuel/air mixtures with temperature inhomogeneities are investigated in Chapter 3. Ignition of a lean biodiesel/air mixture with temperature and composition inhomogeneities at high pressure and the intermediate temperature is then numerically studied in Chapter 4. In Chapter 5, the ignition characteristics of a lean *n*-heptane/air mixture with temperature and composition inhomogeneities relevant to HCCI and SCCI combustion. The ignition characteristics and chemical aspects of a lean PRF/air mixture under RCCI/SCCI conditions are elucidated in Chapter 6 & 7. Chapter 8 is to investigate the effect of injection timing on the ignition of lean PRF/air/EGR mixtures under direct dual fuel stratification conditions. Finally, in the last chapter 9, the conclusions are briefly summarized and the implications and contributions of this study are highlighted.

Chapter 2

Formulation of compressible reacting flows and numerical methods

In this chapter, the governing equations of the fully compressible multi-component reacting flows in conservative form are introduced, and then the numerical methods and boundary conditions used in the present study are discussed.

2.1 Governing equations for reacting flows in conservative form

A system of conservation equations for the fully compressible reacting flows with detailed chemistry and transport is briefly reviewed here. The detailed description can be found in [35, 36].

The conservation equations for mass, momentum, energy and species are written as

$$\frac{\partial \rho}{\partial t} + \frac{\partial}{\partial x_\alpha}(\rho u_\alpha) = 0, \quad (2.1.1)$$

$$\frac{\partial \rho}{\partial t}(\rho u_\alpha) + \frac{\partial}{\partial x_\beta}(\rho u_\alpha u_\beta) = -\frac{\partial p}{\partial x_\alpha} + \frac{\partial \tau_{\beta\alpha}}{\partial x_\beta} + \rho \sum_{i=1}^N Y_i f_{i,\alpha} \quad \alpha = 1, 2, 3, \quad (2.1.2)$$

$$\frac{\partial}{\partial t}(\rho e_0) + \frac{\partial}{\partial x_\alpha}[(\rho e_0 + p)u_\alpha] = -\frac{\partial q_\alpha}{\partial x_\alpha} + \frac{\partial}{\partial x_\beta}(\tau_{\beta\alpha} u_\alpha) + \rho \sum_{i=1}^N Y_i f_{i,\alpha}(u_\alpha + V_{i,\alpha}), \quad (2.1.3)$$

$$\frac{\partial}{\partial t}(\rho Y_i) + \frac{\partial}{\partial x_\alpha}(\rho u_\alpha Y_i) = -\frac{\partial}{\partial x_\alpha}(\rho Y_i V_{i,\alpha}) + W_i \omega_i \quad i = 1, \dots, N, \quad (2.1.4)$$

where t is time, x_α the spatial coordinate of direction α in a rectangular Cartesian system, ρ is the mass-averaged density, u_α is the flow velocity in direction α , p is the pressure, $f_{i,\alpha}$ the body force per unit mass on species i in direction α , Y_i is the mass fraction of species i , N is the total number of species, and W_i is the molecular weight of species i . ω_i is the molar production rate of species i . e_0 is the specific total energy (internal energy plus kinetic energy). Henceforth, α and β denote spatial indices while i and j are used to denote species indices unless stated otherwise. Note that since the summation of the N species equations yields the continuity equation, only $(N - 1)$ species equations are solved such that one species such as nitrogen N_2 is evaluated from the conservation relation, $\sum_{i=1}^N Y_i = 1$.

The specific total specific energy is calculated as follows:

$$e_t = \frac{u_\alpha u_\alpha}{2} + h - \frac{p}{\rho} = \frac{u_\alpha u_\alpha}{2} + \sum_{i=1}^N h_i Y_i - \frac{p}{\rho} \quad (2.1.5)$$

where h is the total enthalpy including sensible and chemical energy.

Constitutive relationships

The equation of state of an ideal gas mixture is

$$p = \rho R_u T / W, \quad (2.1.6)$$

where R_u and W is universal gas constant and the mixture molecular weight, respectively.

The mixture molecular weight, W , is defined as

$$W = \left(\sum_{i=1}^N Y_i / W_i \right)^{-1} = \sum_{i=1}^N X_i W_i, \quad (2.1.7)$$

where Y_i and X_i respectively are the mass and mole fractions of species and they are related by $Y_i / W_i = X_i / W$.

For an ideal gas mixture, the enthalpy is evaluated through the thermodynamic relationships

$$h = \sum_{i=1}^N h_i Y_i, \quad h_i = h_i^0 + \int_{T_0}^T c_{p,i} dT, \quad c_p = \sum_{i=1}^N c_{p,i} / Y_i, \quad c_p - c_v = R_u / W, \quad (2.1.8)$$

where h_i and h_i^0 is the enthalpy and the formation enthalpy of species i at temperature T_0 , and c_p and c_v are the specific heat capacity at constant pressure and volume, respectively.

The stress tensor, $\tau_{\beta\alpha}$, the species diffusion velocities, $V_{i,\alpha}$, and the heat flux vector, q_α , are respectively evaluated as

$$\tau_{\beta\alpha} = \mu \left[\frac{\partial u_\beta}{\partial x_\alpha} + \frac{\partial u_\alpha}{\partial x_\beta} - \frac{2}{3} \delta_{\beta\alpha} \frac{\partial u_k}{\partial x_k} \right], \quad (2.1.9)$$

$$\mathbf{V}_{\alpha i} = \frac{1}{X_i} \sum_{j=1}^N \frac{Y_j}{X_j} D_{ij} \mathbf{d}_{\alpha j} - \frac{D_i^T}{\rho Y_i} \nabla_\alpha (\ln T) \quad (2.1.10)$$

$$q_\alpha = -\lambda \frac{\partial T}{\partial x_\alpha} + \rho \sum_{i=1}^N h_i Y_i V_{i,\alpha}. \quad (2.1.11)$$

where μ is the mixture viscosity, gas constant, D_{ij} are the multicomponent diffusion coefficients, D_i^T is the thermal diffusion coefficient of species i , λ is the thermal conductivity, and $\mathbf{d}_{\alpha j}$ is the diffusion driving force of species i in the α direction.

The reaction rate, ω_i , is written as

$$\omega_i = \sum_{k=1}^M (v''_{i,k} - v'_{i,k}) A_k T^{n_k} \exp(-E_k/R^0T) \prod_{j=1}^N C_i^{v_{j,k}} \cdot C_{M,k}^{m_k}, \quad (2.1.12)$$

where v and v are the forward and backward reaction coefficients for the elementary reactions ($k = 1 \dots, M$), and E_k is the activation energy of reaction k . The molar concentration of species i (moles per unit volume) are written as

$$C_i = \rho Y_i / W_i \quad (2.1.13)$$

and the concentration of third body associated with reaction k , $C_{M,k}$, is computed as

$$C_{M,k} = \sum_{i=1}^N \eta_{i,k} C_i = \sum_{i=1}^N \eta_{i,k} \rho Y_i / W_i \quad (2.1.14)$$

where $\eta_{i,k}$ is the chaperon efficiency of species i in the reaction k . The third body exponent, m_i , is either 1 or 0 depending on whether the reaction k involves a third body or not.

2.2 Turbulent flow fields and scalar fields

The turbulent flow fields and scalar fields of temperature and concentration are prescribed using the 2-D Passot-Pouquet kinetic energy spectrum function [37]. The 2-D Passot-Pouquet energy spectrum function is defined as follows:

$$E(k) = \frac{32}{3} \sqrt{\frac{2}{\pi}} \frac{u'^2}{k_e} \left(\frac{k}{k_e} \right)^4 \exp \left[-2 \left(\frac{k}{k_e} \right)^2 \right], \quad (2.2.1)$$

where k is the wave number magnitude, k_e is the most energetic wave number and u' is the root mean square (RMS) velocity fluctuation.

At the initial time, turbulence velocity fluctuations are superimposed on the stationary mean velocity spectrum. The stationary mean velocity spectrum is initially set to 0 cm/s for all cases. The most energetic length scale, $l_e \sim 1$ mm, is chosen, and then u' is adjusted such

that the turbulence time scale, τ_t , is comparable to the ignition time scale τ_{ig}^0 . With $l_e \sim 1$ mm, the computational domain covers 3 eddies. These carefully selected parameters allow for a significant interaction between turbulence and chemistry and is also relevant to real HCCI conditions.

2.3 The S3D DNS Code

The Sandia DNS code named S3D is used for all simulations in this study. The S3D solver was originally developed at the Sandia national laboratories. S3D solves a system of governing equations for the fully compressible reacting flows including Navier-Stokes, species continuity, and total energy equations [35,36,38]. A high-order accurate, non-dissipative numerical method is used in S3D. In particular, a six-stage fourth-order explicit Runge-Kutta method [39] was used for time integration. An eighth-order central differencing scheme [40] was adopted for spatial discretization. A tenth-order filter, which requires eleven point stencils, is also applied to remove any spurious high-wavenumber fluctuations in the solution. CHEMKIN and TRANSPORT software libraries [41,42] are linked with S3D to evaluate the reaction rates, thermodynamic, and mixture-averaged transport properties of reactive fuel/air mixtures. S3D is constructed on a uniformly structured Cartesian mesh.

The computational domain is decomposed and parallelized using Message Passing Interface (MPI). Each core takes care of a piece of the computational domain such that each MPI process has the same number of grid points and performs the same work load. Interprocessor communication occurs only between nearest neighbors of the topology. At the processor boundaries, a ghost-zone is created by non-blocking MPI sends and receives among the nearest neighbors in the processor topology. All-to-all communications are only performed for monitoring and synchronizing ahead of I/O. S3D was successfully validated under several configurations. It also exhibits good parallel performance with outstanding scalability on several architectures such as Jaguar, Titan, Edison [36,38].

In this study, periodic boundary conditions are imposed in all directions of the fixed 2-D computational domain of 3.2×3.2 mm². For details of the numerical methods, readers are referred to [36].

Chapter 3

Ignition of lean primary reference fuel/air mixtures with temperature inhomogeneities

3.1 Introduction

Many experimental and numerical studies over the past decade have shown that inherent or designed thermal stratification in an HCCI engine cylinder can spread out the rate of pressure rise under high-load conditions by changing the combustion mode of simultaneous auto-ignition into a mixed combustion mode of simultaneous auto-ignition and deflagration [1, 43–53]. In the presence of large temperature fluctuations, auto-ignition of hotter mixtures first occurs and evolves into deflagration waves, which spread to the unburnt mixtures sequentially until the remaining charge auto-ignites simultaneously. In general, the speed of the deflagration waves is much less than that of the ignition front of spontaneous auto-ignition waves and hence, the overall combustion is temporally spread out, resulting in the reduction of the peak of the rate of pressure rise.

Under low-load conditions, however, misfires can occur due to too lean fuel/air mixtures. To overcome such problems, mixture inhomogeneity was proposed [51, 54–57]. The stability and enhancement of HCCI combustion can be achieved through mixture stratification for a low mean equivalence ratio. If relatively richer mixtures exist locally, they usually ignite first and burn hotter, providing heat and radicals to adjacent leaner mixtures and consequently, significantly increase the combustion stability and efficiency.

Even with thermal and composition stratifications, controlling the ignition timing and smoothing the rate of pressure rise are still challenging, and as such, an explicit ignition method such as a spark plug is introduced to HCCI combustion [53, 58–60]. Spark-assisted compression ignition (SACI) is an additional combustion mode to HCCI combustion, in which spark ignition generates deflagration waves prior to simultaneous auto-ignition, similar to HCCI combustion with high thermal stratification. Therefore, it can be used to control the ignition timing and spread out the pressure rise rate under both low- and high- load conditions.

With the help of chemical mechanism reduction techniques and the development of high-performance computing (HPC) clusters, multi-dimensional direct numerical simulations (DNSs) of HCCI combustion of hydrocarbon fuel/air mixtures can now be simulated with realistic kinetic mechanisms and provide detailed understanding of HCCI combustion [48–53]. Chen and co-workers [48–50] elucidated the effects of temperature inhomogeneities and turbulence timescale on the ignition characteristics of lean hydrogen/air mixtures under HCCI conditions. Bansal and Im [51] investigated the effects of composition inhomogeneities together with temperature fluctuations on HCCI combustion of the same lean hydrogen/air mixture. Yoo et al. [52] investigated the ignition characteristics of a lean *n*-heptane/air mixture with different means and root-mean-squares (RMSs) of temperature and the effect of the negative-temperature coefficient (NTC) regime on overall HCCI combustion. Recently, Yoo et al. [53] studied the ignition characteristics of a lean *iso*-octane/air mixture with temperature fluctuations and spark-ignition

timing under both HCCI and SACI conditions. El-Asrag and Ju [61] also investigated the exhaust gas recirculation (EGR) and temperature/mixture stratification effects on the auto-ignition of synthetic dimethyl ether (DME) by adding H_2O_2 in the mixture.

Until now, most previous DNS studies were focused on the effects of thermal and composition stratifications and turbulence timescales on HCCI combustion. The objective of this chapter is to understand and compare the ignition characteristics of different hydrocarbon fuel/air mixtures under HCCI conditions. For this purpose, we selected primary reference fuels (PRFs) because they have been widely used to investigate the combustion characteristics of HCCI engines in the engine research community. PRF is a fuel mixture of *n*-heptane and *iso*-octane. PRF100 and PRF50 comprise 100 % *iso*-octane and 50 % *iso*-octane with 50 % *n*-heptane by liquid volume, respectively. Ultimately, we aim to provide strategies to control the rate of heat release in HCCI combustion by performing two-dimensional parametric DNSs, in which we systematically vary three key parameters: 1) the fuel composition, 2) the initial variance of the temperature, and 3) the ratio of the turbulence to the ignition delay timescale.

3.2 PRF reduced mechanism

The reduced mechanism for PRF oxidation was developed from the detailed Lawrence Livermore National Laboratory (LLNL) mechanism with 874 species and 3,796 elementary reactions [5,6] using a strategy combining directed relation graph (DRG)-based methods, isomer lumping, and timescale analysis [62–65].

As the first step in the reduction, DRG with expert knowledge (DRGX) was employed [21,66,67]. DRGX features a low reduction cost similar to that of DRG, while it can provide a smaller skeletal mechanism through species-specific error control. H radical was used as the starting species for graph searching in DRGX as in previous studies of mechanism reduction using DRG. In DRGX, however, different error tolerances (i.e., x -values) can be specified for selected species based on expert knowledge of the mechanism. The species associated with reactions featuring small uncertainties can typically be assigned small x -values, and those with large uncertainties can be assigned larger x -values, while all other species are assigned a default error tolerance. Errors in heat release were also specified in the same way as the species and errors in temperature could effectively be controlled. For more details of DRGX, readers are referred to [21]. Here, a skeletal mechanism with 368 species and 1,889 reactions was obtained with an x -value of 0.1 for temperature, 0.3 for H radical, and 0.5 for other species.

To reduce the mechanism size further, the isomer lumping method was applied [63]. Isomer lumping detects isomer groups in which intra-group mole fractions do not change and the concentration of each group member can hence be obtained from that of the entire group multiplied

by a constant factor. The group reaction rates can also be computed as the summation of the reaction rate of each isomer group member. As a result, those isomers in one group can be lumped into a single “species” and the mechanism size can further be reduced. By specifying a worst-case error tolerance of 30 % for isomer lumping, 15 isomer groups were identified, resulting in a 328-species skeletal mechanism.

The DRG-aided sensitivity analysis (DRGASA) method [68,69] was subsequently used to minimize the skeletal mechanism size. The sensitivity analysis was performed for auto-ignition delay and extinction residence time in perfectly stirred reactors (PSR). Note that the middle branches of the S-curves in PSR (see Fig. 3-1) were included in the sensitivity analysis because they could be relevant to unsteady flames. By specifying a worst-case error tolerance of 30 %, a skeletal mechanism with 171 species and 861 reactions was developed. Linearized quasi-steady state (QSS) approximation (LQSSA) [70] was further applied to the 171-species skeletal mechanism to reduce the number of transported species. Using a criterion based on computational singular perturbation (CSP) [71], 55 species were identified as global QSS species, while the associated reactions were analytically solved [70]. A 116-species reduced mechanism was obtained. As the last step, the method of dynamic stiffness removal [52,53,64] was employed to eliminate chemical timescales shorter than 10 ns such that explicit time integration could be applied in DNSs.

The skeletal and reduced mechanisms were validated for various PRF compositions with an octane number range of 0 to 100 through auto-ignition delay and extinction residence time over a wide parameter range of pressures from 1 to 50 atm, equivalence ratios from 0.3 to 0.7, and initial temperatures from 750 to 1800 K for auto-ignition and inlet temperature of 300 K for PSR. Figure 3-1 shows a comparison of ignition delays and extinction residence times at an equivalence ratio of 0.3 under different constant pressure conditions and PFR/air mixtures. It is readily observed that both the skeletal and reduced mechanisms reproduce the results of the detailed mechanism accurately. Finally, the laminar flame speeds calculated with the reduced mechanism and those from experimental measurements [72,73] were compared for different pressures and fuel mixtures as shown in Fig. 3-4. The calculated laminar flame speeds show a relatively good agreement with the experimental measurements. Note that for two fuel mixtures, the largest discrepancy between the calculated and measured values was approximately 5 cm/s near the stoichiometric condition.

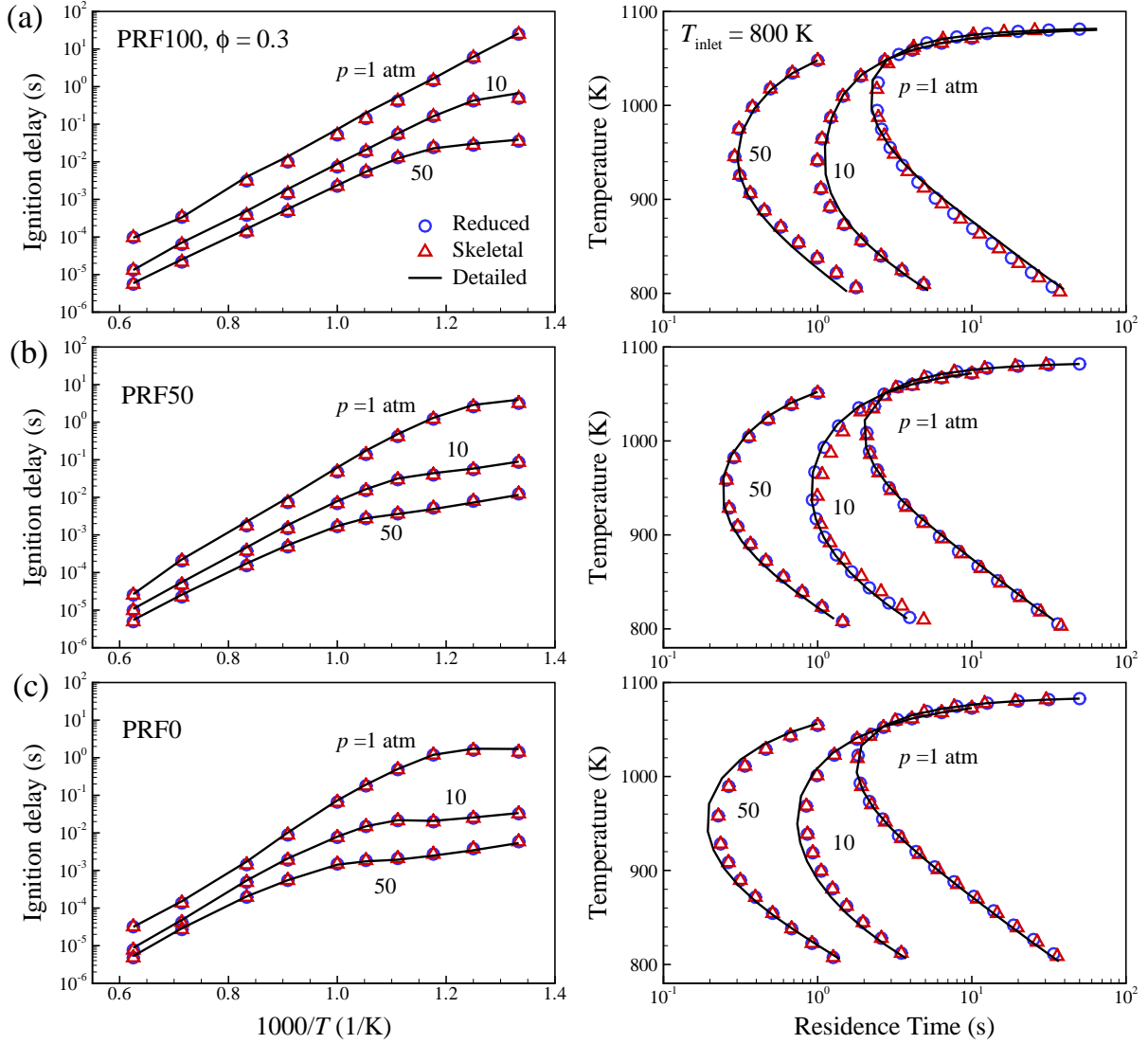


Figure 3-1: Comparison of the 171-species skeletal and the 116-species reduced mechanisms with the detailed mechanism for PRF/air mixtures at different pressures and $\phi = 0.3$.

3.3 Initial conditions

The initial uniform equivalence ratio, ϕ , and pressure, p_0 , were 0.3 and 20 atm, respectively. Note that $p_0 = 20$ atm was adopted to elucidate the ignition characteristics of PRF/air mixtures under elevated pressure similar to that in HCCI engines. Several parametric studies were performed to understand the effects of varying the fuel composition and of varying the ratio of turbulence to the ignition delay timescale. Fifteen different DNSs were performed in the parameter space of the initial physical conditions: different fuel compositions (PRF50, PRF80, and PRF100); temperature fluctuation root mean square (RMS) T' ; most energetic turbulent length scale l_e ; turbulence velocity fluctuation u' ; and turbulence timescale τ_t . Henceforth, τ_{ig} represents the time at which the maximum mean heat release rate occurs for all zero-, one-, and two-dimensional simulations. Especially, the superscript 0 corresponds to the zero-dimensional

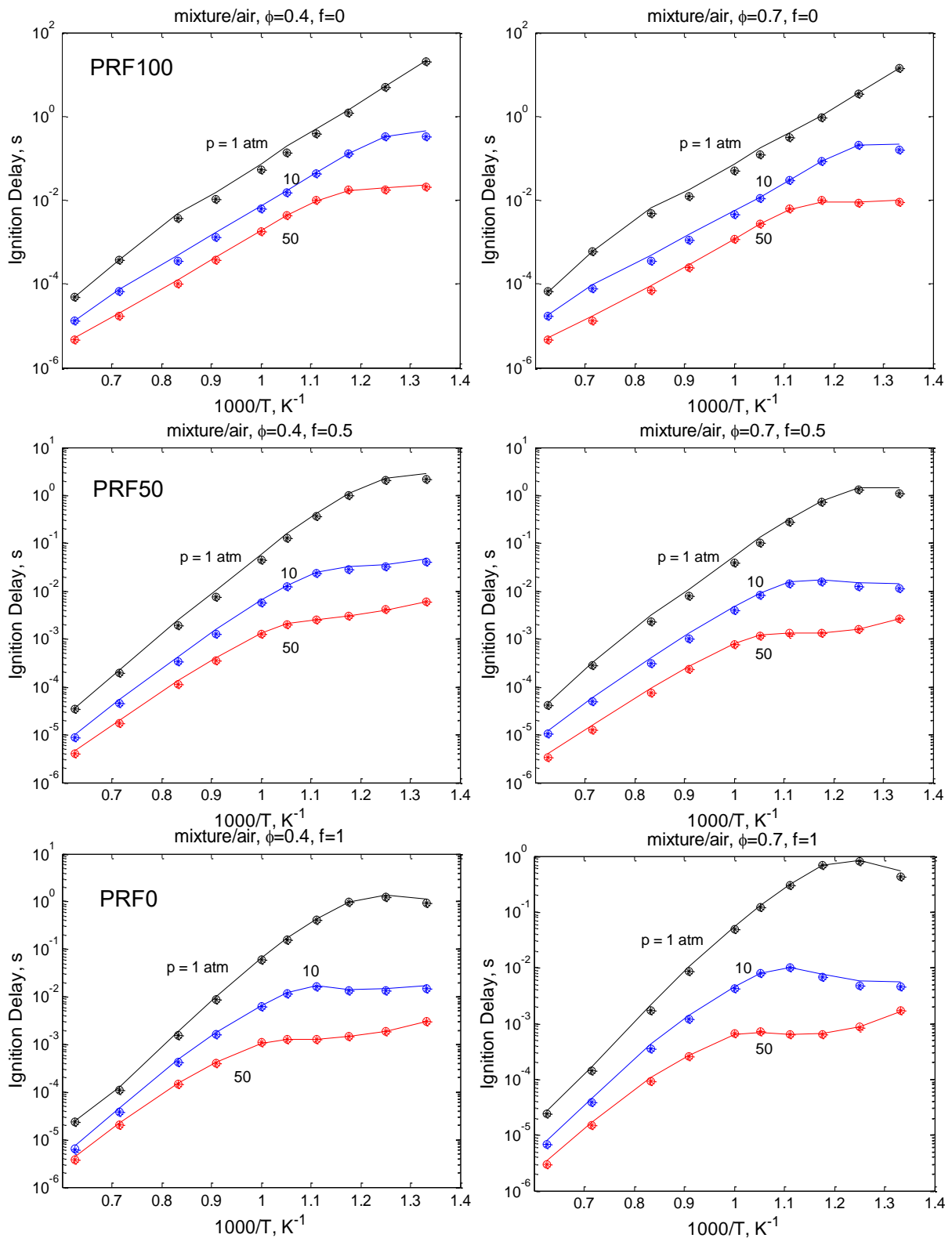


Figure 3-2: Comparison of the ignition delay of the 171-species skeletal and the 116-species reduced mechanisms with the detailed mechanism for PRF/air mixtures at different pressures and equivalence ratios.

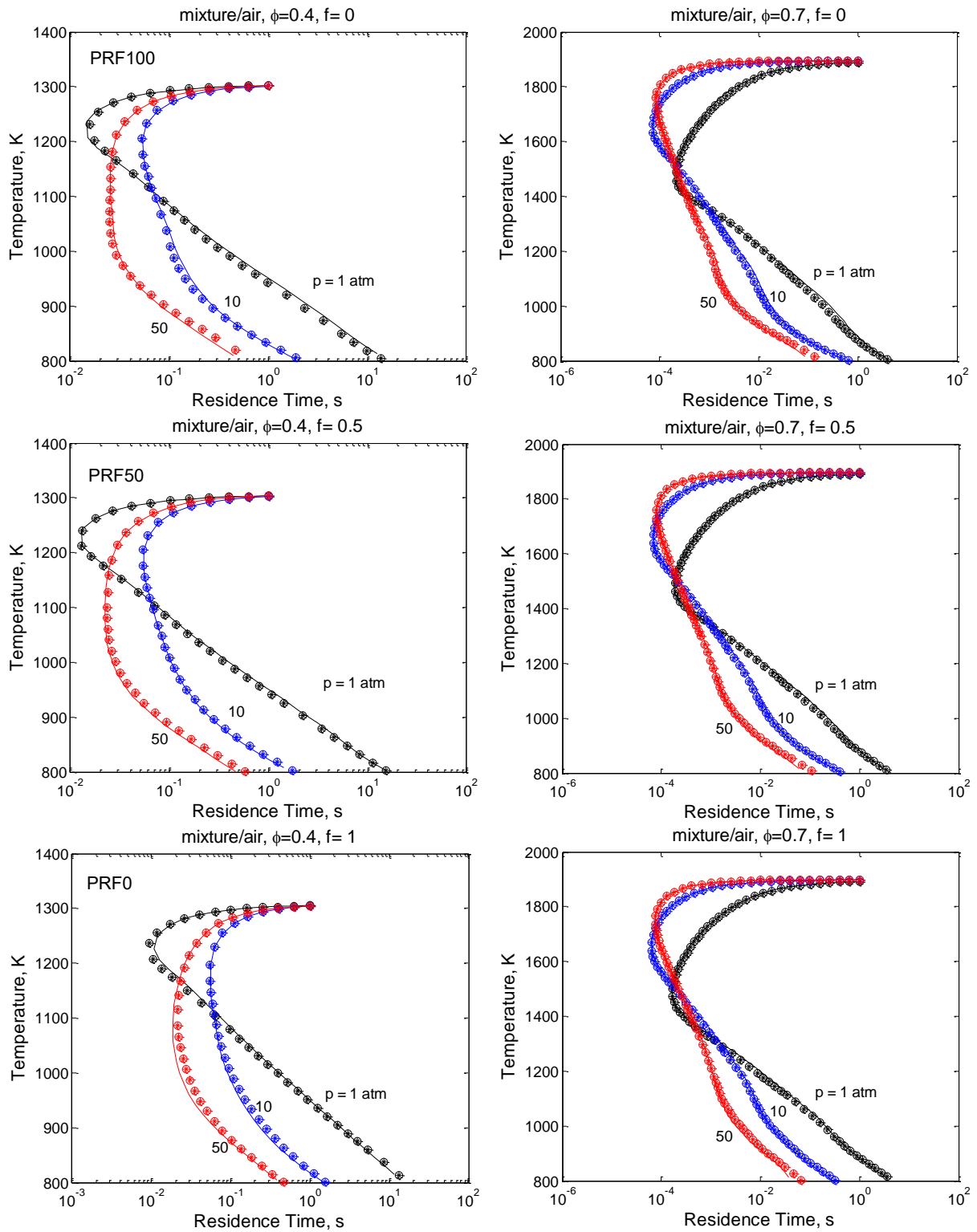


Figure 3-3: Comparison of the extinction residence time of the 171-species skeletal and the 116-species reduced mechanisms with the detailed mechanism for PRF/air mixtures at different pressures and equivalence ratios

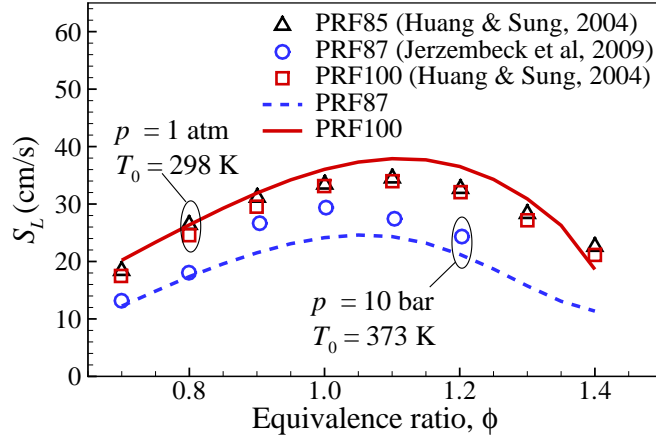


Figure 3-4: Comparison of the laminar flame speed versus the equivalence ratio between experiments (symbols) and calculations with the reduced mechanism (lines) for different PRF/air flames at various pressures.

simulation at a constant volume.

For all simulations, the mean temperature, T_0 , was 1024 K and the homogeneous ignition delays, τ_{ig}^0 , of PRF100, PRF80, and PRF50 were 2.5, 2.39, and 2.29 ms, respectively. T_0 of 1024 K was chosen to approximate the high temperature condition in a gasoline-fueled HCCI engine with EGR at the top dead center. Note that the initial pressure, temperature, and mixture compositions in the present study are not identical to the thermochemical conditions of HCCI engine combustion. However, the ignition characteristics of the PRF/air mixtures under elevated pressure and temperature may provide the insights on the combustion of PRF HCCI engines. The initial turbulent flow field was prescribed by an isotropic kinetic energy spectrum function [37] as in [48–50, 74–76]. The initial temperature field is also generated by a temperature spectrum, similar to the kinetic energy spectrum. Note that the two random fields were uncorrelated. Details of the physical and numerical parameters for the fifteen cases are presented in Table 3-1.

Note that in HCCI combustion, the turbulence timescale is usually more important in determining the combustion characteristics than the absolute values of each parameter [48–53]. The turbulence timescale in real HCCI engines is $\sim O(1 \text{ ms})$ such that the turbulence timescale in the present DNS study is representative of HCCI combustion. It is also of interest to note that two-dimensional turbulence without vortex stretch can be different from three-dimensional turbulence. It is, however, still valuable to investigate HCCI combustion using two-dimensional DNS with a wide range of spectrum of time- and length-scales. Moreover, it was found from previous studies [48–53] that turbulent mixing does not play a major role in HCCI combustion compared to the temperature stratification and hence, it is reasonable to expect that findings resulting from more expensive three-dimensional DNSs may not be very different.

Case	Fuel	T_0 (K)	T' (K)	l_e (mm)	l_{Te} (mm)	u' (m/s)	τ_t (ms)	τ_{ig}^0 (ms)
1	PRF100	1024	15	1.25	1.25	0.5	2.5	2.50
2	PRF100	1024	30	1.25	1.25	0.5	2.5	2.50
3	PRF100	1024	60	1.25	1.25	0.5	2.5	2.50
4	PRF80	1024	15	1.25	1.25	0.5	2.5	2.39
5	PRF80	1024	30	1.25	1.25	0.5	2.5	2.39
6	PRF80	1024	60	1.25	1.25	0.5	2.5	2.39
7	PRF50	1024	15	1.25	1.25	0.5	2.5	2.29
8	PRF50	1024	30	1.25	1.25	0.5	2.5	2.29
9	PRF50	1024	60	1.25	1.25	0.5	2.5	2.29
10	PRF100	1024	15	1.25	1.25	2.5	0.5	2.50
11	PRF80	1024	15	1.25	1.25	2.5	0.5	2.39
12	PRF50	1024	15	1.25	1.25	2.5	0.5	2.29
13	PRF100	1024	60	1.25	1.25	2.5	0.5	2.50
14	PRF80	1024	60	1.25	1.25	2.5	0.5	2.39
15	PRF50	1024	60	1.25	1.25	2.5	0.5	2.29

Table 3-1: Physical parameters of the DNS cases.

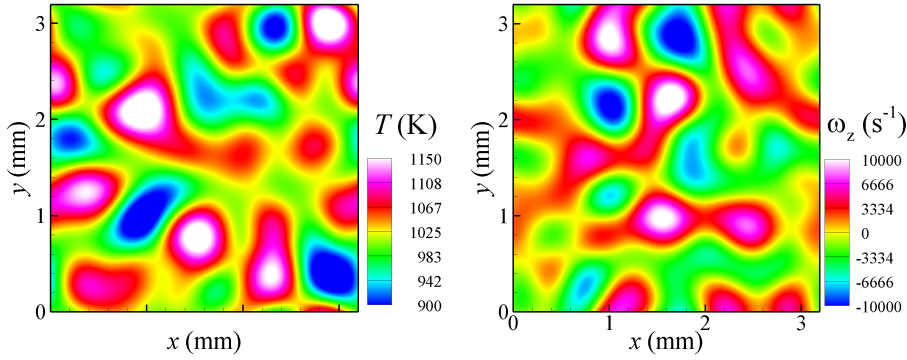


Figure 3-5: Initial temperature and vorticity fields for Case 9.

As in previous studies [52, 53], a square box with the length for each side, L , of 3.2 mm was chosen for the computational domain, which was discretized with 640 grid points for all cases. Note that the gap at the top dead center in real engines is approximately 7 ~ 10 mm, and hence, a box of 3.2 mm of the present simulations represents a good cylinder portion when combustion starts. The most energetic length scale of the temperature fluctuation, l_{Te} , was 1.25 mm for all cases. Typical profiles of the initial temperature and vorticity in the DNS cases are shown in Fig. 3-5. All of the DNSs were performed on the IBM Blue Gene/P at King Abdullah University of Science and Technology (KAUST). Each of the DNSs required approximately 0.5 million CPU-hours.

3.4 Effects of fuel composition and initial temperature RMS

In the first parametric study, the combined effect of the initial fuel composition and temperature fluctuation on the ignition of lean PRF/air mixtures was investigated. Different degrees of temperature fluctuation for different PRF/air mixtures were chosen: i.e., $T' = 15, 30,$ and 60 K. For this parametric study, nine different DNS cases (Cases 1–9) were run (see Table 1 for detailed parameters of the DNSs). Note that the initial mean temperature and pressure of the present DNSs exist outside of the negative temperature coefficient (NTC) regime as shown in Fig. 3-6 such that two-stage ignition in PRF oxidation does not exist under those conditions.

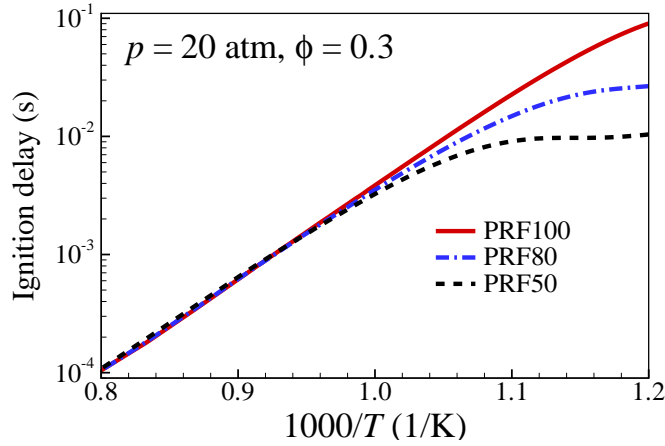


Figure 3-6: Homogeneous ignition delays of different PRF/air mixtures at a constant volume with an initial pressure of 20 atm as a function of the initial temperature.

3.4.1 Overall characteristics of PRF HCCI combustion

Figure 3-7 shows the temporal evolution of the mean pressure, \bar{p} , and the mean heat release rate (HRR), \bar{q} , with different levels of temperature fluctuations for different PRFs (Cases 1–9), where “mean” represents the spatial average over the whole simulation domain. For the purpose of comparison, the temporal evolutions of 0-D homogeneous ignition of the corresponding PRF/air mixtures are also shown in the figure. Note that the homogeneous ignition delay of the PRF100/air mixture ($\tau_{ig}^0 = 2.5$ ms) was chosen as the reference time.

It is readily observed from the figure that \bar{p} increases more slowly and \bar{q} is more distributed over time with increasing T' regardless of the fuel composition. Note that large T' induces more irregularity in the instantaneous HRR field but the mean HRR is more spread out over time. In addition, the overall combustion occurs quickly and the peak \bar{q} decreases with increasing T' for the same PRF/air mixture. Consequently, the duration of the occurrence of significant mean HRR also increases with increasing T' . These results are qualitatively similar to those of the

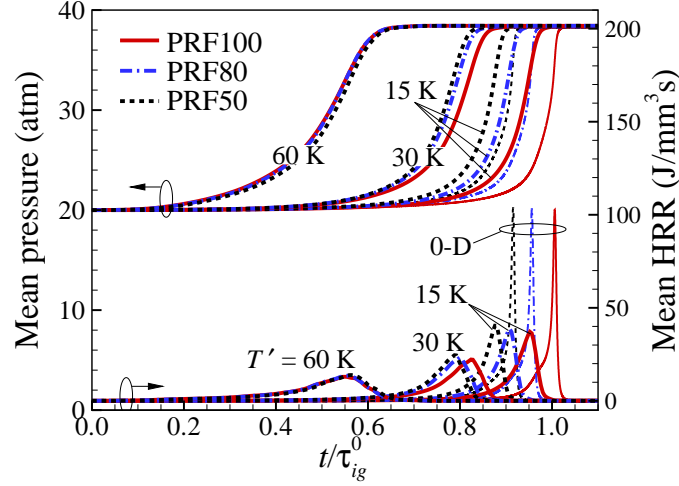


Figure 3-7: Temporal evolution of the mean pressure and the mean heat release rate for Cases 1–9. Thin lines represent the corresponding cases of 0-D homogeneous ignition.

ignition of a lean hydrogen/air mixture [49,50] and of lean hydrocarbon/air mixtures with high initial mean temperatures [52,53]. In short, these results are attributed to the mode change of HCCI combustion with the degree of T' ; i.e., the spontaneous ignition mode is predominant for small T' while the mixed mode of deflagration and spontaneous ignition occurs for large T' . In general, large T' induces more deflagration waves, which results in the spread of \bar{q} and the fast occurrence of the overall combustion.

It is also of interest to note that for the cases with the same T' , the effect of the fuel composition vanishes with increasing T' . For cases with small T' (Cases 1, 4, and 7), τ_{ig} increases with increasing *iso*-octane volume percentage in the PRF (i.e., PRF50 \rightarrow PRF80 \rightarrow PRF100). For cases with large T' (Cases 3, 6, and 9), however, the temporal evolutions of \bar{q} are almost identical for the three cases, implying that the effect of different fuel compositions of PRFs on HCCI combustion may vanish. As explained above, the deflagration mode may be dominant in the overall combustion of the cases with large T' and, hence, the propagation characteristics of each PRF/air deflagration wave become more important than those of the chemical kinetics for initiating nascent ignition kernels. However, the laminar flame speeds of PRF/air mixtures with different octane numbers are nearly identical as shown in Fig. 3-4 such that it can be expected that the overall combustion would be similar even for different PRF/air mixtures only if the deflagration mode were dominant in HCCI combustion. This issue will be discussed further below.

To further identify the mode change in the ignition of PRF/air mixtures, the isocontours of the heat release rate, \dot{q} , for Cases 1–3 approximately at each τ_{ig} are shown in Fig. 3-8. \dot{q} is normalized by the corresponding maximum heat release rate during the 0-D homogeneous ignition of the PRF100/air mixture, $\dot{q}_m^0 = 103.5 \text{ J/mm}^3\text{s}$. For small T' (Case 1), \dot{q} occurs nearly simultaneously over a wide area of the domain as spontaneous ignition. For large T' (Case 3),

however, high \dot{q} is observed primarily in thin sheets. Note that for Case 1, the combustion process completely ends in $0.05\tau_{ig}^0$ past τ_{ig} while it continues nearly $0.13\tau_{ig}^0$ after τ_{ig} for Case 3. These results suggest that spontaneous ignition seems to be predominant for small T' while deflagration seems to be predominant for large T' .

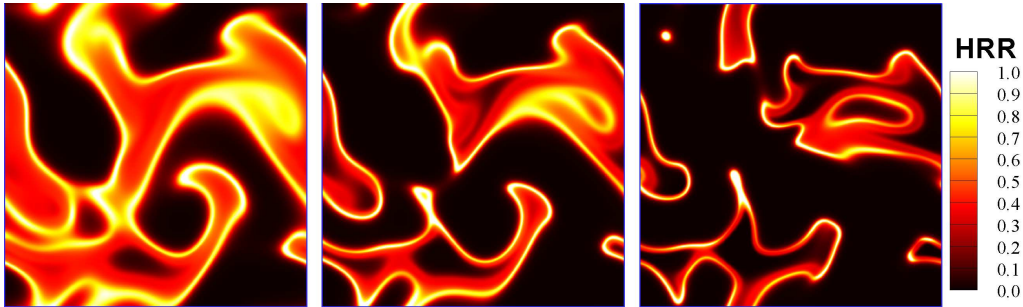


Figure 3-8: Isocontours of the normalized heat release rate for Cases 1–3 (from left to right) at $t/\tau_{ig}^0 = 0.95, 0.82,$ and $0.56,$ respectively.

3.4.2 Chemical explosive mode analysis

Chemical explosive mode (CEM) is adopted to further identify the ignition characteristics of PRF/air mixtures. Chemical explosive mode analysis (CEMA) has been developed for systematically detecting critical flame features such as ignition, extinction, and flame fronts and applied to DNSs of lifted flames in heated coflows [77–80], reacting jets in cross flows [81, 82], and ignition of *n*-heptane/air mixture under HCCI conditions [52, 83].

The CEMA method is briefly introduced here. Readers may refer to [78] for more details about CEMA. The differential equations of a typical reacting flow can be described in discretized form as:

$$\frac{D\mathbf{y}}{Dt} = \mathbf{g}(\mathbf{y}) = \boldsymbol{\omega}(\mathbf{y}) + \mathbf{s}(\mathbf{y}), \quad (3.4.1)$$

where D/Dt is the material derivative, which can be replaced by d/dt in the Lagrangian coordinate, and \mathbf{y} is the solution vector including species concentrations and temperature. Note that for spatially discretized flows, the chemical species concentration at different grid points corresponds to different entries in \mathbf{y} . $\boldsymbol{\omega}$ and \mathbf{s} represent, respectively, the chemical source term and all non-chemical terms such as diffusion and homogeneous mixing.

The Jacobian matrix of the chemical source term, $\mathbf{J}_{\boldsymbol{\omega}}(\equiv \partial\boldsymbol{\omega}/\partial\mathbf{y})$, can fully describe the local chemical information. As such, a chemical mode can be defined as an eigenmode of $\mathbf{J}_{\boldsymbol{\omega}}$, which is associated with an eigenvalue and a corresponding pair of the left and right eigenvectors. CEM is defined as a chemical mode of which the real part of the eigenvalue, λ_e , is positive [78]. By definition, CEM represents the reciprocal chemical time scale of a local mixture such that the existence of CEM implies that the corresponding mixture is explosive in nature. It is, therefore,

likely to auto-ignite if the mixture is put in a lossless environment where the term \mathbf{s} in Eq. 7.2.1 is negligible. Note that ignition may not actually occur in a mixture exhibiting CEM when significant loss in heat or radicals is present. Therefore, CEM remains an intrinsic chemical feature of ignitable mixtures.

In spatially inhomogeneous systems, CEMs interact with diffusion and other mixing processes. As such, ignition may not always result if the time scale of CEM is longer than those of the losses. The competition between CEMs and the losses can be approximately quantified by a Damköhler number defined as [78–80, 83]:

$$Da_c = \lambda_e \cdot \chi^{-1}, \quad (3.4.2)$$

where χ is a reciprocal characteristic timescale of the diffusion or loss term \mathbf{s} ; for instance, the scalar dissipation rate in turbulent flames. In this study, χ , is defined by $\chi = 2D|\nabla c|^2$, where c and D are the progress variable and the thermal diffusivity of local mixture, respectively. c is defined as $c \equiv Y_c/Y_c^{\text{Eq}}$, where $Y_c = Y_{\text{CO}_2} + Y_{\text{CO}}$ and Y_c^{Eq} is the corresponding equilibrium value of Y_c . Note that a mixture with $Da_c \gg 1$ indicates a dominant CEM which will likely result in actual ignition; otherwise, ignition may be suppressed by the losses.

Figure 3-9 shows the isocontours of λ_e , Da_c , temperature, and χ of Case 1 (PRF100 with $T' = 15$ K) at $t = \tau_{ig}$. The sharp boundaries separating the burned and unburned mixtures are the reaction fronts that can be either spontaneous ignition or a deflagration wave. It is readily observed from Fig. 3-9b that the thin reaction fronts separate the whole domain into two bulk regions; i.e., the auto-igniting (red and yellow) region with large positive Da_c where the chemical explosive process (large λ_e) overwhelms the mixing process (relatively small χ), and the post-ignition (blue) regions with large negative Da_c where the mixing process (χ) is dominant compared with large negative λ_e . It can also be observed that Da_c upstream of the reaction fronts is much larger than unity (yellow region), suggesting that the chemical reaction (λ_e) is also much faster than the mixing process (χ). In deflagration waves, the reaction and mixing processes balance each other and, as such, large $Da_c (\gg O(1))$ ahead of the reaction fronts also verifies that the reaction fronts in the figure are attributed to spontaneous ignition rather than to deflagration.

On the contrary, it can be observed from Fig. 3-10b for the high T' case that there exist three bulk regions: the auto-igniting region (red), the post-ignition region (blue), and the greenish region where mixing balances chemical explosion. Note that Da_c upstream of the reaction fronts (greenish region) becomes order of unity because the mixing process (χ in Fig. 3-10d) shows the same order of magnitude as the chemical explosion process (λ_e in Fig. 3-10a). These results also indicate that the reaction fronts of Case 3 are deflagrations rather than spontaneous ignitions.

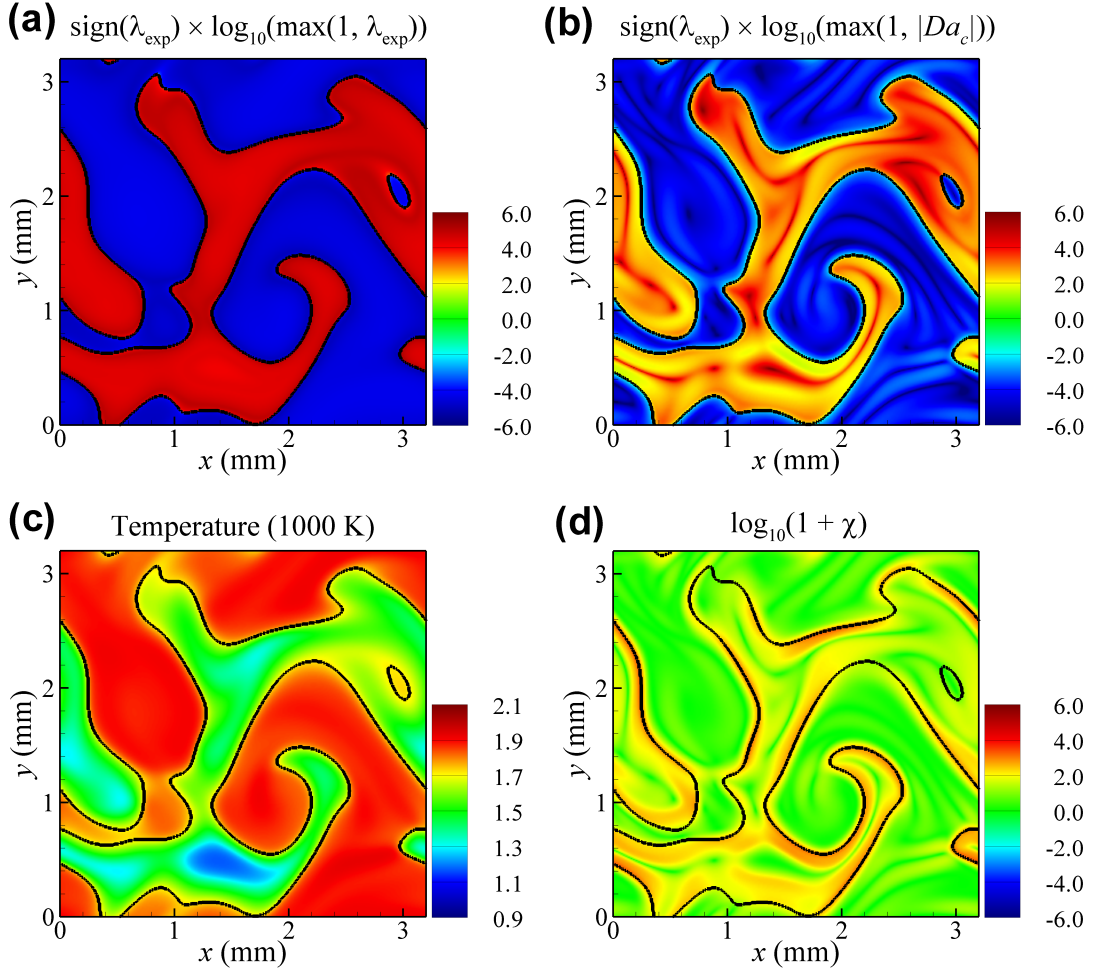


Figure 3-9: Isocontours of (a) the timescale of the chemical explosive mode, (b) Da_c , (c) temperature, and (d) χ for Case 1 ($T' = 15$ K) at $t/\tau_{ig}^0 = 0.95$. The solid line denotes the reaction front ($Da_c = 1$).

It is also of interest to note from Fig. 3-10d that the reaction fronts mostly overlap with the strips with relatively large χ , a feature of deflagration waves propagating through unburned mixtures prior to the occurrence of auto-ignition.

3.4.3 Front speed and burning rate

To clarify the propagation characteristics of the combustion waves, the density-weighted displacement speed, S_d^* , is evaluated for the nine cases. S_d^* is defined by [77, 84, 85]:

$$S_d^* = \frac{1}{\rho_u |\nabla Y_k|} \left(\dot{\omega}_k - \frac{\partial}{\partial x_j} (\rho Y_k V_{j,k}) \right), \quad (3.4.3)$$

where Y_k , $V_{j,k}$, and $\dot{\omega}_k$ denote the species mass fraction, the species diffusion velocity in the j -direction and the net production rate of species k , respectively, and ρ_u is the density of the unburnt mixture. ρ_u is calculated from the local enthalpy and fresh mixture conditions assuming

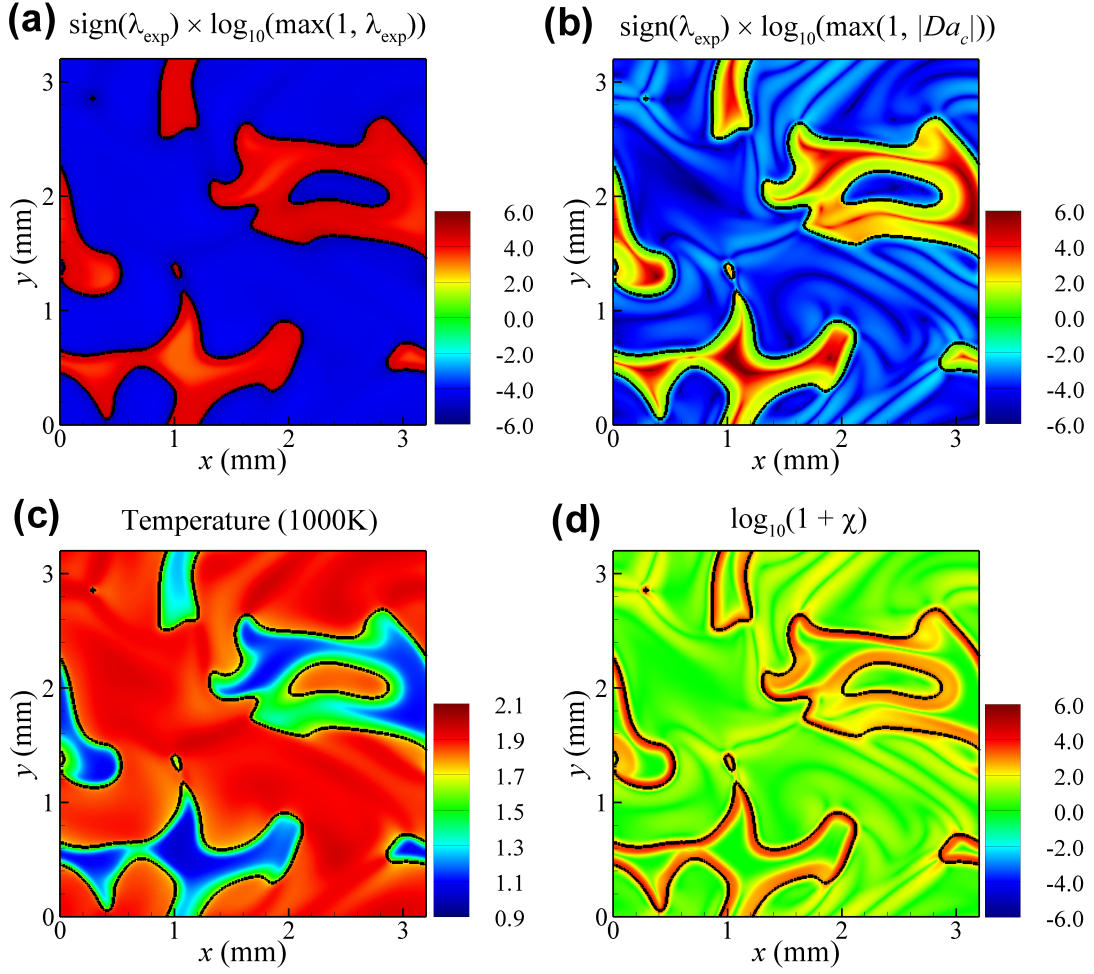


Figure 3-10: Isocontours of (a) the timescale of the chemical explosive mode, (b) Da_c , (c) temperature, and (d) χ for Case 3 ($T' = 60$ K) at $t/\tau_{ig}^0 = 0.56$. The solid line denotes the reaction front ($Da_c = 1$).

that the pressure and enthalpy remain constant across the front [49, 50, 52, 53]. In the present study, the isocontour of $Y_c = 0.049$ is chosen to evaluate the displacement speed for all cases. This particular isocontour coincides approximately with the location of maximum \dot{q} of PRF/air mixtures.

Figure 3-11 shows the temporal evolutions of the mean front speed, $\overline{S_d^*}$, for two-dimensional DNS cases, all of which are normalized by the corresponding laminar flame speed, S_L . The evolutions of the front speed for one-dimensional cases are also shown for comparison. As in previous studies [52, 53], one-dimensional reference cases are simulated using a sinusoidal temperature profile. The wavelength of 1.25 mm in the one-dimensional cases matches the most energetic length scale, l_e , in the two-dimensional DNS cases and the mean and RMS temperature, T_0 and T' , also match the two-dimensional DNS cases. S_L is estimated from a transient one-dimensional reactive simulation as in [52, 53]. The simulation was initialized with a high-temperature ignition source such that a combustion wave emanates from the source,

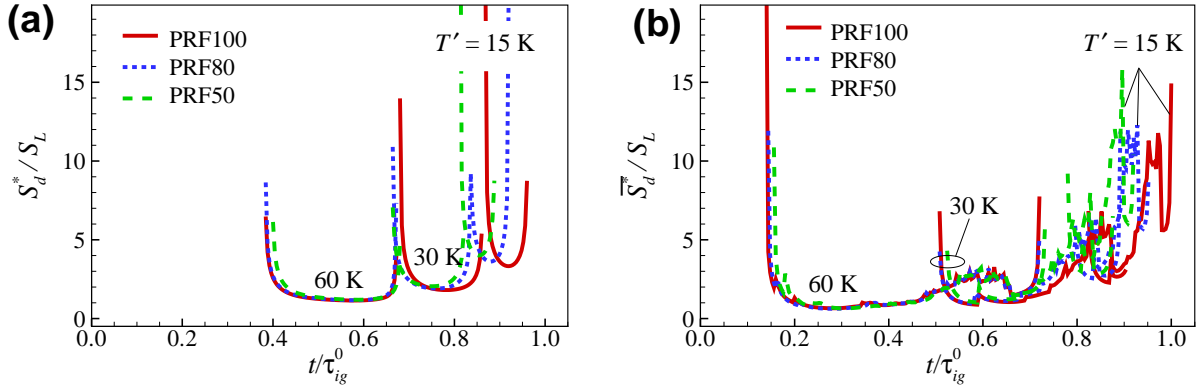


Figure 3-11: Temporal evolution of (a) S_d^* for one-dimensional reference cases and (b) the mean front speed, $\overline{S_d^*}$, for Cases 1-9.

propagating into the reactive mixture ahead of it. From the simulations, S_L is found to be approximately 0.37 m/s for all PRF/air mixtures. It is readily observed from the figure that the mean front speeds of DNS cases exhibit a characteristic ‘U’ shape that is qualitatively consistent with previous studies [52, 53]. The occurrence of the ‘U’-shaped mean front speed is attributed to the initial thermal run-away in the nascent ignition kernel during the early phase of combustion and the burnout of the remaining charge due to compression heating during the last phase of combustion [52, 53, 85].

Figure 3-11 also shows that the mean front speed similar to S_L develops earlier with increasing T' and the duration of the region with a constant front speed at the bottom of the ‘U’ shape also increases with increasing T' . For cases with small T' , however, the mean front speed is much greater than S_L and there is no region with a constant front speed. These results suggest the occurrence of different combustion modes depending on the degree of T' ; for large T' cases, deflagration represented by $\overline{S_d^*} \sim S_L$ occurs at the reaction fronts, and for small T' cases, simultaneous auto-ignition represented by $\overline{S_d^*} \gg S_L$ occurs at the reaction fronts. It is revealed from Figs. 3-8 – 3-11 that for cases with small T' , the spontaneous ignition mode of combustion primarily occurs through the whole domain, resulting in an excessive rate of heat release within a very short time more like in the case of 0-D homogeneous auto-ignition. For cases with large T' , however, the deflagration mode of combustion occurs at the reaction fronts while the spontaneous ignition mode of combustion also occurs upstream of the reaction fronts. Note also that large T' induces more locally hotter mixtures and local auto-ignition, hence, occurs and develops into a deflagration wave sooner than in cases with small T' such that the overall combustion starts sooner and persist longer than that of small T' .

To measure the occurrence of deflagration and spontaneous ignition modes systematically during combustion, the temporal evolutions of the fraction of heat release rate attributed to deflagration for Cases 1–9 are shown in Fig. 3-12. To distinguish between the two modes of

propagation, the Damköhler number, Da , defined by [77, 79, 86], is adopted:

$$Da = \frac{\dot{\omega}_k}{|-\nabla \cdot (\rho Y_k \mathbf{V}_k)|}, \quad (3.4.4)$$

where Y_c is used for the Damköhler number analysis. From a one-dimensional laminar simulation, it is found that Da in the diffusive limit is approximately 3.3, where the diffusive limit represents deflagration wave propagation without auto-ignition, i.e., where diffusion balances reaction. Note that the departure of Da in the diffusive limit from unity is a consequence of the upstream mixture being highly reactive and hence, the reaction term is somewhat larger than the diffusion term [52]. Here, the delineation between the two propagation modes is defined by $Da = 3.3$ such that Da less than 3.3 represents a deflagration wave.

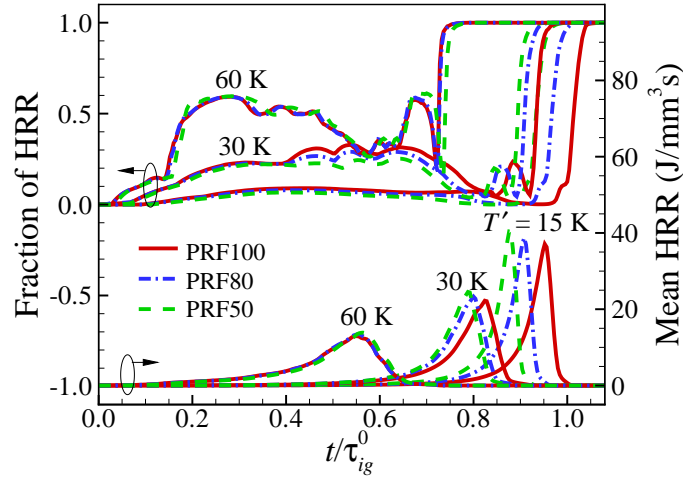


Figure 3-12: Temporal evolution of the fraction of the heat release rate from the deflagration mode and the mean heat release rate for Cases 1–9.

Several points should be noted from Fig. 3-12. First, the fraction of \dot{q} from the deflagration mode increases with increasing T' regardless of the fuel composition as expected from the explanation above. Second, for cases with large T' (Cases 3, 6, and 9), more than half of \dot{q} occurs by the deflagrations during most of the combustion process such that the total heat release from the deflagration mode for Cases 3, 6, and 9 are approximately 40 %. For cases with small T' (Cases 1, 4, and 7), however, the fraction of \dot{q} from deflagrations is relatively small prior to the peak of \dot{q} and continues to increase until the end of the combustion. This observation is attributed to the fact that at the final stage of the ignition, all explosive modes die out and the corresponding Da also vanishes such that the fraction of \dot{q} from the deflagration mode becomes unity. Note that the total heat release from the deflagration mode for Cases 1, 4, and 7 is approximately 1 %.

These results are qualitatively consistent with those in previous studies [49, 50, 52, 53]. In short, for cases with small T' , only a small fraction of combustion occurs by deflagration,

verifying that spontaneous auto-ignition is predominant for the combustion with small T' , and for cases with large T' , a relatively large fraction of combustion occurs by deflagration, indicating that both deflagration and spontaneous ignition occur for large T' . These results verify that the deflagration mode of combustion is attributed to the temporal spreading of the excessive rate of heat release and the vanishing of the effect of the fuel composition in HCCI combustion with large T' .

3.5 Effect of turbulence

As explained in previous studies [49, 52, 53], turbulence with a short turbulence timescale, τ_t , is able to homogenize initial temperature fluctuations of a fuel/air mixture such that the overall combustion can be retarded compared to that with long τ_t and is more apt to occur by spontaneous ignition. It was also found from [53] that the ratio between the temperature fluctuation and turbulence length scales (l_{Te} vs. l_e) play an important role in homogenizing the mixture; turbulence with l_e comparable to l_{Te} can effectively homogenize the mixture together with large u' . However, turbulence with l_e much smaller than l_{Te} is not able to homogenize the mixture although τ_t is short enough. In this section, therefore, the effect of turbulence on the ignition of PRF/air mixtures is elucidated. Six additional DNSs (Cases 10–15) were performed with greater turbulence intensity for different PRF/air mixtures. Note that the six cases have the same turbulence intensity, u' , which is five times greater than the turbulence intensity in the other cases with l_e being identical to l_{Te} to maximize homogenization. Details of the parameters are shown in Table 3-1.

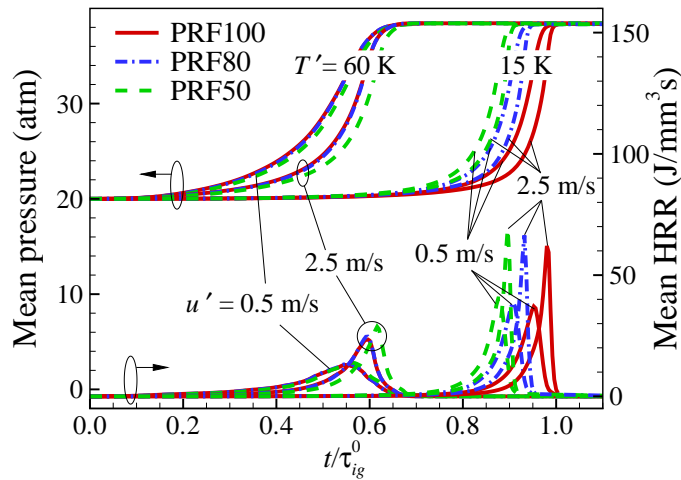


Figure 3-13: Temporal evolution of the mean pressure and the mean heat release rate for Cases 1, 4, 7, 10–12 ($T' = 15$ K) and 3, 6, 9, 13–15 ($T' = 60$ K).

Figure 3-13 shows the temporal evolution of \bar{p} and \bar{q} for the additional cases. For purposes

of comparison, Cases 1, 4, 7 ($T' = 15$ K), and 3, 6, 9 ($T' = 60$ K) are also shown in the figure. Several points are to be noted from the figure. For cases with small T' , turbulence with short τ_t and large u' can effectively homogenize the mixtures. Consequently, both τ_{ig} and the peak of \bar{q} are increased and the combustion is more apt to occur by spontaneous ignition regardless of the fuel composition. Similarly, for cases with large T' , both τ_{ig} and the peak of \bar{q} are also increased with large u' although the effect of large u' on the homogenization of the mixture is not as significant as in cases with small T' .

It is of interest to note that for cases with small T' , turbulence with even large u' has no significant effect on the ignition chemistry of PRF/air mixtures; i.e., ignition occurs in the same order as in the 0-D homogeneous auto-ignition (PRF50 \rightarrow PRF80 \rightarrow PRF100). More specifically, τ_{ig} for Cases 10 \sim 12 are 2.25, 2.32, and 2.45 ms, respectively. For large T' , however, it seems that turbulence with large u' retards the overall combustion of PRF50 a little more than it does the other PRFs. In the large T' condition, the deflagrations cover a significant portion of the overall combustion and, hence, it can be expected that the turbulence-flame interaction becomes significant. In addition, it was observed in experiments [87, 88] that PRF100/air premixed flames are easier to extinguish than PRF0/air ones in the counterflow configuration, which implies that nascent ignition kernels or deflagrations of the PRF100/air mixture are more apt to be dissipated or extinguished by large u' .

However, the Karlovitz number of the present DNSs ($\sim O(0.1)$) is too low to induce flame extinction such that the ignition of locally-hotter mixtures prior to the start of deflagration mode of combustion may govern the start of the heat release. It can be found from Fig. 3-6 that the ignition delay of PRF50 is slightly longer than those of the other PRFs when the initial temperature is greater than 1080 K. Together with the ignition characteristics of PRFs under high temperature condition, the front speeds of the one-dimensional HCCI ignition waves in Fig. 3-11(a) verify that in the large T' condition, the deflagration mode of combustion of PRF50 starts later than the other PRFs. Once the deflagration mode of combustion starts, the overall heat release of the PRFs becomes nearly identical because of the similar propagation characteristics of PRFs. As a result, the overall combustion of PRF50 is slightly more retarded by high u' than those of the other two PRFs. The late start of the deflagration mode of combustion of PRF50 leads to more significant difference of the overall combustion because the homogenization effect by turbulence becomes significant as the peak heat release rate increases.

Finally, the temporal evolutions of \bar{S}_d^* and the fraction of the heat release rate from deflagration are shown in Figs. 3-14 and 3-15 to identify the combustion mode. It is readily observed from Fig. 3-14 that regardless of the magnitude of u' , \bar{S}_d^* is nearly identical for cases with large T' (Cases 3, 6, 9, and 12–15) except in the final stage of ignition. This is because the deflagration mode of combustion is predominant at the reaction fronts, verifying that the deflagration speed

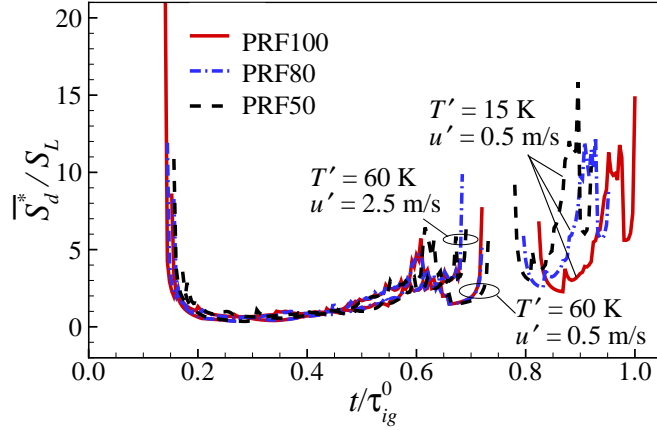


Figure 3-14: Temporal evolution of the mean front speed, \overline{S}_d^* , for Cases 1, 4, 7, 10–12 ($T' = 15$ K) and 3, 6, 9, 13–15 ($T' = 60$ K).

is not affected by turbulence. The retardation of PRF50 ignition under the high u' condition is also identified from the figure. However, for small T' cases with large u' (Cases 10–12) \overline{S}_d^* cannot be evaluated numerically because combustion occurs mostly as spontaneous ignition similar to 0-D auto-ignition and, hence, the reaction fronts do not exhibit deflagrative characteristics.

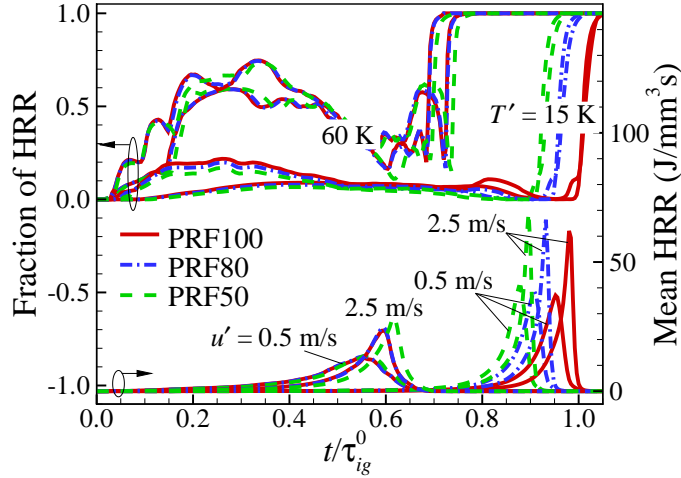


Figure 3-15: Temporal evolution of the fraction of the heat release rate from the deflagration mode and the mean heat release rate for Cases 1, 4, 7, 10–12 ($T' = 15$ K) and 3, 6, 9, 13–15 ($T' = 60$ K).

These combustion characteristics are also found in the fraction of \dot{q} from the deflagration mode as shown in Fig. 3-15. Note that the total heat releases from the deflagration mode for Cases 12–15 are approximately 34, 32, and 28 %, respectively, which are relatively smaller than those of Cases 3, 6, 9 with small u' , implying that high turbulence intensity can effectively homogenize the mixture such that the portion of combustion by deflagration is decreased. Moreover, as mentioned above, the retardation of PRF50 combustion results in more homogenization such that the total heat release from the deflagration mode of PRF50 is the smallest among the three cases.

3.6 Conclusions

The effects of PRF composition, thermal stratification, and turbulence intensity on the auto-ignition of lean homogeneous PRF/air mixtures at constant volume and elevated pressure are investigated by direct numerical simulations with a 116-species reduced mechanism. In the first parametric study, nine cases of HCCI combustion were studied with different degrees of temperature fluctuations for three different PRF/air mixtures. The chemical explosive mode (CEM), displacement speed, and Damköhler number analyses verify that, in general, larger T' induces greater temporal spreading of the mean heat release rate regardless of PRF/air mixtures because the deflagration mode is predominant at the reaction fronts for large T' . On the contrary, spontaneous ignition prevails for small T' and, hence, simultaneous auto-ignition occurs throughout the whole domain, resulting in an excessive rate of pressure rise. It was also found that the effect of fuel composition on the ignition of PRF/air mixtures vanishes for cases with large T' because the deflagration mode prevails at the reaction fronts and the propagation characteristics of deflagrations are nearly identical.

In the second parametric study, the effect of turbulence intensity on the ignition characteristics of PRF/air mixtures was elucidated. It was found that turbulence with large u' and short τ_t can effectively homogenize the mixtures such that the overall ignition is more apt to occur by spontaneous ignition in all the cases. It was, however, found that turbulence with large u' retards the overall combustion of PRF50 more significantly because nascent ignition kernels of a PRF50/air mixture are more likely to be dissipated or extinguished by turbulence than are those of the other PRF/air mixtures. Therefore, these propagation and extinction characteristics result in the retardation of the overall combustion of PRF50/air mixture with large u' .

These results suggest that large thermal stratification provides smooth operation of HCCI engines regardless of the PRF composition. In addition to the ignition characteristics, the propagation and extinction characteristics of deflagrations of different PRF/air mixtures should be considered for the design and operation of HCCI engines.

Chapter 4

Ignition of a lean biodiesel/air mixture with temperature and composition inhomogeneities at high pressure and intermediate temperature

4.1 Introduction

A strategy of controlling mixture inhomogeneities has been proposed as a promising means of controlling the ignition timing and PRR. Thermal stratification can be introduced to a fuel/air mixture by high levels of exhaust gas recirculation (EGR), intake charge heating, and wall heat transfer controls. It has been demonstrated experimentally and numerically that thermal stratification can tailor PRR by prolonging combustion duration, thereby enabling HCCI combustion under conditions of higher load [43–50, 52, 53, 89, 90].

However, the manipulation and exploitation of the thermal stratification of in-cylinder charge is not easy and remains a challenge [1, 91, 92]. For this reason, stratified-charge compression ignition (SCCI) combustion has been investigated as an alternative solution for enlarging the operating range of HCCI combustion [47, 91, 93]. With the help of fuel stratification, a sequential ignition event can be achieved as a locally-richer mixture tends to ignite initially and then ignition propagates towards a nearby leaner mixture. As a result, SCCI combustion enables a smooth combustion sequence, preventing any rapid release of energy and reducing the peak rate of pressure rise. In practice, fuel stratification can be achieved by multiple high-pressure injectors with flexible injection timing [16, 17, 47]. In two-stage injection, for instance, a major fraction of the fuel is initially supplied by port fuel injection to generate a relatively-homogeneous mixture [47]. The remainder of the fuel (up to 20% of total fuel volume) is then directly injected during the late compression stroke or close to the top dead center (TDC) to introduce a certain amount of equivalence ratio (ϕ) fluctuations [17].

SCCI combustion under HCCI condition has been studied extensively [1, 47, 51, 54, 61, 91–106]. Recently, Bansal and Im [51] investigated the ignition characteristics of a hydrogen/air mixture with both temperature and composition inhomogeneities using two-dimensional (2-D) DNSs. It was found that composition inhomogeneities together with temperature fluctuations spread out the heat release rate (HRR) more than temperature fluctuations alone. However, it is not clear that the results will be directly applicable to hydrocarbon/air mixtures exhibiting two-stage ignition.

The objective of this chapter is, therefore, to provide a fundamental understanding of the ignition characteristics of a hydrocarbon/air mixture with temperature and composition stratifications under high pressure and intermediate temperature using 2-D DNSs. The DNSs are conducted by systematically changing three key parameters: (1) initial temperature fluctuation, (2) initial equivalence ratio fluctuation, and (3) turbulence time scale. In the present study, biodiesel is adopted as a fuel exhibiting two-stage ignition similar to *n*-heptane [52] such that the results of its ignition under HCCI condition may be readily extended to other hydrocarbon fuels with similar two-stage ignition behavior. Biodiesel is a renewable fuel that can contribute toward reducing the demand of fossil fuels. In practice, biodiesel can be blended with petrodiesel

to improve the overall combustion performance in terms of efficiency and emissions. For the present study, however, neat biodiesel is utilized to provide a more in-depth understanding of its ignition characteristics under HCCI conditions by using DNSs [107–111].

4.2 Initial conditions

As mentioned above, we adopted biodiesel as a hydrocarbon fuel, which is a mixture of mono-alkyl esters of long-chained fatty acids produced from vegetable oils or animal fats by transesterification in the presence of a catalyst. The chemical kinetics of biodiesel oxidation is extremely complex due to its large molecular structure, especially at low temperatures. For the present DNSs, a 73-species reduced mechanism was developed from a previous skeletal mechanism for a tri-component biodiesel surrogate that consists of 25% methyl decanoate (MD), 25% methyl 9-decanoate (MD9D), and 50% *n*-heptane by volume [80, 112]. The skeletal mechanism was developed from a detailed mechanism of LLNL [113] for the numerical studies of compression ignition engine applications with a reasonable computational time and cost. Linearized quasi steady state approximations (QSSA) are applied to the skeletal mechanism to further reduce the number of transported species [114].

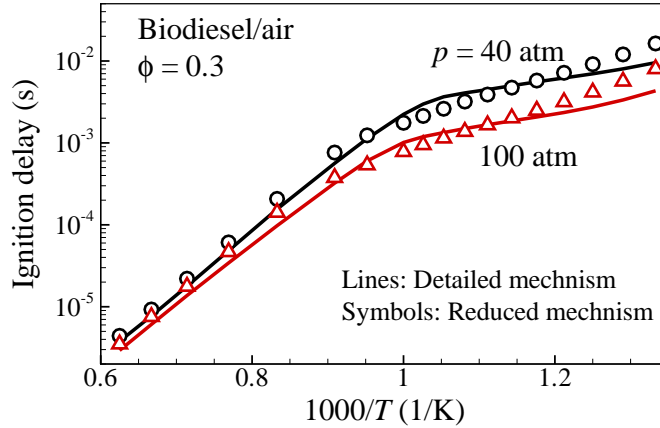


Figure 4-1: Ignition delay of biodiesel/air as function of the initial temperature for constant pressure auto-ignition equivalence ratio of 0.3 and different pressures, calculated with the detailed and reduced mechanisms, respectively.

The skeletal and reduced mechanisms were originally validated based on reaction states sampled from auto-ignition and perfectly stirred reactors (PSR) covering the parameter range of pressures from 1 to 100 atm, equivalence ratios from 0.5 to 2.0, and initial temperature from 700 to 1800 K for auto-ignition [80, 112]. Extended validation of the reduced mechanism relevant to the present DNSs is shown in Fig. 4-1 for biodiesel/air at equivalence ratio of 0.3 and pressure of 40 ~ 100 atm. The accuracy of the reduced mechanism is mostly identical to

that of the skeletal mechanism over the entire parameter range of the reduction. Although it is significantly reduced from the original detailed chemistry, the reduced mechanism shows a good agreement with the detailed mechanism and experimental results in terms of ignition delays, flame propagation speeds, and extinction residence times. Details of the skeletal and reduced mechanisms of biodiesel oxidation can be found in [80,112]. In addition, the method of dynamic stiffness removal [52,53,64,90] is employed to eliminate chemical time scales shorter than 10 ns such that explicit time integration could be applied in DNSs.

For all DNSs in the present study, the initial mean temperature, T_0 , mean equivalence ratio, ϕ_0 , and the initial uniform pressure, p_0 , are 850 K, 0.45, and 40 atm, respectively. The initial conditions are chosen to employ the low temperature heat release of two-stage ignition of biodiesel/air mixture relevant to high-load naturally aspirated HCCI engines such that the initial pressure of 40 atm is relatively low compared to that in modern boosted engines at the TDC. Twelve different DNSs are performed by changing two key parameters: temperature fluctuations, T' , of 15 K and 60 K, and equivalence ratio fluctuations, ϕ' , of 0.05 and 0.10. Three additional DNSs are carried out to elucidate the effect of turbulence on HCCI combustion by varying turbulence intensity, u' , from 1.0 to 5.0 m/s.

Note that ϕ_0 and ϕ' are carefully selected such that local ϕ is maintained precisely below unity, thereby preventing locally-high temperature that may cause excessive NO_x formation [17]. Furthermore, the initial conditions are representative of the TDC under high-load conditions in air-diluted HCCI combustion [89,115]. From 0-D simulations, the homogeneous ignition delay of a biodiesel/air mixture with $\phi_0 = 0.45$ is found to be $\tau_{ig}^0 = 1.0$ ms at the initial mean temperature and pressure. Henceforth, τ_{ig} represents the time at which the maximum mean heat release rate (HRR) occurs for all 0-D and 2-D simulations. The superscript 0 denotes the zero-dimensional simulation at a constant volume.

The initial turbulent flow field is prescribed by an isotropic kinetic energy spectrum function by Passot-Pouquet [37] as in [48–50, 52, 53, 74–76, 90]. For the first fifteen DNS cases, the turbulence intensity, u' , and length scale, l_e , are specified as 1.0 m/s and 1.0 mm respectively. As such, the turbulence time scale, τ_t , is 1.0 ms, which is comparable to the ignition time scale. Note that turbulence time scale in real HCCI engines is $\sim O(1 \text{ ms})$ such that the turbulence time scale in the present DNS study is representative of HCCI combustion. It is also of interest to note that the evolution of 2-D turbulence without 3-D vortex stretching may be different from that of 3-D turbulence. However, investigation of HCCI combustion using DNSs with 2-D random turbulence exhibiting a wide range of spectrum of length and time scales is still of value because the effect of turbulent mixing on HCCI combustion plays a secondary role compared with mixture stratifications [48–53,90]. Therefore, it is reasonable to expect that overall HCCI combustion characteristics from 2-D DNSs may not differ significantly from those of 3-D DNS which is extremely expensive [105].

In addition to the velocity fluctuation, temperature and concentration fluctuations are also superimposed on the corresponding mean fields to investigate the effects of initial hot/cold and/or relatively fuel-rich/lean spots on the ignition characteristics of the biodiesel/air mixture. The scalar fluctuations are generated from the same energy spectrum as turbulence with different random numbers. The most energetic length scales of the temperature fluctuations, l_{Te} , and composition fluctuations, $l_{\phi e}$, are 1.0 mm in all cases. Identical characteristic length and time scales are specified for the ignition delay and all fluctuation fields, so allowing most effective turbulent mixing of initial mixtures to be elucidated. Note that turbulence and other scalar fields such as temperature and concentration are not correlated. Details of the physical and numerical parameters for each case are listed in Table 4-1.

Case	Type	T_0 (K)	T' (K)	ϕ_0	ϕ'	l_e (mm)	l_{Te} (mm)	$l_{\phi e}$ (mm)	u' (m/s)	τ_t (ms)	τ_{ig}^0 (ms)	N
1	BL	850	15	0.45	-	1.0	1.0	1.0	1.0	1.0	1.0	640
2	BL	850	60	0.45	-	1.0	1.0	1.0	1.0	1.0	1.0	640
3	BL	850	-	0.45	0.05	1.0	1.0	1.0	1.0	1.0	1.0	640
4	BL	850	-	0.45	0.10	1.0	1.0	1.0	1.0	1.0	1.0	640
5	UC	850	15	0.45	0.05	1.0	1.0	1.0	1.0	1.0	1.0	640
6	UC	850	15	0.45	0.10	1.0	1.0	1.0	1.0	1.0	1.0	640
7	UC	850	60	0.45	0.05	1.0	1.0	1.0	1.0	1.0	1.0	640
8	UC	850	60	0.45	0.10	1.0	1.0	1.0	1.0	1.0	1.0	1280
9	NC	850	15	0.45	0.05	1.0	1.0	1.0	1.0	1.0	1.0	640
10	NC	850	15	0.45	0.10	1.0	1.0	1.0	1.0	1.0	1.0	640
11	NC	850	60	0.45	0.05	1.0	1.0	1.0	1.0	1.0	1.0	640
12	NC	850	60	0.45	0.10	1.0	1.0	1.0	1.0	1.0	1.0	640
13	BL	850	-	0.45	0.10	1.0	1.0	1.0	5.0	0.2	1.0	640
14	UC	850	60	0.45	0.10	1.0	1.0	1.0	5.0	0.2	1.0	1280
15	NC	850	60	0.45	0.10	1.0	1.0	1.0	5.0	0.2	1.0	640

Table 4-1: Physical and numerical parameters of the DNS cases. BL, UC, and NC represent baseline, uncorrelated $T - \phi$, and negatively-correlated $T - \phi$ distribution, respectively.

Depending on factors including fuel delivery strategies, injection timings, amount of EGR, intake charge heating, and wall heat loss, different $T - \phi$ distributions may occur at the TDC prior to the main auto-ignition event. However, only two most-probable scenarios are considered in the present study: (1) early direct injection (one stage injection) combined with EGR may produce ‘uncorrelated $T - \phi$ ’ fields due mostly to turbulent mixing, and (2) two-stage injection strategy with late second direct injection may result in ‘negatively-correlated $T - \phi$ ’ fields because of the evaporative cooling of injected fuel and incomplete mixing [51, 116]. On this basis, three distinct cases of initial $T - \phi$ correlations are elucidated: (1) baseline cases with fluctuations either in temperature (Cases 1 and 2) or equivalence ratio (Cases 3 and 4), (2) uncorrelated $T - \phi$ distribution (Cases 5–8), and (3) negatively-correlated $T - \phi$ distribution

(Cases 9–12). Figure 4-2 shows various initial $T - \phi$ distributions together with a representative isocontour of the initial equivalence ratio field for Case 12.

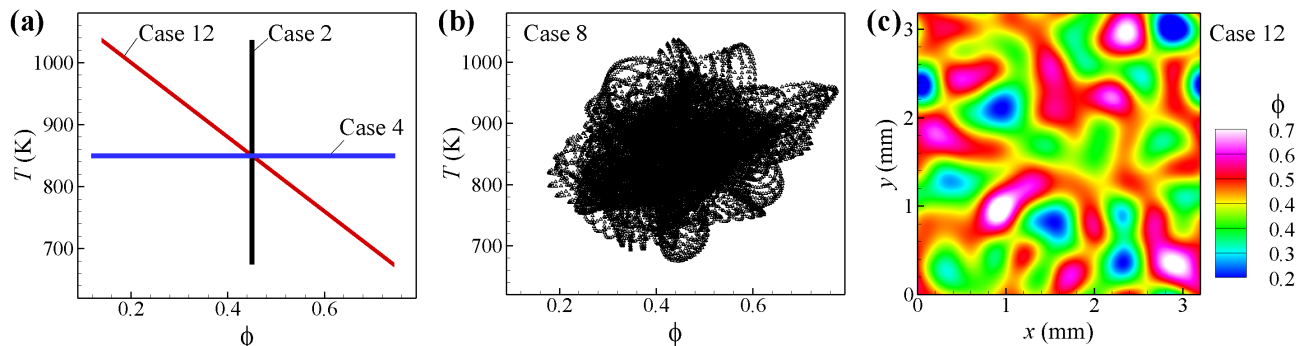


Figure 4-2: Initial $T - \phi$ distribution for (a) Cases 2, 4, 12 and (b) Case 8, and (c) initial ϕ field for Case 12.

All of the cases are simulated in a 2-D computational domain of a $3.2 \text{ mm} \times 3.2 \text{ mm}$ square box. Each direction is discretized with grid points, N , of 640 or 1280 and the corresponding uniform grid sizes are 5 or $2.5 \mu\text{m}$. Note that based on the initial conditions and the integral length scale, L_{11} , the turbulent Reynolds numbers for cases with $u' = 1.0$ and 5.0 m/s are 145 and 730, respectively. The corresponding Kolmogorov length scales, η_K , are approximately 8.2 and $2.5 \mu\text{m}$, respectively. For all DNS cases, therefore, at least half grid point is located within the Kolmogorov length scale as suggested in [117]. Moreover, the thinnest reaction layers in 2D DNSs were resolved with at least $12 \sim 16$ grid points and as such, turbulence and scalar fields are well resolved in the DNSs. The DNSs were performed on the IBM Blue Gene/P at King Abdullah University of Science and Technology (KAUST).

4.3 Effect of T' and ϕ'

Prior to the detailed analysis of 2-D DNS cases, the underlying effects of temperature and composition stratifications on biodiesel HCCI combustion are investigated by evaluating the 0-D ignition delays, τ_{ig}^0 , of homogeneous biodiesel/air mixture with different initial temperatures and equivalence ratios (see Fig. 4-3).

Two points are to be noted from the figure. First, at a high initial temperature ($T > 1100 \text{ K}$) outside the negative temperature coefficient (NTC) regime, in which only one-stage ignition occurs, the ignition delays for different ϕ are nearly identical and change significantly with temperature (see Fig. 4-3a). Therefore, it is reasonable to anticipate that for a fuel/air charge with high initial temperature, thermal stratification is more effective than composition stratification for adjustment of the ignition timing of biodiesel HCCI combustion. Second, at

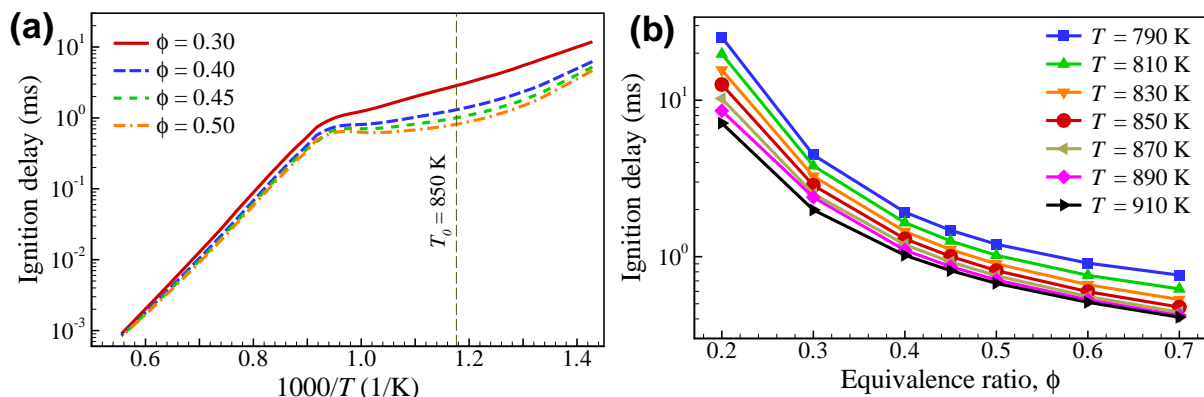


Figure 4-3: 0-D ignition delays at a constant volume with an initial pressure of 40 atm as a function of (a) initial temperature for different ϕ and of (b) equivalence ratio for different T .

an intermediate temperature ($T < 1000$ K), the ignition delay is highly sensitive to variation in ϕ . Especially, near the NTC regime (see Fig. 4-3b), the ignition delay decreases significantly as ϕ increases. For example, at $T_0 = 850$ K, τ_{ig}^0 for ϕ of 0.3, 0.5, and 0.7 are 2.9, 0.8, and 0.5 ms, respectively. However, the ignition delay is less sensitive to temperature variation. As such, it may be conjectured that composition stratification may be more effective than thermal stratification in adjusting the ignition timing of biodiesel HCCI combustion at an intermediate initial temperature.

The temperature and equivalence ratio sensitivities of HCCI combustion have been reported from many numerical and experimental studies [47, 52, 91–94]. It was found from 2-D DNSs of the ignition of a *n*-heptane/air mixture under HCCI conditions [52] that when the initial mean temperature of the mixture exists within the NTC regime, significant temperature fluctuations are necessary to induce the temporal advancement of the overall combustion. It is also of interest to note that HCCI combustion with high octane-number fuels featuring one-stage ignition (e.g., gasoline, *iso*-octane, and ethanol) is found to be insensitive to fuel stratification [47, 91–94]. However, HCCI combustion with low octane-number fuels exhibiting two-stage ignition (e.g., diesel and PRF80) is found to be sensitive to fuel stratification. These results are qualitatively similar to the expectations referred to above for 0-D ignition delays of the biodiesel/air mixture, implying that the fuel stratification can be used effectively together with temperature fluctuations to control the ignition timing of HCCI combustion and to modulate the PRR.

4.3.1 Overall combustion characteristics

In the first parametric study, the combined effect of temperature and composition fluctuations on the ignition of a lean biodiesel/air mixture is investigated. Twelve different 2-D DNS cases are simulated: four baseline cases with T' only or ϕ' only (Cases 1–4), four cases with uncorrelated

$T - \phi$ distribution (Cases 5–8), and four cases with negatively-correlated $T - \phi$ distribution (Cases 9–12). More specifically, two temperature fluctuations, T' , of 15 and 60 K and two equivalence ratio fluctuations, ϕ' , of 0.05 and 0.10 are used (see Table 4-1 for more detailed parameters). Note that under the current initial temperature, equivalence ratio, and pressure condition, the low-temperature chemistry of biodiesel oxidation plays an important role such that a two-stage ignition process of the biodiesel/air mixture occurs.

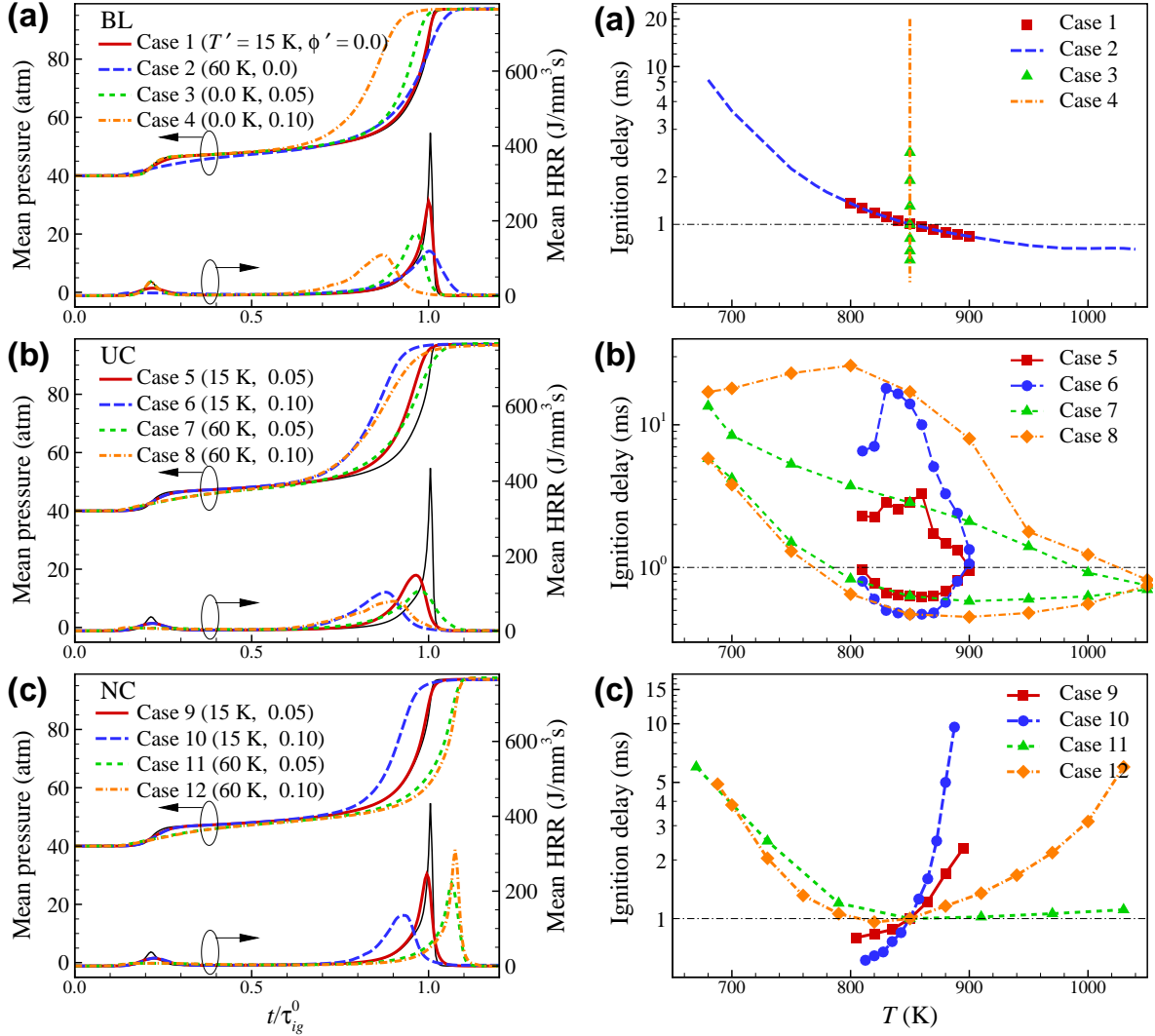


Figure 4-4: Temporal evolution of mean pressure and heat release rate for (a) Cases 1–4, (b) Cases 5–8, and (c) Cases 9–12, and the 95% range of τ_{ig}^0 for (d) Cases 1-4, (e) Cases 5–8, and (f) Cases 9–12. Thin lines represent the corresponding 0-D auto-ignition.

The temporal evolutions of the mean pressure, \bar{p} , and mean heat release rate, \bar{q} , for Cases 1–12 are shown in Fig. 4-4. For the purpose of comparison, the evolution of the corresponding 0-D homogeneous ignition is also shown, as are the 95% ranges of τ_{ig}^0 for initial mixtures for Cases 1–12. The 95% range of τ_{ig}^0 denotes the span of τ_{ig}^0 in the initial mixture, wherein the corresponding T and ϕ lie within 95% of the range of each parameter centered at T_0 and ϕ_0 .

The effect of different $T - \phi$ correlations on HCCI combustion can be investigated by examining the initial temperature and composition distributions of the DNSs, which span a different range of ignition delays for each case. Therefore, the overall ignition characteristics may be estimated from the initial distributions [52].

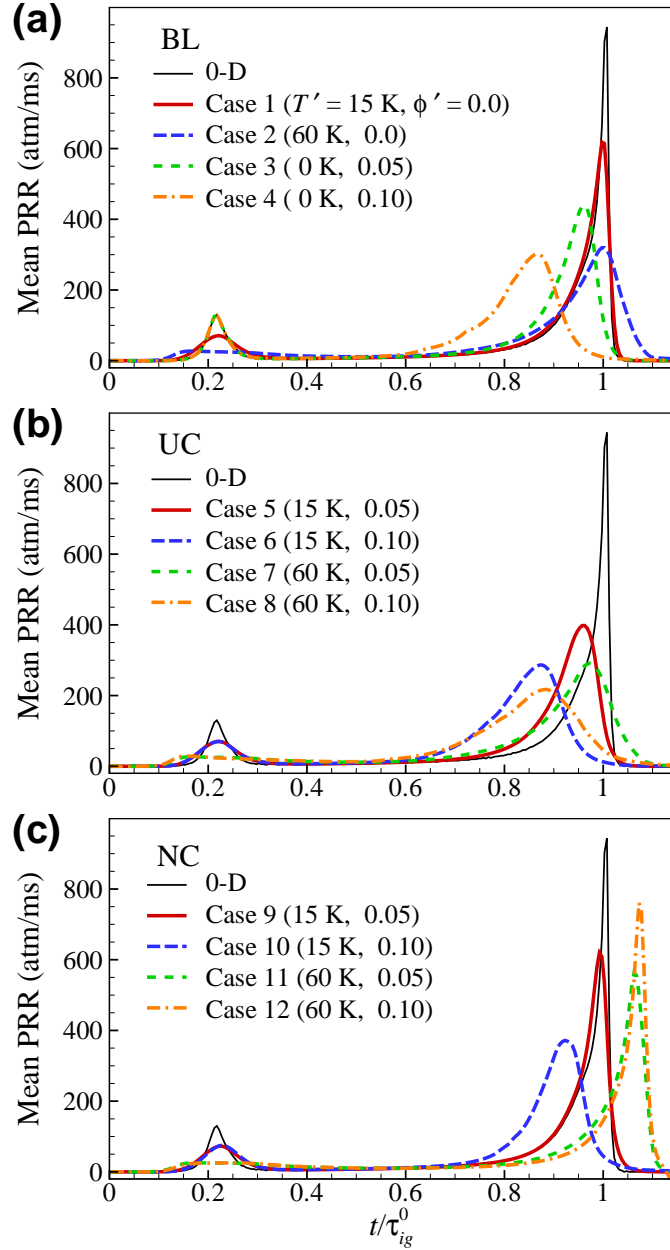


Figure 4-5: Temporal evolution of mean pressure rise rate for (a) Cases 1–4, (b) Cases 5–8, and (c) Cases 9–12. Thin lines represent the corresponding 0-D auto-ignition.

Figure 4-5 also shows the temporal evolution of mean pressure rise rate for the cases. As mentioned earlier, the present DNSs are conducted in a constant volume such that the mean pressure rise is only governed by temperature increase due to heat release. As found in a previous study [118], the overall HCCI combustion is generally advanced by the compression

heating of the piston motion in practical IC engines. In the present study, however, only the effect of biodiesel/air chemical kinetics on HCCI/SCCI combustion is investigated while the compression heating of the piston motion is ignored.

4.3.1.1 Baseline cases

It is readily found from Fig. 4-4a that for cases with T' only (Cases 1 and 2), \bar{p} increases more slowly and \bar{q} is more distributed over time with increasing T' . In general, for a mixture with large T' , the combustion is initiated by the ignition of local hot spots; then nascent ignition kernels develop into deflagrations which consume most of the fresh mixture; subsequently auto-ignition of end-gas mixture is induced at the end of combustion. Therefore, the deflagration mode of combustion becomes predominant over the spontaneous ignition with increasing T' . This result is qualitatively consistent with those of previous studies [48–50, 52, 53, 90].

For Case 1 with small T' , however, the temporal evolutions of \bar{p} and \bar{q} are nearly identical to those of 0-D ignition, which is primarily attributed to the spontaneous ignition of the biodiesel/air mixture induced by its relatively-constant ignition delays at the intermediate temperatures for a fixed ϕ (see Fig. 4-4d). It is of interest to note that although high T' spreads out \bar{q} , the peak \bar{q} for Case 2 occurs at nearly the same time as τ_{ig}^0 and that of Case 1. This result is attributed to the HCCI combustion characteristics affected by the initiation and spread of deflagration waves; the start of overall HCCI combustion is determined by the occurrence of nascent ignition kernels and their evolution into deflagrations, but the duration of combustion is controlled by the propagation characteristics of deflagration waves [52, 53, 90]. As shown in Fig. 4-4d, the range of τ_{ig}^0 for Case 2 is 0.7–8.0 ms. Therefore, the combustion starts earlier than 0-D ignition and the duration of combustion is lengthened to consume local mixture with large τ_{ig}^0 by the deflagration mode.

The effect of ϕ' on the biodiesel HCCI combustion is investigated in Cases 3 and 4 (see Fig. 4-4a). Similar to the effect of T' , \bar{p} increases more slowly and \bar{q} is more distributed over time with increasing ϕ' . Unlike the cases with T' only, however, the overall combustion occurs quickly with increasing ϕ' . It was found in a previous study [52] that, depending on the mean temperature, thermal stratification may advance or retard the overall HCCI combustion of an *n*-heptane/air mixture exhibiting two-stage ignition. However, fluctuation in composition seems more apt to advance the overall HCCI combustion in time regardless of T_0 and ϕ_0 . Moreover, large fuel stratification can more readily be achieved in real engines than thermal stratification. As such, these results suggest that fuel stratification can be more effective in preventing excessive PRR and in controlling the ignition timing for hydrocarbon-fueled HCCI combustion when the mean temperature lies near the NTC regime.

4.3.1.2 Cases with uncorrelated $T - \phi$

Figure 4-4b shows the combined effect of T' and ϕ' on the overall HCCI combustion. Note that there is no correlation between the temperature and equivalence ratio fields. As mentioned previously, port fuel injection or early direct injection combined with heat transfer management may result in a random $T - \phi$ correlation prior to auto-ignition near the TDC [51].

Several observations can be made from the figure. First, for small T' (Cases 5 and 6), the temporal evolutions of \bar{p} and \bar{q} are nearly identical to those of the corresponding baseline cases with the same ϕ' (Cases 3 and 4). As shown in Fig. 4-4a, small T' alone has no significant effect on the overall HCCI combustion (Case 1), and as such, the composition fluctuation has a first-order effect on the ignition characteristics of the biodiesel/air mixture. Second, large T' with ϕ' (Cases 7 and 8) smoothes out \bar{q} more than does small T' (Cases 5 and 6). For these cases, large T' with ϕ' has a synergetic effect in preventing excessive PRR by temporally distributing \bar{q} . However, large T' does not advance the overall combustion in time; τ_{ig} for Cases 5 and 6 are 0.87 and 0.96 ms respectively, whereas τ_{ig} for Cases 7 and 8 are 0.90 and 0.97 ms respectively. Third, the overall combustion occurs quickly with increasing ϕ' , similar to the baseline cases, while the peak \bar{q} is decreased.

The 95% ranges of τ_{ig}^0 shown in Fig. 4-4e further identifies the ignition characteristics of the biodiesel/air mixture with uncorrelated $T - \phi$ fields; the overall HCCI combustion occurs rapidly because the fastest ignition delays for the cases are approximately 0.45–0.63 ms; the mean HRR is more distributed over time due to the wide ranges of τ_{ig}^0 for Cases 5–8.

4.3.1.3 Cases with negatively-correlated $T - \phi$

Figure 4-4c shows the combined effect of negatively-correlated T' and ϕ' on the overall HCCI combustion, which represents one of the most probable $T - \phi$ relations achieved by the late-direct injection. A competitive effect of T' and ϕ' on the biodiesel HCCI combustion can be elucidated with the negatively-correlated $T - \phi$ fields. Similar to the observations from the cases with uncorrelated $T - \phi$ fields, several points are to be noted for Cases 9–12.

First, for Case 9, the temporal evolutions of \bar{p} and \bar{q} are quite similar to those of the corresponding 0-D ignition and Case 1, implying that the temporal advancement and distribution of the overall combustion caused by ϕ' only (Case 3) are practically eliminated by the negative correlation of $T - \phi$ fields. This is attributed primarily to the relatively-constant ignition delays ($0.8 < \tau_{ig}^0 < 2.3$ ms) of the initial mixture as shown in Fig. 4-4f.

Second, large ϕ' (Case 10) can overcome the mutual canceling effect of the negative correlation of $T - \phi$ fields on the overall combustion. As such, \bar{q} is more distributed over time and the

overall combustion occurs quickly. This is because the initial $T - \phi$ fields for Case 10 induce locally much shorter τ_{ig}^0 than 1.0 ms in spite of their negative correlation (see Fig. 4-4f). As a result, the deflagration mode of combustion is more apt to occur at the early phase of HCCI combustion and subsequently spontaneous auto-ignition may occur due to compression heating.

Third, ϕ' with large T' (Cases 11 and 12) retards the overall combustion which seems to occur by the spontaneous ignition mode similar to the corresponding 0-D ignition. This is primarily because initial local ϕ' together with T' almost always increases 0-D ignition delays as shown in Fig. 4-4f. For Cases 11 and 12, the shortest τ_{ig}^0 is approximately 1.0 ms and τ_{ig}^0 of most of the mixtures is much greater than 1.0 ms such that the overall combustion is retarded by turbulent mixing and is more likely to occur by the spontaneous ignition mode.

Regarding HCCI combustion with negatively-correlated $T - \phi$ distributions, there have been two distinct experimental results conflicting each other [47,91,98,99]. If appropriate amount of directly-injected fuel together with suitable injection timing is introduced, the peak HRR can be mitigated and the mean HRR can also be distributed over time [47,91], which is qualitatively consistent with the result of Case 10. However, it was also reported [98,99] that temperature inhomogeneities may offset the effect of fuel stratification induced by the late-fuel injection or even cause an adverse effect on HCCI combustion, leading to excessive PRR/HRR, which are also qualitatively consistent with the results of Cases 9, 11, and 12. The present DNS results together with previous experimental results suggest that the ignition timing and spread of HRR of HCCI combustion can be controlled by varying the degree of temperature and fuel stratifications together with their spatial correlation.

4.3.1.4 Instantaneous HRR fields

To further identify the combustion characteristics of the 2-D DNS cases, the instantaneous structures of the HRR field for Cases 1, 2, 8, and 12 are examined as shown in Fig. 4-6. Note that each HRR field is normalized by $\dot{q}_m^0 = 434.5 \text{ J/mm}^3\text{s}$ which is the maximum HRR of the 0-D homogeneous ignition and the third row represents the HRR fields at τ_{ig} for each case. It is readily observed from the figure that for Cases 1 ($T' = 15 \text{ K}$ only) and 12 ($T' = 60 \text{ K}$, $\phi' = 0.1$ with negative $T - \phi$ correlation), HRR occurs throughout the entire domain in a quite short time; the duration of combustion (10% to 90% of cumulative HRR) for Cases 1 and 12 are approximately 0.17 and 0.09 ms respectively. This result implies that the combustion for Cases 1 and 12 occurs by the spontaneous ignition mode.

However, for Cases 2 ($T' = 60 \text{ K}$ only) and 8 ($T' = 60 \text{ K}$, $\phi' = 0.1$ with uncorrelated $T - \phi$ distribution), large HRR occurs at thin regions as deflagration even though low HRR occurs in much broader regions, implying that mixtures with large T' with/without uncorrelated ϕ may

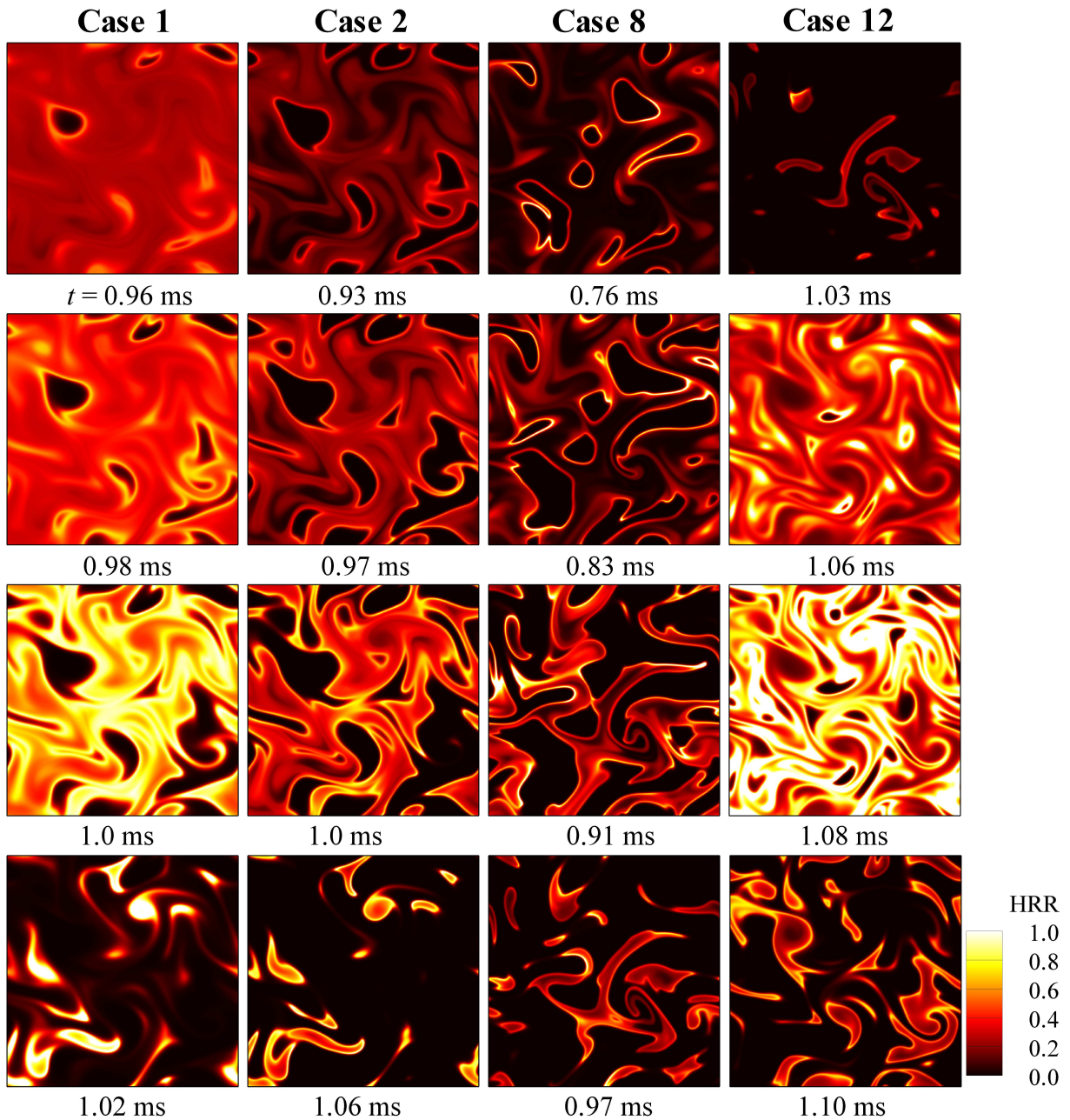


Figure 4-6: Isocontours of normalized heat release rate for Cases 1, 2, 8, and 12 (from left to right) at different times (from top to bottom).

lead to a mixed mode of combustion – involving both deflagration and spontaneous ignition. As a result, it can effectively reduce an excessive HRR and advance the overall combustion by elongating the duration of combustion.

4.3.2 Chemical explosive mode analysis

The ignition characteristics of the biodiesel/air mixture under HCCI conditions is further elucidated by employing chemical explosive mode analysis (CEMA). Note that the reliability of

CEMA in systematically detecting the critical flame features of ignition, extinction, and pre-mixed flame fronts has been demonstrated. CEMA has been applied to DNS studies of lifted flames in heated coflows [77–79, 119], jet flames in cross-flows [81, 82], and ignition of an n -heptane/air mixture and primary reference fuel/air mixtures under HCCI conditions [52, 83, 90]. An outline of CEMA is provided here; refer to [78] for more details.

The differential equations of a typical reacting flow can be described in discretized form as:

$$\frac{D\mathbf{y}}{Dt} = \mathbf{g}(\mathbf{y}) = \boldsymbol{\omega}(\mathbf{y}) + \mathbf{s}(\mathbf{y}), \quad (4.3.1)$$

where D/Dt is the material derivative, which can be replaced by d/dt in the Lagrangian coordinate, and \mathbf{y} is the solution vector including species concentrations and temperature. Note that for spatially discretized flows, a chemical species concentration at different grid points corresponds to different entries in \mathbf{y} . $\boldsymbol{\omega}$ and \mathbf{s} represent the chemical source term and all non-chemical terms such as diffusion and homogeneous mixing, respectively.

The Jacobian matrix of the chemical source term, $\mathbf{J}_\omega (\equiv \partial\boldsymbol{\omega}/\partial\mathbf{y})$, describes the local chemical information. As such, a chemical mode can be defined as an eigenmode of \mathbf{J}_ω , which is associated with an eigenvalue and a corresponding pair of the left and right eigenvectors. A chemical explosive mode (CEM) is defined as a chemical mode of which the real part of the eigenvalue, λ_e , is positive [78]. By definition, CEM represents the reciprocal chemical time scale of a local mixture such that the existence of CEM implies that the corresponding mixture is explosive in nature. Therefore, it is likely to auto-ignite if the mixture is put in a lossless environment where the term \mathbf{s} in Eq. 7.2.1 is negligible. Note that ignition may not actually occur in a mixture exhibiting CEM when significant loss in heat or radicals is present. Therefore, CEM remains an intrinsic chemical feature of ignitable mixtures.

In spatially inhomogeneous systems, CEMs interact with diffusion and other non-chemical processes. As such, ignition may not always occur if the time scale of CEM is longer than those of the losses. The competition between CEMs and the losses can be quantified approximately by a Damköhler number defined as [78, 79, 83, 119]:

$$Da_c = \lambda_e \cdot \chi^{-1}, \quad (4.3.2)$$

where the scalar dissipation rate of a pre-mixture, χ , defined as $\chi = 2D|\nabla c|^2$ is a reciprocal characteristic time scale of the term \mathbf{s} . Here c and D represent the progress variable and the thermal diffusivity of the local mixture, respectively. c is defined as $c \equiv Y_c/Y_c^{\text{Eq}}$, where $Y_c = Y_{\text{CO}_2} + Y_{\text{CO}}$ and Y_c^{Eq} is the corresponding equilibrium value of Y_c . In the present study, Y_c^{Eq} of 0.08 is used for the calculation of χ . It should be emphasized that $\lambda_e = 0$ and $Da_c = 1$ are important criteria for limit phenomena detection. Specifically, a mixture with 1) $Da_c = 1$

implies that CEM balances mixing, typically indicating the ignition or extinction states of steady state combustion; 2) $Da_c \gg 1$ indicates a dominant CEM which is likely to induce actual auto-ignition; 3) $Da_c \ll -1$ indicates strongly burning flames, for example, the post flame zone in premixed flames; 4) $|Da_c| < 1$ indicates mixing controlled zones where CEMA is inconclusive.

In the present study, CEM together with the local scalar dissipation rate, χ , is adopted to 1) distinguish pre- and post-ignition mixtures, 2) to interpret losses due to turbulent mixing, and 3) to identify precisely the location of ignition fronts.

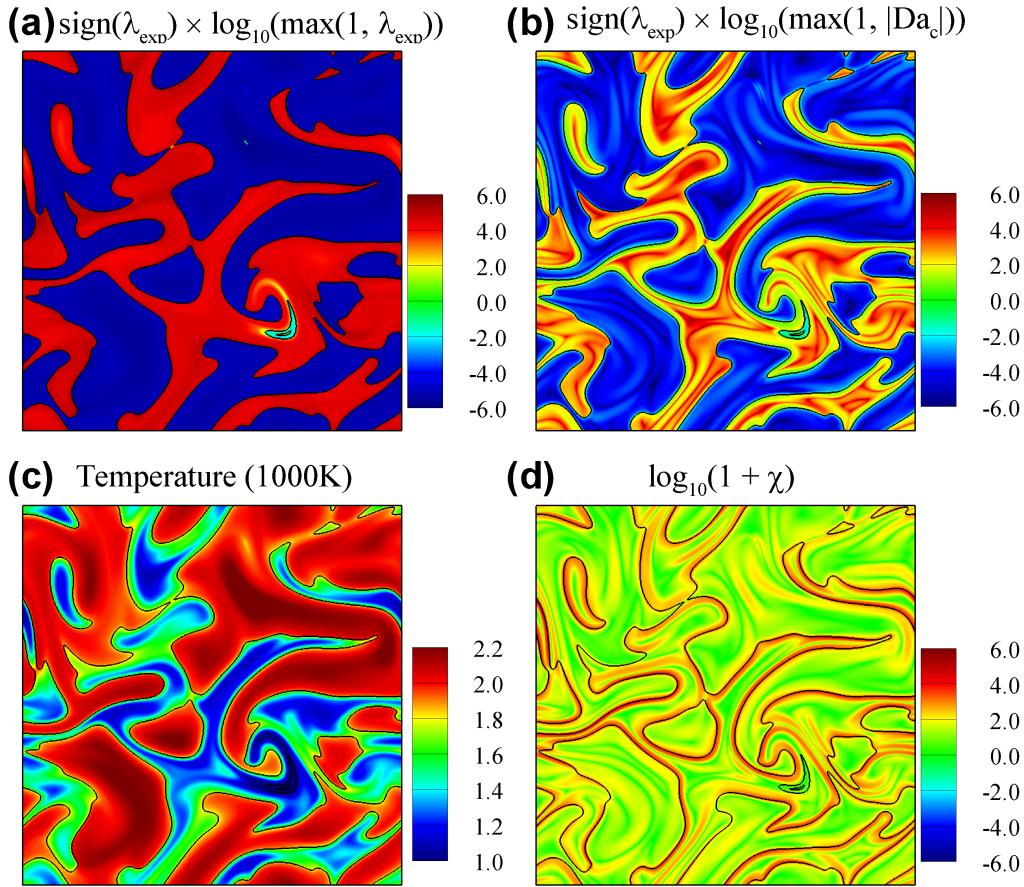


Figure 4-7: Isocontours of (a) the time scale of chemical explosive mode, (b) Da_c , (c) temperature, and (d) χ for Case 8 (UC: $T' = 60$ K and $\phi' = 0.10$) at $t/\tau_{ig}^0 = 0.90$. The solid isoline denotes the reaction front.

Because of their distinctive ignition behaviors, Cases 8 and 12 are selected for CEMA. Figures 4-7 and 4-8 show the isocontours of (a) λ_e , (b) Da_c , (c) temperature, and (d) χ at τ_{ig} for Cases 8 and 12, respectively. Note that the time scale of the CEM is the reciprocal eigenvalue, λ_e , of the CEM, where red regions (large λ_e) indicate fast-explosive or unburned mixtures, and blue regions indicate non-explosive mixtures. Moreover, the burned and unburned mixtures are separated by the reaction fronts indicated as the sharp boundaries, which can be either spontaneous ignition fronts or deflagration waves.

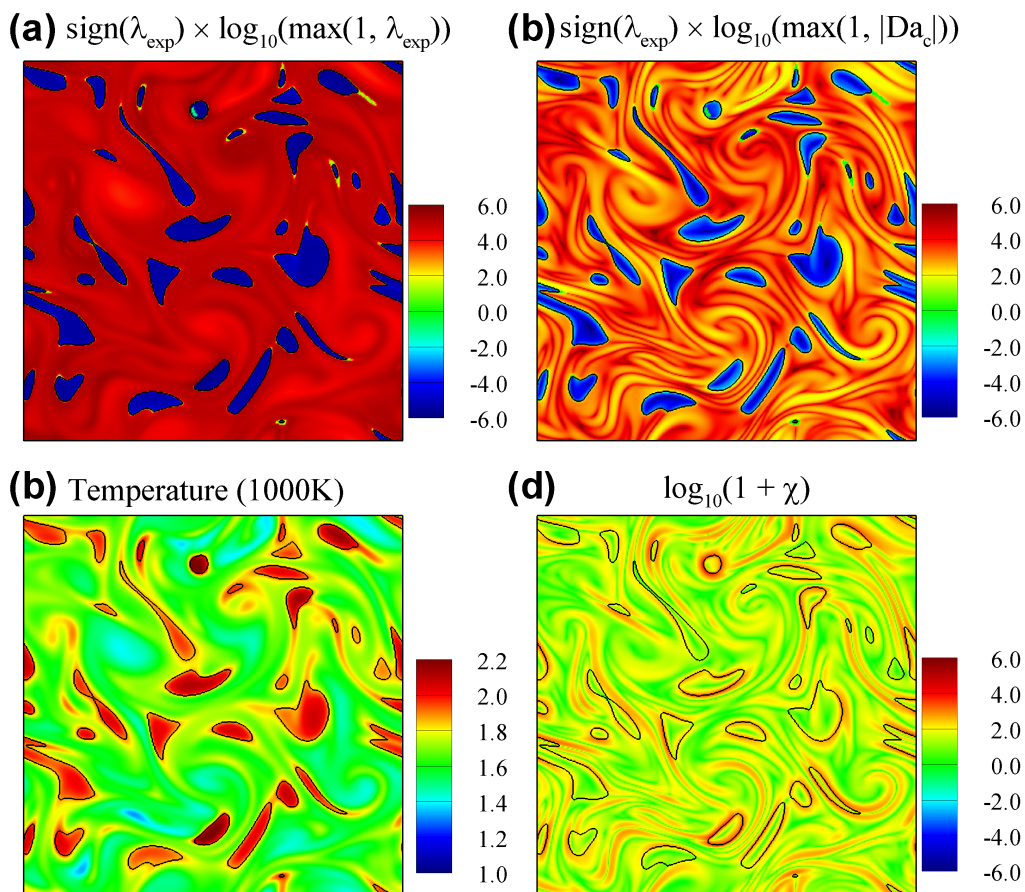


Figure 4-8: Isocontours of (a) the time scale of chemical explosive mode, (b) Da_c , (c) temperature, and (d) χ for Case 12 (NC: $T' = 60$ K and $\phi' = 0.10$) at $t/\tau_{ig}^0 = 1.07$. The solid isoline denotes the reaction front.

From Fig. 4-7b, three bulk regions can readily be observed: the auto-igniting region (red), the post-ignition region (blue), and the greenish region where the mixing balances the chemical explosion. As shown in Fig. 4-7a and Fig. 4-7d, the chemical explosion, λ_e , and the mixing, χ , have the same order of magnitude in the greenish region, and as such, the corresponding Da_c upstream of the reaction fronts is in the order of unity. These results imply that the reaction fronts of Case 8 are deflagrations rather than spontaneous ignition fronts. It is also found from Fig. 4-7d that the reaction fronts almost overlap with the strips with relatively large χ , which is one of a characteristics of deflagration waves propagating through unburned mixtures before auto-ignition occurs. In addition, the mixtures surrounding the deflagration waves in Fig. 4-7c mostly exhibit higher temperatures while those outside the ignition regions show lower temperature, which is a signature of deflagration.

By contrast, for Case 12 which has highly excessive HRR, there exist very thin reaction fronts dividing the domain into two distinctive bulk regions; i.e., the auto-igniting (red and yellow) region with large positive Da_c where the chemical explosive process (large λ_e) dominates the combustion process and thus the effect of the mixing is minor (relatively small χ) (see Fig. 4-

8b). However, for the post-ignition (blue) regions with large negative Da_c , the mixture is near-equilibrium with extremely short chemical time scales. Notably Da_c upstream of the reaction fronts has a magnitude much larger than unity (yellow region), indicating that the CEM (λ_e) is also much faster than the mixing process (χ). In deflagration waves, the reaction balances diffusion terms. As such, the large $Da_c(\gg O(1))$ ahead of the reaction fronts shown in Fig 4-8b is attributed to spontaneous ignition rather than deflagration. Furthermore, the temperature gradient in upstream and downstream regions of the reaction fronts in Fig. 4-8c is relatively moderate, which is not a feature of a deflagration wave, again verifying that the reaction fronts are spontaneous ignition fronts.

4.3.3 Combustion mode

To quantitatively measure the occurrence of deflagration and spontaneous ignition modes during combustion, the temporal evolutions of the fraction of HRR attributed to deflagration mode for Cases 1–12 are examined as shown in Fig. 4-9. To distinguish between the spontaneous ignition and deflagration, the Damköhler number, Da , defined by [52, 53, 77, 86, 90], is adopted:

$$Da = \frac{\dot{\omega}_k}{|-\nabla \cdot (\rho Y_k \mathbf{V}_k)|}, \quad (4.3.3)$$

where Y_c is used for the Damköhler number analysis. From several 1-D laminar simulations of different ϕ , it is found that Da in the diffusive limit is approximately 5.8, where the diffusive limit represents deflagration wave propagation without auto-ignition, i.e., where diffusion balances reaction [49, 50, 52, 53, 90]. Note that $Da = 5.8$ is a specific value for the present DNS cases since Da value can vary depending on the initial mean temperature, pressure, and equivalence ratio. The departure of Da in the diffusive limit from unity is a consequence of the upstream mixture being highly reactive, and hence, the reaction term is somewhat larger than the diffusion term [52, 53, 90]. Here, the delineation between the two propagation modes is defined by $Da = 5.8$ such that Da less than 5.8 represents a deflagration wave.

Several observations are to be made from Fig. 4-9. First, for all cases, the fraction of HRR from the deflagration mode becomes unity at the initial and final stages of the ignition. This is simply because the corresponding reaction rate in Eq. 8.4.1 vanishes, resulting in $Da = 0$. Second, for the baseline and uncorrelated $T - \phi$ cases (i.e., Cases 1–8), the fraction of HRR from the deflagration mode increases with increasing T' or ϕ' . Especially, for Case 8, nearly half of the HRR occurs in the deflagration mode during most of the combustion process such that the total heat release from the deflagration mode is approximately 38%. Third, for Cases 9, 11, and 12 with negatively-correlated $T - \phi$ fields, the fraction of HRR from the deflagration mode vanishes much sooner than the occurrence of the peak \bar{q} , and as such, the total heat release

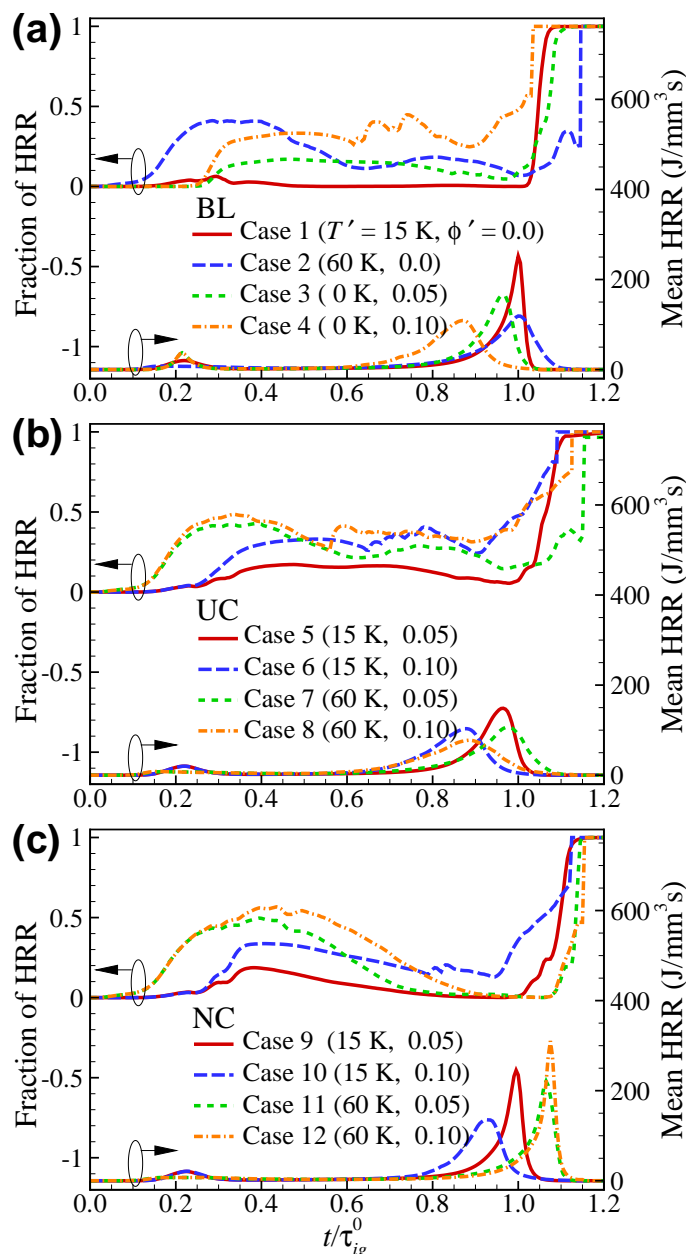


Figure 4-9: Temporal evolution of the fraction of heat release rate from the deflagration mode and mean heat release rate for (a) Cases 1–4, (b) Cases 5–8, and (c) Cases 9–12.

from the deflagration mode is approximately 3, 6, and 9%, respectively; by contrast, for large T' or ϕ' (i.e., Cases 4 and 6–8), a considerable fraction of HRR still occurs by deflagration mode at each peak \bar{q} , resulting in a relatively-large total heat release from the deflagration mode ($> 30\%$). A small fraction of HRR from the deflagration mode verifies that spontaneous auto-ignition occurs primarily for cases with small T' and/or ϕ' or cases with negatively-correlated $T - \phi$ fields. However, a relatively large fraction of HRR from the deflagration mode indicates the occurrence of mixed modes of deflagration and spontaneous ignition for large T' and/or ϕ' except for cases with negatively-correlated $T - \phi$ fields (i.e., Cases 10 and 11).

These results are qualitatively consistent with those of previous studies [49–53, 90]. In

summary, if the shortest τ_{ig}^0 of initial mixture by large T' and/or ϕ' is short enough to induce an early development of deflagrations, a relatively-large fraction of combustion occurs by the deflagration mode during combustion, while spontaneous auto-ignition also occurs in such cases. In addition, these results also verify that the deflagration mode contributes significantly to the temporal spreading of the excessive \bar{q} , the reduction of peak \bar{q} , and the rapid occurrence of the overall combustion.

4.4 Effect of turbulence

In previous studies of ignition of fuel/air mixtures under HCCI conditions [49, 52, 53, 90], it was found that most turbulence with a short time scale, τ_t , is likely to homogenize initial temperature fluctuations of a fuel/air mixture and hence, the overall combustion is retarded compared to that with long τ_t , and is more apt to occur by spontaneous ignition. In general, turbulent mixing tends to dissipate heat and radicals from nascent ignition kernels [86] and as such, the overall HCCI combustion can be more retarded by turbulence with high u' and short τ_t . For the ignition of an *iso*-octane/air mixture under spark-assisted compression ignition (SACI) conditions [53], however, a large turbulence intensity, u' , tends to advance the overall combustion and distribute \bar{q} over time by increasing the turbulent flame area. It was also found from [53] that turbulence with large u' can most effectively homogenize the *iso*-octane/air mixture when its length scale, l_e , is comparable to the temperature fluctuation length scale, l_{Te} . The mixture, however, is not usually homogenized by turbulent flow if l_e is too large or too small compared to l_{Te} despite a short τ_t . More recently, it has been found from [120] that as with SACI cases, turbulence with short τ_t and large u' can advance the overall combustion under HCCI conditions by increasing turbulent flame area if the shortest τ_{ig}^0 of the initial mixture is much shorter than τ_t .

In this section, therefore, the effect of turbulence on ignition of the biodiesel/air mixture is elucidated. Three additional DNSs (Cases 13–15) are performed with greater turbulence intensity for cases with different $T - \phi$ correlations. Note that the three cases have the same turbulence intensity of 5.0 m/s, which is five times greater than that in the other cases with l_e being identical to l_{Te} to maximize turbulent mixing. Details of the parameters are shown in Table 4-1.

Figure 4-10 shows the temporal evolutions of \bar{p} and \bar{q} for the additional cases together with the corresponding cases with small u' of 1.0 m/s (Cases 4, 8, and 12). Several points are to be noted from the figure. For cases with ϕ' only (Cases 4 and 13) and uncorrelated $T - \phi$ fields (Cases 8 and 14), turbulence with short τ_t and large u' can effectively homogenize temperature and composition fluctuations. As such, the overall combustion is retarded; the peaks of \bar{q} are increased; the combustion is more apt to occur by spontaneous ignition. For cases with

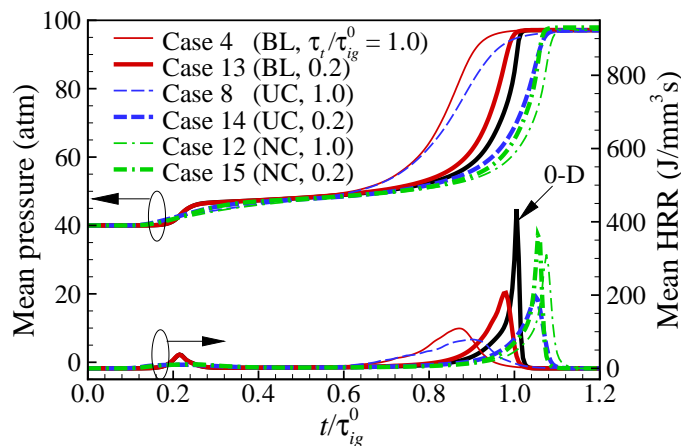


Figure 4-10: Temporal evolution of mean pressure and heat release rate for long τ_t (Cases 4, 8, and 12; thin lines) and short τ_t (Cases 13–15; thick lines).

negatively-correlated $T - \phi$ fields (Cases 12 and 15), however, turbulence with large u' has no significant effect on the ignition characteristics of the biodiesel/air mixture although the overall combustion is slightly advanced and becomes much more like the 0-D auto-ignition. For Cases 12 and 15, τ_{ig}^0 of most initial mixtures are greater than τ_t of 1.0 and 0.2 ms as shown in Fig. 4-4f. This implies that turbulent mixing by large u' can make the mixtures more homogeneous in terms of their ignition delays. As such, the overall combustion becomes nearly identical to the 0-D auto-ignition, resulting in the slight advancement of the overall combustion.

Finally, the temporal evolutions of the fraction of HRR from the deflagration mode are examined to quantify the combustion mode as shown in Fig. 4-11. For cases with large u' , the fraction of HRR from the deflagration mode vanishes much earlier than the occurrence of the peak \bar{q} , and as such, the total heat release from the deflagration mode for Cases 13–15 are approximately 12, 20, and 9%, respectively, which are much smaller than those of the corresponding cases with small u' (Cases 4, 8, and 12). This result indicates that large u' can effectively homogenize the mixture such that the overall combustion occurs primarily by spontaneous ignition, resulting in the decrease of the fraction of HRR by the deflagration mode.

4.5 Discussion

Up to now, the ignition characteristics of a lean biodiesel/air mixture with mixture stratifications under HCCI conditions are investigated, which exhibit quite different behaviors depending on the degrees of fluctuations in temperature, composition, and turbulence, and their spatial correlations. In addition to the present DNS results, there exist plenty of DNS and experimental results regarding HCCI combustion and as such, it is of great interest to generalize the effects

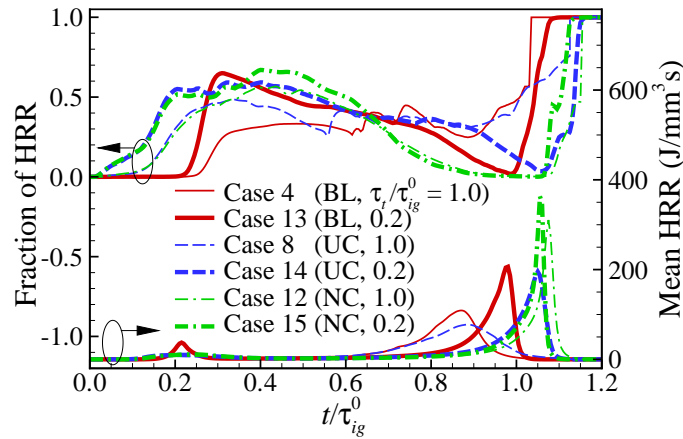


Figure 4-11: Temporal evolution of the fraction of heat release rate from the deflagration mode and mean heat release rate for Cases 13–15 with $\tau_t/\tau_{ig}^0 = 0.2$ and the corresponding cases (Cases 4, 8, and 12) with $\tau_t/\tau_{ig}^0 = 1.0$.

of temperature, equivalence ratio, and velocity fluctuations on the ignition characteristics of various fuel/air mixtures under HCCI combustion.

Prior to discussing the details of the characteristics of HCCI combustion, it should be noted that there are two major types of fuels under HCCI conditions. Hydrogen, ethanol, and *iso*-octane feature ‘one-stage ignition’ and can be categorized as ‘gasoline-like’ fuels of which 0-D ignition does not show the NTC behavior under high pressures and intermediate temperatures. However, PRF50, *n*-heptane, biodiesel, and dimethyl-ether (DME) feature ‘two-stage ignition’ and can be categorized as ‘diesel-like’ fuels whose 0-D ignitions exhibit strong NTC behaviors associated with the low-temperature chemistry at high pressures and intermediate temperatures as schematically shown in Fig. 4-12. Depending on the fuel types and the degrees of mixture and velocity fluctuations, one may find different ignition characteristics of the fuel/air mixture under HCCI conditions.

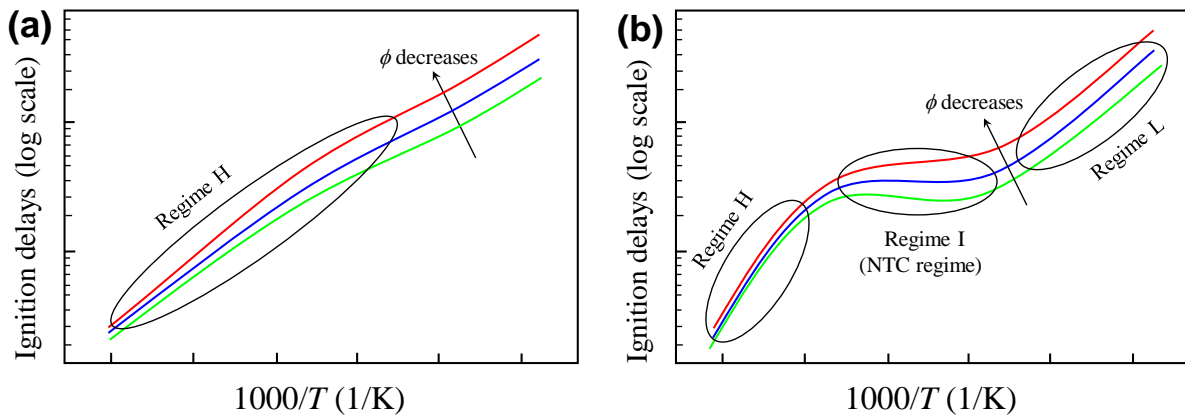


Figure 4-12: Schematics of 0-D ignition delay vs. initial temperature for (a) one-stage ignition fuels and (b) two-stage ignition fuels.

First, the effect of thermal stratifications only on HCCI combustion usually depends on the mean and variance of initial temperature of the fuel/air mixture [52]. For two-stage ignition fuels, if the initial mean temperature lies at high temperature regime (Regime H, see Fig. 4-12) outside of the NTC regime where only high temperature chemistry governs the ignition, the mean HRR is more distributed over time and the peak HRR is more reduced with increasing T' , resulting in advancing the overall combustion [52]. The same results were found for one-stage ignition fuels such as hydrogen [49,50] and ethanol [118] because the ignition of one-stage ignition fuel is also governed by only high temperature chemistry. However, if the initial mean temperature lies within the NTC regime (Regime I) where both high and low temperature chemistries become important, the overall combustion does not change much compared to the corresponding 0-D ignition with increasing T' because of relatively constant 0-D ignition delays in the NTC regime. As such, one may need much larger T' to induce a similar advancement of HCCI combustion as that in Regime H [52]. Finally, if the mean temperature lies at the low temperature regime (Regime L), the overall combustion is more retarded and the mean HRR is more spread out in time with increasing T' because in this regime, T' usually induces much longer ignition delays in the mixtures compared to the corresponding 0-D ignition [52].

Second, regardless of fuel types, fuel stratifications only tend to spread out the mean HRR and advance the overall HCCI combustion in time with increasing ϕ' because fuel stratifications usually induce much shorter ignition delays in the mixtures compared to the corresponding 0-D ignitions as illustrated in Fig. 4-12. It is of interest to note that for two-stage ignition fuels, the effect of fuel stratifications can be manifested in the NTC regime (Regime I) rather than in Regime H because the ignition delays are more sensitive to the equivalence ratio than temperature in Regime I.

Third, the co-existence of temperature and fuel stratifications in the initial mixture may induce more complicated ignition behaviors. In general, uncorrelated $T - \phi$ fields induce much shorter ignition delays in mixtures regardless of fuel types and as such, the mean HRR is more distributed and the overall combustion is more advanced with increasing T' and ϕ' [51,61,106,118]. On the contrary, for cases with negatively-correlated $T - \phi$ fields, the overall combustion is generally retarded in time and becomes more like 0-D ignition due to the cancellation effect of negatively-correlated T and ϕ fields [51,98,99]. For two-stage ignition fuels, however, it is of interest to note that large ϕ' with small T' can advance the overall combustion and distribute the mean HRR in time more compared to 0-D ignition in Regime I because the fuel stratification is the first-order effect on the HCCI combustion in Regime I [47,91,92]. In the same context, it can be conjectured that for two-stage ignition fuels, ϕ'/T' is practically a more effective strategy in spreading out an excessive HRR in Regime I/Regime H because the 0-D ignition is more sensitive to ϕ/T in Regime I/Regime H.

Finally, turbulence with large intensity and short time scale is more likely to homogenize the initial temperature and composition stratifications in HCCI combustion and as such, the overall combustion becomes similar to the corresponding 0-D ignition [52, 90]. However, it was also found from [53, 118] that in SACI combustion, large u' tends to advance the overall combustion over time by increasing turbulent flame area. For SACI combustion, the evolution of the nascent ignition kernel into deflagration is nearly independent of turbulence [53]. Therefore, once deflagration is developed, u' greater than the corresponding laminar flame speed is more apt to increase turbulent flame area, resulting in the advancement of the overall combustion.

4.6 Conclusions

The effects of thermal and compositional stratifications, and turbulence intensity on auto-ignition of a lean biodiesel/air mixture at high pressure, intermediate temperature, and constant volume are investigated by using direct numerical simulations with a 73-species reduced chemistry for biodiesel oxidation.

In the first parametric study, twelve cases of HCCI combustion are studied by systematically varying the degrees of temperature and composition fluctuations with three different $T - \phi$ correlations: 1) the baseline cases with T' only or ϕ' only, 2) uncorrelated $T - \phi$ distribution, and 3) negatively-correlated $T - \phi$ distribution. In general, it is found that the overall combustion is more advanced and the mean HRR is more distributed over time with increasing T' and/or ϕ' for the baseline and uncorrelated $T - \phi$ cases. However, the temporal advancement and distribution of the overall combustion caused by T' only or ϕ' only are nearly eliminated by the negatively-correlated $T - \phi$ fields except for a case with large ϕ' and small T' . These results readily identify that negatively-correlated $T - \phi$ fields can enhance or retard the overall combustion depending on the degree of T' and ϕ' , which is qualitatively similar to previous experiments.

Chemical explosive mode and Damköhler number analyses verify that for the baseline and uncorrelated $T - \phi$ cases, the deflagration mode is predominant at the reaction fronts for large T' and/or ϕ' . By contrast, spontaneous ignition prevails for small T' or ϕ' , especially with the negative $T - \phi$ correlations, and hence, simultaneous auto-ignition occurs throughout the entire domain, resulting in an excessive HRR. These results imply that under high pressure and intermediate temperature conditions within the NTC regime, the composition stratification is more effective than the thermal stratification in advancing the ignition timing of HCCI combustion and distributing the mean HRR over time because τ_{ig}^0 of initial mixtures is more sensitive to the composition stratification.

In the second parametric study, the effect of turbulence intensity on the ignition characteristics of the biodiesel/air mixture is elucidated. It is found that in general, turbulence with large u' and short τ_t can effectively homogenize initial temperature and composition fluctuations such that the overall combustion is more apt to occur by spontaneous ignition for all the cases. For the baseline and uncorrelated $T - \phi$ cases, turbulence with high u' is found to retard the overall combustion and increase the peak of the mean HRR, similar to observations from previous studies [49, 52, 90]. For the case with negatively-correlated $T - \phi$ distribution, however, the overall combustion is slightly advanced, which is also attributed to the homogenization effect of large u' .

These results suggest that the stratification of a fuel/air mixture in both temperature and composition can control the ignition timing of HCCI combustion and provide a smooth HCCI operation under high load conditions. The mixture stratifications, however, need to be carefully introduced to prevent an excessive rate of pressure rise that may be induced by negative $T - \phi$ correlations.

Chapter 5

Ignition of a lean *n*-heptane/air mixture with temperature and composition inhomogeneities relevant to HCCI and SCCI combustion

5.1 Introduction

One of the most effective methods to overcome the excessive PRR under high-load operating conditions in the HCCI engines is to generate a sequential ignition event by using in-cylinder mixture inhomogeneities. Numerous experimental and numerical studies of HCCI combustion have shown that thermal and compositional stratifications of the in-cylinder fuel/air mixture can provide a smooth combustion process under high-load conditions by changing the combustion mode from spontaneous ignition into a mixed combustion mode of spontaneous ignition and deflagration [1, 12, 16, 17, 46–50, 52, 53, 61, 90–93, 104–106, 120, 121].

In many previous direct numerical simulation (DNS) studies [49, 50, 52, 53, 90, 120, 121], it was found that thermal stratification may effectively control ignition timing and smooth out the excessive PRR regardless of the in-cylinder mean temperature near the top dead center (TDC). However, the management and utilization of the in-cylinder thermal stratification is not straightforward and as such, it still remains challenging to apply thermal stratification to the development of prototype HCCI engines [1, 91, 92]. Instead, stratified-charge compression ignition (SCCI) combustion, which introduces a certain degree of fuel inhomogeneities in fuel/air mixture, has been devised as another promising remedy for the problems in HCCI combustion. In general, fuel inhomogeneities may induce a sequential ignition event, resulting in a prolonged combustion process under certain conditions [47, 91, 93, 121].

In practice, the fuel stratification for SCCI combustion can be achieved by multiple high-pressure injectors with precisely-controlled injection timing [16, 17, 47]. In two-stage injection, for instance, the main portion of fuel is first supplied during the intake stroke using a port fuel injector to generate relatively-homogeneous fuel/air mixture [47] and additional fuel (up to 20% of total fuel volume) is then directly injected during the late compression stroke or near the TDC to introduce a certain degree of fuel concentration stratification [17]. Typically, a higher degree of in-cylinder fuel stratification can be obtained by increasing the fraction of directly-injected fuel and/or retarding direct injection timing [103]. Due to the practical importance of SCCI combustion, many fundamental studies of SCCI combustion with different fuels have been investigated [1, 47, 51, 54, 61, 91–106].

Several DNS studies of ignition of thermally and compositionally stratified hydrocarbon/air mixtures have been carried out [121–124]. Mittal et al. [122] investigated the ignition characteristics of *n*-heptane/air mixture with uncorrelated thermal and compositional stratifications under HCCI and diesel combustion limits to develop a generalized multi-regime representative interactive flamelet (RIF) model. Although several different levels of fluctuations were adopted for two-dimensional (2-D) DNSs, only uncorrelated temperature and composition fields were considered to validate the RIF model and as such, the discussion was also limited to the model

validation. Luong et al. [121] elucidated the ignition characteristics of a lean biodiesel/air mixture with both temperature and composition inhomogeneities under HCCI conditions by using 2-D DNSs. It was found that a harmonious combination of composition and temperature fluctuations can prevent an excessive heat release rate (HRR) and control the ignition timing more effectively than temperature fluctuation only. However, the ignition of a lean biodiesel/air mixture under HCCI conditions exhibit relatively-weak NTC behavior and as such, the effects of the strong NTC behavior of fuel/air mixture on the HCCI combustion were not fully appreciated.

Recently, Talei and Hawkes [123] investigated the effects of negatively-correlated temperature and composition stratifications on the ignition of *n*-heptane/air mixture with different levels of mixture stratification. They found that negatively-correlated fields always advance the overall combustion compared to 0-D ignition regardless the degree of the stratifications. However, their parametric study was limited to only a few cases with negatively-correlated temperature and composition fields within the NTC regime. More recently, Bansal et al. [124] examined the characteristics of auto-ignition of stratified dimethyl ether (DME)/air mixture using 2-D and 3-D DNSs. It was found that compression heating can alter the overall HCCI combustion by lowering temperature gradient of initial field. It was also found that the overall combustion of negatively-correlated case occurs primarily by spontaneous ignition but that of uncorrelated case leads to conventional premixed deflagrations. In most studies, however, the effects of temperature and composition stratification together with their correlation on HCCI combustion were investigated fragmentarily and as such, it is not simple to generally understand each effect on HCCI/SCCI combustion.

Therefore, the objective of the present chapter is twofold: (1) to elucidate the effects of initial mean temperature in conjunction with both thermal and compositional stratifications on the ignition characteristics of realistic hydrocarbon fuel/air mixture under HCCI conditions in a comprehensive manner by performing 2-D DNSs and (2) to provide a better understanding of its temporal and spatial ignition characteristics with the chemical explosive mode analysis (CEMA). In this chapter, *n*-heptane is adopted as a hydrocarbon fuel, which exhibits a strong NTC behavior under HCCI conditions. Note that *n*-heptane has been widely used as a viable surrogate in both experimental and numerical studies to elucidate the ignition characteristics of the HCCI combustion [52].

5.2 Initial conditions

As in [52], the 58-species *n*-heptane/air reduced mechanism was adopted. Although the 58-species reduced mechanism is significantly simplified from the detailed mechanism, it still shows a good agreement with the detailed mechanism and experiments in terms of ignition delays,

flame propagation speeds, and extinction residence times under a wide range of initial temperature, equivalence ratio, and pressure conditions. The stiffness removal technique was adopted to remove any chemical timescales shorter than 10 ns [114]. This technique has been extensively validated through numerous homogeneous and 1-D ignition test cases, and 2-D DNS applications [52, 53, 90, 114, 120, 121].

For all DNSs, the initial mean equivalence ratio, ϕ_0 , and initial uniform pressure, p_0 , are 0.45 and 40 atm, respectively. Several parametric studies were performed to elucidate the effects of the initial mean temperatures, T_0 , with the variances of temperature, T' , and/or equivalence ratio, ϕ' , on the ignition of a *n*-heptane/air mixture under HCCI conditions. Total twenty-three 2-D DNSs were carried out by varying three key parameters: (1) T_0 of 805, 933, and 1025 K, (2) T' of 0, 15, and 60 K, and (3) ϕ' of 0, 0.05, and 0.10. Three initial mean temperatures with identical 0-D ignition delay, τ_{ig}^0 , of 1.5 ms were selected. Details of the physical parameters for the twenty-three DNS cases are listed in Table 5-1.

Case	Type	T_0 (K)	T' (K)	ϕ_0	ϕ'	l_e (mm)	l_{Te} (mm)	l_{ϕ_e} (mm)	u' (m/s)	τ_t (ms)	τ_{ig}^0 (ms)
1	BL	805	15	0.45	-	1.25	1.25	-	0.83	1.5	1.5
2	BL	805	60	0.45	-	1.25	1.25	-	0.83	1.5	1.5
3	BL	805	-	0.45	0.05	1.25	-	1.25	0.83	1.5	1.5
4	BL	805	-	0.45	0.10	1.25	-	1.25	0.83	1.5	1.5
5	BL	933	15	0.45	-	1.25	1.25	-	0.83	1.5	1.5
6	BL	933	60	0.45	-	1.25	1.25	-	0.83	1.5	1.5
7	BL	933	-	0.45	0.05	1.25	-	1.25	0.83	1.5	1.5
8	BL	933	-	0.45	0.10	1.25	-	1.25	0.83	1.5	1.5
9	BL	1025	15	0.45	-	1.25	1.25	-	0.83	1.5	1.5
10	BL	1025	-	0.45	0.10	1.25	-	1.25	0.83	1.5	1.5
11	NC	805	15	0.45	0.05	1.25	1.25	1.25	0.83	1.5	1.5
12	NC	805	60	0.45	0.05	1.25	1.25	1.25	0.83	1.5	1.5
13	NC	805	15	0.45	0.10	1.25	1.25	1.25	0.83	1.5	1.5
14	NC	805	60	0.45	0.10	1.25	1.25	1.25	0.83	1.5	1.5
15	NC	933	15	0.45	0.05	1.25	1.25	1.25	0.83	1.5	1.5
16	NC	933	60	0.45	0.05	1.25	1.25	1.25	0.83	1.5	1.5
17	NC	933	15	0.45	0.10	1.25	1.25	1.25	0.83	1.5	1.5
18	NC	933	60	0.45	0.10	1.25	1.25	1.25	0.83	1.5	1.5
19	NC	1025	15	0.45	0.10	1.25	1.25	1.25	0.83	1.5	1.5
20	UC	805	15	0.45	0.10	1.25	1.25	1.25	0.83	1.5	1.5
21	UC	805	60	0.45	0.10	1.25	1.25	1.25	0.83	1.5	1.5
22	UC	933	60	0.45	0.10	1.25	1.25	1.25	0.83	1.5	1.5
23	UC	1025	15	0.45	0.10	1.25	1.25	1.25	0.83	1.5	1.5

Table 5-1: Physical parameters of Cases 1–23. BL represents a baseline case with either T' only or ϕ' only. UC and NC represent uncorrelated $T - \phi$ and negatively-correlated $T - \phi$ distribution, respectively.

Note that Dec and Hwang [46] found that thermal stratification level naturally occurring in

an HCCI engine is approximately $T' = 13.3$ K which corresponds to $T' = 15$ K in the present study. In addition, Kokjohn et al. [125] found that with the presence of fuel stratification produced by the direct injection, the range of ϕ is about $0.1 \sim 0.8$, which corresponds to $\phi' = 0.1$ at $\phi_0 = 0.45$. However, depending on the fuel injection process such as the inject timing and the mass ratio of PFI to DI, the corresponding $T - \phi$ distribution can vary significantly. As such, for a given ϕ' of 0, 0.05, and 0.1, three different T' of 0, 15, and 60 K are adopted. Through this choice of T' and ϕ' , the ignition characteristics of *n*-heptane/air mixture under HCCI conditions can be investigated in a comprehensive manner.

The initial mean temperatures are deliberately chosen such that they lie within or near the NTC regime. Therefore, the ignition characteristics of a *n*-heptane/air mixture can be investigated in three different regimes of the low-, intermediate-, and high-temperature chemistry. In the same way, ϕ_0 and ϕ' are carefully selected to maintain local ϕ below unity as in experiments [17], which is supposed to prevent excessive NOx generation in real engines. The initial conditions are representative of the TDC under high-load conditions in highly air-diluted HCCI combustion [89,115]. The 0-D homogeneous ignition delay is evaluated from the 0-D simulation of a homogeneous *n*-heptane/air mixture of ϕ_0 at initial T_0 and p_0 . Henceforth, τ_{ig} denotes the time at which the maximum mean HRR occurs for all 0-D and 2-D simulations. The superscript 0 represents the 0-D homogenous ignition.

An isotropic kinetic energy spectrum function by Passot-Pouquet [37] is adopted to prescribe the initial turbulent flow field as in [48–50, 52, 53, 74–76, 90, 120, 121]. The initial turbulence decays over time since the combustion occurs in constant volume without any mean shear layer. In general, large turbulence intensity is not favored for the SCCI combustion because it can significantly homogenize mixture inhomogeneities [17,121]. Therefore, intermediate turbulence intensity, u' , of 0.83 m/s and most energetic length scale, l_e , of 1.25 mm are specified to match the corresponding turbulence timescale, τ_t , of 1.5 ms, with τ_{ig}^0 and that in real HCCI engines ($\sim O(1)$ ms).

It is of interest to note that the temporal evolution of 3-D turbulence is qualitatively different from that of 2-D turbulence due to the 3-D vortex-stretching effect. However, it is still valuable to investigate HCCI combustion with 2-D turbulence because the effect of turbulent mixing on HCCI combustion is less important than that of mixture stratifications [48–53, 90, 118, 124]. As such, it is reasonable to expect that the overall HCCI combustion characteristics of 2-D DNSs may not be very different from those of 3-D DNSs as discussed in [105, 118, 124]. Moreover, for many parametric DNS studies, it is more feasible to perform 2-D DNSs than extremely-expensive 3-D DNSs.

Temperature and concentration fields are also generated from the same energy spectrum as turbulence with different random number. The most energetic length scales of temperature and

composition fluctuations, l_{Te} and $l_{\phi e}$, are 1.25 mm for all cases. The identical characteristic length and time scales for turbulence and scalar fields are specified and hence, most effective turbulent mixing of initial mixtures can be elucidated in the present study [53].

At the TDC prior to the main auto-ignition event, different $T - \phi$ correlations may exist due to such factors as fuel delivery strategy, injection timing, amount of EGR, intake charge heating, and wall heat loss. In the present study, two most-probable scenarios are examined as another parameter for DNSs: (1) uncorrelated (UC) $T - \phi$ fields resulting from the early direct injection in the one-stage injection in combination with EGR and turbulent mixing, and (2) negatively-correlated (NC) $T - \phi$ fields caused by the evaporative cooling of the second late-direct injection in the two-stage injection together with short mixing time [51, 116]. Although the uncorrelated $T - \phi$ fields cannot be achieved without expensive intake charge heating, the UC cases are considered here to compare the effect of UC fields with that of NC fields. In addition to two $T - \phi$ correlations, cases with T' or ϕ' only are simulated to isolate their effects on the ignition although cases with ϕ' only are unrealistic. Figures 5-1 and 5-2 show several initial $T - \phi$ relations together with a representative isocontour of the initial equivalence ratio field for Case 14.

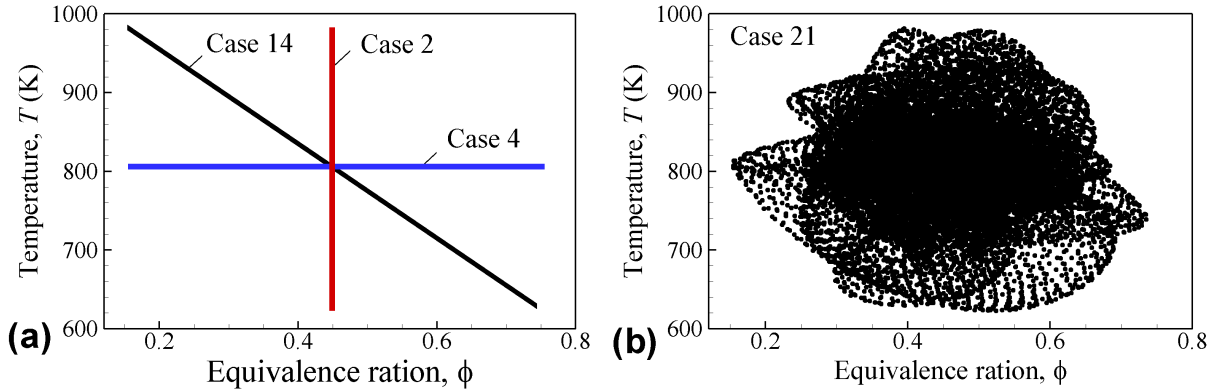


Figure 5-1: Initial $T - \phi$ distribution for (a) Cases 2, 7, 14 and (b) Case 21.

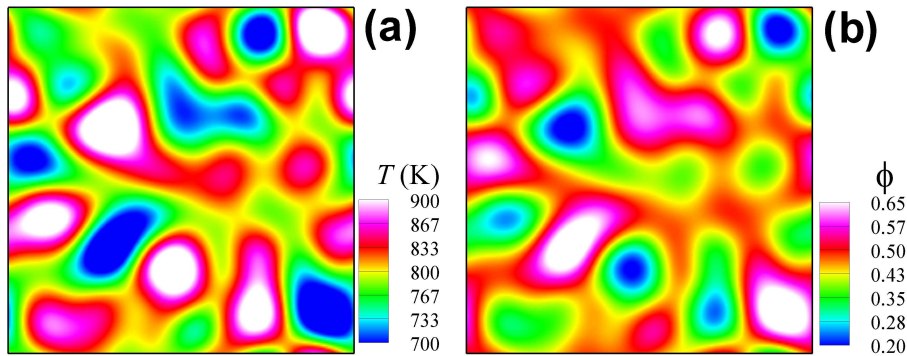


Figure 5-2: Initial field of (a) temperature and (b) equivalence ratio for Case 14.

A square box of $3.2 \times 3.2 \text{ mm}^2$ discretized with 1280 grid points in each direction was used for all 2-D DNSs. The fine grid resolution of $2.5 \text{ }\mu\text{m}$ is required to resolve thin flame fronts generated by locally-high temperature and/or equivalence ratio and as such, the thinnest reaction layers in 2-D DNSs are resolved with at least $11 \sim 15$ grid points. The 2-D DNSs were performed on the IBM Blue Gene/P of the Supercomputing Laboratory at King Abdullah University of Science and Technology (KAUST). Each of the DNSs required approximately 0.8 million CPU-hours.

5.3 Effects of T' and ϕ' at different T_0

5.3.1 0-D ignition characteristics

In general, HCCI combustion is believed to occur through volumetric auto-ignition and as such, the characteristics of the 0-D ignition delay, τ_{ig}^0 , of lean *n*-heptane/air mixtures is first examined here to gain an insight into the effects of T' and ϕ' on *n*-heptane HCCI combustion. Figure 5-3 shows the 0-D ignition delay of lean *n*-heptane/air mixtures with different ϕ_0 as a function of T_0 at $p_0 = 40 \text{ atm}$. It is readily observed from Fig. 5-3 that for the low and high temperature regimes outside the NTC regime ($T_0 < 800 \text{ K}$ or $T_0 > 1000 \text{ K}$), τ_{ig}^0 is more sensitive to T_0 than ϕ_0 . However, for T_0 within/near the NTC regime ($800 \text{ K} < T_0 < 1000 \text{ K}$), τ_{ig}^0 is more sensitive to ϕ_0 than T_0 compared to the low and high temperature regimes. This is primarily because the NTC regime occurs within the intermediate-temperature range (e.g., $875 \text{ K} < T_0 < 975 \text{ K}$ for $\phi_0 = 0.45$), where the low/intermediate temperature heat release advances the second-stage ignition more in time with decreasing T_0 such that τ_{ig}^0 is relatively constant. Moreover, it is further attributed to the strong NTC behavior at relatively-large ϕ_0 . This strong NTC behavior occurs because the temperature increase induced by the first-stage ignition becomes significant at relatively-large ϕ_0 , resulting in the advancement of the second-stage ignition.

The sensitivity of the ignition of hydrocarbon/air mixtures to temperature and composition variations under HCCI conditions has been reported in many previous numerical and experimental studies [47, 52, 91–94, 121]. For example, in 2-D DNSs of the ignition of *n*-heptane/air mixture [52], it was found that the overall combustion proceeds in different ways depending on the relative location of T_0 to the NTC regime and the degree of T' . It was also reported from [91, 92, 121] that the HCCI combustion of high-reactivity fuel/air mixture exhibiting two-stage ignition (e.g., diesel, PRF73, and *n*-heptane) is highly sensitive to mixture stratification. For low-reactivity fuel/air mixture with only one-stage ignition (e.g., gasoline, *iso*-octane, and ethanol), the overall combustion is less sensitive to fuel stratification under naturally aspirated HCCI conditions [47, 91–94]. However, it was found that under boosted intake pres-

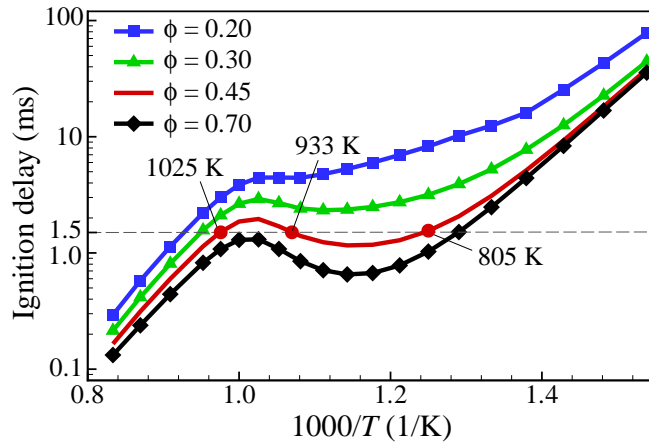


Figure 5-3: 0-D ignition delay of *n*-heptane/air mixtures as a function of initial temperature for different ϕ_0 at $p_0 = 40$ atm.

sure, the HCCI combustion of gasoline/air mixture becomes highly sensitive to fuel stratification [103, 126, 127].

All of these different ignition characteristics under HCCI conditions are primarily attributed to initial mixture conditions such as mean temperature and equivalence ratio from which the overall combustion can go through different reaction pathways: low-, intermediate-, and high-temperature chemistry. In the following sections, therefore, the overall ignition characteristics of thermally and/or compositionally stratified *n*-heptane/air mixture with different $T - \phi$ correlations are elucidated at three different T_0 , which may involve different reaction pathways.

5.3.2 Effects of T' or ϕ' at different T_0 : BL cases

To elucidate the effect of temperature or composition fluctuation only on the overall ignition characteristics of *n*-heptane/air mixture under HCCI conditions, ten baseline (BL) cases with either T' only or ϕ' only are examined. Figure 5-4 shows the temporal evolution of mean pressure, \bar{p} , and mean HRR, \bar{q} , for the BL cases (Cases 1–10) together with the corresponding 0-D homogeneous ignitions during the first- and second-stage ignition. Note that unlike cases with $T_0 = 805$ and 933 K, cases with $T_0 = 1025$ K have no first-stage ignition due to their relatively-high T_0 as shown in Fig. 5-4c; their ignition process is thus solely determined by the transition from the intermediate-temperature to high-temperature chemistry.

5.3.2.1 First-stage ignition: BL cases

For the BL cases with $T_0 = 805$ K (Cases 1–4), it is readily observed from Fig. 5-4a that \bar{q} is more spread out over time and its peak is significantly reduced with increasing T' but they do not change much with increasing ϕ' compared to their corresponding values of 0-D ignition.

This is primarily because the first-stage ignition is governed by the low-temperature chemistry which is more sensitive to T than ϕ as mentioned above. Moreover, under the present initial conditions, the first-stage ignition delay, $\tau_{ig,1}^0$, is much shorter than the turbulence timescale, τ_t ($= \tau_{ig}^0$), and as such, the effect of turbulent mixing on the first-stage ignition is negligible. This implies that the first-stage ignitions of local mixtures with different T (Cases 1 and 2) occur spontaneously with wide time difference, resulting in the temporal spread of \bar{q} . On the contrary, local mixtures with different ϕ (Cases 3 and 4) ignite simultaneously at the same time and as such, the overall first-stage ignition proceeds similarly to the 0-D ignition.

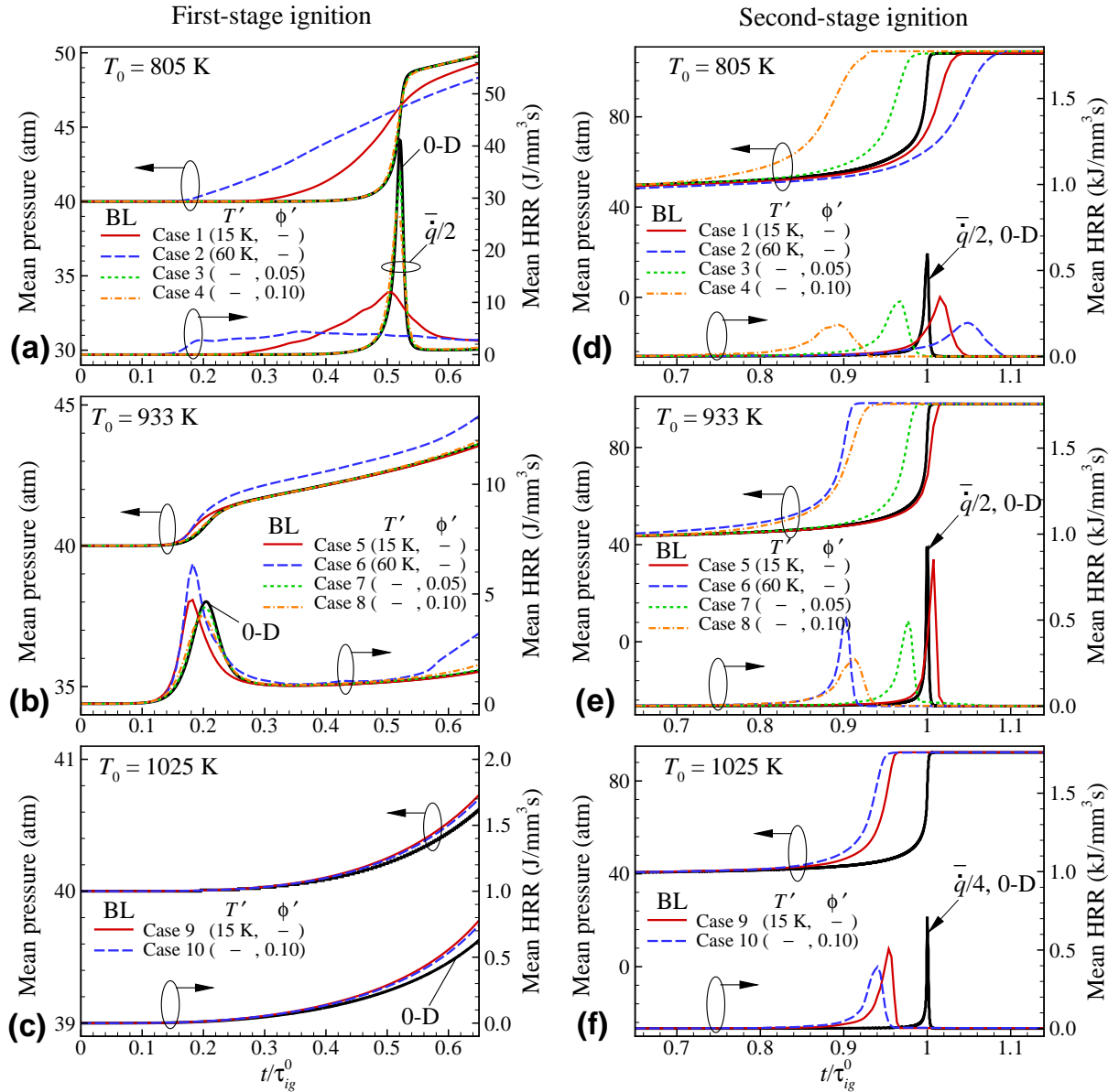


Figure 5-4: Temporal evolutions of the mean pressure and mean HRR for the BL cases with $T_0 = 805$ K (a & d), $T_0 = 933$ K (b & e), and $T_0 = 1025$ K (c & f) during the first-stage (left) and second-stage (right) ignition.

For $T_0 = 933$ K (Cases 5–8) in Fig. 5-4b, however, the overall first-stage ignitions are quite similar to the 0-D ignition regardless of T' and ϕ' . From many 0-D ignition simulations, it is found that unlike cases at $T_0 = 805$ K, $\tau_{ig,1}^0$ remains nearly the same for different T_0 around 933 K. This is because the strength of the first-stage ignition manifested in the maximum HRR is significantly reduced with increasing T_0 and as such, the effect of T_0 on the first-stage ignition becomes significantly limited. Moreover, the first-stage ignition does not change much with ϕ as discussed above and as such, the overall first-stage ignition for cases with T' only or ϕ' only proceeds similarly to the corresponding 0-D ignition. In summary, the first-stage ignitions of local mixtures occur spontaneously with only time difference due to $\tau_{ig,1}^0 < \tau_t$ and T' has a first-order effect on the first-stage ignition at low T_0 in which strong first-stage ignition occurs.

5.3.2.2 Second-stage ignition: BL cases

For the characteristics of the second-stage ignition of the BL cases, several observations are made from Figs. 5-4d–f. First, \bar{q} is more spread out over time and its peak is more decreased with increasing T' or ϕ' for all cases regardless of T_0 . These results are attributed to the general effects of temperature and composition stratifications found in many previous DNS studies [48,49,52,53,90,120,121,123]; as the degree of T' or ϕ' is increased, the deflagration mode of combustion rather than the spontaneous ignition mode prevails during the main combustion event, resulting in the reduction of the peak \bar{q} .

Second, the ignition delay, τ_{ig} , behaves non-monotonically with T' (Cases 1, 2, 5, 6, and 9) at different T_0 but it is always decreased with increasing ϕ' regardless of T_0 (Cases 3, 4, 7, 8, and 10). More specifically, as T' is increased, τ_{ig} is increased for low T_0 of 805 K; whereas, it is decreased for high T_0 of 1025 K. For intermediate T_0 of 933 K, however, τ_{ig} is slightly increased with small T' , while being decreased with large T' , exhibiting the combined effects of both low and high T_0 near the NTC regime as found in [52].

These ignition characteristics can simply be understood by examining the distribution of τ_{ig}^0 of initial fields as demonstrated in [52,120,121]. Figure 5-5 shows the 95% range of τ_{ig}^0 for the initial mixture fields for the BL cases. The 95% range of τ_{ig}^0 represents the span of τ_{ig}^0 in the initial mixture, wherein T and ϕ lie within 95% of the range of each parameter centered at T_0 and ϕ_0 . Note that local mixture with the shortest τ_{ig}^0 is more likely to auto-ignite first and as such, it may determine the start of the main combustion, while the span of τ_{ig}^0 may decide the duration of the main combustion. Nascent ignition kernels from mixtures with the shortest τ_{ig}^0 develop into wave-like fronts and propagate to consume adjacent unburnt fuel/air mixtures. Meanwhile, new ignition kernels also develop due to increased temperature and pressure, which

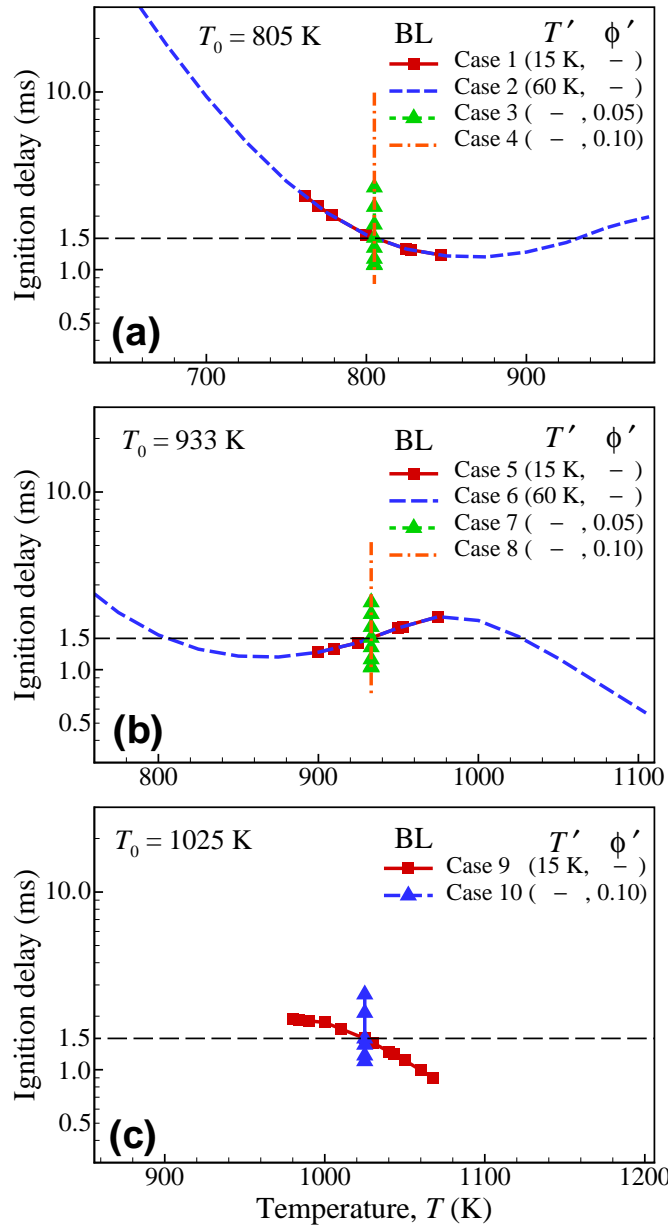


Figure 5-5: The 95% range of τ_{ig}^0 for the BL cases with (a) $T_0 = 805$ K, (b) $T_0 = 933$ K, and (c) $T_0 = 1025$ K.

leads to a sequential ignition process by the combustion mode of deflagration and/or the mode of spontaneous ignition.

As shown in Fig. 5-5, the shortest τ_{ig}^0 and its 95% range become smaller and larger, respectively with increasing T' or ϕ' . As such, the start of the main combustion can be advanced in time and its duration can be prolonged, consequently spreading out the mean HRR over time. However, the overall combustion for Case 4 is finished much later than that for Case 2 and even that for the 0-D ignition. This is because most of local mixtures in Case 4 have much longer ignition delay than τ_{ig}^0 and hence, they are mainly consumed by the deflagration mode of combustion, which leads to the significant retardation of the overall combustion compared to

0-D ignition. Moreover, since the turbulent timescale is nearly identical to the fastest τ_{ig}^0 of the mixtures, significant turbulent mixing can also delay the overall combustion by dissipating heat and radicals in nascent ignition kernels. However, the range of τ_{ig}^0 for Cases 5 in Fig. 5-5b is narrow and their values are nearly comparable to the 0-D ignition delay. As such, their overall combustion becomes more like 0-D ignition as shown in Fig. 5-4b.

It is also readily observed From Fig. 5-4 that unlike the cases with T' only, the overall combustion of the BL cases with ϕ' only (Cases 3, 4, 7, 8, and 10) is advanced in time and the duration of the main combustion is prolonged with increasing ϕ' regardless of T_0 . The BL cases with ϕ' only involve relatively-wide range of τ_{ig}^0 and mixtures with shorter ignition delays compared to the corresponding 0-D ignition as shown in Fig. 5-5. Therefore, deflagrations rather than spontaneous ignition evolve earlier than τ_{ig}^0 and propagate into adjacent unburnt mixtures, resulting in the advancement of the overall combustion and distribution of the mean HRR. It is also of interest to note that when T_0 lies within the high temperature regime (Case 10 with $T_0 = 1025$ K), wherein the overall combustion is primarily governed by the high-temperature chemistry, fuel stratification becomes less effective in reducing the peak \bar{q} and advancing τ_{ig} . Moreover, in this high temperature regime, small T' induces quite similar result to that by large ϕ' in terms of the advancement of the overall combustion [52, 121].

5.3.3 Effects of negatively-correlated $T - \phi$ fields: NC cases

To understand the effect of two different $T - \phi$ correlations on the ignition of *n*-heptane/air mixture, the temporal evolution of the mean HRR for the negatively-correlated (NC) and uncorrelated (UC) cases at three different T_0 is shown in Fig. 5-6 together with the BL cases. During the first-stage ignition, the overall combustion for all NC and UC cases proceeds quite similarly to that of the BL cases with the same T' regardless of ϕ' . As discussed above, this is because the first-stage ignition is mainly determined by the low-temperature chemistry sensitive to temperature variation, and is not affected by turbulence mixing of which timescale, τ_t , is much longer than $\tau_{ig,1}^0$.

For the second-stage ignition of the NC cases, several points are to be noted from Fig. 5-6d-f. First, for cases with $T_0 = 805$ K and 1025 K, the negative $T - \phi$ correlation has an adverse effect on the overall combustion in terms of HRR distribution; the peak \bar{q} is significantly increased and the duration of the main combustion is reduced compared to those of the BL cases. In addition, the overall combustion is finished much later than that of the corresponding BL case.

These results are primarily attributed to the characteristics of the 0-D ignition delays of initial mixtures and the turbulence timescale relative to τ_{ig}^0 . As shown in Figs. 5-7a and c,

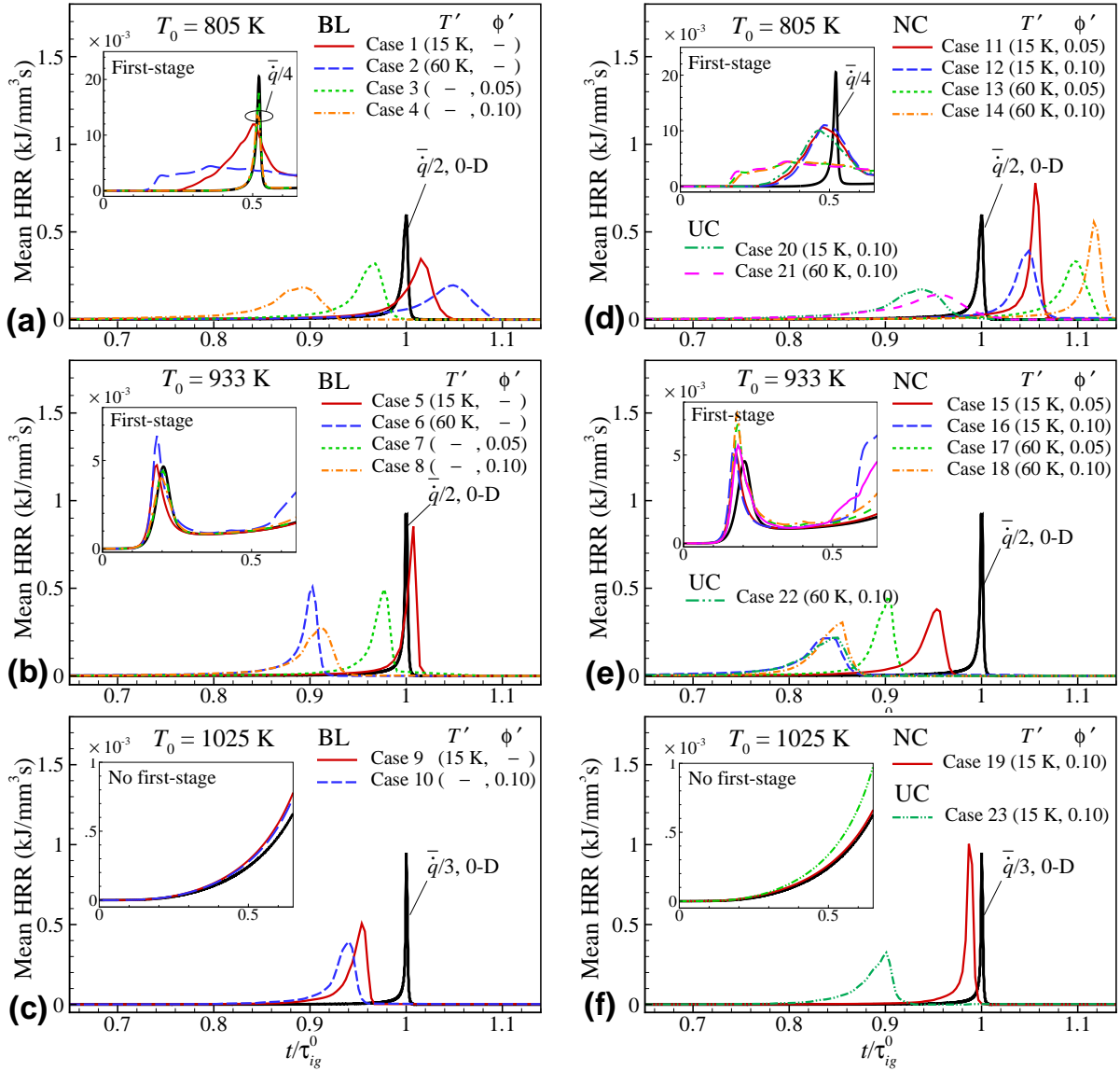


Figure 5-6: Temporal evolutions of the mean HRR for the BL (left column) and NC & UC (right column) cases with $T_0 = 805$ K (a & d), $T_0 = 933$ K (b & e), and $T_0 = 1025$ K (c & f) during the second-stage ignition. The first-stage ignitions are shown in the small boxes.

the 0-D ignition delays for Cases 11 and 19 spans relatively-narrow range close to 1.5 ms such that the overall combustion may occur by the spontaneous ignition even though it is slightly delayed for Case 11 and advanced for Case 19. Moreover, the turbulent timescale is similar to the 0-D ignition delays for the cases and hence, turbulence can effectively homogenize the initial mixture, resulting in the retardation of the overall combustion. For Cases 12–14, the 0-D ignition delays of most mixtures are much greater than 1.5 ms. Although turbulence with τ_t of 1.5 ms can effectively heat and radicals from nascent ignition kernels and homogenize mixtures. As a result, the overall combustion is retarded. These results verify that the positive effects of temperature inhomogeneities in the initial mixture on the HCCI combustion can be diminished by fuel stratification if it is introduced into the engine cylinder opposite to thermal

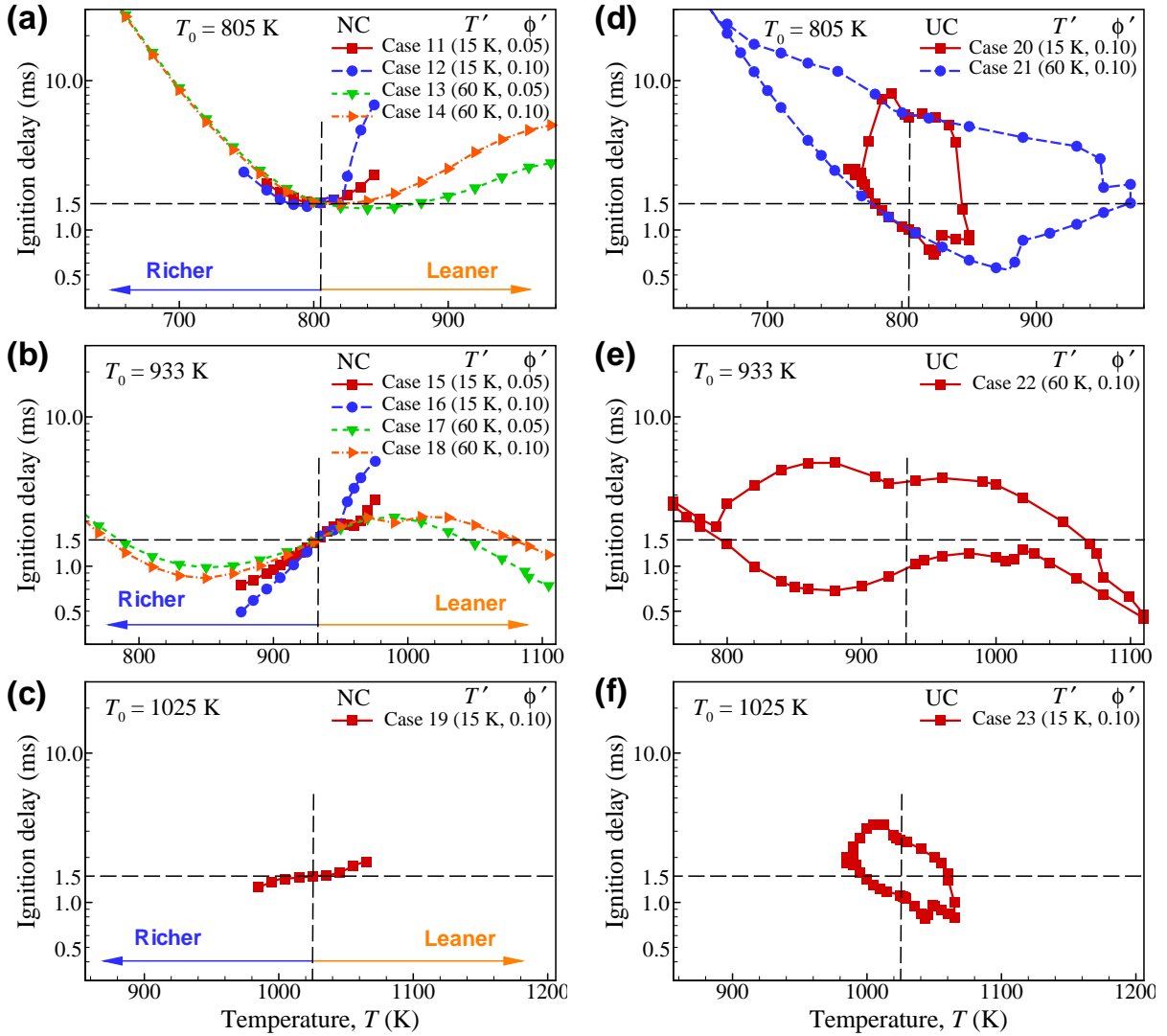


Figure 5-7: The 95% range of τ_{ig}^0 for the NC (left) and UC (right) cases with $T_0 = 805$ K (a & d), $T_0 = 933$ K (b & e), and $T_0 = 1025$ K (c & f).

stratification, leading to rapid volumetric ignition [51, 98, 99, 121].

Second, for cases with intermediate T_0 of 933 K (see Fig. 5-6e), the negative correlation of $T - \phi$ fields has a positive effect on the overall combustion by spreading out \bar{q} over time and reducing the peak \bar{q} . These results can also be understood by examining 0-D ignition delays of initial mixtures. As shown in Fig. 5-7b, the negatively-correlated $T - \phi$ fields for Cases 15–18 induce much shorter 0-D ignition delays of the initial fields than τ_{ig}^0 of 1.5 ms. Therefore, it can be expected that nascent ignition kernels can successfully develop into deflagrations, which subsequently advance the overall combustion and distribute the mean HRR over time. Moreover, for cases with the same T' , the shortest 0-D ignition delay for $\phi' = 0.10$ is much smaller than that for small ϕ' of 0.05 and as such, the overall combustion is more advanced with large ϕ' for cases with same T' .

It is of interest to note from Fig. 5-7b that for cases with $\phi' = 0.10$, the shortest 0-D ignition delay for Case 16 is much smaller than that for Case 18 and as such, it may be expected that the overall combustion for Case 16 is finished much earlier than that for Case 18. In reality, however, the overall combustion of the two cases proceeds quite similarly to each other. The characteristics of overall combustion may be determined not only by the shortest 0-D ignition delay but also by the number of ignition kernels which can successfully develop into deflagrations.

To further elucidate the ignition characteristics of the NC cases at $T_0 = 933$ K, the instantaneous isocontours of HRR field at the times of 5, 50, and 95% cumulative \bar{q} , and the maximum \bar{q} are shown in Fig. 5-8. The local HRR, \dot{q} , is normalized by the maximum HRR of the corresponding 0-D ignition, $\dot{q}_m^0 = 1857$ J/mm³s. For Case 16, deflagration waves emanate from nascent ignition kernels much earlier than those for the other cases because the shortest 0-D ignition delays in Case 16 is smaller than those in other cases. For Cases 16 and 18, however, the temporal evolution of \bar{q} are not quite different. At time of 5% cumulative \bar{q} , more corrugated deflagration waves are observed for Case 18 than for Case 16, implying that Case 18 has more nascent ignition kernels which ultimately develop into deflagrations than Case 16.

This qualitative observation can be verified by examining the probability density function (PDF) of τ_{ig}^0 and its spatial gradient, $|\nabla\tau_{ig}^0|$, of initial mixtures as shown in Fig. 5-9. It is readily observed that only the PDF of τ_{ig}^0 of Case 16 exhibits non-zero values near $\tau_{ig}^0 = 0.5$ ms and the PDF of τ_{ig}^0 of Case 18 has a peak at $\tau_{ig}^0 = 0.95$ ms, which is greater than those of other cases. These results imply that even though the ignition kernels start to develop earlier in Case 16 than in Case 18, more deflagrations in Case 18 consume unburnt mixtures faster than in Case 16. Therefore, the overall combustion of the two cases proceeds similarly to each other. It is also observed from the figure that the PDF of $|\nabla\tau_{ig}^0|$ of Case 18 is slightly more distributed up to very large $|\nabla\tau_{ig}^0|$ than that of Case 16, which implies that once deflagration waves are developed, the deflagration mode can prevail more in Case 18. The characteristics of deflagration mode of combustion is further discussed in the next section.

For the cases with small ϕ' of 0.05 (Cases 15 and 17), however, large T' tends to advance the overall HCCI combustion and increase the peak \bar{q} slightly. In addition, for cases with the same ϕ' , τ_{ig} for the negatively-correlated cases are shorter than those of the corresponding BL cases with ϕ' only (Cases 8 and 9); for example, τ_{ig} for the BL case (Case 9) and negatively-correlated cases (Cases 16 and 18) are approximately 0.91 and 0.85, respectively. Furthermore, as shown in Fig. 5-9, the PDFs of τ_{ig}^0 and $|\nabla\tau_{ig}^0|$ of Case 17 are more distributed than those of Case 15 and as such, the deflagration mode is expected to prevail more in Case 17 than Case 15. All of these results imply that negatively-correlated $T - \phi$ fields at intermediate T_0 within the NTC regime

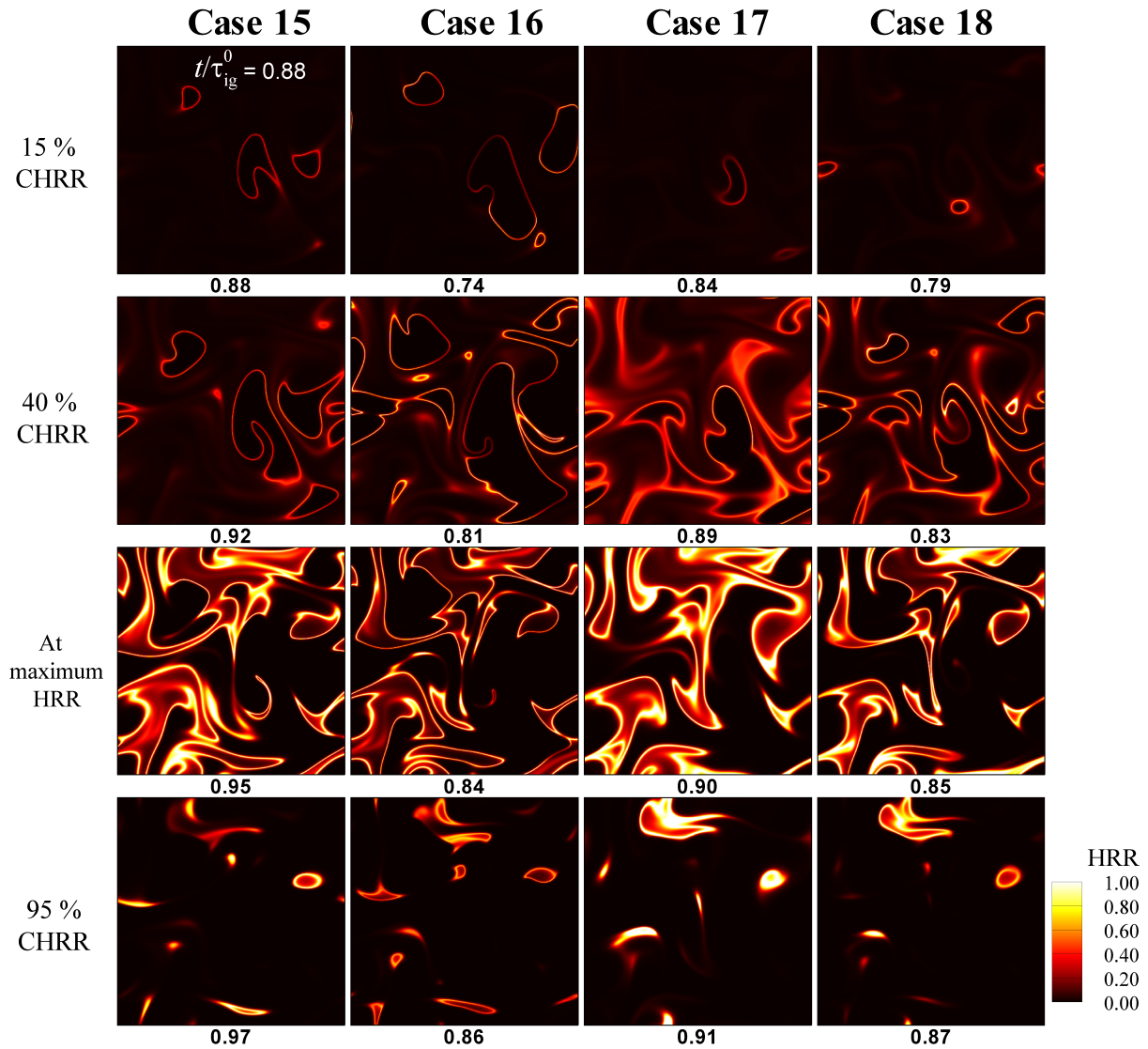


Figure 5-8: Isocontours of normalized HRR for Cases 15–18 (from left to right) at times of 15% (first row), 40% (second row), and 95% (last row) cumulative mean HRR and at the maximum HRR (third row).

have a synergistic effect of advancing the overall combustion and smoothing out the PRR and HRR under high-load HCCI combustion.

5.3.4 Effects of uncorrelated $T - \phi$ fields: UC cases

As mentioned above, the uncorrelated $T - \phi$ distribution prior to the main combustion event is another scenario which may occur in HCCI combustion [51, 121]. For completeness, four cases with uncorrelated $T - \phi$ distribution (Cases 20–23) are examined to understand the combined effects of temperature and composition inhomogeneities in/near the NTC regime on the overall HCCI combustion.

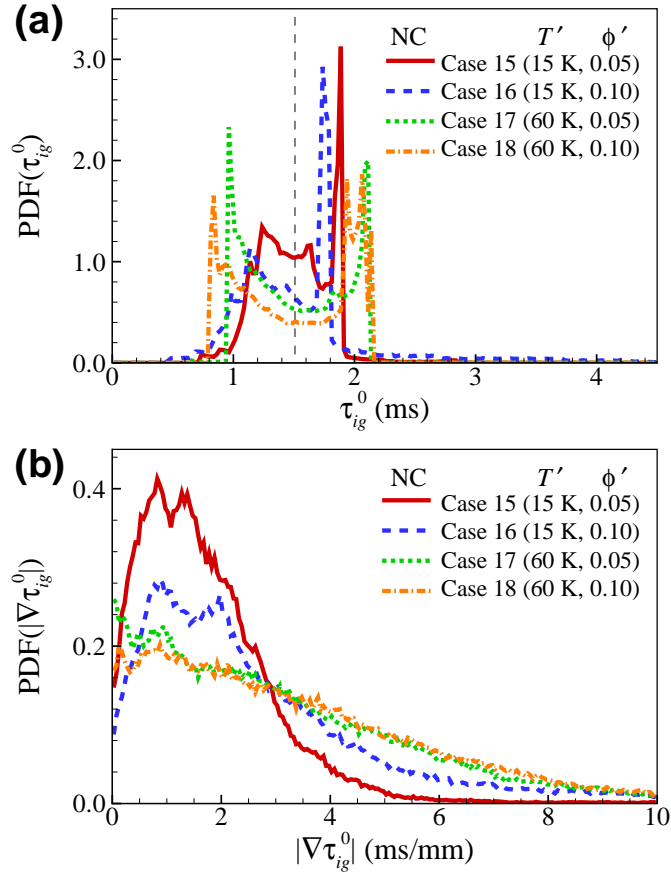


Figure 5-9: The probability density function of (a) 0-D ignition delay and (b) its spatial gradient of initial mixtures for Cases 15–18.

Several observations can be made for the UC cases from Figs. 5-6d–f. Unlike the NC cases, the overall combustion of all UC cases is more advanced in time and the duration of the main combustion is further increased regardless of T_0 compared to their corresponding 0-D ignition. The 95% range of 0-D ignition delay for the UC cases (see Figs. 5-7d–f) can further identify the ignition characteristics of the UC cases; the overall HCCI combustion occurs rapidly because the fastest ignition delay is much shorter than $\tau_{ig}^0 = 1.5$ ms and the mean HRR is more distributed over time due to the wide spread of ignition delay.

Even though the overall combustion characteristics for all UC cases seem to be analogous in many ways, different behaviors of the overall combustion for different T_0 can be observed. For cases with $T_0 = 805$ K (Cases 20 and 21), the temporal distribution of the mean HRR by uncorrelated $T - \phi$ field becomes more significant than the corresponding BL cases with ϕ' only (Cases 3 and 4), which is primarily attributed to the wider range of ignition delay of the UC cases. In the same context, uncorrelated large T' and ϕ' in Case 21 tend to retard the overall combustion compared to Case 4 with ϕ' only. The occurrence of ignition kernels and their development into deflagrations happens at the same time due to their similar fastest ignition delay. However, it takes more time to consume the whole fuel/air mixture of Case 21 with wide

range of ignition delay than does Case 4 with relatively narrow range of ignition delay.

However, for cases with $T_0 = 933$ K (Case 22) and 1025 K (Case 23), the uncorrelated $T - \phi$ fields advance the overall combustion and spread out the mean HRR compared to the BL cases with T' only or ϕ' only, which is also attributed to the shorter fastest ignition delays and wide range of ignition delay in the initial fuel/air mixture. For Case 22, moreover, the effect of uncorrelated $T - \phi$ field becomes comparable to that of negatively-correlated $T - \phi$ field because in the NTC regime, the 95% range of ignition delay for the UC cases becomes comparable to that for the NC cases and as such, the overall HCCI combustion of the UC case proceeds similarly to that of the NC cases. In summary, the uncorrelated $T - \phi$ distribution has a synergetic effect in preventing excessive PRR by temporally distributing \bar{q} compared to the BL cases with T' only or ϕ' only.

5.3.5 Combustion mode

In the previous sections, the spontaneous ignition and deflagration modes of combustion are discussed without any quantitative analysis. As such, in this section, the occurrence of deflagration mode during combustion is quantitatively measured by adopting the Damköhler number, Da , defined as [52, 53, 77, 86, 90, 121]:

$$Da = \frac{\dot{\omega}_k}{|-\nabla \cdot (\rho Y_k \mathbf{V}_k)|}, \quad (5.3.1)$$

where Y_k , \mathbf{V}_k , and $\dot{\omega}_k$ denote the mass fraction, diffusion velocity, and net production rate of species k , respectively. $Y_c \equiv Y_{\text{CO}_2} + Y_{\text{CO}}$ is used for the Damköhler number analysis.

To delineate between the deflagration and spontaneous ignition modes, Da in the diffusive limit is identified from a series of 1-D laminar simulations at various ϕ_0 . Note that the diffusive limit represents a condition in which deflagration wave propagates without auto-ignition or diffusion balances reaction [49, 50, 52, 53, 90, 121]. From the simulations, it is found that Da in the diffusive limit is approximately 2.0. Note that in the diffusive limit under the present specific conditions, Da becomes larger than unity because the mixture upstream of the deflagration wave is highly reactive, and as such, the reaction term of Da becomes larger than the diffusion term [52, 53, 90, 121]. In the present study, combustion is determined to occur by the deflagration mode when the corresponding Da is less than 2.0.

Figure 5-10 shows the temporal evolution of the fraction of HRR from the deflagration mode for all DNS cases. It is readily observed that prior to the main ignition, most of heat release occurs in the deflagration mode except for Cases 1, 5, 11, and 19 in which T' and/or ϕ' are relatively small. It is also found that in most cases, the fraction of HRR from the deflagration

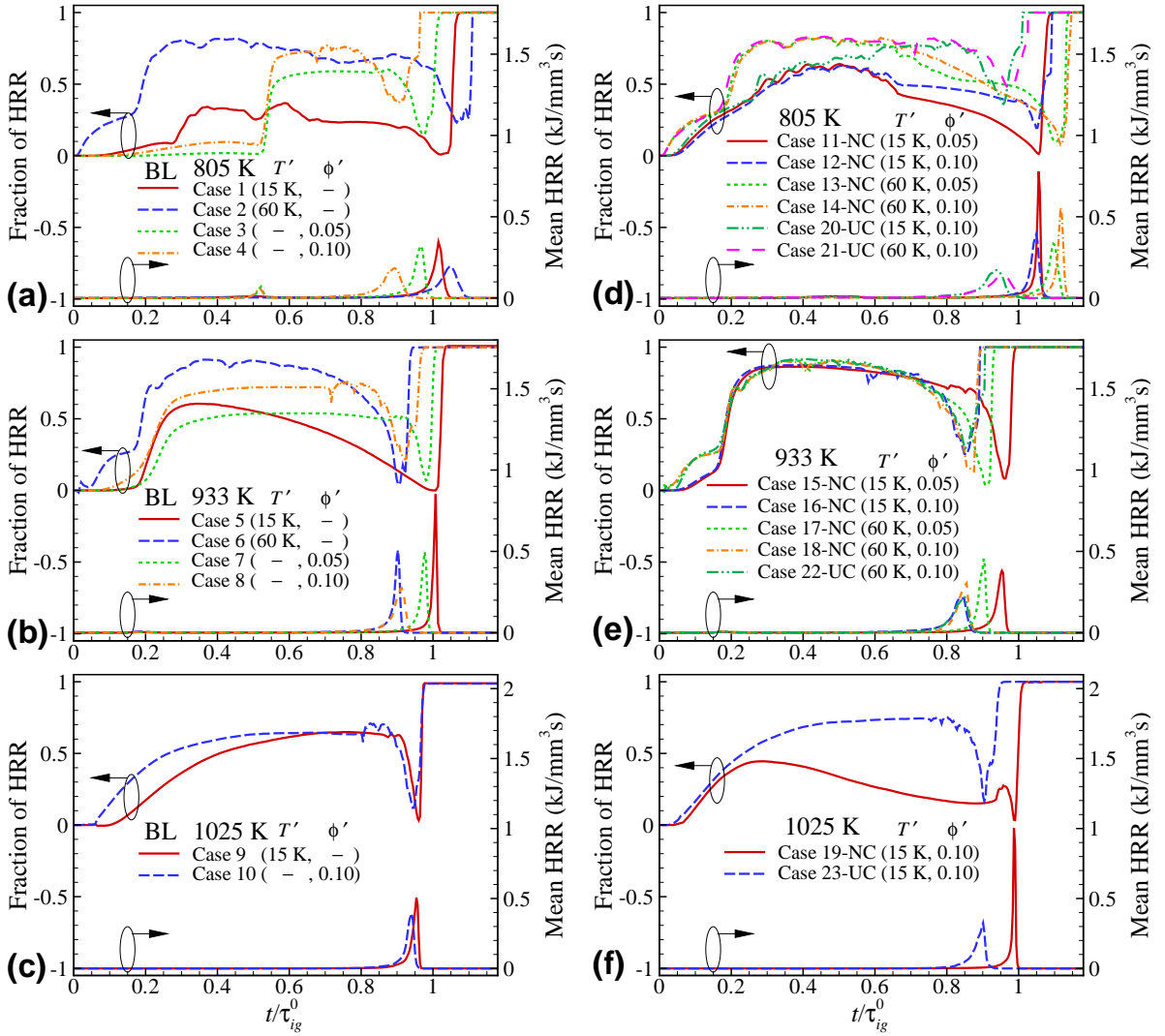


Figure 5-10: Temporal evolution of the fraction of heat release rate from the deflagration mode and mean heat release rate for the BL (left) and NC/UC (right) cases.

mode is rapidly reduced near the occurrence of the peak \bar{q} . These results verify that for large T' and/or ϕ' cases, combustion occurs primarily by the deflagration mode during the early stage of ignition; however, the mixed mode of deflagration and spontaneous ignition takes it over during the main combustion process. Note that at the final stage of ignition, the fraction of HRR from the deflagration mode increases up to unity because $\dot{\omega}_c$ in Eq. 8.4.1 vanishes, consequently leading to $Da = 0$.

To further identify the effect of deflagration mode on the characteristics of HCCI/SCCI combustion, the maximum HRR, burning duration, and total HRR fraction from the deflagration mode for all DNS cases are listed in Table 5-2. In general, the total HRR fraction from the deflagration mode is increased with increasing T' and/or ϕ' , resulting in the reduction of the maximum HRR and the increase of the burning duration. For the NC cases (Cases 12 vs. 14, 15 vs. 17, and 16 vs. 18), however, the total fraction of HRR is reduced when T' is increased from 15 K to 60 K. As T' is increased, more mixtures outside the NTC regime are included in

the initial field and as such, the canceling effect of negatively-correlated $T - \phi$ fields outside the NTC regime is enhanced and the first order effect of ϕ' on the HCCI combustion is slightly reduced.

Case	Type	T_0 (K)	T' (K)	ϕ'	τ_{ig}/τ_{ig}^0	\bar{q}_m/\dot{q}_m^0	τ_{bd}/τ_{ig}^0	\bar{q}_{def} (%)
1	BL	805	15	-	1.02	0.29	0.12	9.3
2	BL	805	60	-	1.05	0.16	0.15	47.2
3	BL	805	-	0.05	0.97	0.27	0.12	28.3
4	BL	805	-	0.10	0.89	0.15	0.15	46.0
5	BL	933	15	-	1.01	0.46	0.07	4.8
6	BL	933	60	-	0.90	0.27	0.09	28.2
7	BL	933	-	0.05	0.98	0.27	0.09	23.2
8	BL	933	-	0.10	0.91	0.15	0.10	40.6
9	BL	1025	15	-	0.95	0.18	0.05	27.1
10	BL	1025	-	0.10	0.94	0.14	0.07	31.4
11	NC	805	15	0.05	1.06	0.65	0.10	14.9
12	NC	805	15	0.10	1.05	0.33	0.12	33.1
13	NC	805	60	0.05	1.10	0.28	0.14	29.0
14	NC	805	60	0.10	1.12	0.46	0.11	25.6
15	NC	933	15	0.05	0.95	0.20	0.08	32.5
16	NC	933	15	0.10	0.84	0.12	0.13	48.1
17	NC	933	60	0.05	0.90	0.24	0.07	24.6
18	NC	933	60	0.10	0.86	0.16	0.11	38.7
19	NC	1025	15	0.10	0.99	0.35	0.04	11.9
20	UC	805	15	0.10	0.94	0.14	0.15	56.8
21	UC	805	60	0.10	0.95	0.12	0.17	64.3
22	UC	933	60	0.10	0.85	0.12	0.13	49.9
23	UC	1025	15	0.10	0.90	0.11	0.13	44.9

Table 5-2: Quantitative data of the DNS cases. \bar{q}_m is the maximum mean HRR; τ_{bd} is the burn duration which represents the period from 10% to 90% cumulative HRR; \bar{q}_{def} is the total fraction of HRR from the deflagration mode.

In summary, deflagration waves can successfully develop at the early stage of combustion only if the shortest τ_{ig}^0 of initial mixture induced by large T' and/or ϕ' is small enough. This early development of deflagrations can render relatively-large portion of combustion to occur by the deflagration mode, which significantly contributes to the temporal spreading of the mean HRR, and the reduction of the peak \bar{q} and τ_{ig} as shown in Table 5-2.

5.4 Chemical aspects of the ignition

In this section, the effects of the initial mean temperatures and temperature/composition stratifications on the overall HCCI combustion are further elucidated by examining the temporal evolution of important species together with the overall reaction pathways of n -heptane oxi-

dation mechanism. Moreover, the spatial characteristics of the ignition are also identified by chemical explosive mode analysis (CEMA).

5.4.1 Characteristics of temporal species evolution

Prior to analyzing the characteristics of important species, the overall reaction pathways of *n*-heptane oxidation relevant to HCCI combustion are first discussed to obtain the insight of the chemical aspects of HCCI combustion. Readers are referred to Fig. 5-11 for a schematic of the reaction pathways composed of three different routes: low-, intermediate-, and high-temperature chemistries [5, 6, 128, 129].

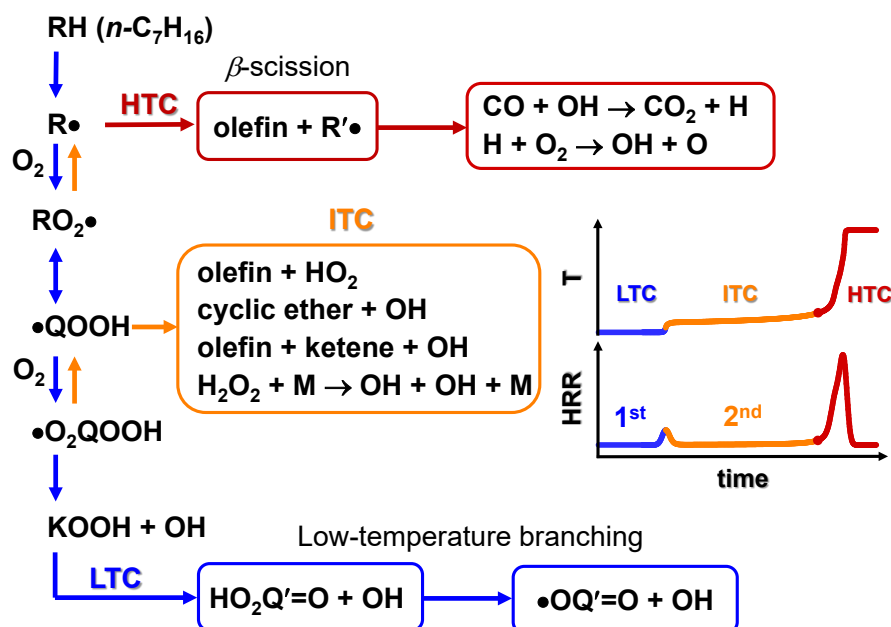


Figure 5-11: Schematic of reaction pathways of *n*-heptane oxidation at different temperatures [5].

The low-temperature chemistry of *n*-heptane oxidation is first initiated by the H-atom abstraction from a fuel molecule, RH , reacting with molecular oxygen ($RH + O_2 \rightarrow R + HO_2$). As such, HO_2 increases significantly as a result of rapid *n*-heptane decomposition during the first-stage ignition. Alkyl radical, R , then reacts with O_2 to produce alkylperoxy radical, RO_2 , via $R + O_2 + M \rightarrow RO_2 + M$. The rate of addition of O_2 to alkyl radical and its equilibrium depend strongly on pressure, temperature, and equivalence ratio and hence, the temperature threshold for separating the low- and high-temperature reaction path varies depending on specific conditions. Next, RO_2 radical isomerization occurs to form hydroperoxyalkyl, $QOOH$, ($RO_2 \rightleftharpoons QOOH$) followed by another O_2 addition ($QOOH + O_2 \rightarrow O_2QOOH$). The overall rate of the low-temperature chemistry is primarily controlled by the rate of chain branching reactions

through the production and decomposition of keto-hydroperoxide, KOOH; i.e., $\text{O}_2\text{QOOH} \rightarrow \text{KOOH} + \text{OH}$ and $\text{KOOH} \rightarrow \text{OH} + \text{KO}$.

The low-temperature reaction cycle is suppressed when temperature exceeds a critical value at which the competing reaction ($\text{R} + \text{O}_2 \rightarrow \text{olefin} + \text{HO}_2$) terminates the first-stage ignition. Between the first- and second-stage ignition, the intermediate-temperature chemistry, which is actually the combination of the low- and high-temperature chemistries, dominates the ignition of *n*-heptane/air mixture; alkyl radical and hydroperoxyalkyl species convert into the other fuel species (e.g., cyclic ether species, olefins, and ketenes) plus OH and HO₂. In this period, the rate of temperature increase is significantly reduced due to a lower reactivity of the system. Over a certain temperature threshold, the chain-branching reaction of hydrogen peroxide ($\text{H}_2\text{O}_2 + \text{M} \rightarrow \text{OH} + \text{OH} + \text{M}$) becomes highly reactive, resulting in large enough temperature increase to initiate the chain branching reactions at high temperatures, controlled by $\text{H} + \text{O}_2 \rightarrow \text{O} + \text{OH}$. At this point, the high-temperature chemistry becomes predominant over the low-temperature chemistry and the second-stage ignition starts to occur.

The high-temperature chemistry of *n*-heptane oxidation can be simply understood as a process of sequential decomposition of large fuel species to small radicals, down to CH₂O, CHO, H₂O₂, HO₂, and CO. At the final stage of the ignition, therefore, reaction pathways involve the core of H₂/CO oxidation mechanism [5, 129].

Based on the above discussion of the overall reaction pathways, the temporal evolution of the mean mass fraction of important species (e.g., *n*-C₇H₁₆, HO₂, H₂O₂, OH, CO, and CO₂) and the mean HRR is shown in Figs. 5-12–5-14 for DNS cases at three different T_0 together with their corresponding 0-D ignition cases. Three distinct behaviors of the species are readily observed from the figures depending on T_0 .

First, for Cases 4 and 11 (see Fig. 5-12 c and d), almost all *n*-heptane is rapidly consumed by the low-temperature chemistry ($\text{RH} + \text{O}_2 \rightarrow \text{R} + \text{HO}_2$) and as such, HO₂ mass fraction increases significantly and has its first peak during the first-stage ignition, which is similar to their corresponding 0-D case with $T_0 = 805$ K. Since T' for Cases 4 and 11 are relatively small compared to those of other cases (Cases 2, 14, and 21), the overall combustion proceeds similarly to their corresponding 0-D ignition during the first-stage of ignition; however, for Cases 2, 14, and 21 with relatively large T' , the wide span of the first-stage ignition delay in the initial mixture results in the gradual reduction of *n*-heptane and increment of HO₂, which is manifested in the relatively-small and temporally-distributed HRR during the early stage of the ignition (see Figs. 5-4a and 5-6a). In either case, however, the temporal spread of HRR (Cases 2, 4, and 21) during the second-stage ignition is manifested in a gradual increase of OH and decrease of H₂O₂ as the high-temperature chemistry dominates the overall combustion,

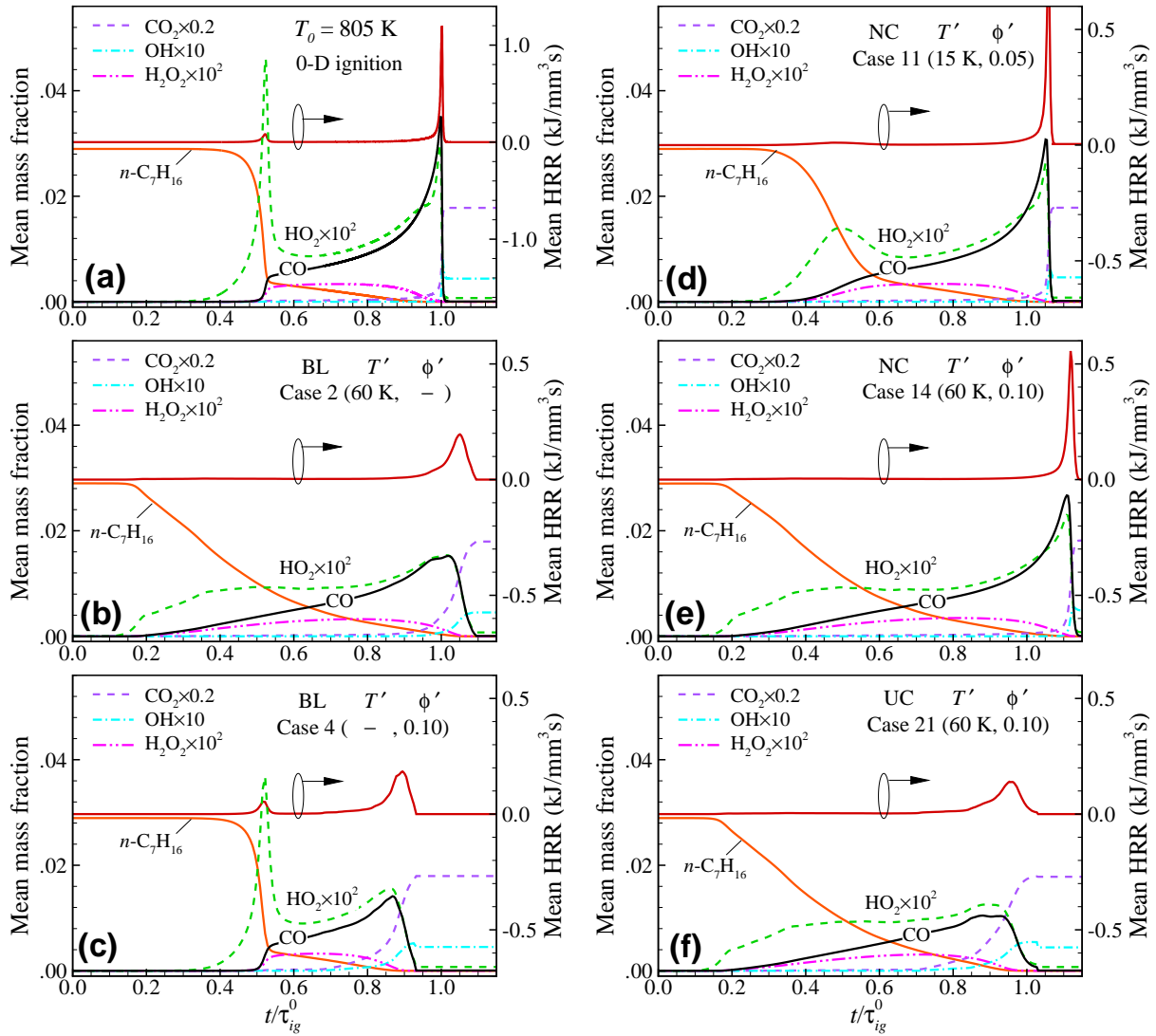


Figure 5-12: Temporal evolutions of the mean mass fractions of important species and mean HRR at $T_0 = 805$ K for (a) 0-D ignition, (b) Case 2, (c) Case 7, (d) Case 11, (e) Case 14, and (f) Case 21.

implying that the overall combustion occurs not only by the spontaneous ignition mode but also by the deflagration mode of combustion.

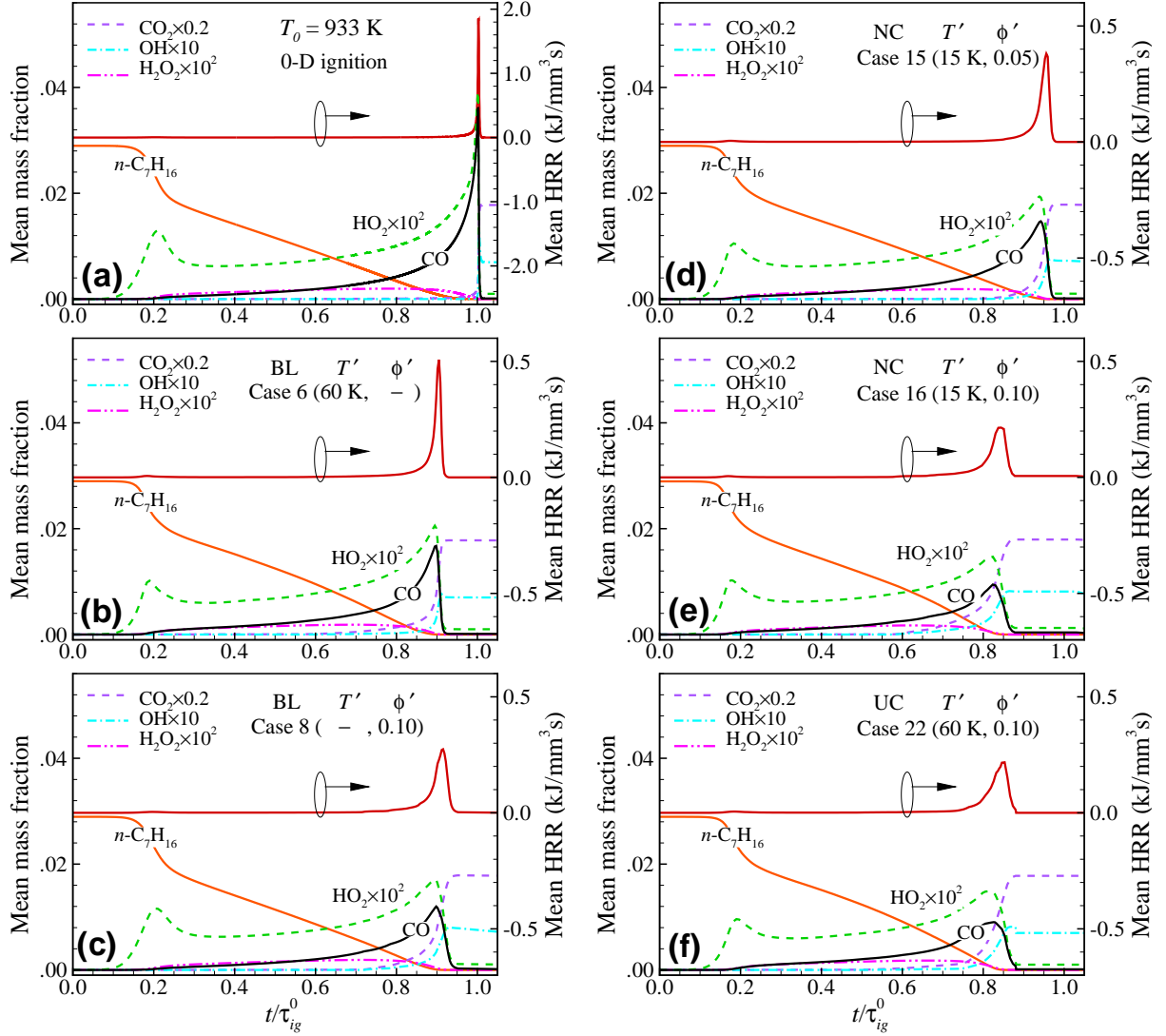


Figure 5-13: Temporal evolutions of the mean mass fractions of important species and mean HRR at $T_0 = 933$ K for (a) 0-D ignition, (b) Case 6, (c) Case 8, (d) Case 15, (e) Case 16, and (f) Case 22.

Second, for cases with $T_0 = 933$ K (see Fig. 5-13), only a small fraction of n -heptane is rapidly consumed during the first-stage ignition and then, it decreases linearly until the end of combustion. Since the HRR from the first-stage ignition at $T_0 = 933$ K is much smaller than at $T_0 = 805$ K, the consumption of n -heptane for cases with $T_0 = 933$ K during the first-stage ignition becomes smaller compared to cases with $T_0 = 833$ K. For all cases with $T_0 = 933$ K, HO_2 has two peaks at the first- and second-stage ignition; as discussed above, the first peak occurs through $\text{RH} + \text{O}_2 \rightarrow \text{R} + \text{HO}_2$ and the second is attributed to the accumulation of HO_2 via $\text{R} + \text{O}_2 \rightarrow \text{olefin} + \text{HO}_2$ of the intermediate-temperature chemistry. Similar to cases with $T_0 = 833$ K, the temporal distribution of the mean HRR during the second-stage ignition is manifested

in the progressive increment of OH and reduction of H_2O_2 . These results are consistent with the previous DNS study of ignition of primary reference fuel (PRF)/air mixtures of which T_0 lies within the NTC regime [120].

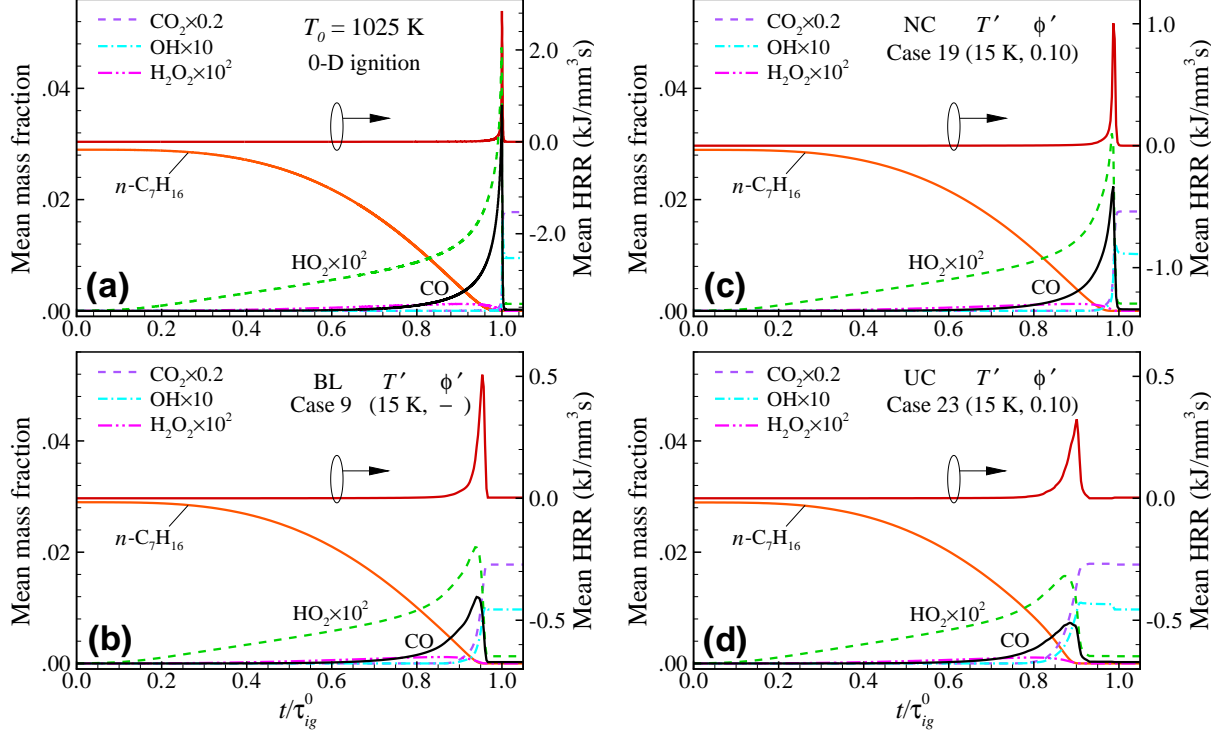


Figure 5-14: Temporal evolutions of the mean mass fractions of important species and mean HRR at $T_0 = 1025$ K for (a) 0-D ignition, (b) Case 9, (c) Case 19, and (d) Case 23.

Third, for cases with $T_0 = 1025$ K (see Fig. 5-14), *n*-heptane is first gradually consumed and then, the consumption rate keeps increasing till the end of the overall combustion. At high T_0 of 1025 K, there is no first-stage ignition and the intermediate-to-high temperature chemistries govern the ignition such that the consumption of *n*-heptane and accumulation of HO_2 occurs gradually through the intermediate-temperature chemistry as shown in Fig. 5-11. As deflagrations developed from ignition kernels propagate into unburnt mixture, significant heat release starts to occur and CO and OH levels increase rapidly. At the final stage, the unburnt mixture is consumed primarily by the spontaneous ignition and as such, the mass fraction of CO and HO_2 decreases rapidly. It is also of interest to note that the level of H_2O_2 concentration is relatively low compared to that at $T_0 = 805$ and 933 K. At high temperature, H_2O_2 decomposes rapidly into OH via $\text{H}_2\text{O}_2 + \text{M} \rightarrow \text{OH} + \text{OH} + \text{M}$ and as such, remains relatively constant till the thermal ignition.

Overall, the evolution characteristics of important species for 2-D DNS cases are similar to those of the corresponding 0-D ignitions and the departure from the 0-D ignition is primarily attributed to the existence of deflagrations during the combustion, which is controlled by the

degree of T' and ϕ' and their spatial correlation.

5.4.2 Chemical explosive mode analysis

In this section, CEMA is adopted to understand the spatial ignition characteristics of the lean *n*-heptane/air mixture by identifying controlling species and elementary reactions at different locations and time. CEMA has been applied to various DNS problems such as turbulent lifted jet flames in heated coflows [77–80], turbulent reacting jet flames in cross flows [81, 82], and ignition of hydrocarbon fuel/air mixtures under HCCI conditions [52, 83, 90, 120, 121]. From these studies, CEMA has been proved as a reliable computational flame diagnostics (CFLD) tool to systematically detect important species and reactions for premixed flames and limited phenomena including ignition and extinction.

CEMA is briefly explained here and for more details of CEMA, readers are referred to [78, 80]. The differential governing equations for a chemically-reacting flow can be described in discretized form as:

$$\frac{D\mathbf{y}}{Dt} = \mathbf{g}(\mathbf{y}) = \boldsymbol{\omega}(\mathbf{y}) + \mathbf{s}(\mathbf{y}), \quad (5.4.1)$$

where D/Dt is the material derivative, which can be replaced by d/dt in the Lagrangian coordinate, and \mathbf{y} represents the solution vector of species concentrations and temperature. The chemical source term is denoted as $\boldsymbol{\omega}$, while all non-chemical source terms such as diffusion in flames and homogeneous mixing term in stirred reactors are represented by \mathbf{s} .

The Jacobian of the chemical source term, \mathbf{J}_ω ($\equiv \partial\boldsymbol{\omega}/\partial\mathbf{y}$), includes the local chemical information of local mixture and as such, it can be used to determine the chemical feature of the mixture. For this purpose, a chemical mode is defined as an eigenmode of \mathbf{J}_ω , which is associated with an eigenvalue, λ_e , and a corresponding pair of the left and right eigenvectors, \mathbf{a}_e and \mathbf{b}_e . Chemical explosive mode (CEM) is a chemical mode of which real part of eigenvalue is positive: $\text{Re}(\lambda_e) > 0$.

The existence of a CEM indicates that the local mixture auto-ignites if there are no thermal and radical losses. In the same way, the auto-ignition of a local mixture exhibiting CEM may be delayed or even fail if the mixture loses significant heat or radicals by strong mixing or diffusion. Nevertheless, CEM remains an intrinsic chemical feature of ignitable mixtures. It is also of interest to note that the critical flame features including ignition, extinction, and premixed flame front locations, are closely related with the transition of CEMs from explosive ($\text{Re}(\lambda_e) > 0$) to non-explosive ($\text{Re}(\lambda_e) < 0$) state as shown in [52, 83, 120, 121].

The competition between the local CEM and mixing loss can be quantitatively measured by a Damköhler number defined as $Da_c = \lambda_e \cdot \chi^{-1}$ [78–80, 83]. χ is a scalar dissipation rate

defined as $\chi = 2D|\nabla c|^2$, where c and D are a progress variable and the thermal diffusivity of the local mixture, respectively. In the present study, c is evaluated using $c = Y_c/Y_c^{\text{Eq}}$, where $Y_c = Y_{\text{CO}_2} + Y_{\text{CO}}$ and Y_c^{Eq} is the corresponding equilibrium value of Y_c which is found to be 0.09 for the present DNS cases. It should be noted that $Da_c = 1$ is an important criterion for limit phenomena detection. Specifically, at a mixture exhibiting $Da_c = 1$, reaction balances mixing, which occurs usually at the ignition front or flame front; whereas $Da_c \gg 1$ indicates that reaction dominates over diffusion and mixture with $Da_c \gg 1$ will auto-ignite in the end.

The contribution of each variable and reaction to the CEM can be quantified by evaluating the explosive index (EI) of each variable and participation index (PI) of each reaction, which can identify critical chemical kinetic processes during the ignition. The **EI** and **PI** vectors are defined as [80, 83]:

$$\mathbf{EI} = \frac{|\mathbf{a}_e \otimes \mathbf{b}_e^T|}{\text{sum}(|\mathbf{b}_e \otimes \mathbf{b}_e^T|)}, \quad (5.4.2)$$

$$\mathbf{PI} = \frac{|\mathbf{b}_e \cdot \mathbf{S} \otimes \mathbf{R}|}{\text{sum}(|(\mathbf{b}_e \cdot \mathbf{S}) \otimes \mathbf{R}|)}, \quad (5.4.3)$$

where \mathbf{S} and \mathbf{R} represent the stoichiometric coefficient matrix and the vector of the net rates for reactions, respectively and the symbol \otimes represents the element-wise multiplication of two vectors. A 88-species skeletal mechanism for *n*-heptane oxidation [52] is used for CEMA to analytically evaluate \mathbf{J}_ω , \mathbf{a}_e , and \mathbf{b}_e .

Figure 5-15 shows the isocontours of HRR, temperature, *n*-heptane mass fraction, the log-scale of $\text{Re}(\lambda_e)$, and the EI values of important variables which exhibit relatively-large EI values for Case 16 at $t/\tau_{ig}^0 = 0.67$. Henceforth, the range of each color legend in figures is determined by the maximum and minimum values of each variable. Two points are to be noted from the figure. First, it is readily observed from Figs. 5-15a-d that mixture with $\text{Re}(\lambda_e) < 0$ is already ignited while the ignition of mixture with $\text{Re}(\lambda_e) > 0$ is still underway. In between the two distinct regions, there exist thin deflagrations with large HRR and $Da_c \sim O(1)$. Second, temperature, *n*-heptane, and H_2O_2 are the main variables that control the ignition in the unburnt region. More specifically, temperature and *n*-heptane are the main source of the CEM at relatively-low temperature region ($T \sim 1000$ K) while H_2O_2 becomes important for the ignition of unburnt mixture at relatively-high temperature region ($T \sim 1100$ K). This is because fuel decomposition still occurs at the relatively-low temperature region with large fuel concentration. At $T \sim 1100$ K, however, the chain-branching reaction of H_2O_2 becomes highly reactive, which subsequently results in initiating high temperature chemistry.

In addition, CO and OH are found to be the most important species in the burnt region (see Figs. 5-15h and i) in which the high-temperature chemistry remains controlling the combustion process. It is also found from 1-D profiles of important species and their EI values (not shown

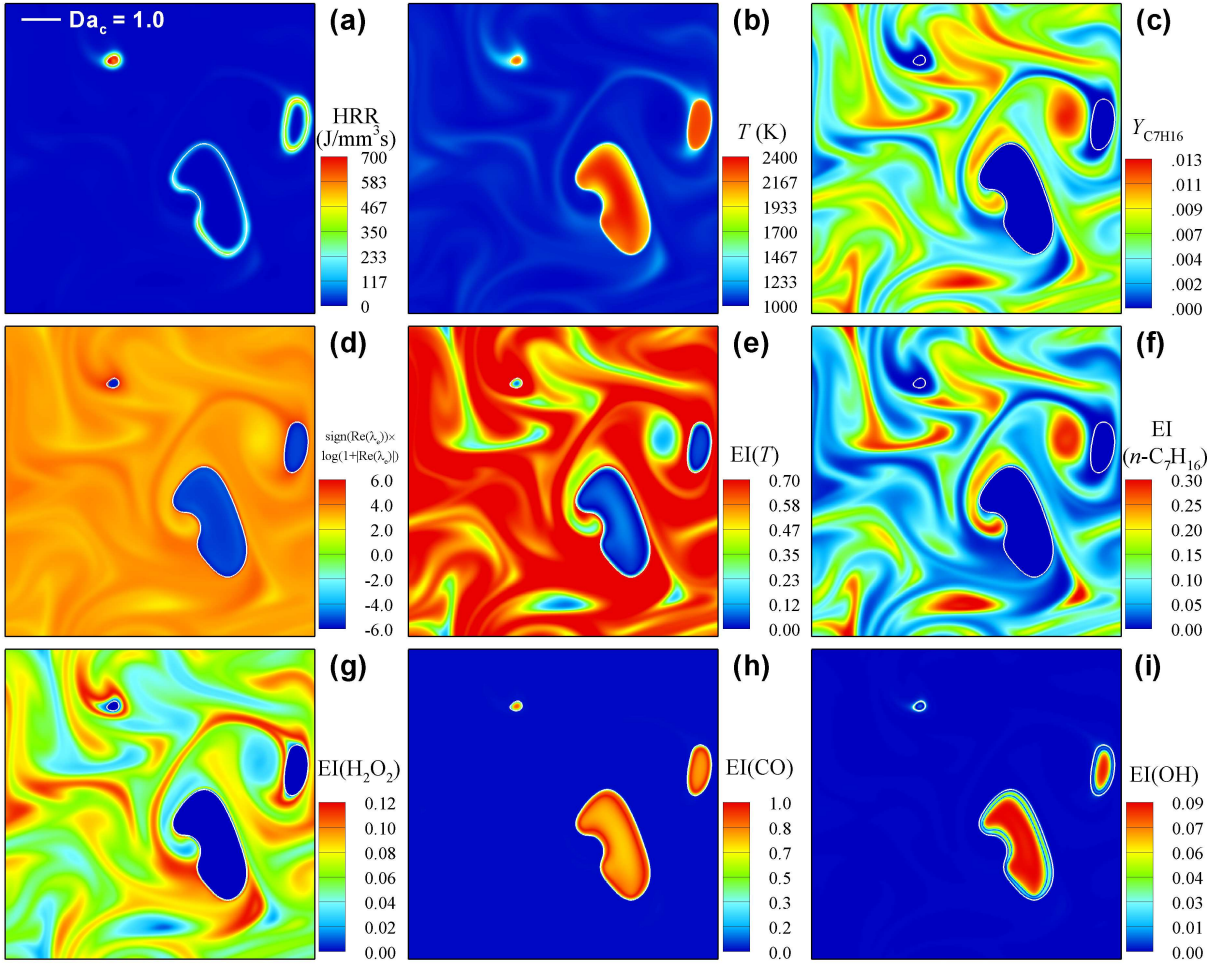


Figure 5-15: Isocontours of (a) HRR, (b) temperature, (c) $Y_{C_7H_{16}}$, (d) $\text{sign}(\text{Re}(\lambda_e)) \times \log(1 + |\text{Re}(\lambda_e)|)$, and EI of (e) temperature, (f) n -heptane, (g) H_2O_2 , (h) CO, and (i) OH for Case 16 ($T_0 = 933$ K, NC: $T' = 15$ K and $\phi' = 0.10$) at $t/\tau_{ig}^0 = 0.67$. The white solid line represents $Da_c = 1.0$.

here) that from upstream to downstream through deflagrations, EI of CO increases nearly up to unity from zero while EIs of temperature and H_2O_2 vanish rapidly, which is consistent with the characteristics of n -heptane oxidation observed in freely-propagating premixed flames and auto-ignition [83].

To further identify critical reactions involving the important species, the isocontours of PI values of important reactions with large PI values are shown in Fig. 5-16. Note that Fig. 5-16f shows the cumulative PI value of R293 \sim R300 through which fuel converts into various isomers of alkyl radicals: $RH + (OH, HO_2) \rightarrow R + (H_2O, H_2O_2)$. It is generally believed that $CO + OH \rightarrow CO_2 + H$ (R7) and $H + O_2 \rightarrow O + OH$ (R8) are two critical reactions in a hydrocarbon/air combustion process regardless of specific fuel type [129]. In the present study, both reactions are also found to be important to the CEM especially across the deflagrations. This is primarily because R7 is the main conversion path of CO to CO_2 and R8 is the most important chain-branching reaction at high temperature. In addition, HO_2 formation reaction,

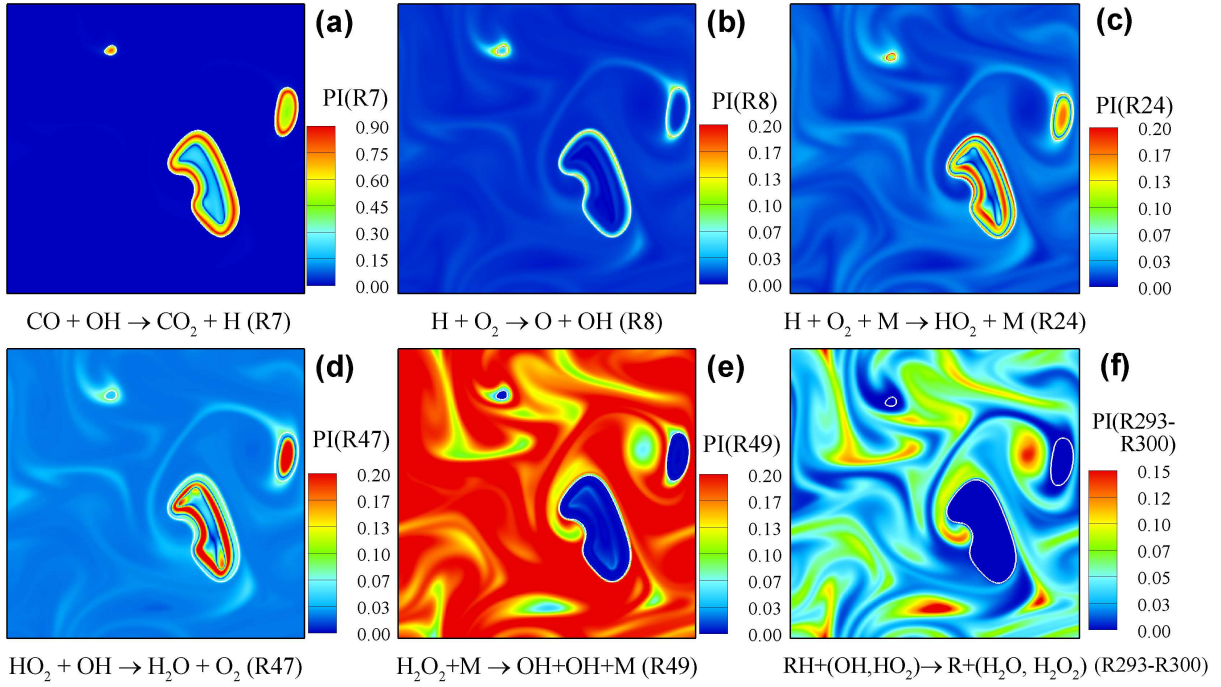


Figure 5-16: Isocontours of PIs of controlling reactions for Case 16 ($T_0 = 933$ K, NC: $T' = 15$ K and $\phi' = 0.10$) at $t/\tau_{ig}^0 = 0.67$. The white solid line represents $Da_c = 1.0$.

$H + O_2 + M \rightarrow HO_2 + M$ (R24), is also found to be important at the deflagrations because it is one of the most exothermic reactions in hydrogen/air premixed flames [129].

In the unburnt region upstream of the deflagrations (see Figs. 5-16e and f), however, it is readily observed that the chain branching of H_2O_2 (R48) and the generation of alkyl radical and H_2O_2 (R292 ~ R300) are the most important reactions to the CEM. Consistent with the EI analysis above, the conversion of fuel to alkyl radical and H_2O_2 is important for unburnt mixtures with $T \sim 1000$ K and relatively-high fuel concentration; however, the chain branching reaction of H_2O_2 becomes more important at $T \sim 1100$ K. The result implies that H_2O_2 generated from fuel decomposition reactions becomes reactive at relatively-high temperature region, subsequently inducing the thermal ignition of the unburnt mixtures as explained earlier.

The same EI and PI analyses are applied to Case 16 at $\tau_{ig} (= 0.83\tau_{ig}^0)$. Figures 5-17 and 5-18 show the isocontours of EI and PI values of the most important species and reactions. Even at the maximum HRR time, thin deflagrations with high HRR and $Da \sim O(1)$ are readily observed with similar characteristics to those of nascent deflagrations at $t = 0.67\tau_{ig}^0$ in terms of EI and PI values. Unlike the ignition characteristics at the early time, however, significant heat is released upstream of the deflagrations by the thermal ignition of unburnt mixtures, which is manifested in large EI values of temperature together with relatively-small EI values of H_2O_2 and non-zero EI values of OH. The occurrence of thermal ignition in the unburnt region is also manifested in relatively-large PI values of high-temperature chain branching re-

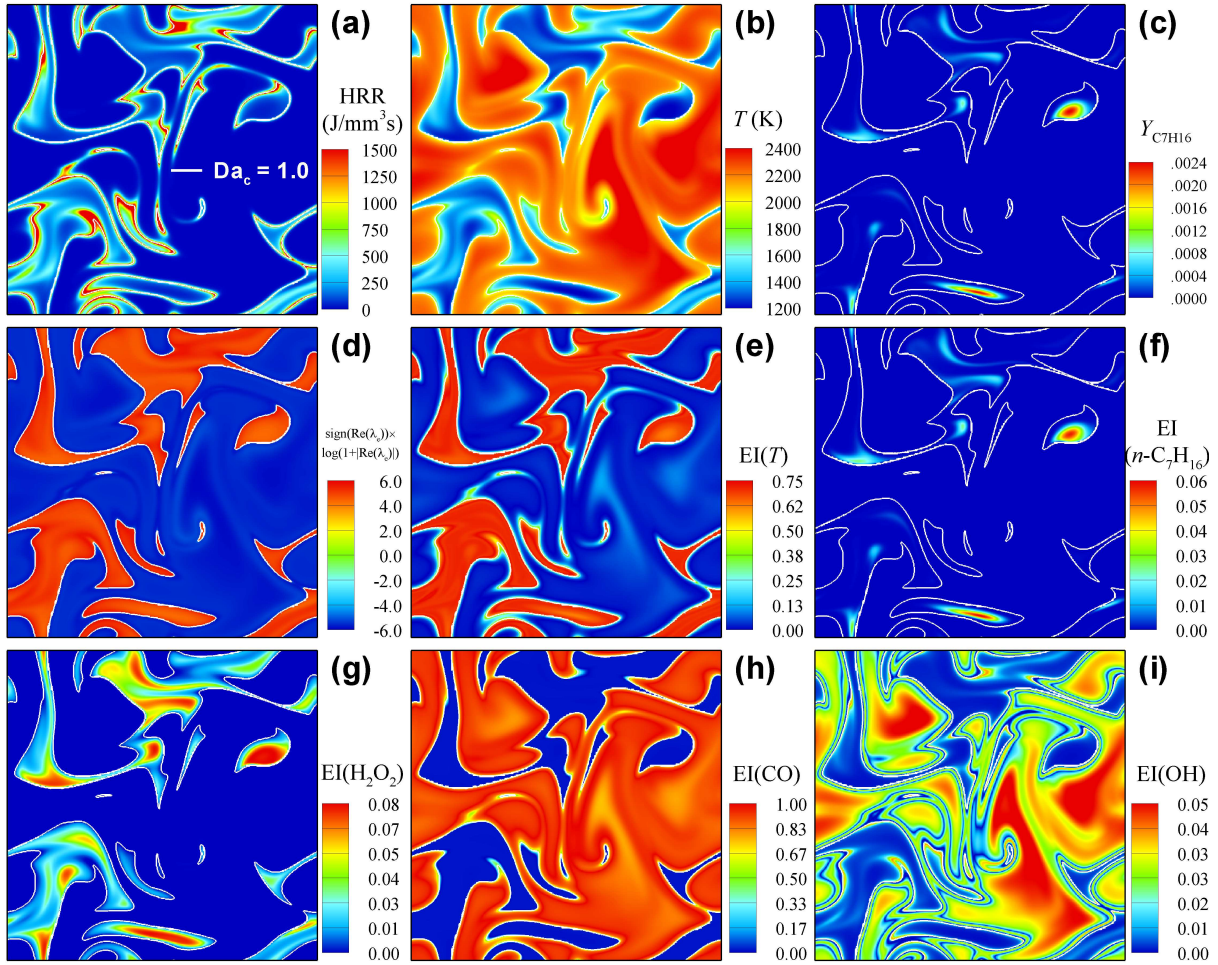


Figure 5-17: Isocontours of (a) HRR, (b) temperature, (c) $Y_{C_7H_{16}}$, (d) $\text{sign}(\text{Re}(\lambda_e)) \times \log(1 + |\text{Re}(\lambda_e)|)$, and EI of (e) temperature, (f) n -heptane, (g) H_2O_2 , (h) CO, and (i) OH for Case 16 ($T_0 = 933$ K, NC: $T' = 15$ K and $\phi' = 0.10$) at $t/\tau_{ig}^0 = 0.83$. The white solid line represents $Da_c = 1.0$.

action (R8) and HO_2 formation/consumption reactions (R24 and R47). Since temperature of the unburnt mixtures is in $1200 \sim 1600$ K range, the high-temperature chemistry dominates the intermediate-temperature chemistry; the high-temperature chain-branching reaction (R8) becomes more important to the CEM than H_2O_2 decomposition reaction (R49). It is also of interest to note that since n -heptane is already decomposed into smaller radicals, it is in low concentration and has little effect on the CEM based on EI and PI values (see Figs. 5-17c & f, and 5-18f).

5.5 Discussion

In the present study, the effects of turbulence and compression heating on the ignition characteristics of HCCI/SCCI combustion are not investigated not only because it requires too

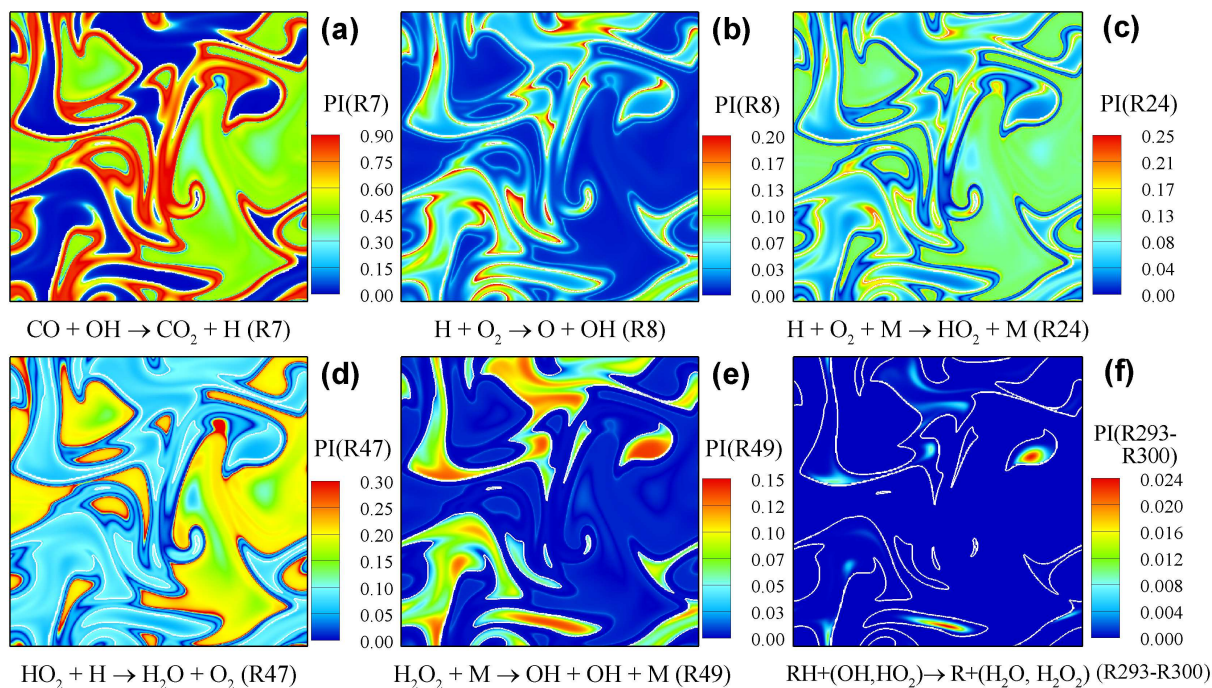


Figure 5-18: Isocontours of PIs of controlling reactions for Case 16 ($T_0 = 933$ K, NC: $T' = 15$ K and $\phi' = 0.10$) at $t/\tau_{ig}^0 = 0.83$. The white solid line represents $Da_c = 1.0$.

many parametric DNS cases but also because their effects may be expected from previous DNS studies [49, 50, 52, 53, 90, 118, 120, 121, 124].

In general, the overall HCCI combustion with large u' and short τ_t proceeds more similarly to the corresponding 0-D ignition because turbulence with large u' and short τ_t is more apt to homogenize the initial mixture as found in [49, 50, 52, 90, 121]. In the spark-assisted compression ignition (SACI) combustion [53, 124] and HCCI combustion with very large T' [120], however, turbulence with large u' and short τ_t can advance the overall combustion. In both cases, the shortest ignition delay of the initial mixture is much smaller than turbulent mixing timescale such that the evolution of nascent ignition kernels to deflagrations is not affected by the turbulence.

In our previous study [120], the ratio of the shortest ignition delay represented by the lowest 10% ignition delay of initial mixture to turbulent mixing timescale is defined as the ignition Damköhler number, $Da_{ig} \equiv \tau_t/\tau_{ig,10\%}$, such that it exhibits $O(10)$ values in the SACI and HCCI combustion with very large T' . In such cases, once the deflagration waves develop successfully from the ignition kernels, turbulence with large u' tends to enhance turbulent burning rate by increasing turbulent flame area because most HCCI/SACI combustion occur within the corrugated flamelet and thin reaction regimes of the premixed turbulent combustion regime diagram [130, 131].

This general description of the effects of turbulent mixing and deflagration on the HCCI combustion can directly be applied to the SCCI combustion. As mentioned earlier, large T' in

the HCCI combustion cannot be easily achieved without expensive fuel charge heating and as such, the shorter ignition delay and larger Da_{ig} of initial mixture can be achieved by adopting the fuel stratification in the SCCI combustion. As shown in Fig. 5-3, the initial ignition delays can be more distributed by the fuel stratification than by the temperature stratification in the intermediate T_0 within the NTC regime. Therefore, turbulent mixing may enhance the overall SCCI combustion if Da_{ig} of the initial mixture is large enough. However, in the SCCI combustion, large ϕ' cannot be expected because local large ϕ can produce more NOx emission and as such, the distribution of local ϕ needs to be strictly below unity as demonstrated in previous experimental studies [54, 125]. From this point of view, it may be conjectured that high turbulent mixing generally retards the overall SCCI combustion by homogenizing the initial mixture stratification.

To overcome the disadvantage of the SCCI combustion in developing deflagration waves by reducing the shortest τ_{ig}^0 , the concept of reactivity-controlled compression ignition (RCCI) combustion has been devised, in which small τ_{ig}^0 can be achieved by utilizing two different types of fuels: one is highly-reactivity fuel such as diesel and the other is low-reactivity fuel such as gasoline. The effect of turbulent mixing and deflagration on the RCCI combustion is an ongoing research topic.

It is also of importance to mention that the combustion phase relative to the TDC can alter the overall HCCI combustion as found in [118, 124]. Based on the results in [118, 124], it can be conjectured that if the combustion occurs near/prior to the TDC, the overall HCCI combustion in the present DNSs can be advanced in time by the compression heating during the compression stroke, featuring in higher peak PRR and shorter burning duration. In experiments, however, the HCCI combustion is designed to occur after the TDC to avoid such excessive PRR under high load conditions. In this situation, the overall HCCI combustion with low T' and/or ϕ' can be further retarded by the expansion effect during the power stroke, resulting in much lower peak PRR and longer burning duration. This expansion effect on the HCCI combustion can be more enhanced by the negatively-correlated $T - \phi$ fields in the low temperature regime. On the contrary, large T' and/or ϕ' can still advance the overall HCCI combustion with higher peak PRR and shorter burning duration even if the combustion occurs after the TDC. This is because large T' and/or ϕ' can render the overall combustion to occur right after the TDC. These conjectures, however, need to be verified by another set of DNSs.

From the present study, it can be concluded that considering the initial mean temperature and the degree of NTC behavior of given fuel/air mixture, the degree of thermal and compositional stratifications and their correlations need to be carefully chosen to prevent the excessive PRR and determine the ignition timing of HCCI combustion. Furthermore, the present DNS data sets can be utilized to develop and validate several turbulent combustion models

for HCCI/SCCI combustion including flamelet-based models [132], probability density function (PDF)-based models [133], and conditional moment closure (CMC)-based model [134, 135] because these models have been reported not to reproduce correctly the results of DNSs of HCCI/SCCI combustion with large T' and/or ϕ' [132–135].

5.6 Conclusions

The ignition characteristics of thermally- and/or compositionally-stratified lean n -heptane/air mixture under HCCI conditions were investigated by performing 2-D DNSs with a 58-species reduced mechanism. From the parametric study, the effects of T' , ϕ' , and their spatial correlations on the ignition of n -heptane/air mixture were elucidated at three different T_0 of 805, 933, and 1025 K. It was found from the 2-D DNSs:

1. For the BL cases with ϕ' only, the overall combustion occurs more quickly and the mean HRR increases more slowly with increasing ϕ' regardless of T_0 .
2. For the BL cases with T' only, the overall combustion is retarded/advanced in time with increasing T' for low/high T_0 relative to the NTC regime resulting from a longer/shorter overall ignition delay of the mixture; for intermediate T_0 within the NTC regime, however, the overall combustion is slightly retarded with small T' , while being advanced with large T' , exhibiting the combined effects of both low and high T_0 near the NTC regime.
3. For the NC cases, the negative $T - \phi$ correlation has an adverse effect on the overall combustion at low and high T_0 : the peak \bar{q} is significantly increased while the duration of the main combustion is reduced compared to their corresponding BL cases.
4. For intermediate T_0 within the NTC regime, however, the negatively-correlated $T - \phi$ fields has a synergistic effect on the overall combustion by spreading out \bar{q} over time and reducing the peak \bar{q} .
5. For the UC cases, the mean HRR is more distributed over time and the overall combustion is more advanced in time compared to the corresponding BL cases with T' or ϕ' only except for cases with low T_0 .
6. For cases with low T_0 , however, the overall combustion is more retarded in time while the mean HRR is more distributed over time compared to the corresponding BL cases with ϕ' only.

These results are primarily attributed to the characteristics of the 0-D ignition delays of initial mixtures such as the shortest τ_{ig}^0 and the span of τ_{ig}^0 , which are determined by T' , ϕ' , and their

correlation at different T_0 . These results suggest that an appropriate combination of T' and ϕ' together with a well-prepared $T - \phi$ distribution can provide a smooth ignition process and control ignition-timing in HCCI/SCCI combustion.

Chemical explosive mode analysis together with the characteristics of temporal evolution of species identifies important species and reactions for the ignition of n -heptane/air mixture at different locations and time. In regions where the spontaneous ignition mode of combustion is predominant, temperature, H_2O_2 , and n -heptane are identified as the key species for the CEM prior to thermal ignition while the chain branching reaction of H_2O_2 and the conversion reaction of n -heptane to alkyl radical and H_2O_2 are the main reactions of the intermediate-temperature chemistry. During thermal ignition, however, temperature is found to be the predominant variable and high-temperature reactions represented by $\text{H} + \text{O}_2 \rightarrow \text{O} + \text{OH}$ are responsible for the thermal ignition. At deflagrations, temperature, CO, and OH are found to be the most important variables while the conversion reaction of CO to CO_2 and high-temperature chain branching reaction of $\text{H} + \text{O}_2 \rightarrow \text{O} + \text{OH}$ are identified to be important to the CEM.

Chapter 6

Ignition of a lean PRF/air mixture under RCCI/SCCI conditions: A comparative DNS study

6.1 Introduction

Despite the promising advantages of HCCI, the development of prototype HCCI engines has not been successful due to difficulties in controlling pressure rise rate (PRR) and ignition timing under high-load conditions. Therefore, several variants of HCCI engines have been proposed to enhance the ignition timing control and to extend the engine operation range. Especially, reactivity-controlled compression ignition (RCCI) and stratified-charge compression ignition (SCCI) engines have been paid considerable attention by the engine community due to their better controlling of combustion-phasing/PRR, and lower fuel consumption/pollutant emissions than the conventional HCCI engines [20, 22–24].

Numerous experimental and computational studies of RCCI and/or SCCI combustion have been conducted [?, ?, 1, 4, 7, 22, 26, 27, 47, 51, 54, 79, 90–105, 121–125, 136–142]. Especially, Kokjohn et al. numerically investigated the combustion characteristics of diesel low temperature combustion (LTC), ethanol-diesel RCCI, and E85-diesel RCCI combustion. It was found that E85-diesel RCCI combustion exhibited a staged consumption of high reactive diesel and low reactive E85, and E85 is not consumed until gradual transition of diesel consumption to the second-stage ignition [27]. Kokjohn et al. also found that under RCCI conditions with either too early or too late injections of *n*-heptane, fuel/air mixture ignites nearly volumetrically due to similar ignition delays of the mixture, resulting in rapid energy release and excessive PRR [138].

Recently, it was also found from an experiment and numerical study of RCCI combustion [125] that the PRF number stratification (i.e., the reactivity stratification) plays a predominant role in controlling the overall combustion process compared to equivalence ratio stratification, while the effect of temperature stratification is negligible because the initial mean temperature, T_0 , lies within the negative temperature coefficient (NTC) regime. However, the predominant role of reactivity stratification may not remain the same when T_0 lies in low- and high-temperature regimes, and hence, the effect of T_0 relative to the NTC regime on the RCCI combustion is still needed. Furthermore, the fundamental understanding of RCCI combustion is still limited by the capability of RANS-based simulations.

From a series of 2-D direct numerical simulation (DNS) studies of HCCI combustion [7, 52, 53, 90, 120, 121, 124], it was found that the ignition characteristics of two-stage ignition fuels relevant to HCCI and SCCI combustion can be significantly changed with (1) different T_0 , and (2) different levels of temperature and equivalence ratio fluctuations (T' and/or ϕ'). It was also found that (1) ϕ' becomes dominant over T' in reducing the peak of heat release rate (HRR) when T_0 lies near/within the NTC regime and, (2) T_0 in the NTC regime together with a negative T - ϕ distribution has a synergistic effect on advancing the overall combustion and smoothing out PRR and HRR under high-load SCCI combustion. It is believed that T_0 in the NTC regime also has a positive effect on enhancing the overall RCCI combustion process.

More recently, Bhagatwala et al. [142] investigated the combustion modes under RCCI conditions using DNSs with a compression heating model. They found that higher *n*-heptane concentration provides a greater degree of flame propagation; the combustion occurs in a large fraction of deflagration mode at low-to-medium pressures; the fraction of deflagration, however, is reduced with increasing pressure. It was also found from several 2-D DNS studies [52, 53, 90, 120, 121] that high turbulent mixing generally retards the overall HCCI and SCCI combustion by homogenizing the initial stratified mixture except for some HCCI combustion with very large fluctuations, resulting in high peak HRR due to dominant spontaneous ignition mode. The understanding of the effect of turbulent mixing and deflagration on the RCCI combustion, however, is still limited.

Therefore, the objective of this chapter is to compare the ignition characteristics of primary reference fuel (PRF)/air mixtures under RCCI and SCCI conditions using 2-D DNSs by varying three key parameters: (1) initial mean temperature, (2) level of fuel stratification, and (3) turbulent time scale such that the relative roles of reactivity, equivalence ratio, and temperature stratification under various conditions can be examined.

6.2 Initial conditions

The initial mean pressure, $p_0 = 40$ atm, and mean equivalence ratio, $\phi_0 = 0.45$, are specified for all DNSs. For comparison purpose, PRF50 is adopted as the mean fuel for RCCI and a single fuel for SCCI. Note that PRF50 is a mixture of 50% *iso*-octane and 50% *n*-heptane by volume. In real dual-fuel RCCI engines, low reactivity fuel/air mixture (e.g., gasoline/air) is first supplied to an engine cylinder through port-fuel injection (PFI) and then, high reactivity fuel (e.g., diesel) is direct-injected. Therefore, the low reactivity fuel/air charge is homogeneously distributed throughout the engine cylinder, while the high reactivity fuel generates inhomogeneities in the reactivity, equivalence ratio, and temperature of the homogeneous mixture. To reproduce similar stratifications in the mixture in the present DNSs, *n*-heptane field for RCCI cases is initialized by $m = \bar{m} + m'$, superimposed onto a uniform *iso*-octane/air field, where m is the mass of *n*-heptane, and ‘overbar’ and ‘prime’ represent the mean and fluctuation, respectively. For SCCI cases, PRF50 is assumed to be supplied through the same two-stage injection and as such, m represents the mass of PRF50.

To account for the evaporative cooling of directly-injected fuel, temperature is assumed to be negatively correlated with *n*-heptane mass fraction. Therefore, local variations in PRF number, equivalence ratio, and temperature are connected to each other. For SCCI cases, however, a single fuel (PRF50) is used, and hence, only variations in equivalence ratio and temperature are negatively-correlated. For both RCCI and SCCI cases, the degree of fuel stratification, r , is

defined as $r = m'/\bar{m}$. Two sets of $(r, T') = (0.22, 15 \text{ K})$ and $(0.44, 30 \text{ K})$ are selected such that the corresponding equivalence ratio fluctuations are given by $\phi' = 0.05$ and 0.10 as in [7, 121]. The corresponding PRF fluctuations for RCCI cases are $\text{PRF}' = 5.8$ and 12.8 , respectively. For $\phi' = 0.05$ and 0.10 with $\phi_0 = 0.45$, local equivalence ratio exists within the range of 0.2 – 0.8 . Note that the means and fluctuations of T and ϕ are carefully chosen to match those from experiments; for instance, T' was measured as 13.3 K in an HCCI engine [46] and the range of ϕ was found as about 0.1 – 0.8 in an RCCI engine [125]. As such, the distribution of T and ϕ lies in the optimal range for RCCI/SCCI combustion to maintain low-temperature combustion with ultra-low emissions [17, 125, 138].

In the first parametric study, twelve 2-D DNSs (Cases 1–12 in Table 6-1) were performed by varying two key parameters: (1) T_0 of 800, 900, and 1000 K, and (2) r of 0.22 and 0.44. Three different T_0 of 800, 900, and 1000 K represent low-, intermediate-, and high-temperature regimes of PRF50, respectively, under the initial conditions of $p_0 = 40 \text{ atm}$ and $\phi_0 = 0.45$. The corresponding 0-D ignition delays, τ_{ig}^0 , of PRF50 for T_0 of 800, 900, and 1000 K are approximately 2.3, 2.2 and 1.25 ms, respectively. Henceforth, τ_{ig} represents the time when the maximum mean HRR occurs for both 0-D and 2-D simulations and the superscript 0 denotes 0-D simulation.

Case	Type	T_0 (K)	r	T' (K)	PRF'	ϕ'	l_e (mm)	u' (m/s)	τ_t (ms)	τ_{ig}^0 (ms)
1	RCCI	800	0.22	15	5.8	0.05	1.0	0.5	2.00	2.30
2	RCCI	800	0.44	30	12.8	0.10	1.0	0.5	2.00	2.30
3	SCCI	800	0.22	15	-	0.05	1.0	0.5	2.00	2.30
4	SCCI	800	0.44	30	-	0.10	1.0	0.5	2.00	2.30
5	RCCI	900	0.22	15	5.8	0.05	1.0	0.5	2.00	2.20
6	RCCI	900	0.44	30	12.8	0.10	1.0	0.5	2.00	2.20
7	SCCI	900	0.22	15	-	0.05	1.0	0.5	2.00	2.20
8	SCCI	900	0.44	30	-	0.10	1.0	0.5	2.00	2.20
9	RCCI	1000	0.22	15	5.8	0.05	1.0	0.8	1.25	1.25
10	RCCI	1000	0.44	30	12.8	0.10	1.0	0.8	1.25	1.25
11	SCCI	1000	0.22	15	-	0.05	1.0	0.8	1.25	1.25
12	SCCI	1000	0.44	30	-	0.10	1.0	0.8	1.25	1.25
13	RCCI	900	0.44	30	12.8	0.10	1.0	1.0	1.00	2.20
14	RCCI	900	0.44	30	12.8	0.10	1.0	2.5	0.40	2.20
15	SCCI	900	0.44	30	-	0.10	1.0	2.5	0.40	2.20

Table 6-1: Physical parameters of the DNS cases.

As in [7, 52, 53, 90, 120, 121], the initial turbulent flow field is generated using an isotropic kinetic energy spectrum function by Passot-Pouquet [37]. The most energetic length scale, l_e , of 1.0 mm is specified for all DNSs. In real HCCI engines, the turbulence time scale, τ_t , is comparable to τ_{ig}^0 . Based on τ_{ig}^0 , therefore, two different turbulence intensities, u' of 0.5 and 0.8 m/s, are selected to match τ_t with τ_{ig}^0 . Concentration and temperature fields are also generated from the same energy spectrum as turbulence with different random numbers. For the concentration and temperature fields, the same characteristic length scale as l_e is used.

The identical characteristic length scales and comparable time scales for turbulence and scalar fields are elaborately chosen such that most effective turbulent mixing of initial mixtures can be expected in the present study [50, 53]. The representative isocontours of initial fields of PRF, ϕ , and T are shown in Fig. 6-1, and the corresponding PRF– T and ϕ – T relations are shown in Fig. 6-2 for Cases 6 (RCCI) and 8 (SCCI).

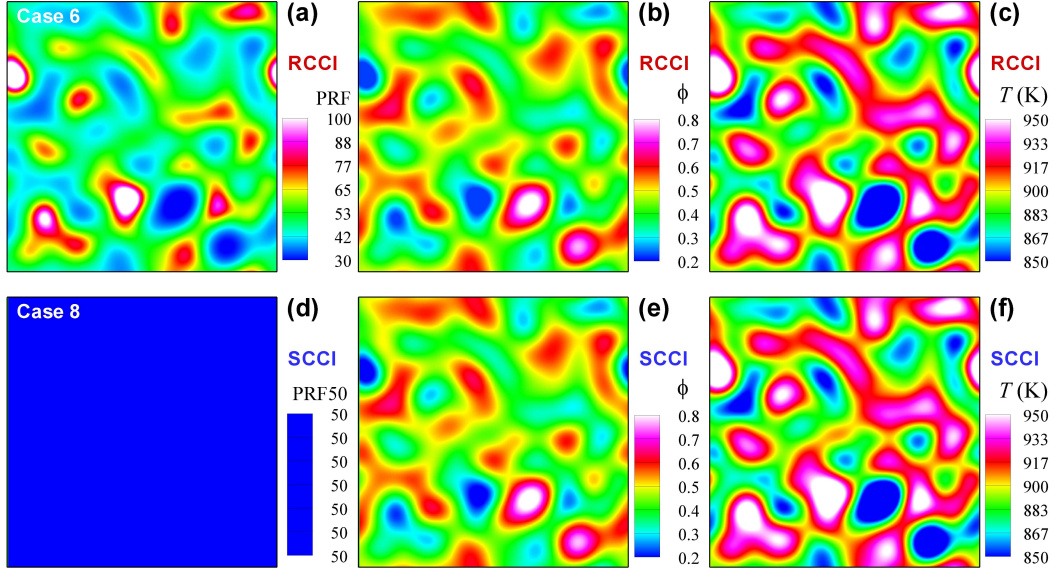


Figure 6-1: Initial PRF, ϕ , and T fields for Cases 6 (top row) and 8 (bottom row).

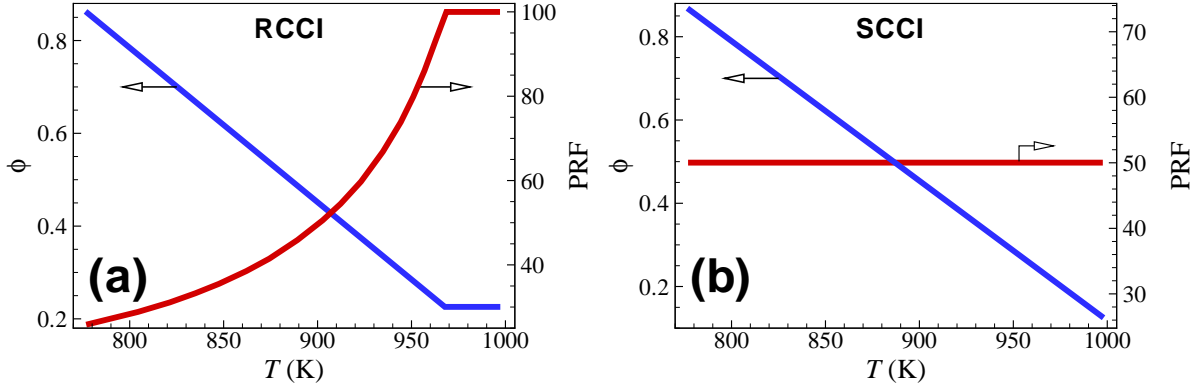


Figure 6-2: Initial T –PRF and T – ϕ relations for (a) Cases 6 (RCCI) and (b) 8 (SCCI).

In the second parametric study, three additional DNSs (Cases 13–15) are performed by varying u' at the intermediate T_0 of 900 K to investigate the effect of turbulence on the overall ignition characteristics of a lean PRF/air mixture under RCCI and SCCI conditions.

A square-box of $3.2 \times 3.2 \text{ mm}^2$ was used as a computational domain for all the DNSs. The domain is discretized with 1280 grid points in each direction, and the corresponding grid resolution is $2.5 \mu\text{m}$. Such a fine grid resolution is required to resolve thin fronts generated from ignition of local mixtures with high reactivity and/or equivalence ratio with short ignition

delay. The 2-D DNSs were performed on the IBM BlueGene/P at King Abdullah University of Science and Technology (KAUST) and each DNS required approximately 4M CPU hours. Note that a 3-D DNS of RCCI/SCCI combustion would require more than 4G CPU hours such that a 3-D DNS of HCCI typed combustion is still not affordable even with state-of-the-art high performance computing (HPC) machines.

6.3 Results and discussion

6.3.1 Effects of PRF', ϕ' , and T' at different regimes

In this section, the ignition characteristics of a PRF/air mixture under RCCI and SCCI conditions are investigated at different T_0 of 800, 900, and 1000 K, which lie within the low-, intermediate-, and high-temperature regimes, respectively. Figure 6-3 shows the temporal evolution of the mean HRR, \bar{q} , for Cases 1–12. Several points are to be noted. First, for T_0 (= 800 and 900 K) in the low- and intermediate-temperature regimes, the overall combustion of an RCCI case occurs much earlier than that of the corresponding SCCI case with the same T' and r ; for both RCCI and SCCI cases, \bar{q} is more distributed over time and its peak is more decreased with increasing T' and r . However, for T_0 (= 1000 K) in the high-temperature regime, the overall combustion of an RCCI case is relatively identical to that of the corresponding SCCI case; for both RCCI and SCCI cases, the peak \bar{q} is slightly decreased with increasing T' and r .

The effects of PRF', ϕ' , and T' on RCCI/SCCI combustion at different T_0 can be estimated by examining the 0-D ignition delays of PRF/air mixtures. Figure 6-4 shows the τ_{ig}^0 of different PRF numbers and ϕ as a function of initial temperature. It is readily observed from the figure that for T in the low-to-intermediate temperatures ($T < 950$ K), τ_{ig}^0 is more sensitive to PRF number variation than variation of ϕ and T . For T in the high-temperature regime ($T > 1000$ K), however, τ_{ig}^0 is relatively less sensitive to the variation of PRF number and ϕ , but becomes highly sensitive to that of T .

This trend of τ_{ig}^0 implies that in the low-to-intermediate temperature regime, a small variation in PRF number can induce a greater disparity in τ_{ig}^0 of mixtures than ϕ' and T' , and as such, some local mixtures can ignite earlier than the others, which may enhance the deflagration mode of combustion rather than the spontaneous ignition mode. Consequently, a sequential combustion can occur in the mixture, leading to the temporal distribution of HRR as in Cases 2 and 6.

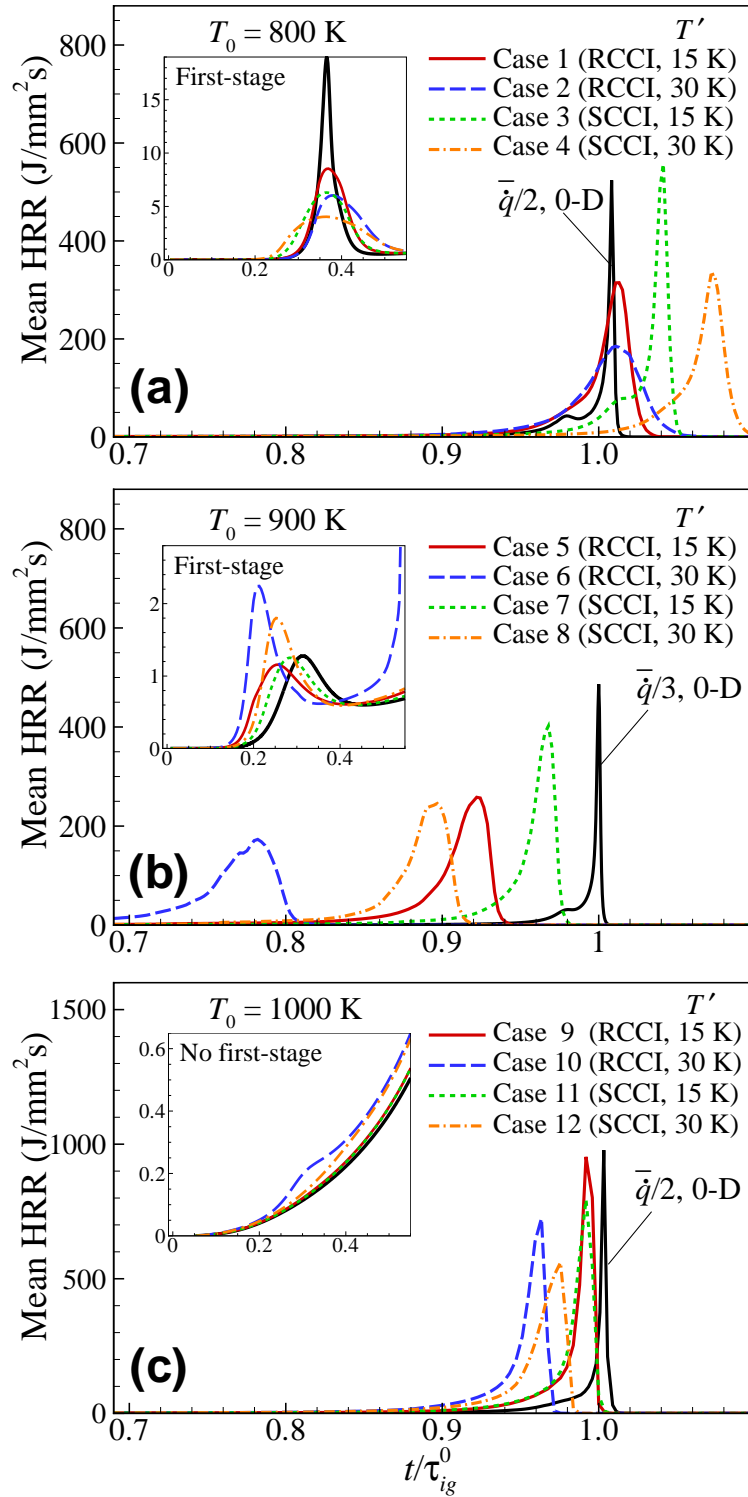


Figure 6-3: Temporal evolution of the mean HRR for (a) Cases 1–4, (b) 5–8, and (c) 9–12. The first-stage ignitions are also shown in the small boxes.

In the high temperature regime, however, T' can take over the role of PRF' in the intermediate temperature regime due to the high sensitivity of τ_{ig}^0 to T' . However, only small disparity in τ_{ig}^0 of the mixture can be achieved by T' because the negative $T-r$ correlation has an adverse effect on the reduction of peak HRR. Therefore, the overall RCCI/SCCI combustion in the

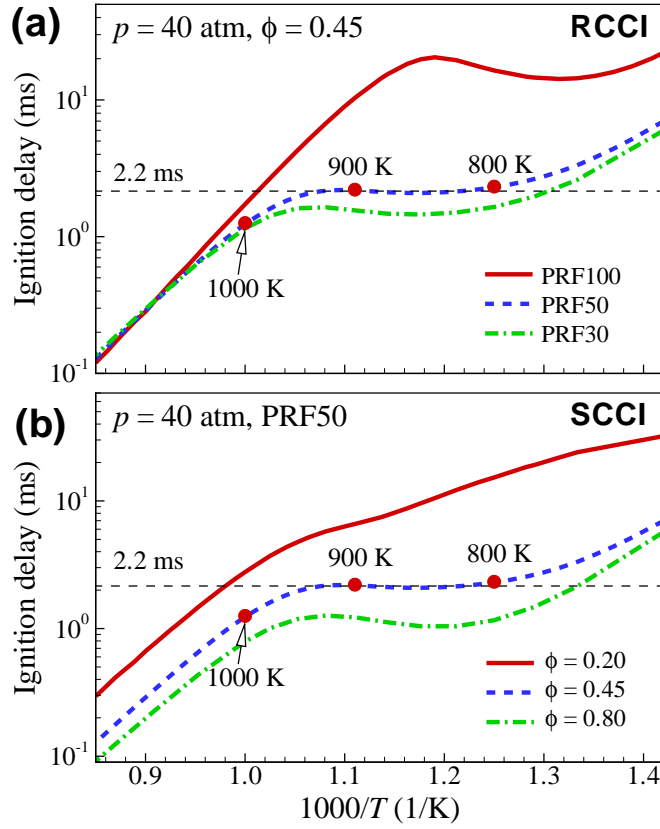


Figure 6-4: 0-D ignition delays of PRF/air mixtures at $p_0 = 40$ atm as a function of T_0 for different (a) PRF and (b) ϕ .

high-temperature regime is more likely to occur similarly to the corresponding 0-D ignition. Moreover, in our previous DNS study [7], it was found that in the high-temperature regime, T' only is more effective than negatively-correlated T' and ϕ' in reducing the peak HRR and advancing the overall combustion.

Based on the foregoing discussion and the present DNS results, it can be conjectured that for T_0 in the low- and intermediate-temperature regimes, PRF' plays a dominant role in reducing the peak \bar{q} , and ϕ' has relatively small but still significant effect on it; for T_0 in the high temperature regime, the effect of PRF' nearly vanishes and ϕ' still plays a moderate role in reducing the peak HRR, while T' has a significant effect on reducing the peak \bar{q} .

6.3.2 Combustion mode analysis

It is also readily observed from Fig. 6-3 that τ_{ig} is retarded compared to its corresponding τ_{ig}^0 for cases with $T_0 = 800$ K because most of ignition delays in the initial mixture are greater than τ_{ig}^0 , resulting in longer τ_{ig} . However, for cases with $T_0 = 900$ and 1000 K, quite a lot of ignition delays in the initial mixtures are shorter than τ_{ig}^0 such that deflagrations can develop during the early phase of combustion and the overall combustion occurs earlier than the corresponding

τ_{ig}^0 [7, 52]. Moreover, for T_0 in the low-temperature regime, τ_{ig} of RCCI cases remains the same with increasing T' and r , featuring $\tau_{ig} \approx \tau_{ig}^0$. For T_0 in the intermediate- and high-temperature regimes, however, τ_{ig} is decreased with increasing T' and r . For SCCI cases, τ_{ig} shows a non-monotonic behavior with increasing r . More specifically, τ_{ig} is increased at low T_0 , but decreased at the intermediate- and high-temperature regimes with increasing T' and r , similar to previous studies [7, 52].

These ignition characteristics of RCCI/SCCI combustion are usually related to the combustion mode (i.e., deflagration vs. spontaneous ignition) after the early phase of ignition [7, 52, 53, 120] and can be elucidated by examining instantaneous HRR fields and the probability density function (PDF) of τ_{ig}^0 and its spatial gradient, $|\nabla\tau_{ig}^0|$, of the initial mixtures. Figure 6-5 shows the instantaneous isocontours of HRR at the times of 15%, 40%, and 95% cumulative \bar{q} and the maximum \bar{q} for both RCCI and SCCI cases with $r = 0.44$. The local HRR, \dot{q} , is normalized by the maximum HRR of the corresponding 0-D ignition, $\dot{q}_m^0 = 1048, 1460,$ and $1956 \text{ J/mm}^3\text{s}$ for $T_0 = 800, 900,$ and 1000 K , respectively. Figure 6-6 shows the PDF of τ_{ig}^0 and $|\nabla\tau_{ig}^0|$ of initial mixtures for Cases 1–12. Several points are to be noted from the figures.

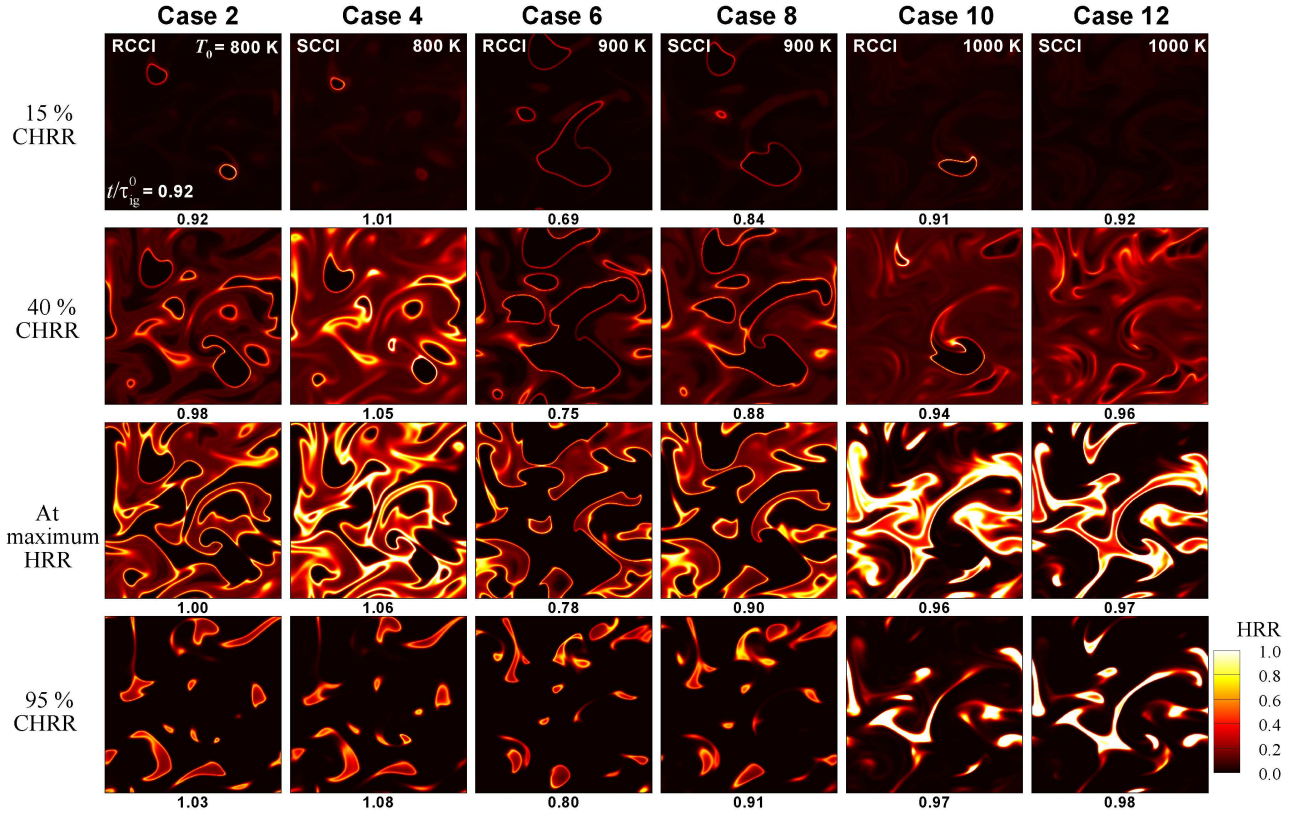


Figure 6-5: Isocontours of normalized HRR for Cases 2, 4, 6, 8, 10, and 12 (from left to right) at times of 15% (first row), 40% (second row), and 95% (last row) cumulative mean HRR and at the maximum HRR (third row).

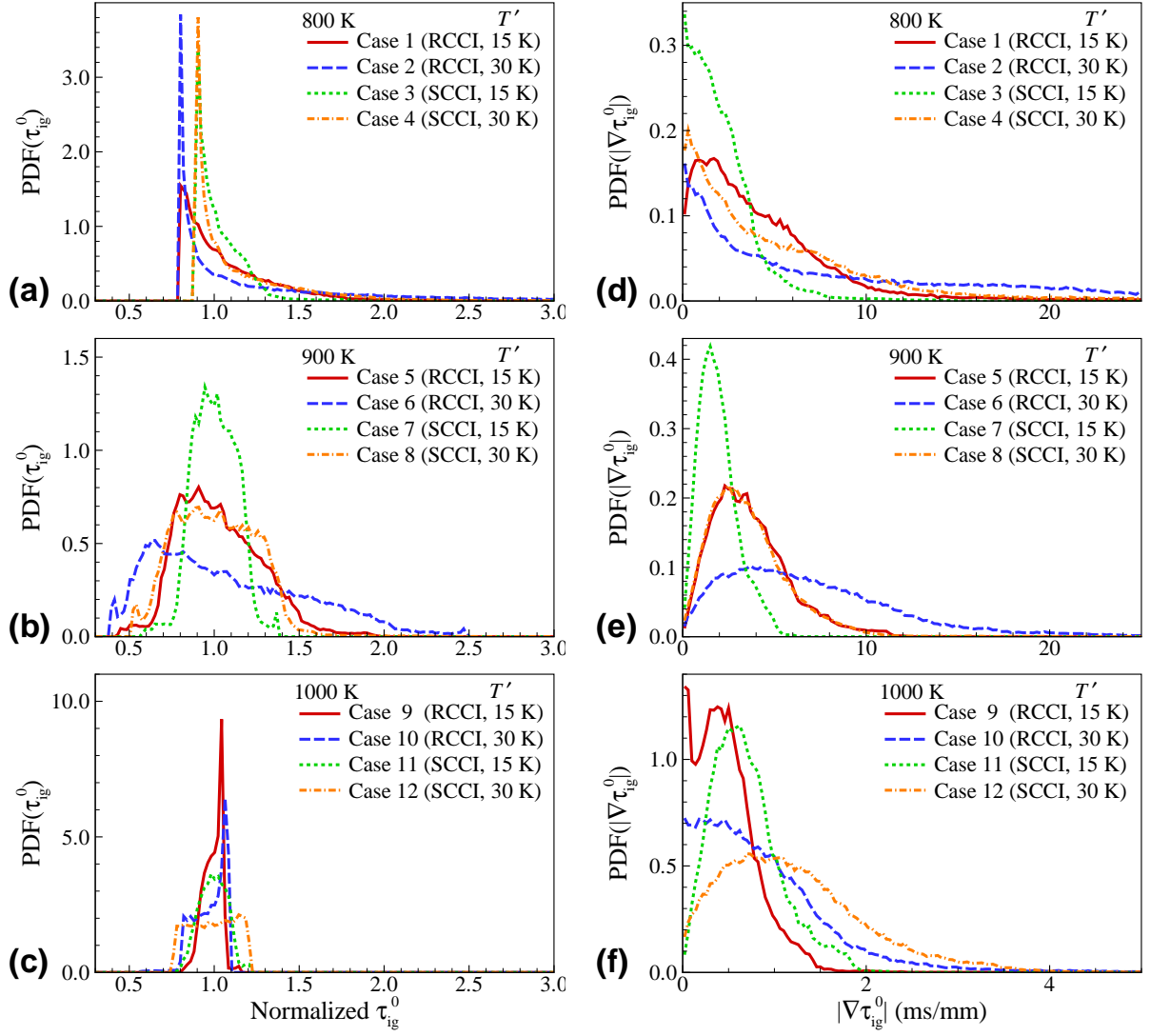


Figure 6-6: Probability density function of 0-D ignition delay (left column) and its spatial gradient (right column) of initial mixtures for Cases 1–12.

First, it is readily observed from the first row of Fig. 6-5 that thin deflagration waves develop earlier in the RCCI cases (Cases 2, 5, and 10) than in the corresponding SCCI cases (Cases 4, 8, and 12) regardless of T_0 . This is because the PDF of τ_{ig}^0 of the RCCI cases usually exhibits larger values at small τ_{ig}^0 than that of SCCI cases (see Figs. 6-6a–c), and as such, the development of deflagration waves from nascent ignition kernels can occur faster in RCCI cases.

Second, for T_0 in the low- and intermediate-temperature regimes, the overall combustion of the RCCI cases is more apt to occur by the deflagration mode than that of the SCCI cases during the early phase of combustion. As shown in Fig. 6-5, the combustion of the RCCI cases (Cases 2 and 6) occurs primarily in thin reaction sheets with relatively lower \bar{q} . Moreover, a widely-distributed PDF of $|\nabla\tau_{ig}^0|$ in the RCCI cases may indicate high probability of deflagration mode of combustion (see Figs. 6-6d and e), based on the identification of spontaneous propagation and premixed deflagration by Zel’dovich [143],

The deflagration mode of combustion can be quantitatively measured by the Damköhler number analysis in which Da is defined as [49, 50, 52, 53, 90, 121]:

$$Da = \frac{\dot{\omega}_k}{|-\nabla \cdot (\rho Y_k \mathbf{V}_k)|}, \quad (6.3.1)$$

where Y_k , \mathbf{V}_k , and $\dot{\omega}_k$ denote the mass fraction, diffusion velocity, and net production rate of species k , respectively. $Y_c \equiv Y_{\text{CO}_2} + Y_{\text{CO}}$ is used for the Damköhler number analysis. As in previous studies [7, 52, 121], local combustion is determined to occur by the deflagration mode when its Da is less than 4.5. A specific value of $Da = 4.5$ is determined through a series of 1-D laminar simulations at various PRF number and ϕ_0 . The Da analysis demonstrates that RCCI combustion occurs by the deflagration mode more than the corresponding SCCI combustion in the low-to-intermediate temperature regime. As shown in Fig. 6-7, for instance, the fraction of HRR from deflagration mode for an RCCI case (Case 6) covers more than 60% during the early phase of combustion and the total HRR from deflagration mode is approximately 28%. For the corresponding SCCI case (Case 8), however, the total HRR from deflagration mode is only 13%.

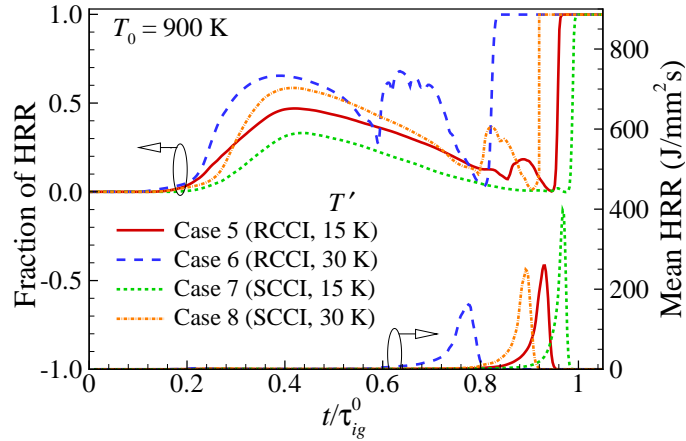


Figure 6-7: Temporal evolution of the fraction of the heat release rate from the deflagration mode and the mean HRR for Cases 5–8.

Third, for T_0 in the high-temperature regime, the spontaneous ignition mode is predominant over the deflagration mode for both RCCI and SCCI combustion. This is because the combustion occurs primarily in broader reaction area with high \bar{q} (see Cases 10 and 12 in Fig. 6-5), and the span of $|\nabla\tau_{ig}^0|$ is very narrow compared to those in the low-to-intermediate regime (see Fig. 6-6d–f).

Fourth, the overall RCCI/SCCI combustion occurs more by the deflagration mode with increasing r and T' regardless of T_0 although the fraction of deflagration mode of combustion is marginal in the high-temperature regime. The span of $|\nabla\tau_{ig}^0|$ is wider and the PDF of $|\nabla\tau_{ig}^0|$ is more distributed with increasing r for both RCCI and SCCI cases, and hence, the peak HRR is

significantly decreased and \bar{q} is more spread out over time with increasing r as already discussed in the previous section.

Note that in general, the deflagration mode of combustion is more apt to spread out the overall HRR than the spontaneous ignition mode, and hence, it can be utilized to mitigate the excessive PRR which usually become acute in HCCI combustion. Note also that the chemical aspects of the ignition of the present PRF/air mixture under RCCI/SCCI condition is further elucidated in [144].

6.3.3 Effect of turbulence

To elucidate the effect of turbulence on ignition of the PRF/air mixture under RCCI/SCCI conditions, three additional 2-D DNSs are performed. Figure 6-8 shows the temporal evolution of \bar{q} for Cases 13–15 with different u' . For comparison purpose, those for Cases 6, 8, and the 0-D ignition are also shown in the figure. Details of the parameters are listed in Table 6-1. In previous DNS studies [7,52,53,120,121], it was found that HCCI/SCCI combustion is more likely to occur by spontaneous ignition mode with increasing turbulence intensity because turbulence with large intensity with short τ_t can effectively homogenize the initial mixture, and hence, the overall HCCI combustion occurs similarly to the 0-D ignition.

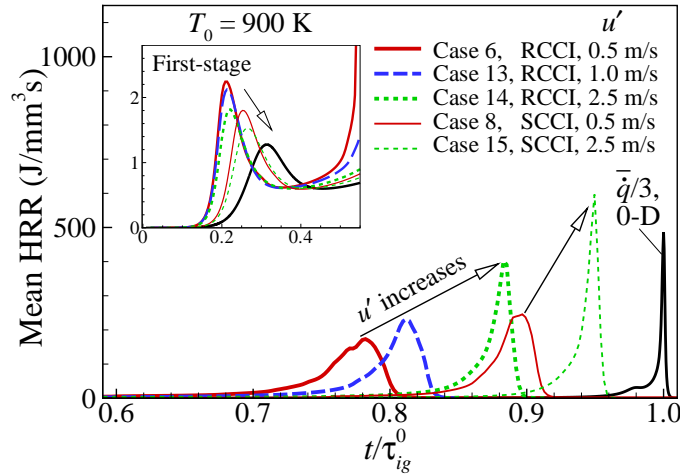


Figure 6-8: Temporal evolution of the mean HRR for Cases 6, 13, and 14 (RCCI), and Cases 8 and 15 (SCCI) with different u' . Temporal evolution of the first-stage ignitions are also shown in the small box.

Similar to previous studies [7,52,53,120,121], it is readily observed that the overall combustion is more retarded and the peak \bar{q} is more increased with increasing u' for both RCCI and SCCI cases. The examination of the isocontours of instantaneous HRR and important species fields (not shown here) verifies that turbulence with high u' effectively homogenizes the stratification of the initial mixture, and significantly dissipates heat and radicals generated during the

first-stage ignition. As such, the development of nascent ignition kernels into deflagrations is delayed, thereby retarding the overall combustion process. Consequently, the overall combustion occurs by the spontaneous ignition mode.

Kim et al. [120] found that turbulence can enhance the overall combustion by increasing turbulent flame area when the shortest ignition delay of initial mixture is significantly smaller than τ_t . In this occasion, ignition kernels can successfully develop into deflagration waves without disturbance by turbulence. In the present RCCI/SCCI cases, the shortest ignition delays of initial mixture (see Figs. 6-6a-c) are quite comparable to τ_t and as such, the enhancement of overall combustion may not be expected.

6.4 Conclusions

The 2-D DNSs of the ignition of a lean PRF/air mixture under RCCI/SCCI conditions were performed by varying r and u' at different T_0 with negatively-correlated $T-r$ fields. It was found that in the low- and intermediate-temperature regimes, the RCCI combustion is more apt to occur earlier than the corresponding SCCI combustion; its mean HRR is more distributed over time. This is primarily attributed to the high sensitivity of the ignition of the PRF/air mixture to PRF' within the negative temperature coefficient (NTC) regime. In the high-temperature regime, however, the difference between RCCI and SCCI combustion becomes marginal because the ignition of the PRF/air mixture is highly-sensitive to T' rather than PRF' and ϕ' . The Damköhler number analysis verifies that the temporal spread of the mean HRR by fuel stratification is due to the increase of deflagration mode of combustion. Finally, it is found that turbulence is more likely to homogenize the initial mixture of both RCCI and SCCI cases, and as such, the overall combustion occurs more by spontaneous ignition mode with increasing u' . These results suggest that an HCCI-type combustion can be controlled by properly adjusting T' , ϕ' , and PRF', depending on T_0 relative to the NTC regime.

Chapter 7

Ignition of a lean PRF/air mixture under RCCI/SCCI conditions: Chemical aspects

7.1 Introduction

Homogeneous-charge compression ignition (HCCI) engines have been developed because they can provide high thermal efficiency and ultra-low emissions compared to the conventional IC engines. However, the development of prototype HCCI engine has been prohibited by its narrow operating range and difficulties in combustion-phasing control. To overcome these problems, some variants of HCCI engines including reactivity controlled compression ignition (RCCI) and stratified charge compression ignition (SCCI) have been proposed thus far. To introduce in-cylinder fuel stratification, dual-fuel RCCI combustion uses in-cylinder blend of two fuels with different ignition characteristics: low reactivity fuel (e.g., *iso*-octane) supplied through port-fuel injection (PFI) and directly-injected high reactivity fuel (e.g., *n*-heptane). However, SCCI combustion uses only a single fuel with the same two-stage injection strategy. With optimized blending of two fuels rather than a single fuel, RCCI combustion can provide better combustion-phasing control with lower pressure-rise rate (PRR) [23, 24].

There have been numerous experimental and computational studies of HCCI-type engines, which primarily focus on the bulk engine characteristics such as emissions and operating performances [7, 23, 24, 27, 79, 90, 121, 125, 138, 142]. However, only a few studies on the chemical combustion process of RCCI/SCCI combustion have been performed [7, 27, 136, 141, 145–152]. For instance, Kokjohn et al. [27] numerically investigated the combustion characteristics of E85-diesel RCCI combustion and found that formaldehyde (CH_2O) and hydroxyl (OH) radicals are the key species for the first- and second-stage ignitions, respectively, and the less reactive fuel was consumed nearly simultaneously with formaldehyde.

From the spectroscopic and chemical-kinetic analysis of HCCI combustion, Hwang et al. [146] identified that significant amount of low-temperature heat release (LTHR) of PRF80/air mixtures occurs in the range of 760 to 880 K with significant formaldehyde production, resulting in rapid temperature rise during the intermediate-temperature heat release (ITHR) and thereby advancing the main combustion. Westbrook [145] pointed out that the overall HCCI combustion can be advanced by adopting variations in engine parameters such as pressure, temperature, and equivalence ratio which enable in-cylinder fuel/air mixtures to reach the H_2O_2 decomposition temperature at earlier time. Ando et al. proposed a universal model describing hydrocarbon ignition reactions that can be categorized into five major groups including RO_2 chemistry, H_2O_2 chemistry, H_2 - O_2 system chemistry, CO - CO_2 chemistry, and fuel fragments and the hydrogen-abstraction/carbon-addition chemistry [147, 153–155]

Recently, Vuilleumier et al. [148] found from an experimental and modeling study that the addition of highly reactive *n*-heptane content induces the increase of ITHR, eventually triggering high-temperature heat release (HTHR) with a significant formaldehyde accumulation. In addition, they identified the dominant reaction pathways: H-atom abstraction from *n*-heptane

by OH and the addition of heptyl radicals to O₂. These previous studies, however, were either RANS and low-dimensional analyses or optical measurement with high uncertainty to discern individual fuel species such that further understanding of the chemical aspects of RCCI/SCCI combustion is still needed.

More recently, Luong et al. [7] investigated the ignition characteristics of *n*-heptane/air mixture under HCCI/SCCI conditions by performing 2-D direct numerical simulations (DNSs). They identified important species and reactions for HCC/SCCI combustion by using chemical explosive mode analysis (CEMA). However, CEMA has not been applied to RCCI combustion. Therefore, the objective of the present study is to provide insights into the chemical ignition process of PRF/air mixture under RCCI/SCCI conditions by analyzing 2-D DNS data with CEMA.

For this purpose, we use the data set generated from 2-D DNSs of the ignition of a lean PRF/air mixture under RCCI/SCCI conditions by Luong et al. [156]. From this study, it is found that the overall combustion of RCCI is more advanced and more distributed in time than that of SCCI due to the dominant role of reactivity stratification in inducing more deflagration mode of combustion in the low-to-intermediate temperature regime. However, both RCCI and SCCI have similar overall combustion characteristics in the high-temperature regime because the ignition of the PRF/air mixture becomes less sensitive to reactivity stratification and/or equivalence ratio.

7.2 Methodology

To investigate the chemical aspects of RCCI and SCCI combustion, we analyze 2-D DNS data set in [156] using CEMA. The 2-D DNSs of the ignition of the PRF/air mixture under RCCI and SCCI conditions were simulated using the Sandia compressible DNS code [36], S3D, with a 116-species reduced chemistry of PRF oxidation [90]. Note that recent theoretical and experimental findings on hydroperoxyalkyl (QOOH) chemistry [157–160] have not been updated in the present PRF reduced mechanism. However, it still shows good agreement with experimental results in terms of ignition delays, flame propagation speeds, and extinction residence times [90].

The initial conditions for DNSs are specified as follows. The initial pressure, p_0 , mean equivalence ratio, ϕ_0 , are 40 atm and 0.45, respectively. PRF50 (i.e., a 50% *iso*-octane and 50% *n*-heptane blend by volume) was adopted as the mean fuel for RCCI combustion and the single fuel for SCCI combustion. For RCCI cases, *n*-heptane field is initialized by $m = \bar{m} + m'$, superimposed on a uniform *iso*-octane/air mixture, where m is the mass of *n*-heptane, and the ‘overbar’ and ‘prime’ represent the mean and fluctuation, respectively. For SCCI cases, PRF50 is supplied through two-stage injection and hence, m represents the mass of PRF50.

The local variations in PRF number, equivalence ratio, and temperature can be achieved for RCCI combustion, while only variations in equivalence ratio and temperature are obtained for SCCI combustion. The initial turbulent flow field is generated using an isotropic kinetic energy spectrum function by Passot-Pouquet [37]. Concentration and temperature fields are also generated from the same energy spectrum as turbulence with different random number and then are superimposed on top of the turbulence field. The periodic boundary conditions are imposed in all directions, and as such, RCCI/SCCI combustion occurs in constant volume. For more details of the numerical setup, readers are referred to [156].

Two representative RCCI/SCCI cases (i.e., Case 6 for RCCI and Case 8 for SCCI in [156]) with the degree of fuel stratification, $r = m'/\bar{m} = 0.44$, temperature fluctuation, $T' = 30$ K, at the initial mean temperature, $T_0 = 900$ K, are chosen for the present CEMA such that both cases are initially involved in the low- and intermediate-temperature chemistries. The 0-D homogeneous ignition delay, τ_{ig}^0 , of PRF50 is 2.2 ms. For both cases, negatively-correlated T - r field is assumed to consider the evaporative cooling effect of directly-injected fuel.

Note that CEMA has been applied to various DNS studies [52, 77, 78, 80–83] to elucidate the chemical aspects of turbulent combustion and is now believed as one of the useful computational flame diagnostics tools for the systematic detection of important species and reactions in premixed flames and flame ignition/extinction. Also note that the characteristics of two-stage ignition of large hydrocarbon fuel/air mixtures have been numerically investigated by adopting the computational singular perturbation method [161] and CEMA [7, 79, 83, 90, 120, 121, 162].

CEMA is briefly explained here. For more details of CEMA, readers are referred to [78, 80, 83]. For a chemically-reacting system, the discretized conservation equations can be expressed as:

$$\frac{D\mathbf{y}}{Dt} = \mathbf{g}(\mathbf{y}) = \boldsymbol{\omega}(\mathbf{y}) + \mathbf{s}(\mathbf{y}), \quad (7.2.1)$$

where D/Dt is the material derivative, which can be replaced by d/dt in the Lagrangian coordinate. \mathbf{y} denotes the solution variables including species concentrations and temperature. $\boldsymbol{\omega}$ and \mathbf{s} represent respectively the chemical source term and all the other non-chemical source terms such as diffusion in flames and homogeneous mixing term in stirred reactors.

Since the Jacobian of the chemical source term, $\mathbf{J}_{\boldsymbol{\omega}} (\equiv \partial\boldsymbol{\omega}/\partial\mathbf{y})$, retains the chemical information of local mixture, the chemical feature of the mixture can be determined based on the Jacobian. To capture the chemical feature in CEMA, a chemical mode is defined as an eigenmode of $\mathbf{J}_{\boldsymbol{\omega}}$, which is associated with an eigenvalue, λ_e , and a corresponding pair of the left and right eigenvectors, \mathbf{a}_e and \mathbf{b}_e . Chemical explosive mode (CEM) is a chemical mode of which real part of eigenvalue is positive, $\text{Re}(\lambda_e) > 0$.

In general, a local mixture with a CEM is destined to auto-ignite if there are no thermal

and radical losses. Therefore, CEM indicates an intrinsic chemical feature of ignitable mixture: i.e., a mixture with $\text{Re}(\lambda_e) > 0$ is more apt to ignite while a mixture with $\text{Re}(\lambda_e) < 0$ is already burnt or fails to ignite.

The critical chemical kinetic processes in RCCI and SCCI combustion can further be identified by evaluating the explosive index (EI) and participation index (PI) of local mixture. **EI** and **PI** are defined as [80, 83]:

$$\mathbf{EI} = \frac{|\mathbf{a}_e \otimes \mathbf{b}_e^T|}{\text{sum}(|\mathbf{b}_e \otimes \mathbf{b}_e^T|)}, \quad (7.2.2)$$

$$\mathbf{PI} = \frac{|\mathbf{b}_e \cdot \mathbf{S} \otimes \mathbf{R}|}{\text{sum}(|(\mathbf{b}_e \cdot \mathbf{S}) \otimes \mathbf{R}|)}, \quad (7.2.3)$$

where **S** and **R** represent the stoichiometric coefficient matrix and the vector of the net rates for reactions, respectively. The symbol \otimes represents the element-wise multiplication of two vectors. Since **EI** and **PI** indicate the normalized contribution of each variable and reaction to the CEM, respectively, and as such, controlling species and reactions for RCCI/SCCI combustion can be elucidated by evaluating **EI** and **PI** values. Since the mass fractions of quasi-steady state species in the reduced chemistry are functions of the other species, the 171-species skeletal mechanism for PRF oxidation [90] is used to analytically evaluate \mathbf{J}_ω , \mathbf{a}_e , and \mathbf{b}_e .

7.3 Results and discussion

7.3.1 Overall RCCI/SCCI combustion

The characteristics of RCCI/SCCI combustion are first elucidated by examining the temporal evolution of the mean heat release rate (HRR) and temperature together with two main fuel mass fractions as shown in Fig. 7-1. Several points are to be noted from the figures. First, the overall RCCI combustion occurs earlier and its mean HRR is more distributed over time than the SCCI combustion. This is because local mixtures with small PRF number or relatively-high *n*-heptane concentration in RCCI case auto-ignite rapidly, which enhances deflagration mode of combustion and smoothes out the mean HRR as explained in [156].

The difference between RCCI and SCCI combustion can be explained by the consumption rate of *n*-heptane and *iso*-octane through the whole ignition process. It is readily observed from Fig. 7-1b that for both RCCI and SCCI cases, overall, *n*-heptane is consumed more rapidly than *iso*-octane throughout the whole combustion process. Similar to the previous results in [163, 164], the first-stage ignition delays of RCCI/SCCI combustion in the present study are nearly unchanged with the equivalence ratio and/or reactivity stratification. During the early stage of ignition, however, *n*-heptane in RCCI case is consumed slightly faster than in

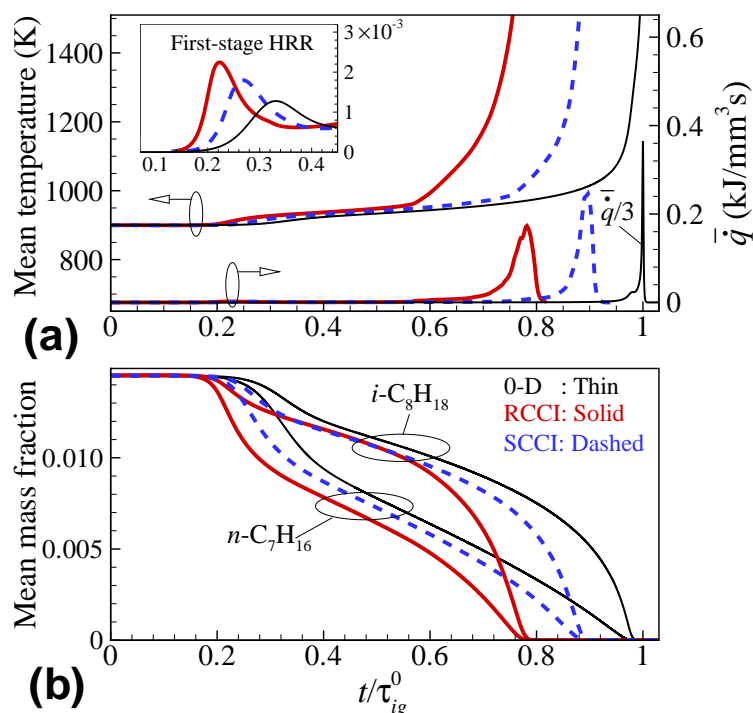


Figure 7-1: Temporal evolution of (a) the mean HRR and temperature and (b) the mean mass fraction of n -heptane and iso -octane for RCCI, SCCI, and 0-D ignition.

SCCI case, which leads to more intense first-stage ignition in RCCI case manifested in higher mean HRR during the first-stage ignition, ultimately resulting in earlier second-stage ignition.

Based on Bilger's mixture fraction [131], Z , the conditional means of HRR on Z at different times are evaluated. The results revealed that during the first-stage ignition and the start of the main combustion of RCCI case, a significant amount of heat is released from mixtures with large Z , which corresponds to local mixtures with high reactivity (high n -heptane concentration) and ϕ . Local mixtures with high n -heptane concentration (\sim PRF30 with $\phi = 0.74$) auto-ignite first and then initiate the ignition of adjacent less-reactive mixtures, resulting in a sequential ignition process.

For SCCI case, the start of the main combustion is also originated from mixtures with large Z . However, these local mixtures have a lower n -heptane concentration (i.g., \sim PRF50 with $\phi = 0.74$), and as such, less heat is released during the first-stage ignition, resulting in a delayed second-stage ignition.

It is of importance to understand the difference between chemical processes occurring in these local mixtures in RCCI and SCCI combustion. Therefore, in the next section, CEMA is applied to 0-D ignitions under the similar conditions of these local mixtures.

7.3.2 CEMA: 0-D ignition

As mentioned above, CEMA is applied to the 0-D ignitions of PRF30/air mixture at $p_0 = 40$ atm, $T_0 = 812$ K, and $\phi_0 = 0.74$, which corresponds to mixture with high *n*-heptane concentration with low temperature in RCCI case. Figure 7-2 shows the temporal evolution of temperature, λ_{exp} , EI and PI values of important species and reactions. To facilitate discussion, the schematic of overall reaction pathways of PRF oxidation under HCCI condition is shown in Fig. 7-3. Note that to separately evaluate the contribution of *n*-heptane and *iso*-octane to the CEM, R, Q, K, and Q' denote radicals originated from *n*-heptane only. Several points are to be noted from the Fig. 7-2.

First, it is readily observed that prior to the first-stage ignition featured by positive λ_{exp} , *n*-heptane and radicals originated from *n*-heptane are the main variables contributing to CEM. As shown in Fig. 7-3, *n*-heptane consumption proceeds in the low-temperature chemistry (LTC) pathway: i.e., the H-atom abstraction from a fuel molecule, RH, initiates the oxidation of *n*-heptane via $\text{RH} + \text{O}_2 \rightarrow \text{R} + \text{HO}_2$; alkyl radical, R, from RH converts into alkylperoxy radical, RO_2 , via $\text{R} + \text{O}_2 + \text{M} \rightarrow \text{RO}_2 + \text{M}$ and then, the radical isomerization of RO_2 takes place to generate hydroperoxyalkyl, QOOH, via $\text{RO}_2 \rightleftharpoons \text{QOOH}$. QOOH converts into O_2QOOH by another O_2 addition via $\text{QOOH} + \text{O}_2 \rightarrow \text{O}_2\text{QOOH}$. It is important to note that the chain branching reactions involving the production and decomposition of keto-hydroperoxide, KOOH, (i.e., $\text{O}_2\text{QOOH} \rightarrow \text{KOOH} + \text{OH}$ and $\text{KOOH} \rightarrow \text{OH} + \text{KO}$) determine the overall rate of the LTC [5–7].

As expected from the LTC in Fig. 7-3, the EI and PI values in Fig. 7-2 also indicate that RO_2 and O_2QOOH are the most important species, and the H-atom abstraction reaction ($\text{RH} + (\text{O}, \text{OH}, \text{HO}_2) \rightarrow \text{R} + (\text{OH}, \text{H}_2\text{O}, \text{H}_2\text{O}_2)$), isomerization of RO_2 , and chain-branching decomposition of O_2QOOH are the most important reactions to CEM for the 0-D ignition of PRF30/air mixture. For 0-D ignition of PRF50/air mixture under the same initial conditions (not shown here), the above two species and three reactions are also identified as the most important species/reactions but their contribution to CEM is slightly reduced due to low *n*-heptane concentration. Due to local high concentration of *n*-heptane in RCCI case, the first-stage ignition in RCCI case occurs more rapidly and more intensely than that in SCCI case under the same initial conditions as shown in Fig. 7-1a.

Second, near the first-stage ignition ($\sim t/\tau_{ig}^0 = 0.27$), temperature, *n*-heptane, and CH_2O are identified as the most important variables to CEM, which is featured by the peak PIs of the chain-branching low-temperature reactions, $\text{O}_2\text{QOOH} \rightarrow \text{KOOH} + \text{OH}$ and $\text{KOOH} \rightarrow \text{OH} + \text{KO}$ (see Fig. 7-2c).

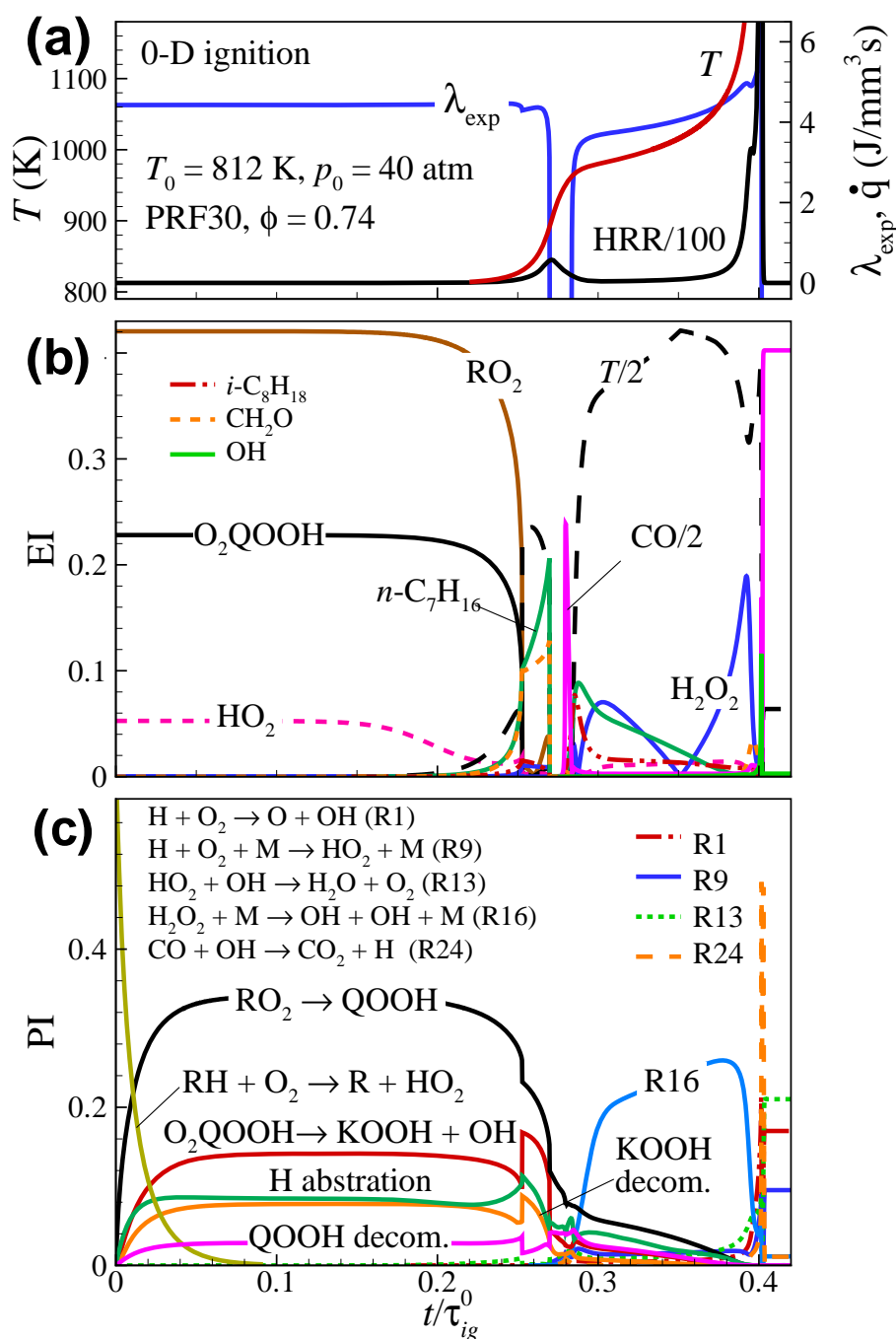


Figure 7-2: Temporal evolution of (a) temperature, $\lambda_{\text{exp}} = \text{sign}(\text{Re}(\lambda_e)) \times \log(1 + |\text{Re}(\lambda_e)|)$, and HRR, (b) EI of important variables, and (c) PI of key elementary reactions for 0-D ignition of PRF30/air mixture.

Third, between the first- and second-stage ignition, or in the intermediate-temperature chemistry (ITC) regime, temperature is found to be the main source of the CEM compared to *n*-heptane, *iso*-octane, and H_2O_2 . During the period, the low-temperature reactions are suppressed gradually by the competing intermediate-temperature reactions of QOOH decomposition (see Fig. 7-3) and $\text{H}_2\text{O}_2 + \text{M} \rightarrow \text{OH} + \text{OH} + \text{M}$ (R16) is identified as the most important reaction from the PI analysis as shown in Fig. 7-2c. Due to the low overall reactivity

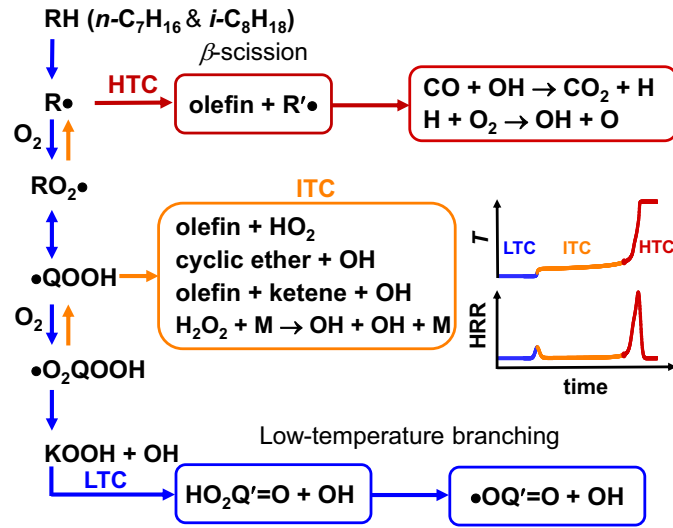


Figure 7-3: Schematic of reaction pathways of *n*-heptane and *iso*-octane oxidation at different temperatures [5–7].

of the ITC [5, 6], the increase of temperature during this period becomes marginal until the second-stage ignition starts.

As temperature increases over 1000 K, the chain-branching reaction of hydrogen peroxide, $H_2O_2 + M \rightarrow OH + OH + M$ (R16), occurs very intensively, which increases temperature large enough to initiate the high-temperature chain branching reactions represented by $H + O_2 \rightarrow O + OH$. As such, temperature, CO and OH are identified as the key variables to CEM at the second-stage ignition. Meanwhile, the chain-branching reaction, $H + O_2 \rightarrow O + OH$ (R1), the conversion reaction of CO to CO_2 , $CO + OH \rightarrow CO_2 + H$ (R24), and HO_2 formation reaction, $H + O_2 + M \rightarrow HO_2 + M$ (R9), are found to be the most important reactions to CEM.

It is also identified from CEMA that the ignition of PRF50/air mixture also exhibits the same characteristics as that of PRF30/air mixture except that the overall ignition is delayed due to the lower concentration of *n*-heptane in PRF50.

7.3.3 CEMA: 2-D DNS of RCCI/SCCI combustion

In this section, the same EI and PI analyses are applied to the 2-D DNS of RCCI/SCCI combustion to identify controlling species and reactions at two different times of the first-ignition delay, $\tau_{ig,1}$, and the onset of the main combustion at which the deflagration mode of combustion becomes dominant. The dominance of the deflagration mode of combustion was verified not only by examining the local flame structure but also by performing the Damköhler number analysis (not shown here) [156].

Figure 7-4 shows the isocontours of selected variables for RCCI case at $\tau_{ig,1}$, from which the

key variables and reactions to the CEM can be identified at different locations. For instance, *n*-heptane and CH₂O have large EI values in relatively-low temperature regions while H₂O₂ and HO₂ have large EI values at relatively-high temperature regions. In the same way, LTC and ITC can be identified at different locations based on the PI values of important reactions. Although specific chemical information of local mixtures can be obtained from the isocontours of EI and PI values, the effects of each variable and reaction on the overall ignition and their relations are not readily observed. As such, the conditional mean of HRR, λ_{exp} , and EI/PI values of important variables/reactions for both RCCI and SCCI cases at their $\tau_{ig,1}$ are shown in Fig. 7-5. In this study, a conditional mean value is obtained by averaging a variable conditioned on temperature to clarify the contribution of LTC, ITC, and HTC to the overall combustion. Several points are to be noted from the figure.

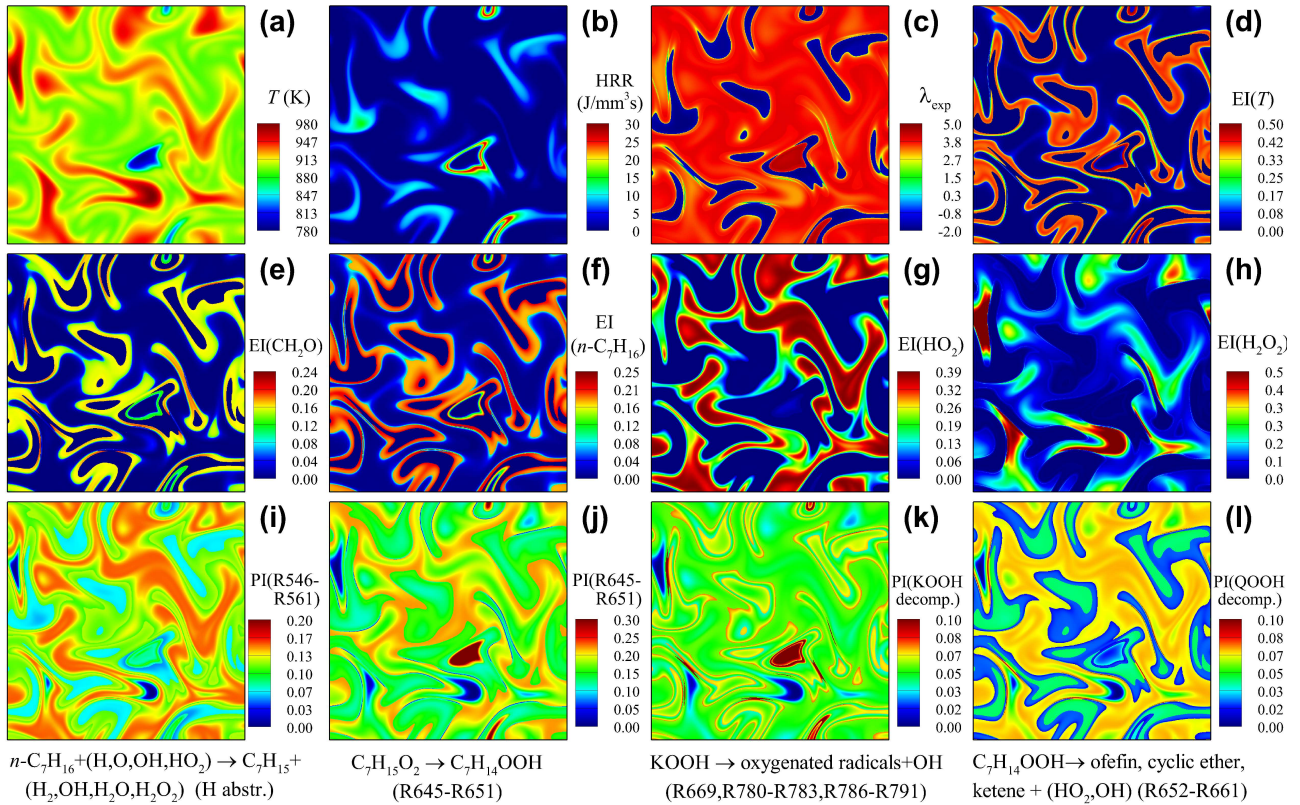


Figure 7-4: Isocontours of (a) temperature, (b) HRR, (c) λ_{exp} , EI of (d) temperature and (e)–(h) critical species, and (i)–(l) PI of critical reactions at the first-ignition delay, $\tau_{ig,1}/\tau_{ig}^0 = 0.22$.

First, at the region where most heat is released ($830 \text{ K} < T < 900 \text{ K}$), LTC represented by the isomerization of RO₂, chain branching reactions of KOOH, and H-atom abstraction from *n*-heptane is predominant for both RCCI and SCCI combustion. As such, temperature, *n*-heptane, and CH₂O are the most important variables to the CEM. Note that at the early stage of combustion, local mixtures with low temperature correspond to high *n*-heptane concentration or low PRF number with high ϕ due to the negatively-correlated T –*n*-heptane relation. As such,

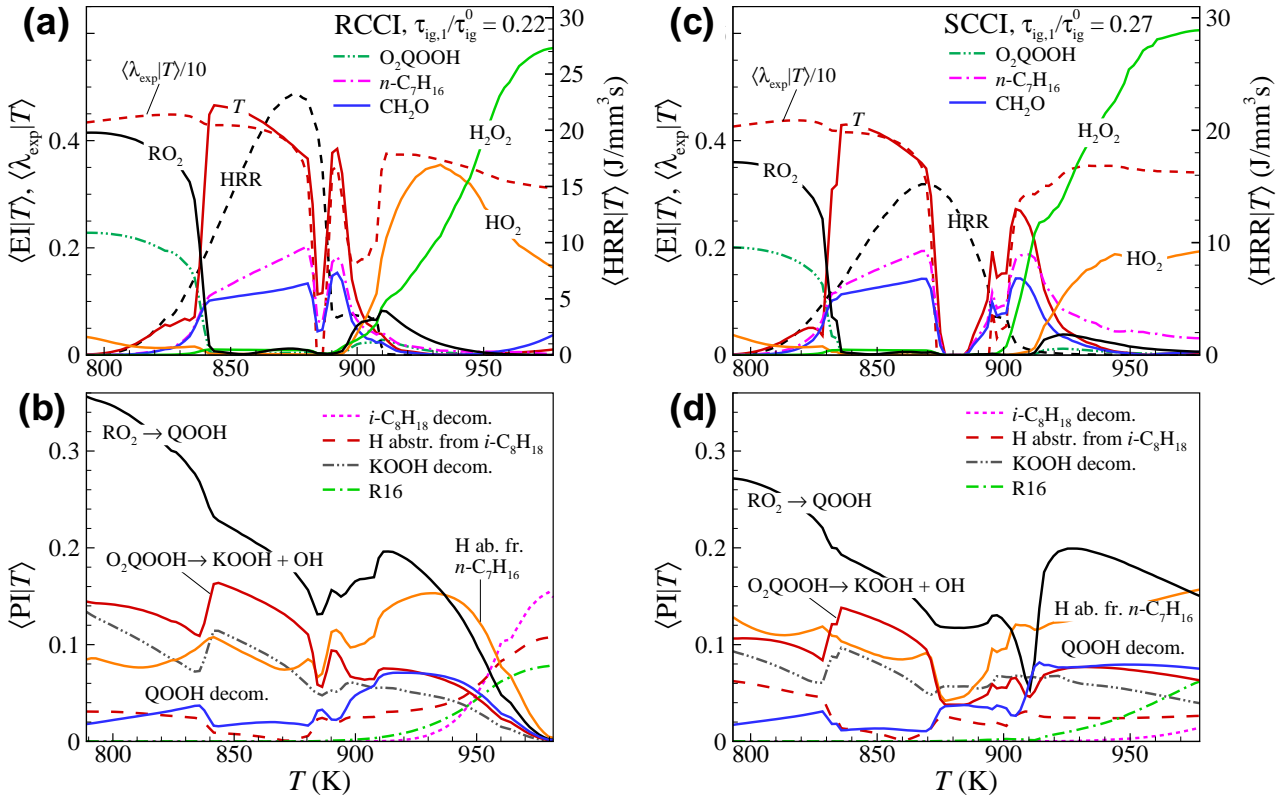


Figure 7-5: Conditional mean of HRR, λ_{exp} , and EI of critical species, and PI of critical reactions at the first-stage ignition for RCCI (left column) and SCCI (right column).

these results imply that LTHR from local mixtures with relatively large ϕ is primarily responsible for temperature increase at this stage, similar to the 0-D ignition in Fig. 7-3. Furthermore, HRR occurs slightly more intensively in the RCCI case than in the SCCI case, which ultimately leads to the early second-stage ignition in the RCCI case.

Second, at the region with $T > 900$ K, the contribution of LTC to the CEM is negligible and that of ITC represented by H_2O_2 decomposition (R16) and H-atom abstraction/decomposition of *iso*-octane is significant such that no HRR occurs at this region. Consistent to the CEMA of 0-D ignition, HO_2 from $QOOH$ decomposition and H_2O_2 via R16 are the key species for the CEM in this intermediate-temperature region.

Third, based on PI values of reactions associated with *iso*-octane decomposition in Fig. 7-5b, it can be conjectured that during the first-stage ignition, *iso*-octane is primarily consumed by *iso*-octane decomposition reactions at intermediate temperature rather than by the LTC unlike the case of *n*-heptane.

In the same way, the conditional means of important variables and reactions at the time of 10% cumulative heat release rate (CHRR) for both RCCI and SCCI cases are shown in Fig. 7-6. On the contrary to the early stage of combustion, most heat is released from the high-temperature region ($T > 1500$ K) where HTC represented by CO oxidation (R24) and hydrogen

chemistry (R1, R9, and R13) is predominant for for both RCCI and SCCI combustion. As such, temperature, CO, and OH are identified as the most important variables to the CEM and HTHR determines temperature increase at this stage. At the region with $T < 1500$ K, however, the contribution of HTC to the CEM is negligible and that of ITC represented by H_2O_2 decomposition (R16) is again significant as in Figs. 7-5b and d such that HRR from ITC is marginal at this region.

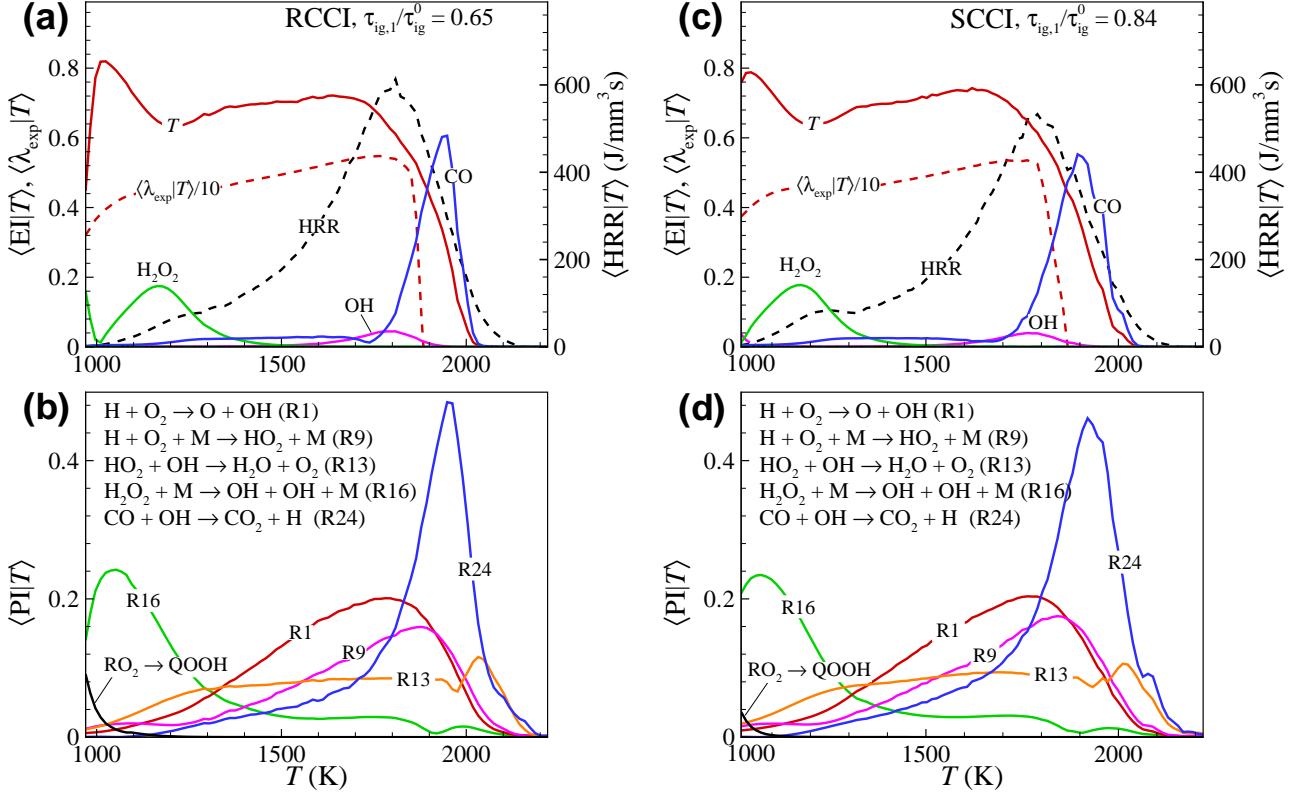


Figure 7-6: Conditional means of HRR, λ_{exp} and EI of critical species, and PI of critical reactions at 10% CHRR for RCCI (left column) and SCCI (right column).

These combustion characteristics can be further identified by the isocontours of important variables and reactions for RCCI case as in Fig. 7-7. It is readily observed from the figure that most HRR occurs at very thin deflagration waves where the conversion reaction of CO to CO_2 and high-temperature chain-branching reaction (R1) are identified to be important to the CEM.

From a series of our DNS studies [7, 120, 156] together with the present study, it can be concluded that the overall RCCI/SCCI combustion can be simply understood by mapping the variation of 2-D RCCI/SCCI combustion in temperature space (Figs. 7-5 and 7-6) onto the temporal evolution of 0-D ignition (Fig. 7-3). However, the small difference induced by the inhomogeneities in temperature, equivalence ratio, and reactivity in 2-D DNS can significantly change its overall combustion characteristics including the overall ignition delay and mean HRR

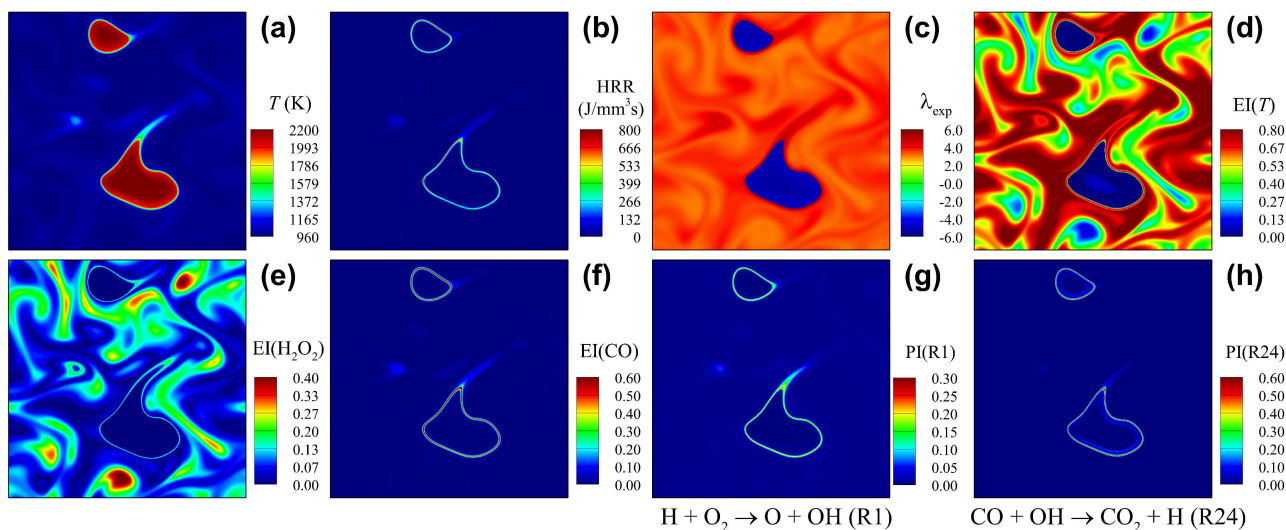


Figure 7-7: Isocontours of (a) temperature, (b) HRR, (c) λ_{exp} , EI of (d) temperature and (e)–(f) critical species, and (g)–(h) PI of critical reactions at 10% CHRR, $t/\tau_{ig}^0 = 0.65$.

behavior, which can be used to control RCCI/SCCI combustion. For instance, the equivalence ratio and/or reactivity stratification needs to be utilized for controlling RCCI/SCCI combustion rather than temperature stratification within the negative temperature coefficient (NTC) regime. This is because the 0-D ignition delays in the NTC regime are more sensitive to the equivalence ratio and reactivity stratifications such that they can induce more deflagration waves during the early-stage of combustion, which ultimately spreads out the mean HRR more in time and reduces an excessive PRR [7, 156].

7.4 Conclusions

The chemical characteristics of the ignition of a lean PRF/air mixture under RCCI and SCCI conditions are investigated by analyzing 2-D DNS data set with CEMA. It is found that at the first ignition delay, LTC represented by the isomerization of RO_2 , chain branching reactions of KOOH , and H-atom abstraction of n -heptane is predominant for both RCCI and SCCI combustion. Moreover, PI and EI analyses together with conditional means of their values clarify that LTHR from mixtures with relatively-high n -heptane concentration occurs more intensively in RCCI combustion than in SCCI combustion, and as such, the overall RCCI combustion is more advanced in time and its mean HRR is more distributed over time than those of SCCI combustion. It is also found that at the onset of the main combustion (10% CHRR point), HTHR occurs primarily in thin deflagrations where temperature, CO, and OH are found to be the most important species for the CEM. In addition, the conversion reaction of CO to CO_2 and hydrogen chemistry including R1, R9, and R13 are identified as the most important reactions for the CEM at this stage of combustion. These overall RCCI/SCCI combustion characteristics can

be simply understood by mapping the variation of 2-D RCCI/SCCI combustion in temperature space onto the temporal evolution of 0-D ignition.

Chapter 8

On the effect of injection timing on the ignition of lean PRF/air/EGR mixtures under direct dual fuel stratification conditions

8.1 Introduction

One approach for expanding the operation range to a higher load and avoiding excessive pre-mixing of the charge of the RCCI combustion is to stratify both fuels by directly injecting gasoline and diesel into the engine cylinder [4,30–33]. This method allows more flexible controllability of the in-cylinder reactivity distribution of the two fuels. Kavuri et al. elucidated the characteristics of the RCCI combustion using direct injection of both gasoline and diesel fuels at high load and compared its performance with gasoline compression ignition (GCI) combustion [33]. They found that both RCCI and GCI combustion have similar overall combustion characteristics with a near top dead center (TDC) injection; however, the RCCI combustion has better control of the combustion phasing than GCI combustion. Lim et al. studied numerically the RCCI combustion with dual direct injections of *iso*-octane and *n*-heptane under high-load conditions [30]. They showed that the RCCI combustion can achieve very-high gross thermal efficiency of 48.7% with 21 bar gross indicated mean effective pressure (IMEP) by an optimal injection strategy compared to 47–48% efficiency with up to 16 bar gross IMEP in a boosted HCCI engine using E10 fuel (a 10% ethanol and 90% gasoline blend) [34].

Recently, Wissink and Reitz demonstrated that compared to the RCCI combustion, direct dual fuel stratification (DDFS) combustion is more effective in distributing HRR and reducing PRR at high-load conditions [4,31,32]. The DDFS combustion combines the high thermal efficiency of the RCCI combustion with the high load capability of partially premixed combustion (PPC) while reducing exhaust gas recirculation (EGR) rate, noise, and combustion instabilities. In the DDFS combustion, the start of the heat release is controlled by the direct injection of diesel while the peak and duration of the heat release are governed by near-TDC gasoline injection. Similar to the RCCI combustion, in particular, the DDFS combustion utilizes an early injection of gasoline to form premixed background charge, followed by direct injection of diesel to generate some degrees of reactivity and equivalence ratio stratification. These two injections are designed to control the start of the main combustion occurring at about -10°CA after the TDC (ATDC). Inspired by the PPC, the DDFS combustion utilizes high-pressure direct injection of gasoline right before the TDC (BTDC). As such, DDFS combustion can achieve a capability to independently control ignition timing and combustion duration by combining reactivity stratification with diffusion-limited gasoline injection [4,31,32]. However, the effect of the timing of the late gasoline injection on the combustion process of both fuel stratification is not well-understood.

In previous direct numerical simulation (DNS) studies, the ignition characteristics of HCCI [48–50,52,53,61,90,105,106,120,165], SCCI [7,51,93,121–123], and RCCI [144,156] combustion have been investigated at constant volume. In real IC engines, however, the combustion process is highly affected by both the compression heating before TDC and the expansion cooling after

the TDC by the piston motion. Moreover, two-stage ignition fuels such as diesel, primary reference fuel (PRF), and dimethyl ether (DME) exhibit a significant amount of radical build-up resulting from low-temperature heat release (LTHR) during the compression stroke at temperature below about 850 K [17]. The LTHR from the first-stage ignition can increase in-cylinder temperature by about 10–20 K, which can cause the main combustion to occur earlier. Recently, the effects of compression heating and expansion cooling were considered in several DNS studies by adopting compression heating models [118, 124, 142, 166].

In previous DNS studies of HCCI combustion, it was assumed that all of the multiple injections are finished to save computational cost. With the assumption, DNSs were then set up with appropriate initial fields with equivalence ratio and/or concentration inhomogeneities to account for the degree of in-cylinder stratification in fuel/air mixture induced by direct injections. Different degrees of initial fuel/air mixture inhomogeneities were imposed to account for variations in the timing/duration of late direct injections. Based on this approach, Zhang et al. numerically investigated the effect of split fuel injection on HRR and pollutant emissions of PRF70/air/EGR mixtures in a PPC engine [166]. The initial fields were initialized by assuming that the first/second injection forms a slight/high fuel inhomogeneity. 2-D DNSs started with such initial fields after the end of the second fuel injection, 10°CA BTDC [166]. A similar technique was used in a multi-zone based study for RCCI combustion [167]. For multiple injection strategies, however, the previous approach is not capable of reproducing the timing and duration of a late direct injection, especially for cases in which the remaining fuel may be injected into an undergoing reacting charge as in [4, 31, 32].

Therefore, the objective of this chapter is two-fold: (1) to develop a pseudo-*iso*-octane model to mimic the timing and duration of the late direct injection, and (2) to investigate the effect of the late-direct-injection timing on the combustion process of *n*-heptane/*iso*-octane/air mixture with inhomogeneities in both fuels using 2-D DNSs. The effect of the compression heating and expansion cooling by the piston motion is also taken into account by adopting a novel compression heating model. Note that DNSs of the ignition of hydrocarbon/air mixtures with composition inhomogeneities under high pressure conditions, which incorporate some practical models such as the compression heating and fuel injection models, can provide unprecedented data sets to understand its fundamental combustion characteristics and to ultimately develop and validate novel turbulence and combustion models.

8.2 Model development

8.2.1 Compression heating model

The reciprocating motion of the piston causes compression heating and expansion cooling of the charge within the engine cylinder. As such, it is of importance to capture the effects of the compression heating before the TDC on the unburned mixture because the pressure and temperature rise during the induction period can have a significant influence on the low-temperature chemistry and radical accumulation. Likewise, the temperature drop due to expansion cooling should also be considered because it has a profound effect on the accurate prediction of incomplete combustion and formation of unburned hydrocarbons. While the fixed mesh flow solver used in the present study allows for a high order of numerical accuracy, it does not provide a straightforward way to account for the effects of moving boundaries such as the piston motion.

There have been several studies [118,124,142,168,169] in which the effects of pressure change were incorporated through the use of additional source terms in the governing equations instead of moving the meshes or varying the volume of the computational domain. Following this approach, we add additional source terms to the governing equations. These terms inject/remove mass, momentum, and energy to mimic the effects of compression and expansion. Our formulation for the source terms ensures that the thermodynamic pressure of the system is varied without introducing any variations in the local hydrodynamic pressure, as the latter would unphysically affect the development of the turbulent flow. More specifically, the compression heating model in [142] was adopted not only to account for volume change due to the piston motion but also to match an experimental pressure trace of a fired engine. As such, the thermodynamic pressure in their DNSs [142] followed the imposed pressure trace. In the present study, however, the compression heating model is used only to reproduce a motored pressure trace of an experimental engine and hence, the pressure rise due to combustion is allowed to evolve on its own. The formulation of the mass source terms is similar to that presented in [142] but it is repeated here for convenience.

The chamber volume of an internal combustion engine can be determined using the slider-crank relation [170]. Based on that, close to the TDC, the motored pressure trace can be approximated by:

$$P_m(t) = P_{0,m} \left[1 + g^2 \pi^2 \frac{(t - t_0)^2}{t_c^2} \right]^{-n}, \quad (8.2.1)$$

where $P_{0,m}$ is the motored TDC pressure, t_c is the time taken for one crank rotation, t_0 is the time at the TDC and g is a model factor to account for the crank slider geometry. The experimental pressure trace from Wissink et al. [4] is used to calibrate the geometry factor in Eq. 8.2.1 and obtain the analytical expression for the motored pressure trace.

To include the effects of the pressure change due to the piston motion, the DNS governing equations need to be modified with appropriate mass source term, along with the corresponding momentum and energy source terms. The fully compressible Navier-Stokes equations: continuity, momentum, total energy, and species continuity equations are solved in conservative form with detailed chemistry,

$$\begin{aligned}
 \frac{\partial \rho}{\partial t} &= -\frac{\partial \rho u_i}{\partial x_i} + \dot{m} \\
 \frac{\partial \rho u_i}{\partial t} &= -\frac{\partial \rho u_i u_j}{\partial x_j} - \frac{\partial P}{\partial x_i} + \frac{\partial \tau_{ij}}{\partial x_j} + \dot{m} u_i \\
 \frac{\partial \rho e_t}{\partial t} &= -\frac{\partial \rho e_t u_j}{\partial x_j} - \frac{\partial P u_j}{\partial x_j} + \frac{\partial (\tau_{ij} \cdot u_i)}{\partial x_j} - \frac{\partial q_j}{\partial x_j} + \dot{m} e_t \\
 \frac{\partial \rho Y_k}{\partial t} &= -\frac{\partial \rho Y_k u_j}{\partial x_j} - \frac{\partial J_{k,j}}{\partial x_j} + \omega_k + \dot{m} Y_k
 \end{aligned} \tag{8.2.2}$$

where ρ is the density, u_i are the Cartesian velocity components, P is pressure, Y_k is the species mass fraction of the k -th species and ω_k is its reaction rate, τ_{ij} is the viscous stress tensor given by $\tau_{ij} = \mu(\frac{\partial u_i}{\partial x_j} + \frac{\partial u_j}{\partial x_i} - \frac{2}{3}\delta_{ij}\frac{\partial u_l}{\partial x_l})$. The total specific energy is given by $e_t = u_i u_i / 2 + h - P / \rho$ and the heat flux vector is given by $q_i = -\lambda \frac{\partial T}{\partial x_i} + \sum_k h_k J_{k,i}$. The species diffusive flux is computed through a mixture averaged formulation based on a form of Fick's law, $J_{k,i} = -\rho D_k \frac{\partial Y_k}{\partial x_i} - \frac{\rho D_k Y_k}{M} \frac{\partial M}{\partial x_i}$ where M is the mixture-averaged molecular weight and D_k is a mixture-averaged diffusion coefficient [36, 171]. Nitrogen is used as the bath gas, i.e. the diffusion flux of nitrogen balances the sum of the diffusion fluxes for the other species in order to ensure that the net diffusion flux is zero.

The ideal gas equation of state is used such that

$$P(\mathbf{x}, t) = P_t(t) + p(\mathbf{x}, t) = \rho RT, \tag{8.2.3}$$

where $P_t = \bar{P}$ is the thermodynamic pressure of the domain, p is the local hydrodynamic pressure and R is the specific gas constant. The thermodynamic pressure change due to the piston motion, dP_m/dt , is obtained by differentiating Eq. 8.2.1 with respect to time. The local mass source term that needs to be added is then given by:

$$\dot{m} = \frac{\rho}{P} \frac{dP_m}{dt}. \tag{8.2.4}$$

The compression heating model adopted in the present study has an improved feature compared to those used in the previous studies [118, 124, 168, 169]. The previous models used a mass source term which is uniform across all grid points regardless of the presence of temperature and equivalence ratio inhomogeneities. Such a uniform mass source term may induce pressure disturbance in the domain. The mass source term in the present model is, therefore,

not uniform across the domain, but rather depends on local density as seen from the relation of Eq. 8.2.4. As such, the thermodynamic pressure varies uniformly across the domain to ensure that the original hydrodynamics pressure distribution is retained, and no steep thermodynamic pressure gradients are created. Figure 8-1 shows the modeled motored-pressure trace that perfectly matches the experimental one without any noticeable discrepancies in the time duration of interest considered in the present study. The relevant engine parameters taken from [4] are listed in Table 8-1 with the compression ratio, intake pressure, and engine speed of 14.88, 1.84 atm, and 1300 rpm, respectively.

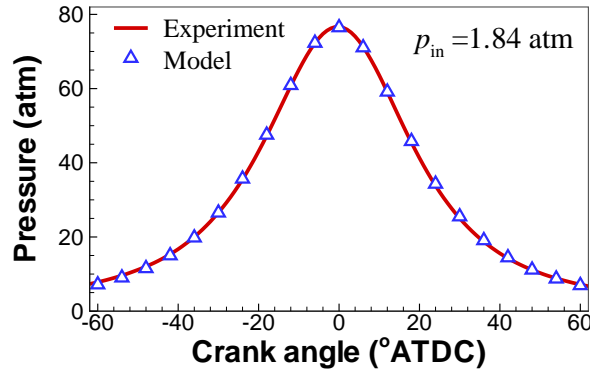


Figure 8-1: Experimental and modeled motored-pressure history as a function of crank angle degrees ($^{\circ}$ CA). Experimental motored-pressure trace is taken from experiment by Wissink and Reitz [4] operating at 1300 RPM and $p_{in} = 1.84$ atm.

Relevant engine parameters	
Ratio of connecting-rod length to crank radius	3.17
Compression ratio	14.88:1
Intake pressure	1.84 (atm)
Engine speed	1300 (RPM)
Parameters at initial conditions	
Initial crank angle	-25 ($^{\circ}$ CA ATDC)
Initial mean temperature, T_0	735 (K)
Initial temperature fluctuation, T'	20 (K)
Initial mean pressure, P_0	35 (atm)
EGR mass fraction	40%
EGR compositions (in mass fraction)	19% CO_2 , 8% H_2O , and 73% N_2
RCCI	
Initial mean equivalence ratio, ϕ_0	0.60
Initial mean PRF number, PRF_0	PRF70
DDFS	
Initial mean equivalence ratio before injection	0.41
Initial mean PRF number before injection	PRF55
Mean equivalence ratio after injection	0.60
Mean PRF number after injection	PRF70
Sweep of injection timing, t_{inj}	-25 to 2.3 ($^{\circ}$ CA ATDC)
Effective injection duration, t_{dur}	0.8 (ms)

Table 8-1: Engine specifications [4] and key parameters of the DNS cases. RPM, $^{\circ}$ CA ATDC, and EGR denote revolutions per minute, degrees of crank-angle after the top dead center, and exhaust gas recirculation, respectively.

8.2.2 Pseudo-*iso*-octane model

In this section, the development of a pseudo-*iso*-octane (denoted as PC_8H_{18}) model capable of resembling multiple direct injections is discussed. The PC_8H_{18} model is then used to study the influence of late injection of *iso*-octane on the ignition characteristics of PRF/air/EGR mixture under DDFS conditions.

As in the DDFS combustion [4, 31, 32], the initial mixture field is primarily composed of a uniform *iso*-octane/air mixture representative of a well-mixed charge resulting from very early gasoline injection. A stratified *n*-heptane composition is then superimposed to mimic the second injection, which corresponds to the direct injection of diesel fuel. The injection of the diesel fuel occurs prior to the TDC with insufficient time for complete mixing. Therefore, the composition inhomogeneities of the diesel fuel is to be expected. In addition, there is very little reactivity and heat release during the diesel injection event, which allows the diesel stratification to be represented through the initial condition. The last injection event is the gasoline direct injection close to the TDC, during which combustion and heat release have already commenced. Injecting nascent fuel into the system in the presence of significant heat release is especially challenging in a direct numerical simulation. This can lead to strong pressure variations and scalar gradients that cannot be handled by the dissipation free numerical methods used in the present study.

In this section, we develop the PC_8H_{18} model to simulate the effects of the late injection of gasoline with a two-step process. As a part of the initial condition, stratified *iso*-octane composition is added to the mixture field, using a pseudo-*iso*-octane molecule. The chemical species, PC_8H_{18} , that forms a stratified mixture field is non-reactive during the initial phases of the simulation. Once the simulation has advanced close to the TDC, the PC_8H_{18} species is converted to the usual reactive *iso*-octane species, $i\text{-C}_8\text{H}_{18}$. This introduces reactive *iso*-octane in the system at the appropriate juncture when gasoline injection is needed. The consumption of PC_8H_{18} and its conversion to reactive $i\text{-C}_8\text{H}_{18}$ occurs through a source term, which resembles a Gaussian function in time. The form of the Gaussian conversion function is chosen to achieve the desired timing and duration, t_{inj} and t_{dur} , of gasoline injection. This conversion step allows the effects of gasoline injection during active combustion to be simulated without numerical instability issues. While all the thermochemical and transport properties of the PC_8H_{18} are chosen to identically match those of $i\text{-C}_8\text{H}_{18}$, the enthalpy of formation of PC_8H_{18} is chosen to be lower than $i\text{-C}_8\text{H}_{18}$. This difference in the enthalpy of formation causes a drop in temperature, thereby allowing the simulations to also account for the temperature drop due to the latent heat of evaporation of direct gasoline fuel injection.

In summary, the underlying idea behind the PC_8H_{18} model is that at the beginning, PC_8H_{18} is initialized with other fuels (*n*-heptane + *iso*-octane), and acts as an inert gas. At a specific time, so-called t_{inj} , PC_8H_{18} is gradually converted to real *iso*-octane for a given time duration

of t_{dur} to participate in the combustion process. The process of converting PC_8H_{18} to $i\text{-C}_8\text{H}_{18}$ is representative of the late direct injection of gasoline [4]. For illustration, Fig. 8-2 shows that PC_8H_{18} starts to be converted to $i\text{-C}_8\text{H}_{18}$ via the Gaussian function at t_{inj} of -25°CA ATDC. The effective injection duration or the conversion time of PC_8H_{18} to $i\text{-C}_8\text{H}_{18}$, t_{dur} , of 0.8 ms is chosen as in [4] for all the DDFS cases in the present study.

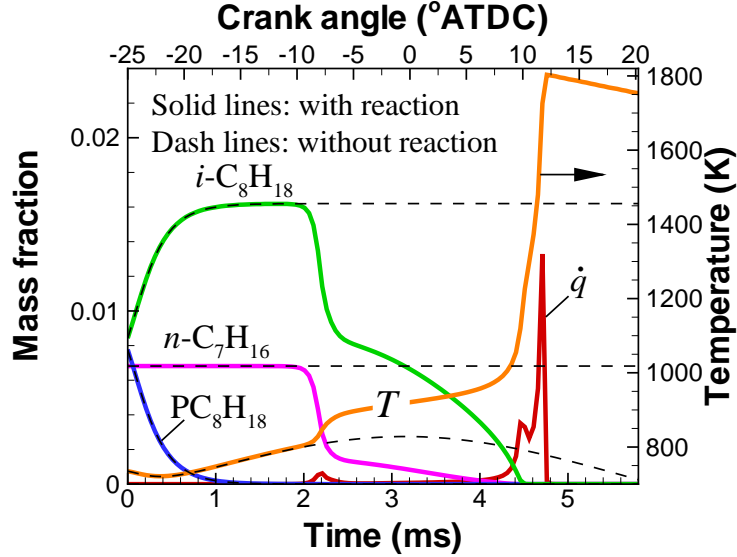


Figure 8-2: Temporal evolutions of the mass fraction of $i\text{-C}_8\text{H}_{18}$, PC_8H_{18} , and $n\text{-C}_7\text{H}_{16}$, temperature, and heat release rate of the 0-D ignition for Case 3 with and without reaction. The initial pressure, temperature, and t_{inj} are 35 atm, 735 K, and -25°CA ATDC, respectively. The effective injection duration, t_{dur} , is approximately 0.8 ms.

8.3 Initial conditions

A 116-species reduced mechanism for PRF oxidation [90] is adopted to simulate the RCCI/DDFS combustion [4]. PRF is a mixture of n -heptane and iso -octane, which have widely been used as a realistic surrogate for high- and low-reactivity fuels, diesel and gasoline, respectively. The reduced mechanism was developed from the LLNL detailed chemistry with 874 species and 3796 elementary reactions for DNSs of HCCI combustion [5,6]. The reduced mechanism was validated under a wide range of PRF composition, pressure, and temperature conditions. Details of the reduced and skeletal mechanisms for PRF oxidation can be found in [90]. The stiffness removal technique was adopted to remove any chemical timescales shorter than 10 ns [114]. PC_8H_{18} is incorporated into the 116-species mechanism [90], forming a 117-species mechanism. Note that except the difference in the number of species, the 117-species mechanism has the same features as the 116-species mechanism because PC_8H_{18} is a non-reactive species and just acts as an inert gas. Note that for RANS-based engine simulations, several compact-size reduced PRF mechanisms such as 32 species with 55 reactions [172], 41 species with 130 reactions [173],

and 73 species with 296 reactions reduced mechanisms [174] have been developed considering a trade-off between the computational efficiency and the mechanism accuracy.

The relevant engine specifications and the physical and numerical parameters for DNSs are summarized in Table 8-1–8-3. To save computational cost, all the simulations (Cases 1–8) start at -25°CA ATDC, at which the injection of *n*-heptane is assumed to be already finished. Based on the motored pressure trace with an intake pressure of 1.84 atm as shown in Fig. 8-1, the mean pressure, P_0 , at -25°CA ATDC is set to be 35 atm. The initial mean temperature, T_0 of 735 K, mean equivalence ratio, ϕ_0 of 0.60, and mean fuel, PRF_0 of PRF70, are chosen for all DNSs except for Case 1 with ϕ_0 of 0.41 and PRF_0 of PRF55. Note that in Case 1, the conversion process of PC_8H_{18} to *i*- C_8H_{18} does not occur, and hence, its overall equivalence ratio is much lower than those of the other cases. To reduce excessive HRR, EGR is added to the initial PRF/air mixture. In the present study, the composition of EGR is assumed to be the complete combustion products of stoichiometric PRF70/air mixture [118], which composes of 19% CO_2 , 8% H_2O , and 73% N_2 by mass. The EGR ratio is defined as the mass fraction of EGR in the fuel/air/EGR mixture. As in [4], a dilution level of 40% mass fraction of EGR is used for all cases. The temperature of EGR is assumed to be the same as that of the reactants.

Composition	RCCI	DDFS	Distribution
<i>n</i> - C_7H_{16}	0.324	0.324	inhomogeneous
PC_8H_{18}	-	0.324	inhomogeneous
<i>i</i> - C_8H_{18}	0.676	0.352	homogeneous
PRF_0	PRF70	PRF70	

Table 8-2: Mean mole, \bar{x} , of *n*- C_7H_{16} , PC_8H_{18} , and *i*- C_8H_{18} in RCCI and DDFS cases. Both *n*- C_7H_{16} and PC_8H_{18} fields are initialized by $x = \bar{x} + x'$, where \bar{x} of 0.324, and x' of 0.1 represent the mean value and variance, respectively.

Case	Type	t_{inj} (ms or $^\circ\text{CA}$ ATDC)	ϕ_0	PRF_0	ϕ'	PRF'	T' (K)	τ_{ig}^0 (ms)
1	BL	-	0.41	55	0.07	9.7	20	3.4
2	RCCI	-	0.60	70	0.07	7.7	20	3.2
3	DDFS	0.0 (-25.0)	0.60	70	0.10	8.3	20	4.7
4	DDFS	1.0 (-17.2)	0.60	70	0.10	8.3	20	3.6
5	DDFS	2.5 (-5.5)	0.60	70	0.10	8.3	20	3.5
6	DDFS	3.0 (-1.6)	0.60	70	0.10	8.3	20	3.6
7	DDFS	3.5 ($+2.3$)	0.60	70	0.10	8.3	20	3.8
8	DDFS	2.0 (-9.4)	0.60	70	0.10	8.3	20	-

Table 8-3: Physical parameters of the eight 2-D DNS cases. For all 2-D DNS cases, $l_e = l_{T_e} = l_{n-\text{C}_7\text{H}_{16e}} = l_{\text{P}_8\text{H}_{18e}} = 1.2$ mm, $u' = 0.4$ m/s, and $\tau_t = 3.0$ m/s. Note that Case 1 is a baseline (BL) case in which PC_8H_{18} is not converted into *i*- C_8H_{18} . t_{inj} and τ_{ig}^0 denote the injection timing and the 0-D ignition delay time, respectively. τ_{ig} represents the time at which the maximum mean HRR occurs for both 0-D and 2-D simulations and the superscript 0 denotes 0-D simulation. Case 8 has no τ_{ig}^0 due to misfire.

Six DDFS cases (Cases 3-8 in Table 8-3) are simulated by varying the injection timing of the

late *iso*-octane direct injection, t_{inj} , ranging from -25 to 2.3°CA ATDC. For the DDFS cases, both PC_8H_{18} and n -heptane are initialized so that they are inhomogeneously superimposed onto a uniform $i\text{-C}_8\text{H}_{18}/(\text{air} + \text{EGR})$ field (see Table 8-2). More specifically, both $n\text{-C}_7\text{H}_{16}$ and PC_8H_{18} fields are initialized by $x = \bar{x} + x'$, where x denotes mole of either $n\text{-C}_7\text{H}_{16}$ or PC_8H_{18} , and \bar{x} of 0.324, and x' of 0.1 represent the mean value and variance, respectively. At a given time, t_{inj} , during the simulation, PC_8H_{18} is gradually converted into $i\text{-C}_8\text{H}_{18}$ to account for the late injection process of $i\text{-C}_8\text{H}_{18}$. Note that the DNSs of Cases 3–8 are restarted from Case 1 at each t_{inj} to reduce the computational cost and minimize the effects of different initial scalar and turbulence fields.

To make a direct comparison between the DDFS and RCCI combustion, a representative case of RCCI combustion (Case 2) is simulated. Unlike the DDFS cases with both n -heptane and $i\text{-C}_8\text{H}_{18}$ fluctuations (Cases 3–7), only n -heptane concentration fluctuation is generated for Case 2. As listed in Table 8-2, $n\text{-C}_7\text{H}_{16}$ field is initialized by $x = \bar{x} + x'$, superimposed onto a uniform $i\text{-C}_8\text{H}_{18}/(\text{air} + \text{EGR})$ field. Due to the inhomogeneities in the n -heptane field, the fluctuation in the reactivity (PRF) and equivalence ratio can be attained.

Figure 8-3 shows the temporal evolutions of the pressure and HRR for 0-D ignition of Case 1 (PRF55, $\phi_0 = 0.41$), and Case 2 (PRF70, $\phi_0 = 0.60$). The corresponding 0-D ignition delays of Cases 1 & 2 are approximately 3.4 and 3.2 ms, respectively. Henceforth, τ_{ig} represents the time at which the maximum mean HRR occurs for both 0-D and 2-D simulations and the superscript 0 denotes 0-D simulation. Based on the first-stage ignition delay time, $\tau_{ig,1}^0$, of Case 1, the injection timing of $i\text{-C}_8\text{H}_{18}$ is chosen such that for Cases 3–4, it occurs prior to the beginning of the first-stage ignition, while for Cases 5–8, the injection of $i\text{-C}_8\text{H}_{18}$ occurs after the end of the first-stage ignition.

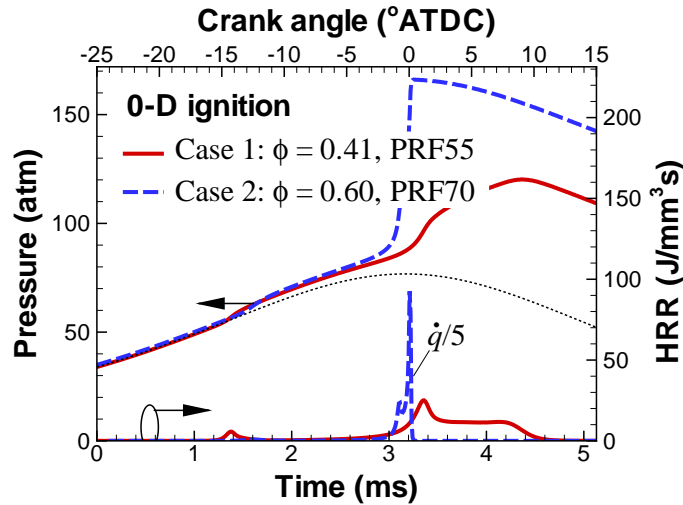


Figure 8-3: Temporal evolutions of the pressure and the HRR of the 0-D ignition for Cases 1 and 2 with the initial pressure of 35 atm and temperature of 735 K. The dot line represents the modeled motored-pressure trace.

As in [49, 51, 52, 61, 75–77, 79, 120, 122, 144, 169], the initial turbulent flow field is prescribed by an isotropic kinetic energy spectrum function of Passot and Pouquet [37]. Initial fuel concentration and temperature fields are also generated by the same energy spectrum with different random numbers. For all DNSs, the most energetic length scale, l_e , of 1.2 mm is chosen. The characteristic length scale of the concentration and temperature fields is selected identical to l_e . Turbulence intensity, u' , of 0.4 is deliberately selected to ensure that the turbulence time scale, $\tau_t = l_e/u' = 3.0$ ms, is equivalent to τ_{ig}^0 in a real HCCI engine. Due to the identical characteristic length scales and comparable time scales for turbulence and scalar fields, most effective turbulent mixing of the initial mixture can be expected in the present study [50, 53]. The representative isocontours of initial fields of ϕ and PRF are shown in Fig. 8-4 for Cases 3–8.

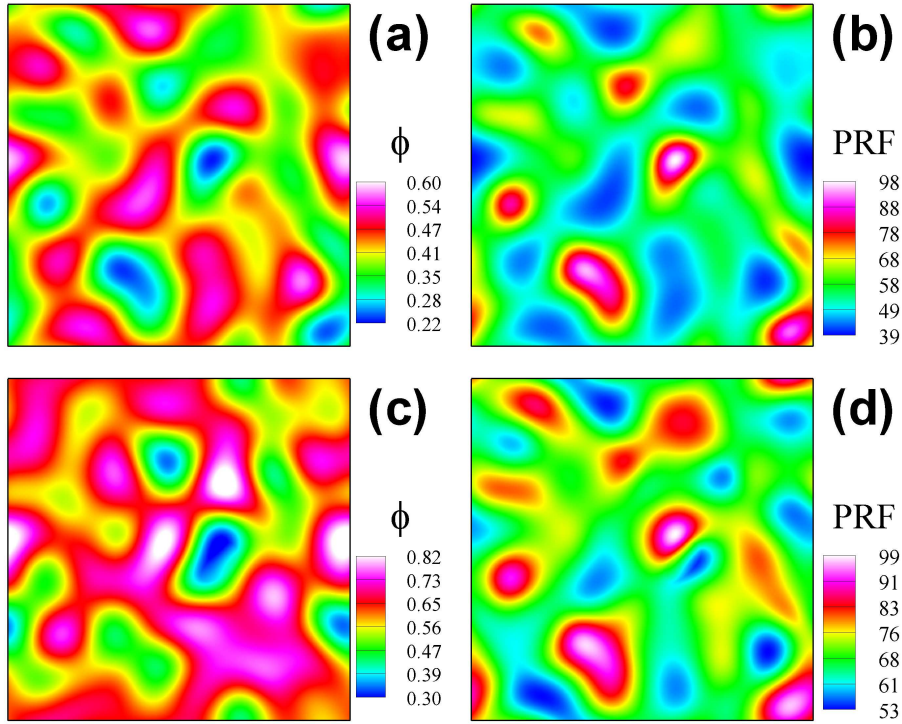


Figure 8-4: Initial ϕ and PRF fields for n -C₇H₁₆ stratification only before the injection of i -C₈H₁₈ (top) and both n -C₇H₁₆ and PC₈H₁₈ stratifications after the injection of i -C₈H₁₈ (bottom).

Wang and Rutland [175] found that at the end of the evaporation process, (i) the difference in temperature field is approximately 100 K, (ii) ϕ distribution is within a range of 0.1–0.9, and (iii) temperature is inversely proportional to ϕ due to the fuel evaporation cooling effect. These results are also consistent with recent experimental findings [46, 54, 125, 138]. Following the previous results, temperature and concentration fluctuation RMS, T' , and x' are chosen as 20 K and 0.1, respectively such that similar ranges of T and ϕ distributions can be obtained as shown in Fig. 8-4. In addition, n -heptane concentration is initialized to be negatively correlated with temperature. Inhomogeneities of n -C₇H₁₆ and/or i -C₈H₁₈ concentration, in turn, lead to

inhomogeneities in the reactivity and equivalence ratio. The corresponding equivalence ratio and PRF fluctuation for each case are listed in Table 8-3. Since diesel and gasoline fuels are direct-injected by two separate injectors at different times, the initial fields of $n\text{-C}_7\text{H}_{16}$ and PC_8H_{18} are intentionally generated to be unconnected as shown in Fig. 8-5a.

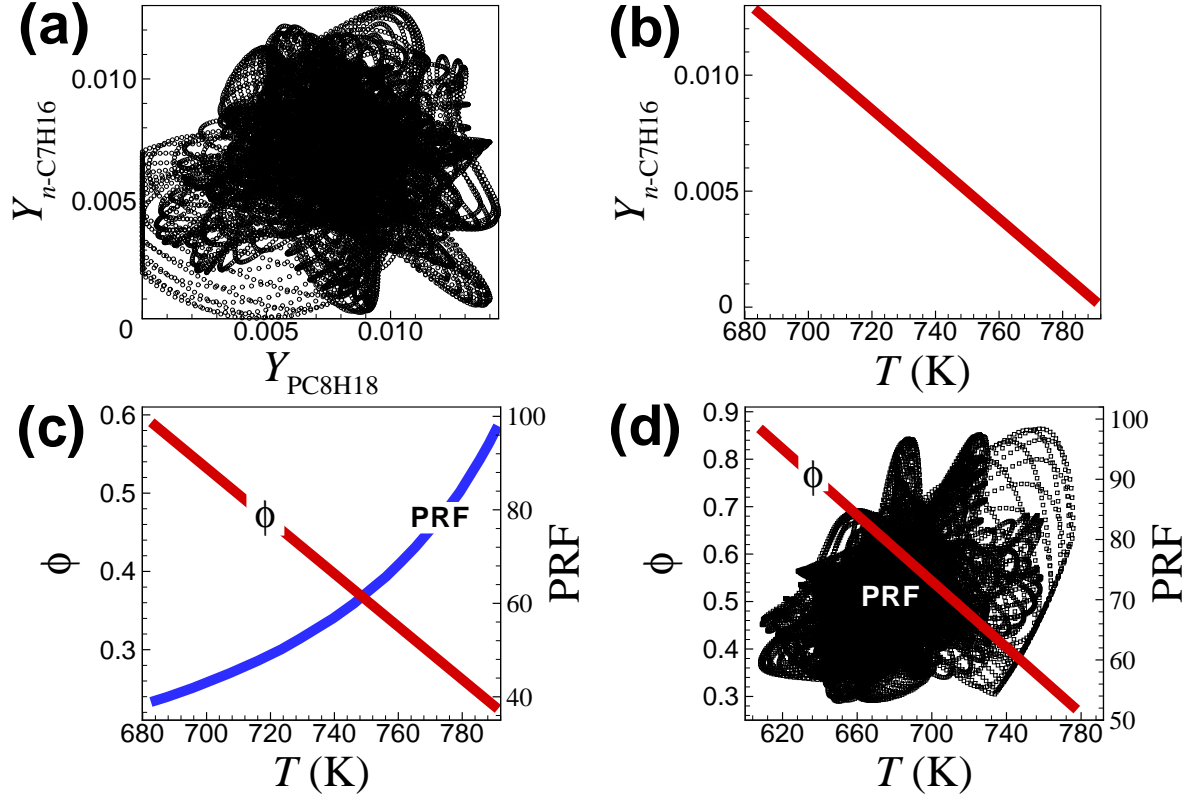


Figure 8-5: Initial distributions of (a) the mass fractions of n -heptane and pseudo- iso -octane, $Y_{n\text{-C}_7\text{H}_{16}}\text{-}Y_{\text{PC}_8\text{H}_{18}}$, (b) $T\text{-}Y_{n\text{-C}_7\text{H}_{16}}$, and (c) $T\text{-}\phi$ and $T\text{-PRF}$, and (d) the distributions of $T\text{-}\phi$ and $T\text{-PRF}$ after the injection of $i\text{-C}_8\text{H}_{18}$ for Cases 3–8.

The scatter plots in Fig. 8-5 demonstrate the relations of uncorrelated $Y_{n\text{-C}_7\text{H}_{16}}\text{-}Y_{\text{PC}_8\text{H}_{18}}$, negatively-correlated $T\text{-}Y_{n\text{-C}_7\text{H}_{16}}$, negatively-correlated $T\text{-}\phi$, and $T\text{-PRF}$ distribution before and after the $i\text{-C}_8\text{H}_{18}$ injection. As can be seen, without the late injection of $i\text{-C}_8\text{H}_{18}$, local variations in the PRF number, equivalence ratio, and temperature are connected to each other, which is quantitatively similar to those of a real RCCI engine; however, there is virtually no correlation between T and PRF after the injection of $i\text{-C}_8\text{H}_{18}$. As such, the DDFS combustion can be more effective in controlling the reactivity distribution by adjusting the timing/duration/amount of the late $i\text{-C}_8\text{H}_{18}$ injection.

The same mean mole fraction of $n\text{-C}_7\text{H}_{16}$ and PC_8H_{18} is intentionally selected (see Table 8-2), and hence, the temperature drop by the latent heat of evaporation from the direct injection of either $n\text{-C}_7\text{H}_{16}$ or $i\text{-C}_8\text{H}_{18}$ is likely to be the same. Therefore, a difference in the enthalpy of formations of PC_8H_{18} and $i\text{-C}_8\text{H}_{18}$ is chosen equal to 90,000 erg/mole. This results in a

temperature-drop field (see Fig. 8-6b), which accounts for the evaporation cooling effect of i - C_8H_{18} injection. The corresponding variance of the temperature drop is approximately 19.2 K. As shown in Fig. 8-6, the range of each temperature field is nearly the same as approximately 100 K.

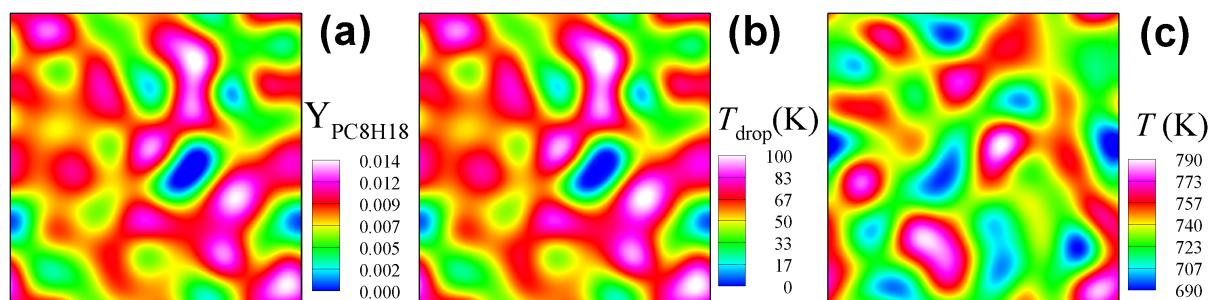


Figure 8-6: Isocontours of (a) initial PC_8H_{18} field, (b) its corresponding T_{drop} field ($T' = 19.2$ K) after the conversion of PC_8H_{18} to i - C_8H_{18} for Cases 3–8, and (c) initial temperature field with $T' = 20$ K for all Cases 1–8.

A 2-D computational domain of 3.2×3.2 mm² with 1280×1280 grids points was used for all DNSs. The corresponding grid resolution is 2.5 μ m. This fine grid resolution is needed to resolve thin flame structures at high pressure. The DNSs were performed on Shaheen, a 36 rack Cray XC40 system, at King Abdullah University of Science and Technology (KAUST). Each of the DNSs consumed approximately 0.3 million CPU-hours.

8.4 Results and discussion

8.4.1 Overall combustion characteristics

In this section, the effects of t_{inj} on the combustion characteristics of the DDFS combustion (Cases 3–7) are investigated by examining and comparing the temporal evolutions of the mean pressure and the mean HRR with those of the RCCI combustion (Case 2) as shown in Fig. 8-7. Several points are to be noted. First, it is readily observed from the figure that Cases 3–7 (DDFS combustion) exhibit much lower peak HRR and longer combustion duration than Case 2 (RCCI combustion) and its corresponding 0-D ignition. This is primarily attributed to elongated combustion by the sequential conversion of PC_8H_{18} to i - C_8H_{18} in the DDFS combustion.

Despite the presence of the reactivity inhomogeneity in Case 2, however, an excessive HRR occurs due to a very short combustion duration similar to the 0-D ignition. This is mainly because the ignition delay decreases exponentially with increasing pressure during the compression stroke [176], which eventually removes the differences in the ignition delays of local fuel/air

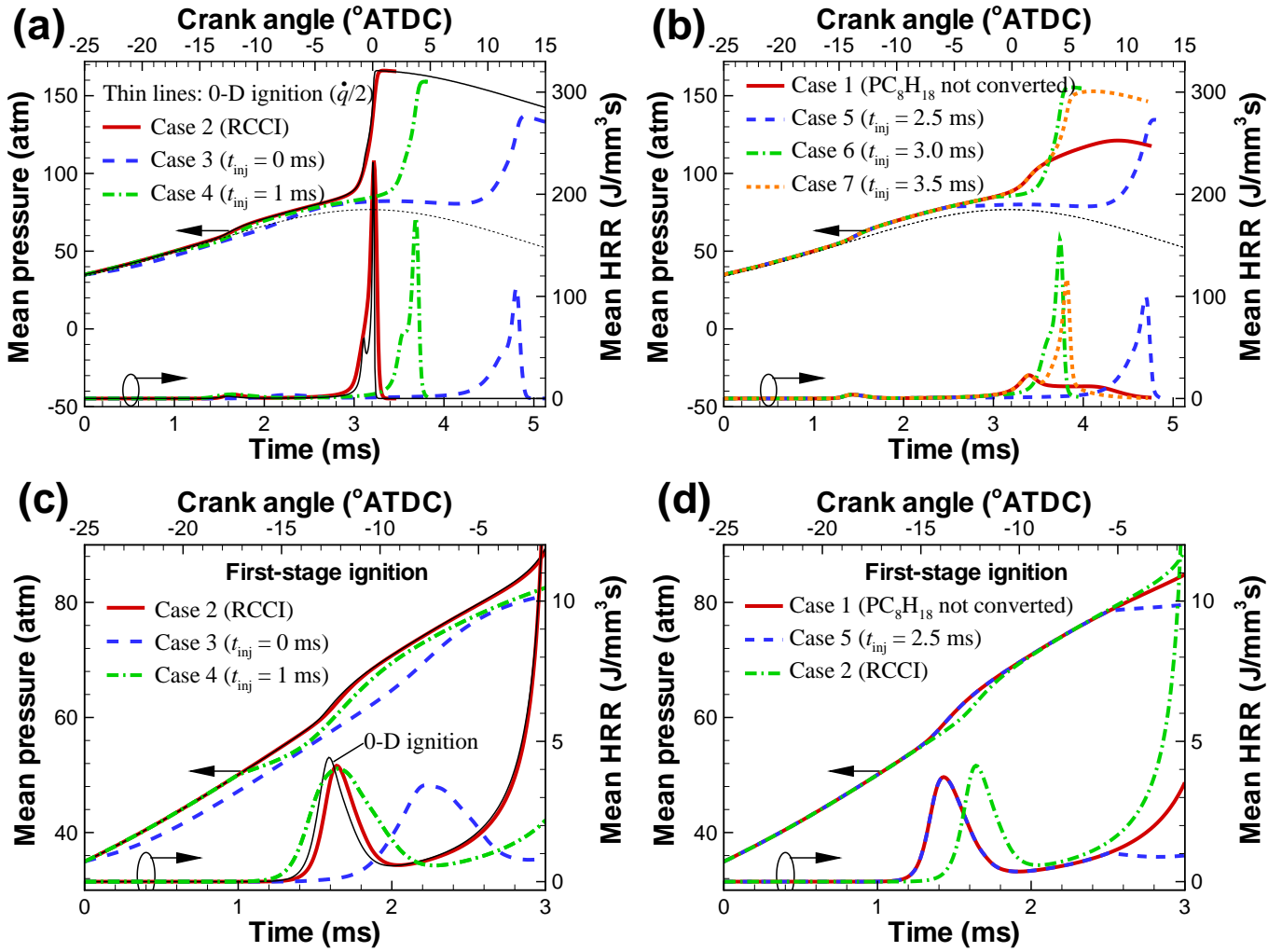


Figure 8-7: Temporal evolutions of the mean pressure and the mean HRR for Cases 1–7 (top), and the mean HRR during the first-stage ignition (bottom). During the first-stage ignition, the temporal evolutions of the mean HRR for Cases 6 and 7 are identical to that of Case 1.

mixtures in Case 2. As such, the RCCI combustion is more likely to occur by the spontaneous ignition mode of combustion rather than the deflagration mode as in the conventional HCCI combustion [142]. In addition, the uncontrolled HRR of Case 2 implies that under very high-pressure condition by the intake boosting as in the present study, an alternative fuel-delivery method like the DDFS should be utilized to alleviate such an excessive HRR. Note that for Case 1, the conversion process of PC₈H₁₈ to *i*-C₈H₁₈ does not proceed, and hence, its overall equivalence ratio is much lower than those of other cases, leading to the lowest peak HRR. In addition, the widely-distributed HRR in Case 1 is due to the slowdown of the high-temperature chemistry (HTC) of the PRF oxidation under such extremely-diluted conditions as Case 1 with $\phi_0 = 0.41$ and 40% EGR [43].

Second, the overall DDFS combustion is delayed compared to the RCCI combustion regardless of the injection timing, t_{inj} . This can simply be understood by the effects of the late delivery of *iso*-octane and subsequent evaporating cooling on the DDFS combustion. Moreover,

it is also observed that the ignition delay, τ_{ig} , of Cases 3–7 features a non-monotonic behavior with increasing t_{inj} : i.e. τ_{ig} first decreases from $t_{inj} = 0$ to 1.0 ms; it increases from $t_{inj} = 1.0$ to 2.5 ms; it decreases again from $t_{inj} = 2.5$ to 3.0 ms; finally, it increases a little bit from $t_{inj} = 3.0$ to 3.5 ms. This non-monotonic behavior of τ_{ig} is also attributed to the evaporation cooling effect of directly-injected i -C₈H₁₈ together with its injection timing relative to the first- and second-stage ignition of the baseline case (Case 1). Prior to examining the DNS cases, it should be noted that a misfire occurs for Case 8 with $t_{inj} = 2.0$ ms because the temperature drop by the injection of i -C₈H₁₈ prohibits the occurrence of the main combustion at the right moment. This issue will be discussed in the following section.

For Case 3, the direct injection of i -C₈H₁₈ is finished much earlier than the onset of the first-stage ignition of the baseline case. Therefore, the drop of temperature and pressure by the evaporation cooling of i -C₈H₁₈ (i.e. $\Delta T \approx 54$ K and $\Delta P_t \approx 2.8$ atm at the end of i -C₈H₁₈ injection) is large enough to delay the occurrence of the first-stage ignition, thereby retarding the main combustion significantly. For Case 4, however, i -C₈H₁₈ is gradually supplied during the early stage of the first-stage ignition as shown in Fig. 8-7c, and hence, the drop of temperature and pressure becomes marginal (i.e. $\Delta T \approx 24$ K and $\Delta P_t \approx 1.3$ atm), which consequently delays the main combustion to a small extent compared to that of Case 3.

On the contrary, the ignitions of Cases 5–7 exhibit different characteristics compared to those of Cases 3 and 4 due to t_{inj} greater than $\tau_{ig,1}$ of the baseline case. The injection of i -C₈H₁₈ for Case 5 starts at $t_{inj} = 2.5$ ms (-5.5°CA ATDC). At this moment, the temperatures of local mixtures are in the range of 930 to 946 K (see Fig. 8-8a) which corresponds to the intermediate-temperature chemistry (ITC) regime of the PRF oxidation [5–7, 156]. For Cases 6 and 7, the PC₈H₁₈ conversion to i -C₈H₁₈ starts at 3.0 and 3.5 ms, respectively, at which the temperature range of local mixtures (e.g., $1050 \leq T \leq 1270$ for Case 7 as shown in Fig. 8-8b) corresponds to the HTC regime. Therefore, the i -C₈H₁₈ injection comes to affect the ITC for Case 5 and the HTC for Cases 6 and 7, respectively.

More specifically, the overall combustion of Case 5 is more delayed than those of Cases 6 and 7 due to the adverse effect of temperature drop on the ITC. This is manifested in the retardation of the main ITC reactions: $\text{H} + \text{O}_2 + \text{M} \rightarrow \text{HO}_2$ (R1), $\text{RH} + \text{HO}_2 \rightarrow \text{R} + \text{H}_2\text{O}_2$ (R2), and $\text{H}_2\text{O}_2 + \text{M} \rightarrow \text{OH} + \text{OH} + \text{M}$ (R3), where RH represents a fuel molecule. In general, the hydrogen peroxide decomposition reaction of R3, which is one of the key reactions to initiate the HTC in the second-stage ignition, becomes active above approximately 1000 K [145, 146], and hence, the mixtures need a longer time to overcome the temperature drop and render the HTC to start.

To verify the effect of temperature drop on the ITC and HTC of Cases 5 and 7, the temporal evolutions of the mean mass fractions of fuel and important minor species are shown in Fig. 8-9

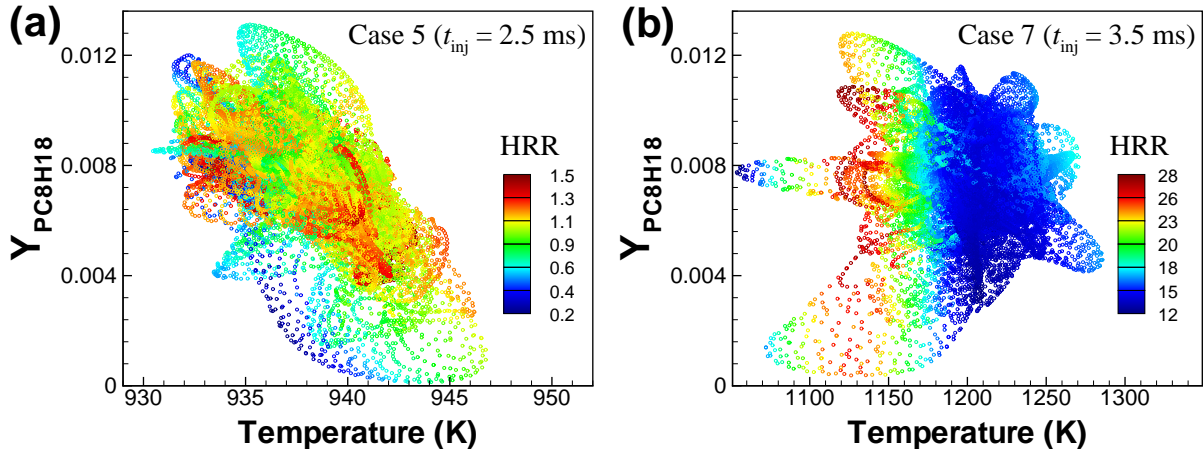


Figure 8-8: Scatter plots of temperature and the mass fraction of pseudo-*iso*-octane colored by the heat release rate for (a) Case 5 at t_{inj} of 2.5 ms, (b) Case 7 at t_{inj} of 3.5 ms.

together with those of the mean temperature and HRR. It is readily observed from the figure that for Case 5, the mass fraction of *i*-C₈H₁₈, $Y_{i-C_8H_{18}}$, increases right after the conversion of PC₈H₁₈ to *i*-C₈H₁₈ and then, decreases while $Y_{H_2O_2}$ also keeps increasing till the start of the second-stage ignition. For Case 7, however, $Y_{i-C_8H_{18}}$ keeps decreasing even after the *i*-C₈H₁₈ injection and $Y_{H_2O_2}$ almost vanishes prior to the *i*-C₈H₁₈ injection. These results demonstrate that for Case 5, the temperature drop by the *i*-C₈H₁₈ injection retards the decomposition and consumption of *i*-C₈H₁₈ and prohibits the H₂O₂ decomposition, consequently delaying the beginning of the high-temperature heat release (HTHR). Moreover, they also indicate that for Case 7, the effect of temperature drop on the HTC is marginal because under the HTC regime, the injected *i*-C₈H₁₈ immediately converts into small fragments, down to CH₂O, HCO, H₂O₂, HO₂, and CO due to highly active HTC and hence, the HTHR easily overcomes the temperature drop induced by *i*-C₈H₁₈ injection.

Third, unlike Cases 3–5 in which the ignition characteristics such as the ignition timing and combustion duration are not well controlled by the injection of *i*-C₈H₁₈, the main combustion in Cases 6 and 7 occurs right after the beginning of the *i*-C₈H₁₈ injection. As explained above, the fuel/air charge in Cases 6 and 7 has already undergone the HTC regime before the injection of *i*-C₈H₁₈. Under the HTC regime, the injected *i*-C₈H₁₈ burns immediately, and hence, the consumption of *i*-C₈H₁₈ coincides with the production of heat. As such, the injection rate of *i*-C₈H₁₈ directly controls the consumption rate of *i*-C₈H₁₈, which in turn governs the rate and peak of heat release of the main combustion. These results are consistent with those in Wissink and Reitz [4, 31]. They demonstrated that the DDFS combustion is controlled by the mixing of the directly-injected fuel, which is referred to as ‘diffusion-limited injection’. The timing and duration of the diffusion-limited injection allows a precise control of the HRR and PRR of the DDFS combustion. They also found that the late direct fuel injection should start after the end

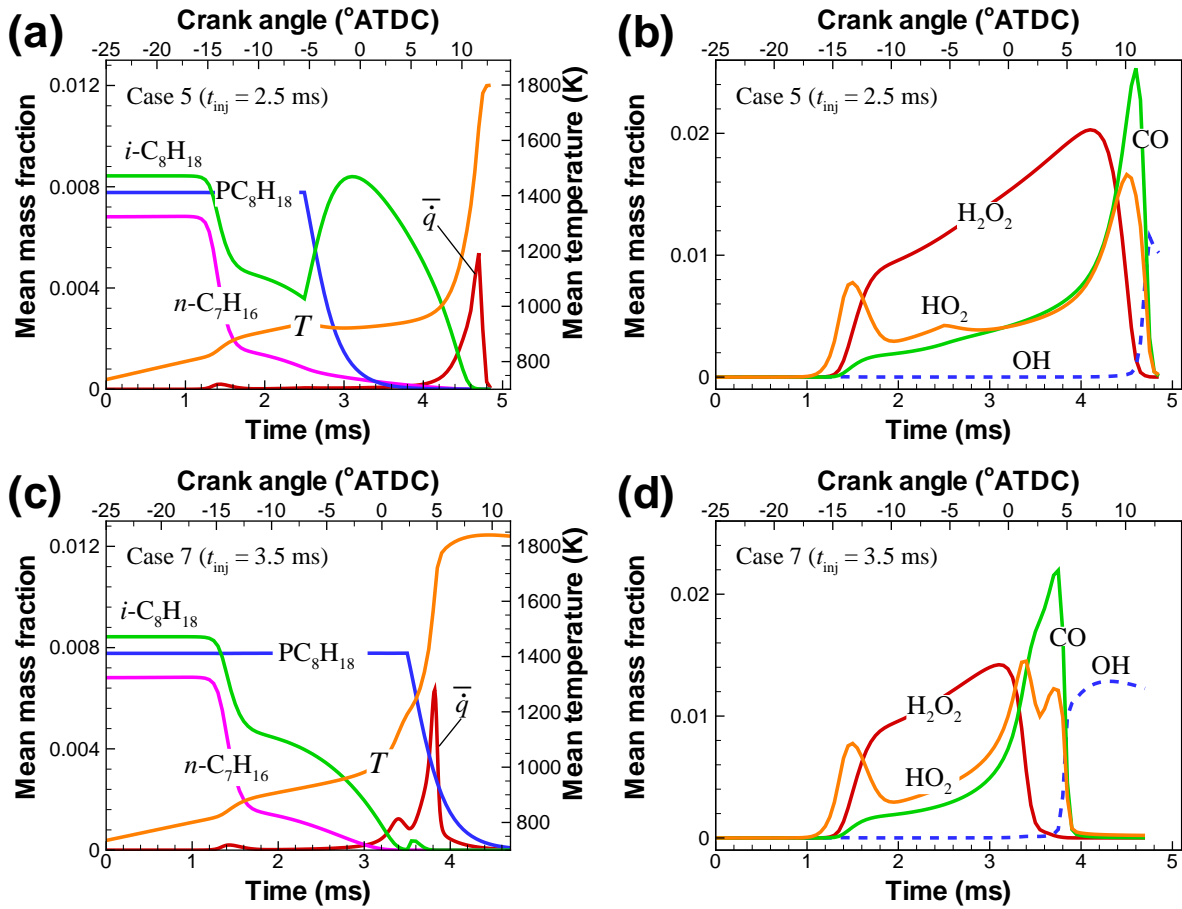


Figure 8-9: Temporal evolutions of the mean mass fraction of the fuels, temperature, and HRR (left), and important minor species (right) for Cases 5 (top) and 7 (bottom). In order to display in the same scale, the mean mass fractions of H_2O_2 , OH , and HO_2 species are increased by a factor of 8, 100, and 100, respectively.

of the LTHR to fully utilize the advantage of the diffusion-limited injection while the t_{inj} also needs to be adjusted by considering a trade-off between NO_x and soot emissions.

In summary, the DDFS combustion can be used as an alternative to HCCI combustion under very high-pressure conditions because it can effectively control the ignition timing and alleviate the peak HRR by adjusting the injection timing. Furthermore, the DDFS combustion can precisely control the occurrence of the main combustion especially when the direct injection of fuel starts during the HTC regime.

8.4.2 Combustion mode analysis

In previous studies [20, 52], it was found that as the degree of thermal inhomogeneity of the fuel/air charge increases at the onset of the main combustion, the overall combustion is more likely to occur by the deflagration mode of combustion, which in turn reduces the peak HRR by slowing down the overall combustion process and prolonging the combustion duration. In

addition, it was also found that the negatively-correlated $T - \phi$ distribution in the mixture has an adverse effect on the HCCI combustion because the evaporation cooling effect of direct fuel injection offsets that of mixture inhomogeneity by narrowing the differences in the ignition delays of local fuel/air mixtures with different reactivity, consequently leading to a shorter combustion duration and an excessive HRR [20,90,98,99,121,124]. Recently, Bansal et al. [124] demonstrated that the HCCI combustion with compression heating is more apt to occur by the spontaneous ignition mode than that under constant volume because the compression heating tends to reduce temperature gradients before the main combustion.

As one of the variants of the HCCI combustion, therefore, the DDFS combustion has both advantages and disadvantages over the HCCI combustion in developing the deflagration mode of combustion. To investigate the effects of the late injection of $i\text{-C}_8\text{H}_{18}$ into the burning charge on the DDFS combustion mode, therefore, we first measure the degree of thermal inhomogeneity by evaluating the temporal evolutions of the temperature variance, T' , and the mean temperature gradient, $|\nabla T|$, for Cases 1–7 as shown in Fig. 8-10.

It is readily observed that both of T' and $|\nabla T|$ almost vanish after each first-stage ignition of Cases 3–7. Such small T' and $|\nabla T|$ prior to the main combustion are more apt to induce the spontaneous ignition fronts with a short combustion duration like Case 2. Therefore, the predominance of the spontaneous ignition mode may be expected for all the DDFS cases.

To further investigate the characteristics of instantaneous DDFS combustion mode, the isocontours of normalized HRR for Cases 1–3, 5, and 7 at different times of 15%, 40%, 50%, and 80% cumulative mean HRR are shown in Fig. 8-11. As shown in the figure, the instantaneous RCCI combustion of Case 1 and 2 seems to occur almost simultaneously throughout the entire domain by the spontaneous ignition mode. For the DDFS combustion of Cases 3 and 5, however, strong heat release occurs in several thin flame-like fronts while weak heat is also released in broad regions during the early phase of combustion (up to 50% CHRR time). During the later phase of combustion, most heat seems to be released in thicker regions by the spontaneous ignition mode. These results suggest that the spontaneous ignition mode can be predominant for the RCCI combustion while a mixed mode of combustion seems to occur in the DDFS combustion (Cases 3 and 5). Unlike Cases 3 and 5, however, the combustion of Case 7 seems to occur over a broad area by the spontaneous ignition mode.

To figure out whether the local thin reaction fronts in Case 5 are a deflagration wave or not, a budget analysis is carried out by comparing the relative magnitudes of reaction and diffusion terms of a given species equation as in [105,124,142,177]. For the analysis, CO radical is adopted because it is one of the most important species in a deflagration wave via its conversion reaction to CO_2 (i.e. $\text{CO} + \text{OH} \rightarrow \text{CO}_2 + \text{H}$) [5–7,146,156]. Figure 8-12 shows the isocontours of the

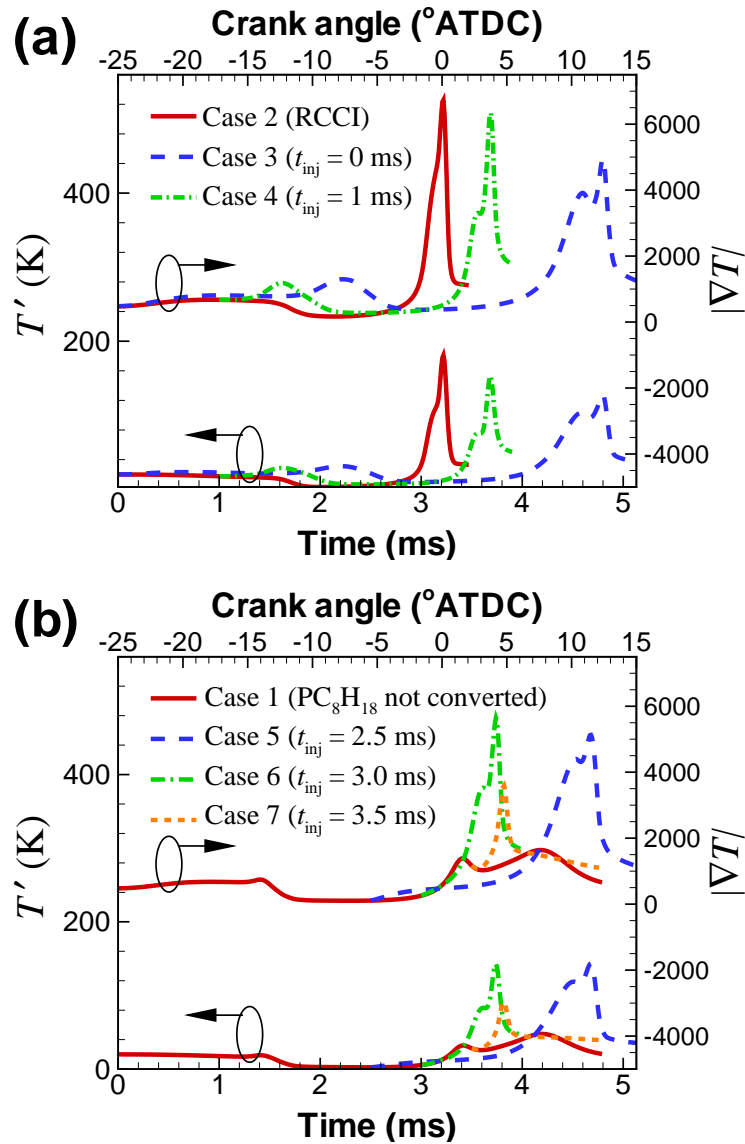


Figure 8-10: Temporal evolutions of the mean temperature fluctuation RMS and the mean temperature gradient for Cases 1–7.

normalized HRR and the scatter plot and several cut plots of the reaction and diffusion rates of CO at 40% CHRR time.

As shown in the scatter plot of Fig. 8-12b, the reaction terms generally have much greater absolute values than the diffusion terms, which implies that the DDFS combustion of Case 5 occurs primarily by the spontaneous ignition mode rather than the deflagration mode. However, the peak HRR coincides with the peak diffusion and reaction rates of CO species, which also corresponds with the thin reaction fronts in Fig. 8-12a. This is one of the characteristics of a deflagration wave, suggesting that the thin reaction fronts can be a deflagration wave. Note that in the diffusive limit of 1-D laminar simulations, where the diffusive limit represents deflagration wave propagation without auto-ignition [49, 53, 79], the reaction term of CO is $2 \sim$

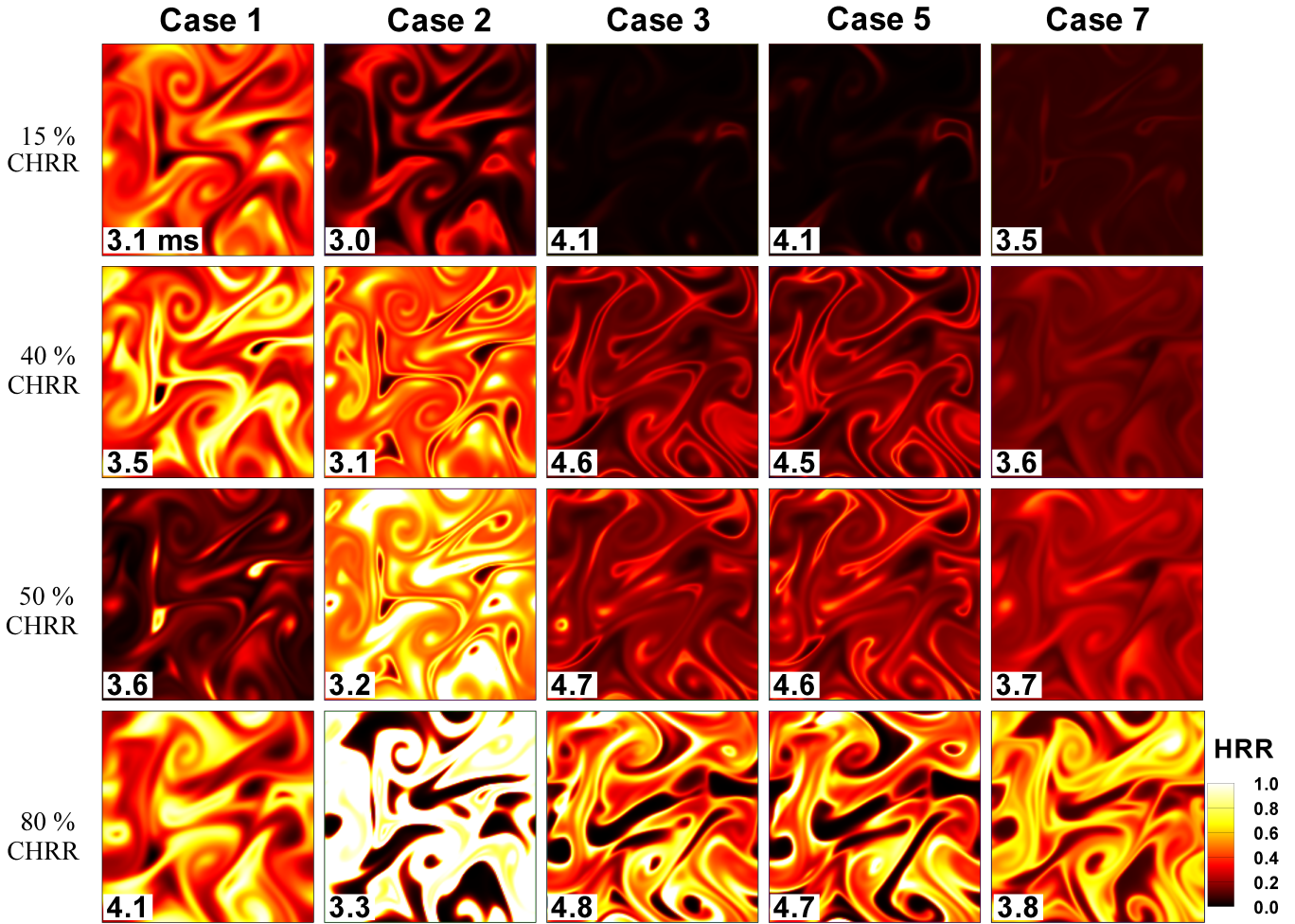


Figure 8-11: Isocontours of normalized HRR for Cases 1–3, 5, and 7 (from left to right) at times of 15% (first row), 40% (second row), 50% (third row) and 80% (last row) cumulative heat release rate (CHRR).

4 times greater than its diffusion term. This is because although the reaction front propagates under the diffusive limit, the mixture upstream of the front is already highly reactive, and thus, the reaction term is somewhat larger than the diffusion term.

The local cut plots of the reaction fronts verify their characteristics as a deflagration wave. As readily observed in the cut plots of A, B, and D in Fig. 8-12, the absolute values of diffusion rates are comparable to the reaction rates, considering their relative magnitudes in the diffusive limit. This indicates that the reaction fronts of A, B, and D are representative of a deflagration wave. Note that the combustion wave at cut C results from a meroence of two deflagration waves, and as such, the reaction term is significantly greater than the diffusion term.

Finally, the Damköhler number analysis is performed to quantitatively evaluate the deflagration mode of combustion. The Damköhler number, Da , is defined as [7, 49, 50, 52, 53, 90, 121, 144]:

$$Da = \frac{\dot{\omega}_k}{|-\nabla \cdot (\rho Y_k \mathbf{V}_k)|}, \quad (8.4.1)$$

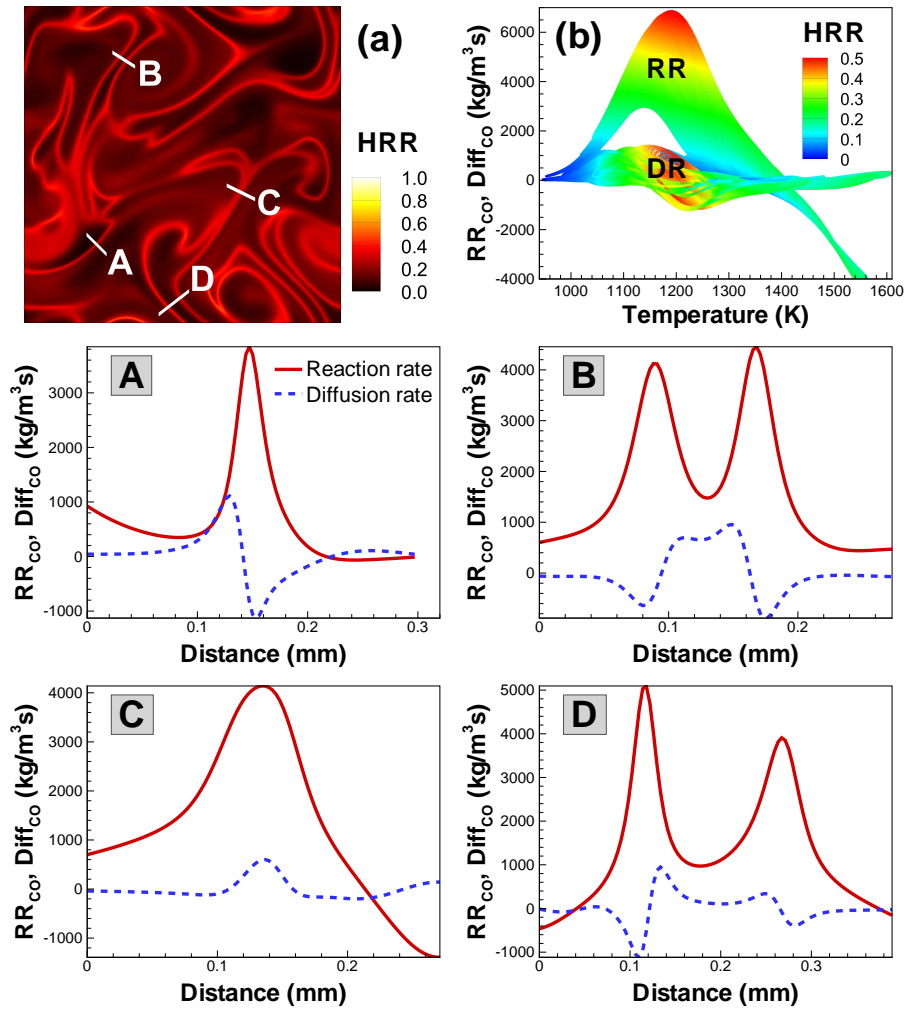


Figure 8-12: (a) Isocontours of normalized HRR, (b) scatter plot of temperature versus reaction and diffusion rates of CO colored by normalized HRR for Case 5 at 4.5 ms (40% cumulative HRR), and (A)–(D) spatial profiles of reaction and diffusion rates of CO along each cut line in (a).

where Y_k , \mathbf{V}_k , and $\dot{\omega}_k$ denote the mass fraction, diffusion velocity, and net production rate of species k , respectively. $Y_c \equiv Y_{\text{CO}_2} + Y_{\text{CO}}$ is used for the Damköhler number analysis. As mentioned above and in previous studies [7, 49, 52, 121, 144], Da value in the diffusive limit is found to be approximately 4.0 through a series of 1-D laminar simulations of which initial conditions are the same as those of the 2-D DNSs. As such, local combustion is determined to occur by the deflagration mode when its Da is less than 4.0.

Figure 8-13 shows the temporal evolutions of the fraction of HRR from the deflagration mode for Cases 1–7. It is readily observed that up to 30% of heat is released in the deflagration mode between the first- and second-stage ignition. During the main combustion, however, most of heat release occurs in the spontaneous ignition mode. As a result, the total heat release from the deflagration mode for Cases 3 and 5 is approximately 5.5% while those for other Cases are less than 3%.

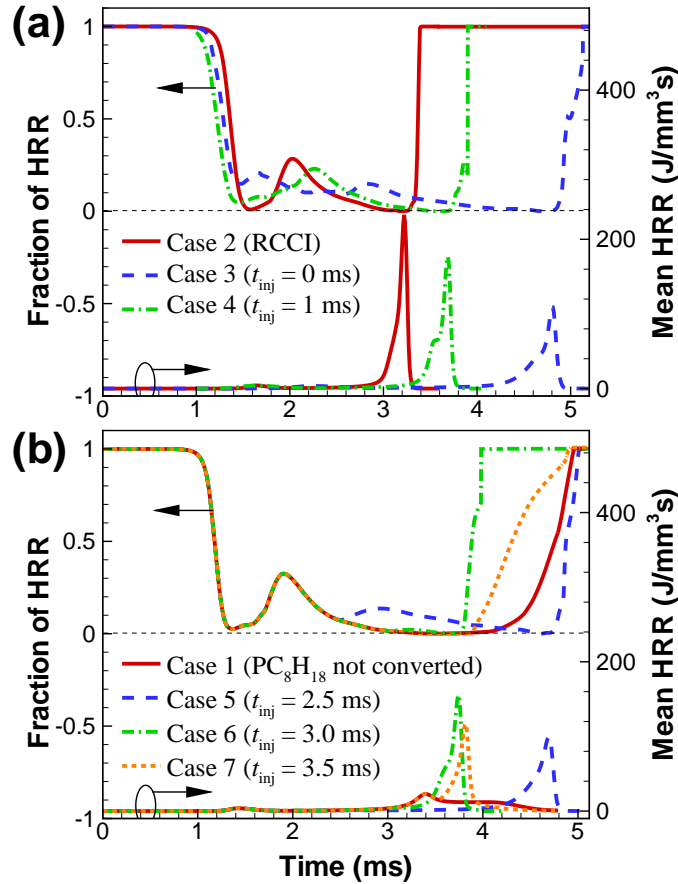


Figure 8-13: Temporal evolutions of the fraction of HRR from the deflagration mode and the mean HRR for Cases 1–7.

In summary, the budget analysis and the Damköhler number analysis verify that although a mixed combustion mode of both deflagration and spontaneous ignition exists during the early phase of the DDFS combustion (Cases 5 and 7), the spontaneous ignition is the dominant combustion mode for both DDFS and RCCI combustion. These results suggest that the spread-out of the HRR in the DDFS combustion is attributed not to the deflagration but to the sequential injection of $i-C_8H_{18}$.

8.4.3 Misfire

As mentioned earlier, a misfire occurs for Case 8 with $t_{inj} = 2.0$ ms. It is also found from a series of 0-D simulations that a misfire occurs for the DDFS combustion with $t_{inj} = 1.3 \sim 2.2$ ms. It seems that the misfire may occur due to the large temperature drop by the late $i-C_8H_{18}$ injection. To verify the temperature drop effect on the misfire, therefore, one additional 2-D DNS (Case 9) is carried out. The initial conditions for Cases 8 and 9 with $t_{inj} = 2.0$ ms are identical except for the degree of temperature drop by the late $i-C_8H_{18}$ injection. The temperature drop by the $i-C_8H_{18}$ injection in Case 9 is set to a half of those of other DDFS

cases (Cases 3–8), which is realized by changing the difference in the enthalpy of formations of $i\text{-C}_8\text{H}_{18}$ and PC_8H_{18} from 90,000 to 45,000 erg/mole.

Figure 8-14 shows the temporal evolutions of the mean pressure and temperature, and the maximum temperature, T_{max} , together with the mean HRR and the mean mass fraction of some important species for Cases 8 and 9. As readily observed in the figure, the second-stage ignition for Case 8 fails to occur while it successfully occurs for Case 9. The misfire for Case 8 is primarily attributed to the effect of the large temperature drop by $i\text{-C}_8\text{H}_{18}$ evaporation on the combustion together with the expansion cooling effect after the TDC. The temporal evolution of the maximum T_{max} reveals that for Case 9, T_{max} increases gradually up to 1000 K at 3.6 ms (3°CA ATDC) and the main combustion commences afterwards. For Case 8, however, T_{max} remains nearly the same as approximately 970 K even after 3°CA ATDC. As mentioned earlier, this temperature is not high enough to trigger the HTC. Moreover, the mean temperature and pressure of the fuel/air charge continuously decrease after the TDC due to the expansion without significant heat release from the charge, which ultimately leads to the misfire.

To further identify the effect of temperature drop by the $i\text{-C}_8\text{H}_{18}$ injection, the instantaneous isocontours of HRR for Cases 8 and 9 at 3.6 ms are shown in Fig. 8-15. It is readily observed that for Case 8, the HRR from nascent ignition kernels becomes very weak and their corresponding local temperatures are much less than 1000 K such that the conversion of the ITC to the HTC cannot occur. On the contrary, for Case 9, the HRR from ignition kernels becomes high enough and most of the corresponding local temperatures are greater than 1000 K such that the HTC can successfully take over from the ITC as the main chemistry in the ignition kernels, eventually leading to a success of combustion.

These results indicate that a successful development of the second-stage ignition in the DDFS combustion highly depends on the degree of temperature drop by the late $i\text{-C}_8\text{H}_{18}$ injection. In RCCI engine experiments, Kokjohn et al. [125] observed a small drop of the mean pressure and temperature by a late direct injection, which is actually less than those in the present study. This is because in reality, the directly-injected fuel can occupy only a part of the engine cylinder such that the overall temperature and pressure drop is less than that considered in the present DNS configuration. In fact, the temperature drop in the present DNSs with a limited domain size represents that in a region where $i\text{-C}_8\text{H}_{18}$ fuel is directly injected.

8.5 Conclusions

The ignition characteristics of lean PRF/air/EGR mixture under the DDFS and RCCI conditions were investigated by 2-D DNSs with a 116-species reduced mechanism. The 2-D DNSs of

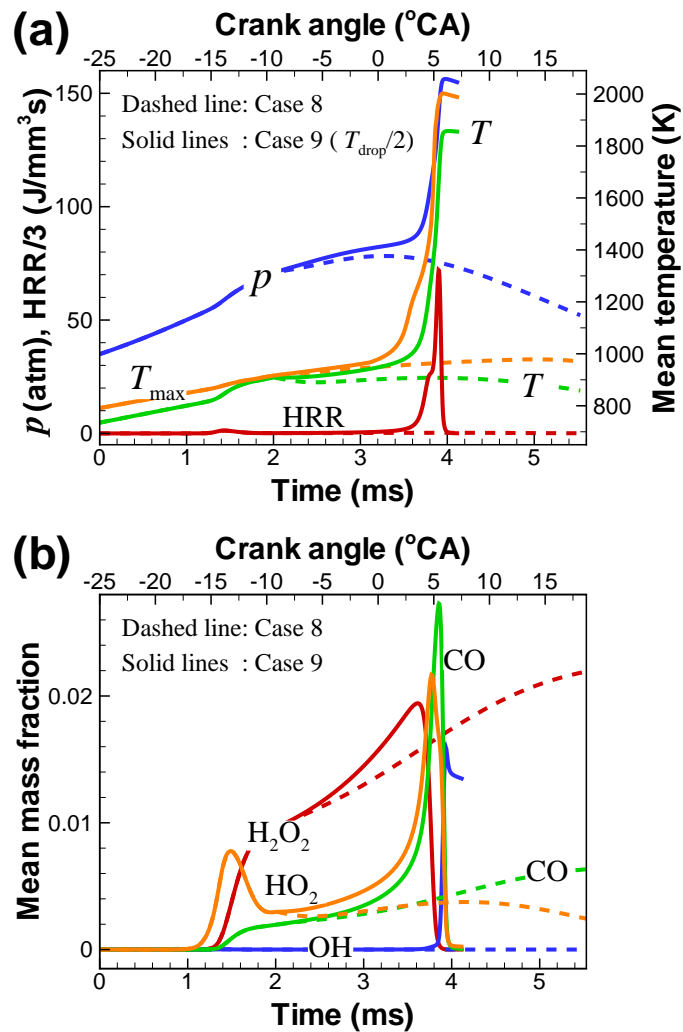


Figure 8-14: Temporal evolutions of (a) the mean pressure, the mean temperature, the mean HRR, and the maximum temperature, and (b) the mean mass fractions of OH, CO, HO₂, and H₂O₂ for Cases 8 and 9. In order to display in the same scale, the mean mass fractions of H₂O₂ and HO₂ species are increased by a factor of 8 and 100, respectively.

the DDFS combustion were performed by varying the injection timing of $i\text{-C}_8\text{H}_{18}$ with a pseudo-*iso*-octane model which was newly developed to mimic the timing, duration, and cooling effects of the direct injection of $i\text{-C}_8\text{H}_{18}$ onto a premixed background charge of PRF/air/EGR mixture. A novel compression heating model was also incorporated in the DNSs to account for the compression heating and expansion cooling effects of the piston motion in an engine cylinder.

It was found that under high-pressure conditions, the RCCI combustion occurs very fast with an excessive HRR due to the dominance of the spontaneous ignition while the DDFS combustion exhibits much lower peak HRR and longer combustion duration regardless of the fuel-injection timing because of the sequential injection of $i\text{-C}_8\text{H}_{18}$. It was also found that the ignition delay of the DDFS combustion features a non-monotonic behavior with increasing fuel-injection timing. This is primarily attributed to the evaporation cooling effect of the directly-injected $i\text{-C}_8\text{H}_{18}$ on the LTC, ITC, and HTC of the PRF oxidation, which is determined by the injection timing

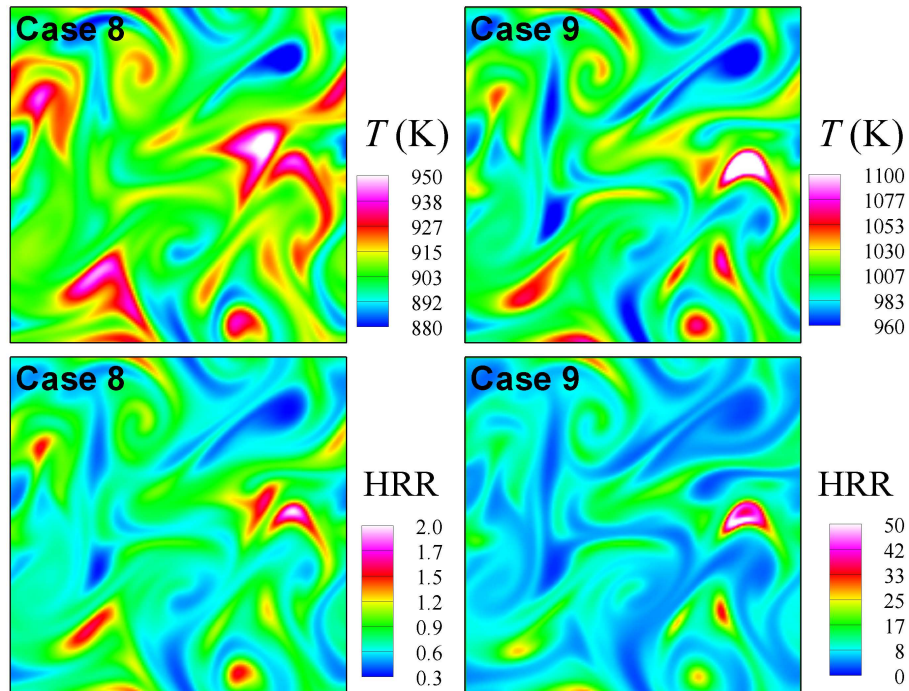


Figure 8-15: Isocontours of temperature (top) and HRR (bottom) for Cases 8 and 9 at 3.6 ms (3°CA ATDC).

relative to the first- and second-stage ignition of the baseline case. Especially when $i\text{-C}_8\text{H}_{18}$ is delivered during the second-stage ignition, the injection rate of $i\text{-C}_8\text{H}_{18}$ can directly control its consumption rate due to the highly-reactive HTC, which in turn manipulates the rate and peak of heat release of the main combustion. It was further identified from the budget and Damköhler number analyses that although a mixed combustion mode of both deflagration and spontaneous ignition exists during the early phase of the DDFS combustion, the spontaneous ignition becomes predominant for the main DDFS combustion, and hence, the spread-out of HRR in the DDFS combustion is solely determined by the direct injection process of $i\text{-C}_8\text{H}_{18}$. Finally, a misfire was observed in the DDFS combustion when the direct injection of $i\text{-C}_8\text{H}_{18}$ occurs during the ITC regime between the first- and second-stage ignition. This is mainly because the temperature drop induced by the direct injection of $i\text{-C}_8\text{H}_{18}$ prevents the main ITC reactions from inducing the HTC even after the TDC, and hence, the main combustion related to the HTC fails to occur.

These results demonstrate that the DDFS combustion can allow a precise control of the combustion phasing and the peak HRR by adjusting the injection timing of $i\text{-C}_8\text{H}_{18}$. Moreover, the rate and duration of the main DDFS combustion can effectively be controlled when the direct injection of $i\text{-C}_8\text{H}_{18}$ occurs during the HTC regime.

Chapter 9

Conclusion and future work

9.1 Conclusions

This study focuses on the ignition characteristics of hydrocarbon fuels under HCCI-like conditions of elevated pressure and low temperature. HCCI-variant combustion concepts including HCCI with thermal stratification (TS), stratified-charge compression ignition (SCCI), and reactivity-controlled compression ignition (RCCI), and direct dual fuel stratification (DDFS) are systematically investigated using direct numerical simulations (DNS). DNSs allow better understandings of the ignition process (i.e. combustion modes, flame speed, turbulence-chemistry interactions, controlling species and reactions) of different fuel/air compositions under the HCCI-like conditions. Many hydrocarbon fuels are used including primary reference fuels (PRF)–PRF100, PRF70, PRF80, and PRF50, *n*-heptane, and biodiesel.

The key findings of the study on the ignition characteristics of different fuels under HCCI-like conditions are summarized as follows

- Regardless of the PRF composition, the mean HRR increases slowly, and the overall combustion advances as T' increases. The effect of the fuel composition on the ignition characteristics of PRF/air mixtures is also found to vanish with increasing thermal inhomogeneities. The vanishing of the fuel effect under the high degree of thermal inhomogeneities is caused by the nearly identical propagation characteristics of deflagrations of different PRF/air mixtures.
- In general, turbulence with large intensity and short timescale can effectively homogenize the initial inhomogeneous temperature and/or concentration mixtures such that the overall ignition mechanism is more apt to occur by spontaneous ignition.
- For two-stage ignition fuels, it is found that (1) for cases with ϕ' only, the overall combustion occurs more quickly and the mean HRR increases more slowly with increasing ϕ' regardless of T_0 ; (2) for cases with T' only, the overall combustion is retarded/advanced in time with increasing T' for low/high T_0 relative to the NTC regime; (3) for intermediate T_0 within the NTC regime, however, the overall combustion is slightly retarded with small T' , while being advanced with large T' , exhibiting the combined effects of both low and high T_0 near the NTC regime; (4) for cases with negatively-correlated $T - \phi$ fields, the temporal evolution of the overall combustion exhibits quite non-monotonic behavior with increasing T' and ϕ' depending on T_0 . For the cases, the negative $T - \phi$ correlation has an adverse effect on the overall combustion at low and high T_0 . However, for intermediate T_0 within the NTC regime, the negatively-correlated $T - \phi$ fields has a synergistic effect on the overall combustion by spreading out \bar{q} over time and reducing the peak \bar{q} . In short, the deflagration mode is predominant at the reaction fronts for large T' and/or ϕ' . On the

contrary, the spontaneous ignition mode prevails for cases with small T' or ϕ' , especially for cases with negative $T - \phi$ correlations.

- In the low- and intermediate-temperature regimes, the overall combustion of RCCI cases occurs earlier, and its mean HRR is more distributed over time than those of the corresponding SCCI cases. This is because PRF number stratification, PRF', plays a dominant role, and T' has a negligible effect on the overall combustion within the NTC regime. In the high-temperature regime, however, the difference between RCCI and SCCI combustion becomes marginal because the ignition of the PRF/air mixture is highly-sensitive to T' rather than PRF' and ϕ' . The portion of HRR from deflagration mode becomes larger with increasing fuel stratification.
- The key species and controlling reactions of SCCI/RCCI combustion at different locations and times are identified using chemical explosive mode analysis (CEMA). It is found that at the first ignition delay, low-temperature chemistry (LTC) represented by the isomerization of alkylperoxy radical, chain branching reactions of keto-hydroperoxide, and H-atom abstraction of *n*-heptane is predominant for both RCCI and SCCI combustion. Temperature is found to be the predominant variable, and high-temperature reactions represented by $\text{H} + \text{O}_2 \rightarrow \text{O} + \text{OH}$ are responsible for the thermal ignition. At deflagrations, temperature, CO_2 , and OH are found to be the most important variables while the conversion reaction of CO to CO_2 and high-temperature chain branching reaction of $\text{H} + \text{O}_2 \rightarrow \text{O} + \text{OH}$ are identified to be important. The conversion reaction of CO to CO_2 and hydrogen chemistry are identified as important reactions for HTHR. The overall RCCI/SCCI combustion can be understood by mapping the variation of 2-D RCCI/SCCI combustion in temperature space onto the temporal evolution of 0-D ignition.
- Finally, the PC_8H_{18} model is newly developed to mimic the timing, duration, and cooling effects of the direct injection of *i*- C_8H_{18} onto a premixed background charge of PRF/air/EGR mixture with composition inhomogeneities under direct duel fuel stratification (DDFS) conditions. It is found that the DDFS combustion has much lower peak HRR and longer combustion duration regardless of the fuel injection timing, t_{inj} , compared to those of the RCCI combustion, which is primarily attributed to the sequential injection of *i*- C_8H_{18} . The spread-out of heat release rate in the DDFS combustion is mainly governed by the direct injection process of *i*- C_8H_{18} . The ignition delay of the DDFS combustion features a non-monotonic behavior with increasing t_{inj} , due to the different effect of fuel evaporation on the low-, intermediate-, and high-temperature chemistry of the PRF oxidation.

9.2 Future research directions from DNS towards LES

Although substantial progress has been made, which has shown promise for practical application of various forms of HCCI combustion, additional research and development are needed so that these advanced combustion concepts can become viable. The existing understanding is confined mainly to the laminar flamelet or reaction-sheet regimes. However, for higher efficiencies and lower emissions, advanced combustion engines are operated under extreme conditions. Advanced combustion technology has explored new combustion regimes, which have not previously been considered in model development or validation such as LTC regime in HCCI engines. Particularly, these advanced combustion engines are operated under ultra-lean, highly-diluted, partially premixed, and elevated pressure, low-temperature conditions. Significant progress and advancements in experimental devices and diagnostic techniques have been achieved. However, the underlying understanding of the complex turbulent-chemistry interaction of premixed flames featuring high pressure and low-temperature chemistry remains inconclusive. As of today, the main impediment to the development and improvement of predictive combustion models is the lack of data. The details of experimental data are often not sufficient for rigorous analysis of model deficiencies. Therefore, the demand for accurately predictive modeling capabilities of partially-premixed combustion process of advanced engines operated under the extreme conditions of higher Reynolds and Karlovitz numbers is higher than ever.

In experiments, it is challenging or even impossible to obtain such detailed richness of all desired quantities from DNSs. High-fidelity DNSs taking advantage of the petascale-to-exascale hybrid computing architectures coupled with more-accurate mathematical schemes, therefore, keep playing a pivotal role in unraveling complex dynamics of turbulence-flame interactions [178, 179]. Landmark DNS simulations with maximum achievable scales and parameter ranges have been already underway. Well-defined canonical DNS simulations can help to discover the further understanding of the underlying physical mechanisms of critical phenomena encountered in advanced combustion concepts. The huge amount of dataset from such DNS simulations will provide a large ensemble for the development and validation of turbulent combustion models. The DNS results are also capable of directing comparison and cross-validation against laser diagnostic measurements. These accurate turbulent combustion models will be used in the optimal design of industrial combustion engines to reduce development costs. As such the full potential of highly-efficient ultra-low-emission combustion engines could be realized.

Despite the advantages of DNS approach, however, there is still a gap to bridge between these combustion devices and state-of-the-art DNS studies. Recently, large-eddy simulations (LES) has become more affordable in the design, research and development of combustion devices. LES takes advantage of resolving the large-scale turbulent structures whereas only the small-scale turbulent structures require to be modeled. Moreover, LES allows capturing the

large-scale unsteadiness of flow and combustion. Rapid advances in LES modeling accompanied by simultaneous progress in computer science as well as computer hardware have enabled LES of realistic combustion geometries [178, 180, 181]. Because of these reasons, the present study could be extended to the following research directions.

- High fidelity DNSs studies will help address the knocking issues in the direct-injected, boosted, downsized SI/GDICI/SACI engines. Downsize by boosting is being a major development trend for advanced LTC engines. Therefore the fundamental understanding of the knocking mechanism becomes more and more critical for accurate knock and superknock prediction, and ultimately prevent knocking [182–186].
- Cool flame is an essential phenomenon associated with the low-temperature combustion engines that significantly affects the combustion dynamics [187, 188]. Cool flame may result in flame instabilities, cycle-to-cycle variations, losing combustion phasing control, and knocking in advanced engines. However, a rational understanding of the cool flame behavior and its effect on high-temperature ignition is still questionable [189, 190]. DNSs with the capability of resolving all temporal and spatial scales can complement physical experiments supposed that a well-defined configuration such as a co-flow of two different fuels of gasoline and diesel are appropriately set up.
- By performing OpenFOAM-based LES simulations with a realistic geometry, we can elucidate more multi-physics effects and realistic combustion scenarios. In particular, HCCI combustion process can be investigated using OpenFOAM-based LES approach by incorporating the compression-heating model and pseudo-iso-octane model with a realistic computational geometry [180, 181, 191].
- Finally, the available DNS dataset of RCCI/SCCI studies can be used for the development of CMC models using OpenFOAM [134, 135, 192].

In conclusion, thanks to the rapid growth of computational capabilities, DNS studies of turbulent combustion coupled with the LES-based simulations will be an increasingly prominent research tool in future combustion modeling and model development. Furthermore, they will help to address scientific combustion questions such as combustion instabilities, IC engine knocking phenomena, etc.

References

- [1] J. E. Dec, Advanced compression-ignition engines—understanding the in-cylinder processes, *Proc. Combust. Inst.* 32 (2009) 2727–2742.
- [2] A. McIlroy, G. McRae, V. Sick, D. L. Siebers, C. K. Westbrook, P. J. Smith, C. Taatjes, A. Trouve, A. F. Wagner, E. Rohlfing, D. Manley, F. Tully, R. Hilderbrandt, W. Green, D. Marceau, J. O’Neal, M. Lyday, F. Cebulski, T. R. Garcia, D. Strong, Basic research needs for clean and efficient combustion of 21st century transportation fuels, US Department of Energy Report (2006) <https://www.osti.gov/scitech/servlets/purl/935428>.
- [3] A. B. Dempsey, S. J. Curran, R. M. Wagner, A perspective on the range of gasoline compression ignition combustion strategies for high engine efficiency and low no_x and soot emissions: Effects of in-cylinder fuel stratification, *Int. J. Engine Res.* 17 (2016) 897–917.
- [4] M. Wissink, R. D. Reitz, Direct dual fuel stratification, a path to combine the benefits of RCCI and PPC, *SAE Int. J. Engines* 8 (2015) 878–889.
- [5] H. J. Curran, P. Gaffuri, W. J. Pitz, C. K. Westbrook, A comprehensive modeling study of *n*-heptane oxidation, *Combust. Flame* 114 (1998) 149–177.
- [6] H. J. Curran, P. Gaffuri, W. J. Pitz, C. K. Westbrook, A comprehensive modeling study of *iso*-octane oxidation, *Combust. Flame* 129 (2002) 253–280.
- [7] M. B. Luong, G. H. Yu, T. Lu, S. H. Chung, C. S. Yoo, Direct numerical simulations of ignition of a lean *n*-heptane/air mixture with temperature and composition inhomogeneities relevant to HCCI and SCCI combustion, *Combust. Flame* 162 (2015) 4566–4585.
- [8] R. Reitz, Directions in internal combustion engine research, *Combust. Flame* 160 (2013) 1–8.
- [9] J. Voelcker, 1.2 billion vehicles on world’s roads now, 2 billion by 2035: Report, *Green car Reports* 7 4.

-
- [10] F. Zhao, T. W. Asmus, D. N. Assanis, J. E. Dec, J. A. Eng, P. M. Najt, Homogeneous Charge Compression Ignition (HCCI) Engines: Key Research and Development Issues, illustrated edition Edition, SAE International, 2003.
- [11] H. Zhao (Ed.), HCCI and CAI Engines for the Automotive Industry, 1st Edition, Elsevier, 2007.
- [12] M. Yao, Z. Zheng, H. Liu, Progress and recent trends in homogeneous charge compression ignition (HCCI) engines, *Prog. Energy Combust. Sci.* 35 (2009) 398–437.
- [13] J. E. Dec, A conceptual model of DI diesel combustion based on laser-sheet imaging, SAE paper (1997) 970873.
- [14] T. Kitamura, T. Ito, J. Senda, H. Fujimoto, Mechanism of smokeless diesel combustion with oxygenated fuels based on the dependence of the equivalence ration and temperature on soot particle formation, *Int. J. Engine Res.* 3 (2002) 223–248.
- [15] S. Kook, C. Bae, P. C. Miles, D. Choi, L. M. Pickett, The influence of charge dilution and injection timing on low-temperature diesel combustion and emissions, SAE paper (2005) 2005-01-3837.
- [16] X. Lü, D. Han, Z. Huang, Fuel design and management for the control of advanced compression-ignition combustion modes, *Prog. Energy Combust. Sci.* 37 (2011) 741–783.
- [17] S. Saxena, I. D. Bedoya, Fundamental phenomena affecting low temperature combustion and HCCI engines, high load limits and strategies for extending these limits, *Prog. Energy Combust. Sci.* 39 (2013) 457–488.
- [18] B. Johansson, Fuels and combustion, in: M. Boot (Ed.), *Biofuels from Lignocellulosic Biomass: Innovations beyond Bioethanol*, Wiley-VCH Verlag GmbH & Co. KGaA, 2016, pp. 1–27.
- [19] A. K. Agarwal, A. P. Singh, R. K. Maurya, Evolution, challenges and path forward for low temperature combustion engines, *Prog. Energy Combust. Sci.* 61 (2017) 1–56.
- [20] J. E. Dec, Advanced compression-ignition combustion for high efficiency and ultra-low no_x and soot, in: T. K. D. Crolla, D.E. Foster, N. Vaughan (Eds.), *Encyclopedia of Automotive Engineering*, John Wiley & Sons, Ltd, 2014, pp. 1–40.
- [21] X. Lu, D. Han, Z. Huang, Fuel design and management for the control of advanced compression-ignition combustion modes, *Prog. Energy Combust. Sci.* 37 (2011) 741–783.
- [22] S. L. Kokjohn, R. M. Hanson, D. A. Splitter, R. D. Reitz, Fuel reactivity controlled compression ignition (RCCI): a pathway to controlled high-efficiency clean combustion, *Int. J. Engine Res.* 12 (2011) 209–226.

-
- [23] R. D. Reitz, G. Duraisamy, Review of high efficiency and clean reactivity controlled compression ignition (RCCI) combustion in internal combustion engines, *Prog. Energy Combust. Sci.* 46 (2015) 12–71.
- [24] A. Paykani, A.-H. Kakaee, P. Rahnama, R. D. Reitz, Progress and recent trends in reactivity-controlled compression ignition engines, *Int. J. Engine Res.* (2016) 481–524.
- [25] G. Kalghatgi, B. Johansson, Gasoline compression ignition approach to efficient, clean and affordable future engines, *Proc. IMechE D-J. Aut.* (2017) <http://dx.doi.org/10.1177/0954407017694275>.
- [26] D. Splitter, R. Hanson, S. Kokjohn, R. Reitz, Reactivity controlled compression ignition (RCCI) heavy-duty engine operation at mid-and high-loads with conventional and alternative fuels, SAE paper (2011) 2011-01-0363.
- [27] S. L. Kokjohn, D. A. Splitter, R. M. Hanson, R. D. Reitz, V. Manente, B. Johansson, Modeling charge preparation and combustion in diesel fuel, ethanol, and dual-fuel PCCI engines, *Atom. Sprays* 21 (2011) 107–119.
- [28] D. E. Nieman, A. B. Dempsey, R. D. Reitz, Heavy-duty RCCI operation using natural gas and diesel, *SAE Int. J. Engines* 5 (2012) 270–285.
- [29] Y. Zhang, I. Sagalovich, W. De Ojeda, A. Ickes, T. Wallner, D. D. Wickman, Development of dual-fuel low temperature combustion strategy in a multi-cylinder heavy-duty compression ignition engine using conventional and alternative fuels, *SAE Int. J. Engines* 6 (2013) 1481–1489.
- [30] J. H. Lim, R. D. Reitz, High load (21 bar IMEP) dual fuel RCCI combustion using dual direct injection, *J. Eng. Gas. Turbines Power-Trans. ASME* 136 (2014) 101514–101514.
- [31] M. Wissink, R. Reitz, Exploring the role of reactivity gradients in direct dual fuel stratification, *SAE Int. J. Engines* 9 (2016) 1036–1048.
- [32] M. Wissink, R. Reitz, The role of the diffusion-limited injection in direct dual fuel stratification, *Int. J. Engine Res.* 18 (2017) 351 – 365.
- [33] C. Kavuri, J. Paz, S. L. Kokjohn, A comparison of reactivity controlled compression ignition (RCCI) and gasoline compression ignition (GCI) strategies at high load, low speed conditions, *Energy Conv. Manag.* 127 (2016) 324–341.
- [34] J. E. Dec, Y. Yang, N. Dronniou, Improving efficiency and using E10 for higher loads in boosted engines, *SAE Int. J. Engines* 5 (3) (2012) 1009–1032.
- [35] J. C. Sutherland, C. A. Kennedy, *J. Comput. Phys.* 191 (2003) 502–524.

-
- [36] J. H. Chen, A. Choudhary, B. de Supinski, M. DeVries, E. R. Hawkes, S. Klasky, W. K. Liao, K. L. Ma, J. Mellor-Crummey, N. Podhorszki, R. Sankaran, S. Shende, C. S. Yoo, Terascale direct numerical simulations of turbulent combustion using S3D, *Comput. Sci. Discov.* 2 (2009) 015001.
- [37] T. Passot, A. Pouquet, Numerical simulation of compressible homogeneous flows in the turbulent regime, *J. Fluid Mech.* 118 (1987) 441–466.
- [38] J. H. Chen, Petascale direct numerical simulation of turbulent combustion-fundamental insights towards predictive models, *Proc. Combust. Inst.* 33 (2011) 99–123.
- [39] C. A. Kennedy, M. H. Carpenter, Several new numerical methods for compressible shear-layer simulations, *Appl. Num. Math.* 14 (1994) 397–433.
- [40] C. A. Kennedy, M. H. Carpenter, R. M. Lewis, Low-storage, explicit Runge-Kutta schemes for the compressible Navier-Stokes equations, *Appl. Num. Math.* 35 (2000) 117–219.
- [41] R. J. Kee, F. M. Rupley, E. Meeks, J. A. Miller, CHEMKIN-III: A FORTRAN chemical kinetics package for the analysis of gas-phase chemical and plasma kinetics, Tech. Rep. SAND96-8216, Sandia National Laboratories (1996).
- [42] R. J. Kee, G. Dixon-Lewis, J. Warnatz, M. E. Coltrin, J. A. Miller, A Fortran computer code package for the evaluation of gas-phase multicomponent transport properties, Tech. Rep. SAND86-8246, Sandia National Laboratories (1986).
- [43] J. E. Dec, W. Hwang, M. Sjöberg, An investigation of thermal stratification in HCCI engines using chemiluminescence imaging, *SAE Trans.* (2006) 2006-01-1518.
- [44] J. A. Eng, Characterization of pressure waves in HCCI combustion, SAE paper (2002) 2002-01-2859.
- [45] A. Babajimopoulos, G. A. Lavoie, D. N. Assanis, Modeling HCCI combustion with high levels of residual gas fraction - a comparison of two VVA strategies, SAE paper (2003) 2003-01-3220.
- [46] J. E. Dec, W. Hwang, Characterizing the development of thermal stratification in an HCCI engine using planar-imaging thermometry, SAE Trans. paper (2009) 2009-01-0650.
- [47] M. Sjöberg, J. E. Dec, Smoothing heat-release rates using partial fuel stratification with two-stage ignition fuels, SAE paper.
- [48] R. Sankaran, H. G. Im, E. R. Hawkes, J. H. Chen, The effects of non-uniform temperature distribution on the ignition of a lean homogeneous hydrogen-air mixture, *Proc. Combust. Inst.* 30 (2005) 875–882.

-
- [49] J. H. Chen, E. R. Hawkes, R. Sankaran, S. D. Mason, H. G. Im, Direct numerical simulation of ignition front propagation in a constant volume with temperature inhomogeneities: I. fundamental analysis and diagnostics, *Combust. Flame* 145 (2006) 128–144.
- [50] E. R. Hawkes, R. Sankaran, P. Pébay, J. H. Chen, Direct numerical simulation of ignition front propagation in a constant volume with temperature inhomogeneities: II. parametric study, *Combust. Flame* 145 (2006) 145–159.
- [51] G. Bansal, H. G. Im, Autoignition and front propagation in low temperature combustion engine environments, *Combust. Flame* 158 (2011) 2105–2112.
- [52] C. S. Yoo, T. Lu, J. H. Chen, C. K. Law, Direct numerical simulations of ignition of a lean *n*-heptane/air mixture with temperature inhomogeneities at constant volume: Parametric study, *Combust. Flame* 158 (2011) 1727–1741.
- [53] C. S. Yoo, Z. Luo, T. Lu, H. Kim, J. H. Chen, A DNS study of ignition characteristics of a lean *iso*-octane/air mixture under ϕ and SACI conditions, *Proc. Combust. Inst.* 34 (2013) 2985–2993.
- [54] W. Hwang, J. E. Dec, M. Sjöberg, Fuel stratification for low-load HCCI combustion: Performance & fuel-PLIF measurements, *SAE Trans. paper* 116 (2007) 2007-01-4130.
- [55] J. E. Dec, M. Sjöberg, A parametric study of HCCI combustion - the sources of emissions at low loads and the effects of GDI fuel injection, *SAE Trans. paper* 112 (2003) 2003-01-0752.
- [56] R. R. Steeper, S. D. Zilwa, Improving the no_x - co_2 .
- [57] P. W. Aroonsrosopon, P. Werner, J. O. Waldman, Expanding the HCCI operation with the charge stratification, *SAE Tran. paper* 113 (2004) 2004-01-1756.
- [58] L. Koopmans, I. Denbratt, A four stroke camless engine, operated in homogeneous charge compression ignition mode with commercial gasoline, *SAE paper* (2001) 2001-01-3610.
- [59] A. Fuhhapter, W. F. Piock, G. K. Fraidl, CSI - controlled auto ignition - the best solution for the fuel consumption - versus emission trade-off?, *SAE paper* (2003) 2003-01-0754.
- [60] H. Persson, A. Hultqvist, B. Johanass, A. Remón, Investigation of the early flame development in spark assisted combustion using high speed chemiluminescence imaging, *SAE paper* (2007) 2007-01-0212.
- [61] H. A. El-Asrag, Y. Ju, Direct numerical simulations of exhaust gas recirculation effect on multistage autoignition in the negative temperature combustion regime for stratified HCCI flow conditions by using H_2O_2 addition, *Combust. Theory Model.* 17 (2013) 316–334.

-
- [62] T. Lu, C. K. Law, Diffusion coefficient reduction through species bundling, *Combust. Flame* 148 (2007) 117–126.
- [63] T. Lu, C. K. Law, Strategies for mechanism reduction for large hydrocarbons: *n*-heptane, *Combust. Flame* 154 (2008) 153–163.
- [64] T. Lu, C. K. Law, C. S. Yoo, J. H. Chen, Dynamic stiffness removal for direct numerical simulations, *Combust. Flame* 156 (2009) 1542–1551.
- [65] T. Lu, C. K. Law, Toward accommodating realistic fuel chemistry in large-scale computations, *Prog. Energy Combust. Sci.* 35 (2009) 192–215.
- [66] W. Liu, R. Sivaramakrishnan, M. J. Davis, S. Som, D. E. Longman, T. Lu, Development of a reduced biodiesel surrogate model for compression ignition engine modeling, *Proc. Combust. Inst.* 34 (2013) 401–409.
- [67] S. M. Sarathy, U. Niemann, C. Yeung, R. Ghehlich, C. K. Westbrook, M. Plomer, Z. Luo, M. Mehl, W. J. Pitz, K. Seshadri, M. J. Thomson, T. Lu, *Proc. Combust. Inst.* 34 (2013) 1015–1023.
- [68] X. L. Zheng, T. Lu, C. K. Law, Experimental counterflow ignition temperatures and reaction mechanisms of 1,3-butadiene, *Proc. Combust. Inst.* 31 (2007) 367–375.
- [69] R. Sankaran, E. R. Hawkes, J. H. Chen, T. Lu, C. K. Law, Structure of a spatially developing turbulent lean methane-air bunsen flame, *Proc. Combust. Inst.* 31 (2007) 1291–1298.
- [70] T. Lu, C. K. Law, Systematic approach to obtain analytic solutions of quasi steady state species in reduced mechanisms, *J. Phys. Chem. A* 110 (2006) 13202–13208.
- [71] T. Lu, C. K. Law, A criterion based on computational singular perturbation for the identification of quasi steady state species: A reduced mechanism for methane oxidation with NO chemistry, *Combust. Flame* 154 (2008) 761–774.
- [72] Y. Huang, C. J. Sung, Laminar flame speeds of primary reference fuels and reformer gas mixtures, *Combust. Flame* 139 (2004) 239–351.
- [73] S. Jerzembeck, N. Peters, P. Pepiot-Desjardins, H. Pitsch, Laminar burning velocities at high pressure for primary reference fuels and gasoline: Experimental and numerical investigation, *Combust. Flame* 156 (2009) 292–301.
- [74] C. S. Yoo, Y. Wang, A. Trouvé, H. G. Im, Characteristic boundary conditions for direct simulations of turbulent counterflow flames, *Combust. Theory Model.* 9 (2005) 617–646.

-
- [75] C. S. Yoo, H. G. Im, Characteristic boundary conditions for simulations of compressible reacting flows with multi-dimensional, viscous and reaction effects, *Combust. Theory Model.* 11 (2007) 259–286.
- [76] C. S. Yoo, H. G. Im, Transient soot dynamics in turbulent nonpremixed ethylene-air counterflow flames, *Proc. Combust. Inst.* 31 (2007) 701–708.
- [77] C. S. Yoo, R. Sankaran, J. H. Chen, Three-dimensional direct numerical simulation of a turbulent lifted hydrogen jet flame in heated coflow: Flame stabilization and structure, *J. Fluid Mech.* 640 (2009) 453–481.
- [78] T. Lu, C. S. Yoo, J. H. Chen, C. K. Law, Three-dimensional direct numerical simulation of a turbulent lifted hydrogen jet flame in heated coflow: a chemical explosive mode analysis, *J. Fluid Mech.* 652 (2010) 45–64.
- [79] C. S. Yoo, E. S. Richardson, R. Sankaran, J. H. Chen, A DNS study of a turbulent lifted ethylene jet flame in highly-heated coflow, *Proc. Combust. Inst.* 33 (2011) 1619–1627.
- [80] Z. Luo, C. S. Yoo, E. S. Richardson, J. H. Chen, C. K. Law, T. Lu, Chemical explosive mode analysis for a turbulent lifted ethylene jet flame in highly-heated coflow, *Combust. Flame* 159 (2012) 265–274.
- [81] R. W. Grout, A. Gruber, C. S. Yoo, J. H. Chen, Direct numerical simulation of flame stabilization downstream of a transverse fuel jet in cross-flow, *Proc. Combust. Inst.* 33 (2011) 1629–1637.
- [82] H. Kolla, R. W. Grout, A. Gruber, J. H. Chen, Mechanisms of flame stabilization and blowout in a reacting turbulent hydrogen jet in cross-flow, *Combust. Flame* 159 (2012) 2755–2766.
- [83] R. Shan, C. S. Yoo, J. H. Chen, T. Lu, Computational diagnostics for *n*-heptane flames with chemical explosive mode analysis, *Combust. Flame* 159 (2012) 3119–3127.
- [84] C. S. Yoo, H. G. Im, Transient dynamics of edge flames in a laminar nonpremixed hydrogen-air counterflow, *Proc. Combust. Inst.* 20 (2005) 349–356.
- [85] C. S. Yoo, J. H. Chen, J. H. Frank, A numerical study of transient ignition and flame characteristics of diluted hydrogen versus heated air in counterflow, *Combust. Flame* 156 (2009) 140–151.
- [86] T. Echekki, J. H. Chen, Direct numerical simulation of autoignition in non-homogeneous hydrogen-air mixtures, *Combust. Flame* 134 (2003) 169–191.

-
- [87] T. Bieleveld, A. Frassoldti, A. Cuoci, T. Faravelli, E. Ranzi, U. Niemann, K. Seshadri, Experimental and kinetic modeling study of combustion of gasoline, its surrogates and components in laminar non-premixed flows, *Proc. Combust. Inst.* 32 (2009) 493–500.
- [88] K. Tanoue, T. Baba, T. Matsunaga, Experimental study of combustion of ethanol and primary reference fuels in laminar nonuniform flows, *Proc. Combust. Inst.* 33 (2011) 1029–1035.
- [89] A. Hultqvist, M. Christenson, B. Johansson, M. Richter, J. Nygren, J. Hult, M. Alden, The HCCI combustion process in a single cycle - speed fuel tracer LIF and chemiluminescence imaging, SAE paper (2002) 2002–01–0424.
- [90] M. B. Luong, Z. Luo, T. Lu, S. H. Chung, C. S. Yoo, Direct numerical simulations of the ignition of lean primary reference fuel/air mixtures with temperature inhomogeneities, *Combust. Flame* 160 (2013) 2038–2047.
- [91] Y. Yang, J. Dec, N. Dronniou, M. Sjöberg, W. Cannella, Partial fuel stratification to control HCCI heat release rates: Fuel composition and other factors affecting pre-ignition reactions of two-stage ignition fuels, *SAE Int. J. Engines* 4 (2011) 1903–1920.
- [92] Y. Yang, J. E. Dec, N. Dronniou, M. Sjöberg, Tailoring HCCI heat-release rates with partial fuel stratification: Comparison of two-stage and single-stage-ignition fuels, *Proc. Combust. Inst.* 33 (2011) 3047–3055.
- [93] A. Krisman, E. R. Hwakes, S. Kook, M. Sjöberg, J. E. Dec, On the potential of ethanol fuel stratification to extend the high load limit in stratified-charge compression-ignition engines, *Fuel* 99 (2012) 45–54.
- [94] J. E. Dec, M. Sjöberg, Isolating the effects of fuel chemistry on combustion phasing in an HCCI engine and the potential of fuel stratification for ignition control, SAE paper (2004) 2004–01–0557.
- [95] J. Ma, L-Xingcai, L. Ji, Z. Huang, Evaluation of SCCI potentials in comparison to HCCI and conventional DICI combustion using *n*-heptane, *Energy Fuels* 22 (2) (2008) 954–960.
- [96] D. Dahl, M. Andersson, A. Berntsson, I. Denbratt, L. Koopmans, Reducing pressure fluctuations at high loads by means of charge stratification in HCCI combustion with negative valve overlap, SAE paper (2009) 2009–01–1785.
- [97] Y. Wada, J. Senda, Demonstrating the potential of mixture distribution control for controlled combustion and emissions reduction in premixed charge compression ignition engines, SAE paper (2009) 2009–01–0498.

-
- [98] R. E. Herold, J. M. Krasselt, D. E. Foster, J. B. Ghandhi, D. L. Reuss, P. M. Najt, Investigations into the effects of thermal and compositional stratification on HCCI combustion – part II: optical engine results, SAE paper (2009) 2009–01–1106.
- [99] J. Krasselt, D. Foster, J. Ghandhi, R. Herold, D. Reuss, P. Najt, Investigations into the effects of thermal and compositional stratification on HCCI combustion – part I: Metal engine results, SAE paper (2009) 2009–01–1105.
- [100] G. Kalghatgi, L. Hildingsson, A. Harrison, B. Johansson, Autoignition quality of gasoline fuels in partially premixed combustion in diesel engines, *Proc. Combust. Inst.* 33 (2) (2011) 3015–3021.
- [101] A. Viggiano, V. Magi, An investigation on the performance of partially stratified charge CI ethanol engines, SAE paper (2011) 2011–01–0837.
- [102] D. Jung, O. Kwon, O. T. Lim, Comparison of DME HCCI operating ranges for the thermal stratification and fuel stratification based on a multi-zone model, *Journal of Mechanical Science and Technology* 25 (2011) 1383–1390.
- [103] J. E. Dec, Y. Yang, N. Dronniou, Boosted HCCI - controlling pressure-rise rates for performance improvements using partial fuel stratification with conventional gasoline, *SAE Int. J. Engines* 4 (2011) 1169–1189.
- [104] Y. Yang, J. Dec, N. Dronniou, W. Cannella, Boosted HCCI combustion using low-octane gasoline with fully premixed and partially stratified charges, *SAE Int. J. Engines*.
- [105] R. Yu, X.-S. Bai, Direct numerical simulation of lean hydrogen/air auto-ignition in a constant volume enclosure, *Combust. Flame* 160 (2013) 1706–1716.
- [106] H. A. El-Asrag, Y. Ju, Direct numerical simulations of no_x effect on multistage autoignition of DME/air mixture in the negative temperature coefficient regime for stratified HCCI engine conditions, *Combust. Flame* 161 (2014) 256–269.
- [107] F. Ma, M. A. Hanna, Biodiesel production: a review, *Bioresource Technol.* 70 (1999) 1–15.
- [108] A. K. Agarwal, Biofuels (alcohols and biodiesel) applications as fuels for internal combustion engines, *Prog. Energy Combust. Sci.* 33 (2007) 233–271.
- [109] A. Demirbas, Progress and recent trends in biofuels, *Prog. Energy Combust. Sci.* 33 (2007) 1–18.
- [110] G. Knothe, Biodiesel and renewable diesel: A comparison, *Prog. Energy Combust. Sci.* 36 (2010) 364–373.

-
- [111] N. Komninos, C. Rakopoulos, Modeling HCCI combustion of biofuels: A review, *Renew. Sust. Energ. Rev.* 16 (2012) 1588–1610.
- [112] Z. Luo, M. Plomer, T. Lu, S. Som, D. E. Longman, S. Sarathy, W. J. Pitz, A reduced mechanism for biodiesel surrogates for compression ignition engine applications, *Fuel* 99 (2012) 143–153.
- [113] C. Westbrook, C. Naik, O. Herbinet, W. Pitz, M. Mehl, S. Sarathy, H. Curran, Detailed chemical kinetic reaction mechanisms for soy and rapeseed biodiesel fuels, *Combust. Flame* 158 (2011) 742–755.
- [114] T. Lu, C. K. Law, C. S. Yoo, J. H. Chen, Dynamic stiffness removal for direct numerical simulations, *Combust. Flame* 156 (2009) 1542–1551.
- [115] J. B. Martz, H. Kwak, H. G. Im, G. A. Lavoie, D. N. Assanis, Combustion regime of a reacting front propagating into an auto-igniting mixture, *Proc. Combust. Inst.* 33 (2011) 1540–7489.
- [116] R. Hasegawa, H. Yanagihara, HCCI combustion in DI diesel engine, SAE paper (2003) 2003-01-0745.
- [117] S. B. Pope, *Turbulent flows*, Cambridge University Press, 2000.
- [118] A. Bhagatwala, T. Lu, J. H. Chen, Direct numerical simulations of HCCI/SACI with ethanol, *Combust. Flame* 161 (2014) 1826–1841.
- [119] Z. Luo, M. Plomer, T. Lu, S. Som, D. E. Longman, A reduced mechanism for biodiesel surrogates with low temperature chemistry for compression ignition engine applications 16 (2012) 369–385.
- [120] S. O. Kim, M. B. Luong, J. H. Chen, C. S. Yoo, A DNS study of the ignition of lean PRF/air mixtures with temperature inhomogeneities under high pressure and intermediate temperature, *Combust. Flame* 162 (2015) 717–726.
- [121] M. B. Luong, T. Lu, S. H. Chung, C. S. Yoo, Direct numerical simulations of the ignition of a lean biodiesel/air mixture with temperature and composition inhomogeneities at high pressure and intermediate temperature, *Combust. Flame* 161 (2014) 2878–2889.
- [122] V. Mittal, D. Cook, H. Pitsch, An extended multi-regime flamelet model for IC engines, *Combust. Flame* 159 (2012) 2767–2776.
- [123] M. Talei, E. R. Hawkes, Ignition in compositionally and thermally stratified *n*-heptane/air mixtures: A direct numerical simulation study, *Proc. Combust. Inst.* 35 (2015) 3027–3035.

-
- [124] G. Bansal, A. Mascarenhas, J. H. Chen, Direct numerical simulations of autoignition in stratified dimethyl-ether (DME)/air turbulent mixtures, *Combust. Flame* 162 (2015) 688–702.
- [125] S. L. Kokjohn, M. P. B. Musculus, R. D. Reitz, Evaluating temperature and fuel stratification for heat-release rate control in a reactivity-controlled compression-ignition engine using optical diagnostics and chemical kinetics modeling, *Combust. Flame* 162 (2015) 2729–2742.
- [126] J. E. Dec, Y. Yang, Boosted HCCI for high power without engine knock and with ultra-low no_x emissions - using conventional gasoline, SAE paper (2010) 2010-01-1086.
- [127] B. Wolk, J.-Y. Chen, J. E. Dec, Computational study of the pressure dependence of sequential auto-ignition for partial fuel stratification with gasoline, *Proc. Combust. Inst.* 35 (2015) 2993–3000.
- [128] S. Tanaka, F. Ayala, J. C. Keck, J. B. Heywood, Two-stage ignition in combustion and control by fuels and additives, *Combust. Flame* 132 (2003) 219–239.
- [129] C. K. Law, *Combustion Physics*, Cambridge University Press, 2006.
- [130] R. Borghi, Turbulent combustion modelling, *Prog. Energy Combust. Sci.* 14 (1988) 245–292.
- [131] N. Peters, *Turbulent combustion*, Cambridge University Press, 2000.
- [132] D. J. Cook, H. Pitch, J. H. Chen, E. R. Hawkes, Flamelet-based modeling of auto-ignition with thermal inhomogeneities for application to HCCI engines, *Proc. Combust. Inst.* 31 (2007) 2903–2911.
- [133] F. Bisetti, J.-Y. Chen, J. H. Chen, E. R. Hawkes, Probability density function treatment of turbulence/chemistry interactions during the ignition of a temperature-stratified mixture for application to HCCI engine modeling, *Combust. Flame* 155 (2008) 571–584.
- [134] F. Salehi, M. Talei, E. R. Hawkes, C. S. Yoo, T. Lucchini, G. D’Errico, S. Kook, Conditional moment closure modelling for with temperature inhomogeneities, *Proc. Combust. Inst.* 35 (2015) 3087–3095.
- [135] F. Salehi, M. Talei, E. R. Hawkes, C. S. Yoo, T. Lucchini, G. D’Errico, S. Kook, A comparative study of conditional moment closure modelling for ignition of *iso*-octane and *n*-heptane in thermally stratified mixtures, *Flow Turbul. Combust.* 95 (2015) 1–28.
- [136] S. L. Kokjohn, R. M. Hanson, D. A. Splitter, R. D. Reitz, Experiments and modeling of dual-fuel and PCCI combustion using in-cylinder fuel blending, *SAE Int. J. Engines* 2 (2010) 24–39.

-
- [137] S. Kokjohn, R. Hanson, D. Splitter, J. Kaddatz, R. Reitz, Fuel reactivity controlled compression ignition (RCCI) combustion in light- and heavy-duty engines, *SAE Int. J. Engines* 4 (2011) 360–374.
- [138] S. Kokjohn, R. Reitz, D. Splitter, M. Musculus, Investigation of fuel reactivity stratification for controlling PCI heat-release rates using high-speed chemiluminescence imaging and fuel tracer fluorescence, *SAE paper* (2012) 2012-01-0375.
- [139] R. M. Hanson, S. L. Kokjohn, D. A. Splitter, R. D. Reitz, An experimental investigation of fuel reactivity controlled PCCI combustion in a heavy-duty engine, *SAE Int. J. Engines* 3 (2010) 700–716.
- [140] R. Hanson, S. Kokjohn, D. Splitter, R. Reitz, Fuel effects on reactivity controlled compression ignition (RCCI) combustion at low load, *SAE Int. J. Engines* 4 (2011) 394–411.
- [141] D. Splitter, S. Kokjohn, K. Rein, R. Hanson, S. Sanders, R. Reitz, An optical investigation of ignition processes in fuel reactivity controlled PCCI combustion, *SAE Int. J. Engines* 3 (2010) 142–162.
- [142] A. Bhagatwala, R. Sankaran, S. Kokjohn, J. H. Chen, Numerical investigation of spontaneous flame propagation under RCCI conditions, *Combust. Flame* 162 (2015) 3412–3426.
- [143] Y. B. Zeldovich, Regime classification of an exothermic reaction with nonuniform initial conditions, *Combust. Flame* 39 (1980) 211–214.
- [144] M. B. Luong, G. H. Yu, S. H. Chung, C. S. Yoo, Ignition of a lean PRF/air mixture under RCCI/SCCI conditions: A comparative DNS study, *Proc. Combust. Inst.* 36 (2017) 3623–3631.
- [145] C. Westbrook, Chemical kinetics of hydrocarbon ignition in practical combustion system, *Proc. Combust. Inst.* 28 (2000) 1563–1577.
- [146] W. Hwang, J. E. Dec, M. Sjöberg, Spectroscopic and chemical-kinetic analysis of the phases of HCCI autoignition and combustion for single- and two-stage ignition fuels, *Combust. Flame* 154 (2008) 387–409.
- [147] H. Ando, Y. Sakai, K. Kuwahara, Universal rule of hydrocarbon oxidation, *SAE paper* (2009) 2009-01-0948.
- [148] D. Vuilleumier, D. Kozarac, M. Mehl, S. Saxena, W. J. Pitz, R. W. Dibble, J.-Y. Chen, S. Mani Sarathy, Intermediate temperature heat release in an engine fueled by ethanol/*n*-heptane mixtures: An experimental and modeling study, *Combust. Flame* 161 (2014) 680–695.

-
- [149] C. K. Westbrook, Y. Mizobuchi, T. J. Poinso, P. J. Smith, J. Warnatz, Computational combustion, *Proc. Combust. Inst.* 30 (2005) 125–157.
- [150] C. K. Westbrook, W. J. Pitz, O. Herbinet, H. J. Curran, E. J. Silke, A comprehensive detailed chemical kinetic reaction mechanism for combustion of n-alkane hydrocarbons from n-octane to n-hexadecane, *Combust. Flame* 156 (2009) 181–199.
- [151] C. K. Westbrook, Biofuels combustion, *Annu. Rev. Phys. Chem.* 64 (2013) 201–219.
- [152] C. K. Westbrook, W. J. Pitz, Fundamental chemical kinetics, in: T. K. D. Crolla, D.E. Foster, N. Vaughan (Eds.), *Encyclopedia of Automotive Engineering*, John Wiley & Sons, Ltd, 2014, pp. 1–14.
- [153] K. Kuwahara, Y. Hiramura, S. Ohmura, M. Furutani, Y. Sakai, H. Ando, Chemical kinetics study on effect of pressure and fuel, O_2 and N_2 molar concentrations on hydrocarbon ignition process, *SAE Int. J. Engines* 6 (2012) 520–532.
- [154] H. Tanaka, S. Somezawa, T. Sako, Y. Sakai, H. Ando, K. Kuwahara, Fuel design concept for robust ignition in HCCI engine and its application to optimize methane-based blend, *SAE Int. J. Engines* 7 (2014) 807–819.
- [155] K. Kuwahara, T. Tada, M. Furutani, Y. Sakai, H. Ando, Chemical kinetics study on two-stage main heat release in ignition process of highly diluted mixtures, *SAE Int. J. Engines* 6 (2013) 520–532.
- [156] M. B. Luong, G. H. Yu, S. H. Chung, C. S. Yoo, Ignition of a lean PRF/air mixture under RCCI/SCCI conditions: Chemical aspects, *Proc. Combust. Inst.* 36 (2017) 3587–3596.
- [157] J. Zádor, C. A. Taatjes, R. X. Fernandes, Kinetics of elementary reactions in low-temperature autoignition chemistry, *Prog. Energy Combust. Sci.* 37 (4) (2011) 371–421.
- [158] J. Zádor, H. Huang, O. Welz, J. Zetterberg, D. L. Osborn, C. A. Taatjes, Directly measuring reaction kinetics of QOOH - a crucial but elusive intermediate in hydrocarbon autoignition, *Phys. Chem. Chem. Phys.* 15 (2013) 10753–10760.
- [159] C. F. Goldsmith, W. H. Green, S. J. Klippenstein, Role of $O_2 + QOOH$ in low-temperature ignition of propane. 1. temperature and pressure dependent rate coefficients, *J. Phys. Chem. A.* 116 (2012) 3325–3346.
- [160] A. Miyoshi, Systematic computational study on the unimolecular reactions of alkylperoxy (RO_2), hydroperoxyalkyl (QOOH), and hydroperoxyalkylperoxy (O_2QOOH) radicals, *J. Phys. Chem. A.* 115 (2011) 3301–3325.

-
- [161] A. Kazakov, M. Chaos, Z. Zhao, F. L. Dryer, Computational singular perturbation analysis of two-stage ignition of large hydrocarbons, *J. Phys. Chem. A.* 110 (21) (2006) 7003–7009.
- [162] C. K. Law, P. Zhao, NTC-affected ignition in nonpremixed counterflow, *Combust. Flame* 159 (3) (2012) 1044–1054.
- [163] G. Mittal, M. Chaos, C.-J. Sung, F. L. Dryer, Dimethyl ether autoignition in a rapid compression machine: Experiments and chemical kinetic modeling, *Fuel Process. Technol.* 89 (12) (2008) 1244–1254.
- [164] P. Zhao, C. K. Law, The role of global and detailed kinetics in the first-stage ignition delay in NTC-affected phenomena, *Combust. Flame* 160 (11) (2013) 2352–2358.
- [165] H. Zhang, E. R. Hawkes, J. H. Chen, S. Kook, A numerical study of the autoignition of dimethyl ether with temperature inhomogeneities, *Proc. Combust. Inst.* 34 (2013) 803–812.
- [166] F. Zhang, R. Yu, X. S. Bai, Effect of split fuel injection on heat release and pollutant emissions in partially premixed combustion of PRF70/air/EGR mixtures, *Appl. Energy* 149 (2015) 283–296.
- [167] U. Egüz, N. C. J. Maes, C. a. J. Leermakers, L. M. T. Somers, L. P. H. D. Goey, Predicting auto-ignition characteristics of RCCI combustion using a multi-zone model, *Int.J Automot. Technol.* 14 (2013) 693–699.
- [168] P. Domingo, L. Vervisch, Triple flames and partially premixed combustion in autoignition of non-premixed turbulent mixtures, *Symp. (Int.) Combust.* 26 (1996) 233–240.
- [169] F. Zhang, R. Yu, X. S. Bai, Direct numerical simulation of PRF70/air partially premixed combustion under IC engine conditions, *Proc. Combust. Inst.* 35 (2015) 2975–2982.
- [170] J. B. Heywood, *Internal combustion engine fundamentals*, McGraw-Hill New York, 1988.
- [171] J. O. Hirschfelder, C. F. Curtiss, B. R. Bird, *Molecular Theory of Gases and Liquids*, Wiley New York, 1965.
- [172] S. Tanaka, F. Ayala, J. C. Keck, A reduced chemical kinetic model for HCCI combustion of primary reference fuels in a rapid compression machine, *Combust. Flame* 133 (4) (2003) 467–481.
- [173] Y. Ra, R. D. Reitz, A reduced chemical kinetic model for IC engine combustion simulations with primary reference fuels, *Combust. Flame* 155 (4) (2008) 713–738.

-
- [174] H. Wang, M. Yao, R. D. Reitz, Development of a reduced primary reference fuel mechanism for internal combustion engine combustion simulations, *Energy Fuels* 27 (12) (2013) 7843–7853.
- [175] Y. Wang, C. J. Rutland, Effects of temperature and equivalence ratio on the ignition of *n*-heptane fuel spray in turbulent flow, *Proc. Combust. Inst.* 30 (2005) 893–900.
- [176] N. Peters, H. Pitsch, Solving combustion chemistry in engine simulations, in: T. K. D. Crolla, D.E. Foster, N. Vaughan (Eds.), *Encyclopedia of Automotive Engineering*, John Wiley & Sons, Ltd, 2014, pp. 1–9.
- [177] F. Zhang, H. F. Liu, R. Yu, M. Yao, X. S. Bai, Direct numerical simulation of H₂/air combustion with composition stratification in a constant volume enclosure relevant to engines, *Int. J. Hydrog. Energy* 41 (2016) 13758–13770.
- [178] P. Trisjono, H. Pitsch, Systematic analysis strategies for the development of combustion models from DNS: a review, *Flow Turbul. Combust.* 95 (2015) 231–259.
- [179] H. G. Im, P. G. Arias, S. Chaudhuri, H. A. Uranakara, Direct numerical simulations of statistically stationary turbulent premixed flames, *Combust. Sci. Technol.* 188 (2016) 1182–1198.
- [180] H. Pitsch, Large-eddy simulation of turbulent combustion 38 (1) (2006) 453–482.
- [181] C. J. Rutland, Large-eddy simulations for internal combustion engines ? a review, *Int. J. Engine Res.* 12 (5) (2011) 421–451.
- [182] G. T. Kalghatgi, The outlook for fuels for internal combustion engines, *Int. J. Engine Res.* 15 (4) (2014) 383–398.
- [183] G. T. Kalghatgi, *Fuel/engine interactions*, SAE International, 2014.
- [184] G. T. Kalghatgi, Developments in internal combustion engines and implications for combustion science and future transport fuels, *Proc. Combust. Inst.* 35 (2015) 101–115, 00072.
- [185] G. Kalghatgi, I. Algunaibet, K. Morganti, On knock intensity and superknock in SI engines, *SAE Int. J. Engines* 10 2017–01–0689.
- [186] Z. Wang, H. Liu, R. D. Reitz, Knocking combustion in spark-ignition engines, *Prog. Energy Combust. Sci.* 61 (2017) 78–112.
- [187] Y. Ju, C. B. Reuter, S. H. Won, Numerical simulations of premixed cool flames of dimethyl ether/oxygen mixtures, *Combust. Flame* 162 (2015) 3580–3588.
- [188] Y. Ju, On the propagation limits and speeds of premixed cool flames at elevated pressures, *Combust. Flame* 178 (2017) 61–69.

- [189] A. Krisman, E. R. Hawkes, M. Talei, A. Bhagatwala, J. H. Chen, Characterisation of two-stage ignition in diesel engine-relevant thermochemical conditions using direct numerical simulation, *Combust. Flame* 172 (2016) 326–341.
- [190] A. Krisman, E. R. Hawkes, M. Talei, A. Bhagatwala, J. H. Chen, A direct numerical simulation of cool-flame affected autoignition in diesel engine-relevant conditions, *Proc. Combust. Inst.* 36 (3) (2017) 3567–3575.
- [191] H. Lu, C. J. Rutland, Structural subgrid-scale modeling for large-eddy simulation: A review, *Acta Mech. Sin.* 32 (4) (2016) 567–578.
- [192] F. Salehi, M. Talei, E. R. Hawkes, A. Bhagatwala, J. H. Chen, C. S. Yoo, S. Kook, Doubly conditional moment closure modelling for HCCI with temperature inhomogeneities, *Proc. Combust. Inst.* 36 (2017) 3677–3685.